Ultra-High Intense Laser on Dense Plasmas : from Periodic to Chaotic Dynamics

Guillaume Blaclard

Thèse de doctorat

NNT : 2020UPASS133

université PARIS-SACLAY

Ultra-High Intense Laser on Dense Plasmas: from Periodic to Chaotic Dynamics

Thèse de doctorat de l'université Paris-Saclay

École doctorale n° 572 Ondes et Matières (EDOM)
Spécialité de doctorat : Physique
Unité de recherche : Université Paris-Saclay, CEA, CNRS, LIDYL
91191, Gif-sur-Yvette, France
Référent : Faculté des sciences d'Orsay

Thèse présentée et soutenue à Orsay, le 2 juillet 2020, par

Guillaume BLACLARD

Composition du Jury

Jean-Marcel RAX Professeur des Universités, Ecole Polytechnique (Palaiseau)	Président
Paul GIBBON Professeur, Forschungszentrum Jülich	Rapporteur & Examinateur
Jérôme FAURE Directeur de recherche (HDR), LOA (Palaiseau)	Rapporteur & Examinateur
Julia MIKHAILOVA Professeur Assistant, Princeton University	Examinatrice
Laurent GREMILLET Ingénieur-Chercheur, CEA Bruyères-le-Châtel	Examinateur
Guy BONNAUD Professeur, INSTN	Directeur de thèse
Henri VINCENTI Ingénieur-Chercheur, CEA Saclay	Co-Encadrant
Jean-Luc VAY Chercheur Senior, LBNL (Berkeley)	Co-Encadrant

À mes deux grand-pères, Christian et Jean-Pierre,
et à mon petit frère Arthur, parti trop tôt.

Acknowledgment

Il n'est des douleurs que rien n'égale autant que celles de perdre un être cher. Malheureusement pour ma famille, la période consacrée à l'écriture de ma thèse fut endeuillée par le décès de mon petit frère Arthur, fauché au crépuscule de ses seize ans. À ce titre, je voudrais lui rendre hommage en lui dédiant ce manuscrit.

J'adresse aussi ce document à mes deux grands-pères, Christian Bernard et Jean-Pierre Blaclard. Ils m'ont tous deux à leurs manières transmis le goût des sciences et en particulier de la physique, mais aussi cette curiosité d'observer la nature, caractéristique essentielle pour un scientifique.

Pour revenir à mon travail de thèse, probablement rien ne serait arrivé si je n'avais pas rencontré en février 2015 celui qui deviendra mon directeur de thèse: Guy Bonnaud. Non seulement, j'ai eu la chance d'avoir été accepté dans son master Physique des Plasmas et de la Fusion mais il m'a en plus donné l'opportunité de réaliser un stage avec lui au sein du CEA Saclay. Je ne le remercierai jamais assez pour la confiance qu'il m'a accordée et le temps qu'il m'a consacré au cours de ces cinq dernières années.

Je voudrais aussi chaleureusement remercier mon encadrant de thèse, Henri Vincenti, pour son implication, sa rigueur et son expertise. Nous avions commencé à travailler ensemble à Berkeley lors de mon stage de master et, à ses côtés, j'ai appris les rudiments du développement informatique, de la physique des hautes intensités et de l'importance des simulations numériques. Son soutien a été sans faille lors de l'écriture de la thèse ou de la préparation de la soutenance mais, surtout, il a su être présent lors de l'épreuve familiale que j'ai vécue et cela m'a profondément touché.

Je remercie aussi grandement Fabien Quéré, responsable du groupe PHI (Physique à Haute Intensité) pour m'avoir accueilli dans son équipe. Ses grandes qualités humaines et scientifiques m'ont permis de m'épanouir au sein de son équipe. Il impose toujours plus de rigueur dans l'écriture, le traitement des données, les présentations, et je crois que c'est cela qui rend ce groupe si performant.

Je voudrais ensuite sincèrement remercier Jean-Luc Vay pour m'avoir accueilli pendant quasiment deux ans dans son équipe au Lawrence Berkeley National Laboratory. Travailler en Californie était pour moi un projet personnel dont je rêvais et j'ai beaucoup apprécié sa bonne humeur, son dynamisme et son management agile.

J'aimerais aussi adresser tous mes remerciements à l'ensemble de mes collègues que j'ai pu croiser lors de ces quatre années. Tout d'abord à Haythem Kallala et Antoine Jeandet, mes deux compagnons de route, nous aurons réussi à se motiver ensemble pour arriver au bout de

cette aventure. Ils resteront tous les deux bien plus que de simples collègues. Ensuite, à Ludovic Chopineau, Adrien Denoeud, Guillaume Bouchard, Luca Fedeli et Antonin Sainte-Marie pour leurs discussions enrichissantes et leur entrain. Enfin, à Rémi Lehe et Maxence Thévenet, mes deux collègues de Berkeley, pour m'avoir formé à coder proprement, en particulier coder à plusieurs, ce qui me sera très utile dans ma future carrière.

J'aimerais également remercier tous les membres de mon jury: le Pr Jean-Marcel Rax pour en avoir accepté la présidence, le Pr Paul Gibbon et M. Jérôme Faure en leur qualité de rapporteurs pour avoir pris le temps de lire et commenter ce manuscrit et, enfin, Mme Julia Mikhailova et M. Laurent Gremillet pour leurs questions pertinentes en tant qu'examinateurs.

Je voudrais également exprimer toute ma gratitude à l'École Doctorale Ondes et Matière et à son comité décisionnaire pour m'avoir remis le prix de thèse Physique des Ondes et de la Matière (PhOM) 2020 de l'Université Paris-Saclay, dans la spécialité « Lumière Extrême ». Je suis honoré de l'intérêt qu'ils ont porté à mon travail.

Finalement, je voudrais adresser un grand merci à tous les gens qui m'ont accompagné de près ou de loin durant ma thèse, ma famille, à commencer bien sûr par mes parents et mon frère Antoine, ou mes amis. Ils m'ont tous soutenu dans ce choix de formation qui a pu quelque fois s'avérer éprouvant mais qui se révèle tellement gratifiant quand on en arrive enfin à terme.

Et enfin merci à toi, lecteur ou lectrice, qui j'espère trouvera du plaisir à lire ces quelques lignes autant que j'ai en pris à les rédiger.

Guillaume Blaclard

This thesis manuscript is a flipbook, try it !

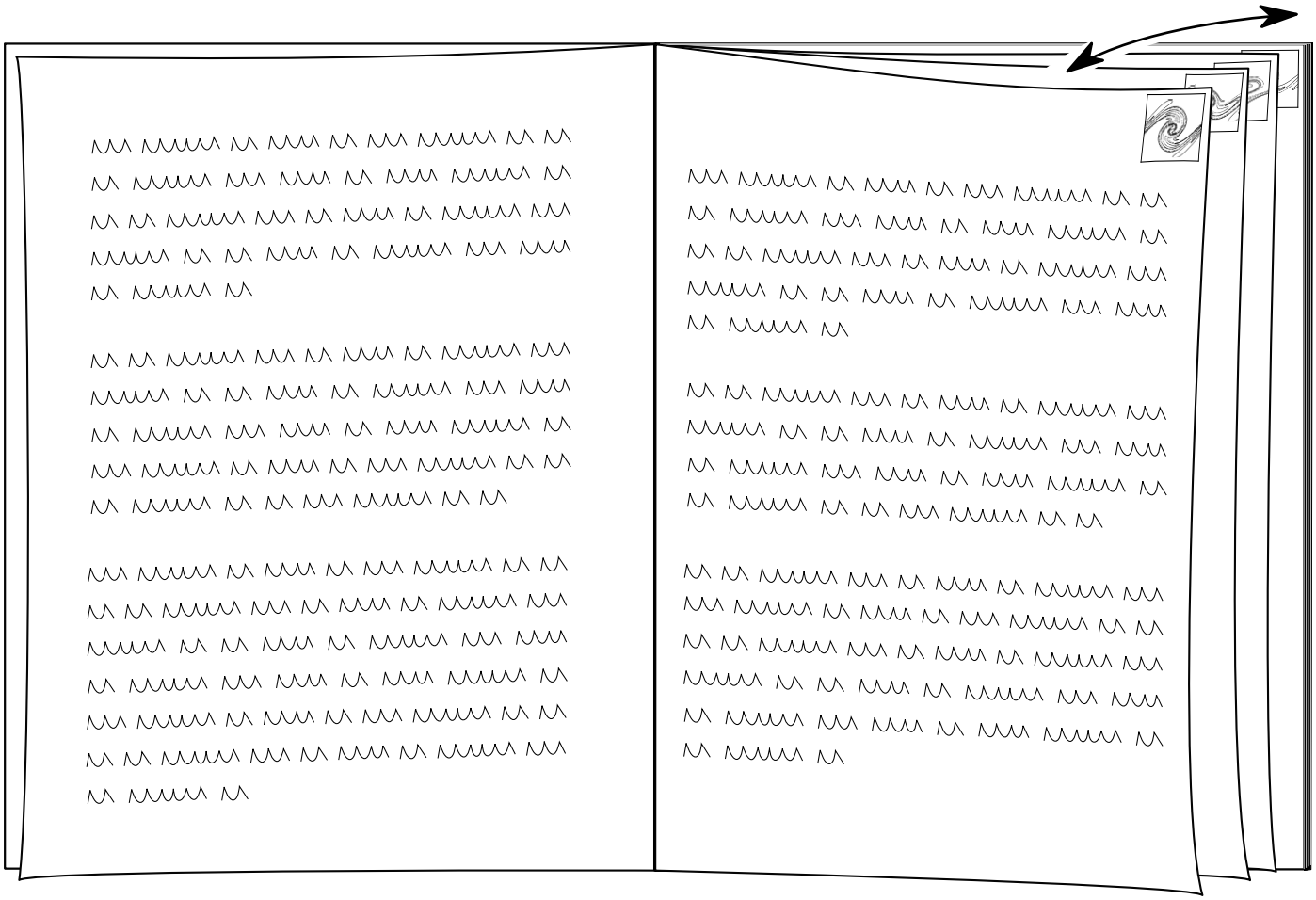

Contents

Introduction

Context

When lasers were invented in the early 1960s by [Schawlow and Townes, 1958] and [Maiman, 1960], they were immediately described as "a solution looking for a problem". Since then, such coherent light sources have found utilities in a tremendous number of applications from fundamental fields of research (chemistry, astrophysics...) to daily and industrial uses (medicine, optical discs, metallurgy, remote detection...).

Few years after the laser invention, [Lamb, 1964] proposed the *mode-locking* technique to produce pulses of light of ultra-short duration in the order of few picoseconds (1 ps = 10^{-12} s) to femtoseconds (1 fs = 10^{-15} s). Such extremely short light sources can probe the dynamics of matter at timescales not accessible otherwise. To properly track a dynamical system, the measurement process has to be faster than the evolution of this system. The laser technology thus enables temporal precision down to a few femtoseconds. The study of ultrafast dynamics is typically achieved via pump-probe experiments: an ultrashort beam (pump) first induces a perturbation in a sample ; a second pulse (probe) then monitors the state of the system after some delay. By varying the time delay between the two pulses, one can reconstruct the time evolution of the system. This technique has led to a new field of chemistry, called femtochemistery, that studies atom rearrangement within molecules during extremely short timescales. For his pioneering work in the domain [Zewail, 1988; Zewail, 1994], Ahmed Zewail received the Nobel prize in chemistry in 1999.

In 1985, the advent of the Chirped Pulse Amplification (CPA) technique and its application to lasers [Strickland and Mourou, 1985] had another formidable impact on the laser community. This technique, awarded by the Nobel Physics price in 2018, has enabled the compression of significant amount of energy ($\sim 10\,$mJ to J) in ultrashort pulses ($\sim$ tens of femtoseconds) leading to peak powers of few TW to several PW (petawatts). When tightly focused, the laser intensity I_0 on target reaches up to 10^{18-20} W.cm^{-2}. At these intensities, ordinary matter is rapidly ionized by the strong laser fields and turns into an out of equilibrium plasma, which features electrons accelerated up to the speed of light (*relativistic* velocity). The use of these lasers for scientific purposes has opened up a new research branch commonly known as ultra-high intensity (UHI) physics, which still largely remains to be explored.

The interest of the scientific community for the study of UHI physics is twofold. First, it represents a huge fundamental interest to study matter dynamics in strong electromagnetic fields. In particular, it gives access in a laboratory to physical phenomena that only occur in remote violent astrophysical processes [Remington et al., 2000]. Second, the interaction between a ultra-intense lasers and a plasma can provide novel tabletop sources of bright ionizing radiation

(extreme ultra-violet (XUV), X-rays, gamma) radiations or energetic particles (electrons, ions).

Natural phenomena such as electron motion in atoms occur on timescales even shorter than a femtosecond, as brief as few attoseconds (1 as $= 10^{-18}$ s). To gauge these processes, the light wavelength should lie in the XUV range: for a laser period $T_0 = 100$ as, the corresponding laser wavelength would be $\lambda_0 = 30$ nm. However, it turns out to be rather challenging to efficiently amplify light in that spectral range. That is why present high-power laser sources rely on titanium-sapphire lasers that emit near-infrared light at $\lambda_0 = 800$ nm. To produce XUV light, a better approach consists of using already existing femtosecond laser pulses and to create directly attosecond pulses *in situ* by a mechanism known as *high harmonic generation* (HHG). The underlying idea is to distort laser wavefronts by non-linear interactions with matter. As the deformation should be temporally periodic, the resulting wave is characterized in Fourier space by a comb of harmonic frequencies, integer multiples of the driving laser frequency (e.g., for the 30th harmonic, $\lambda_{30} = \lambda_0/30 \simeq 27$ nm or $T_{30} = 89$ as).

Alongside XUV pulses, bright relativistic electron bunches can also be used to probe matter at attosecond timescales. Indeed, due their short de Broglie length, electrons easily penetrate into most media, even those opaque for XUV radiations. Their cross section for inelastic scattering is also far smaller than for photons. They thus deposit less energy into samples, lowering the risk of non-reversible damages. The standard method to accelerate electrons up to velocities close to the speed of light relies on radiofrequency accelerators. However, because the electric fields within radiofrequency chambers are relatively low to avoid electric breakdown of the cavities ($\sim$ tens of MV.m^{-1}), electrons have to traveled over long distances (up to kilometer scales) to reach high energies.

On the other hand, compact and affordable femtosecond electron sources have been proposed that rely yet on high-power femtosecond lasers [Corde et al., 2013; Guénot et al., 2017]. When an intense laser beam ($I_0 \gtrsim 10^{18}$ W.cm^{-2}) is traveling through a gas jet, it excites a plasma wave in its wake. This wake is characterized by a succession of ion cavities void of electrons that can sustain strong space-charge electric fields (~ 100 GV.m^{-1}). These can accelerate injected electrons up to relativistic velocities within few centimeters [Tajima and Dawson, 1979; Faure, Glinec, et al., 2004; Geddes et al., 2004; Mangles et al., 2004; Esarey, Schroeder, et al., 2009]. The record of the highest energetic electron beam generated by lasers is currently held by the BELLA team in the Lawrence Berkeley Laboratory that successfully produced a 5pC-charge electron beam up to 7.8 GeV in a capillary [Gonsalves et al., 2019]. However, despite significant progress since 1990, laser wakefield acceleration currently suffers from low charge (due to the low density of a gas medium) and low reproducibility at high energy that might prevent their use in many targeted applications (colliders for example).

The proper control of these sources of particle and light however requires a very good understanding of the laser-plasma interaction processes. Due to the extremely short time and length scales at play, a deep physical insight on the interaction is however not always accessible in experiments. In that regard, the interpretation and guiding of laser-plasma experiments would probably not have been possible without the support of numerical simulations and in particular Particle-In-Cell (PIC) simulations. The latter rely on a particle-mesh approach to simulate the plasma dynamics by self-consistently solving Maxwell's equations on a grid and the Vlasov's equation discretized in phase space using Lagrangian superparticles (each superparticle representing a sample of the distribution in phase space) [Evans and Harlow, 1957; Morse and Nielson,

1969; Dawson, 1983; Birdsall and Langdon, 1985; Arber et al., 2015]. PIC codes proved their reliability and their importance in many fields of plasma physics where kinetic effects play a major role from cold discharges to ultra-high intensity physics.

An efficient modeling of laser-plasma interaction experiments however requires to describe the plasma dynamics with high spatial and temporal resolutions. This often results in large simulation boxes and high number of particles (typically 10^{5-7} superparticles and grid points in 2D, 10^{8-11} in 3D) that simply cannot be handled by personal desktops. Therefore, *realistic* numerical simulations have to be run on massively-parallel supercomputers, in which particle and field data are distributed over many different processing units. Nowadays, current machines[1] are able to treat routinely 10^{15-16} float operations per second ($= 1-10$ petaflops) and the iconic threshold of 10^{18} float operations per second ($= 1$ exaflop) should be reached within the coming year by the Intel-Cray Aurora[2] system slated for 2021.

Objectives

In this context, the objective of this PhD thesis was to better understand the interaction between a high-power laser and a dense plasma through numerical simulations and theoretical models. This physics topic was particularly studied both experimentally and theoretically in the PHI group at CEA led by F. Quéré in the context of high harmonic generation. It gave rise to multiple PhD works[3].

When an intense femtosecond laser pulse is focused on a solid target, the electric field is sufficiently high to quasi-instantly ionize matter that is reflective for the incident light. If the laser is short enough, the plasma vacuum interface barely has time to expand in vacuum before the interaction, on a spatial scale much shorter than the laser wavelength. The dense plasma therefore acts as an optical mirror that specularly reflects the incident light: it is a *plasma mirror*. Upon reflection of the laser on the plasma mirror surface, non-linear mechanisms are responsible for the emission of high order laser harmonics along the specular direction in the form of a train of attosecond pulses. Nowadays, high harmonic generation on plasma mirrors are mostly well-understood and have been clearly demonstrated both experimentally and numerically[4].

Simultaneously to the high harmonic generation, a large number of electrons ($\sim$ nC) is also emitted from the solid surface towards vacuum in the form of attosecond bunches. These electrons will co-propagate into vacuum with the laser reflected wave and undergo vacuum laser acceleration. Recently, teams of PHI and LOA (Laboratoire d'Optique Appliquée) demonstrated the use of plasma mirror as an electron injector in a high-power laser field providing high-charge and relativistic collimated beams (10 MeV at 1.5 nC) [Thévenet, Leblanc, et al., 2016].

The PHI team operates the UHI100 Titanium-Sapphire beam line, which emits 100 TW and 25 fs laser pulses in $\lambda_0 = 800$ nm. The specificity of the UHI100 laser is the high quality of the beams that it delivers in term of temporal contrast [Nantel et al., 1998]. This is achieved thanks to a set of optical systems [Lévy et al., 2007] located before the main experimental vacuum chamber that remove the long and intense pedestal preceding the main pulse. An excellent

[1] https://www.top500.org/lists
[2] https://aurora.alcf.anl.gov/
[3] Thaury, 2008; Vincenti, 2011; Monchocé, 2014; Leblanc, 2016; Chopineau, 2019; Bouchard, 2020
[4] Lichters et al., 1996; Dromey et al., 2006; Baeva et al., 2006; Quéré et al., 2006; Thaury and Quéré, 2010; Vincenti, 2011; Borot, 2012; Leblanc, 2016

temporal contrast is absolutely mandatory in plasma mirror experiments, because a too intense pedestal would lead to premature creation and expansion of the plasma in front of the solid surface. This ruins the expected profile of the target before the arrival of the main pulse and complicates the interpretations.

My research precisely aimed to identify the different coupling mechanisms between light and dense plasmas at play when the surface in front of the plasma mirror is not steplike but features a finite (and controlled) density gradient characterized by a scale length in the order of the laser wavelength. Under these conditions, electron and harmonic signals are observed to collapse that clearly indicates a change of regime of interaction. My work provided a crucial support in the interpretation of recent experiments performed by A. Leblanc, A. Denoeud and L. Chopineau, with whom I worked in close collaboration.

Outline

This manuscript breaks down into four large parts and eight chapters. The first part introduces the basics of the interaction between an ultra-short and ultra-intense laser and a dense plasma, from its creation by ionization processes to applications as a source of high harmonics or relativistic electrons. Then, we take a slight step aside from the main scope to introduce nonlinear and chaotic dynamics. Basic knowledge on that topics should prove useful to describe plasma electron motion in the density gradient. By choice, this heavily mathematical topic is treated from a physicist's point of view by emphasizing intuitive features of simple chaotic systems instead of focusing on complex analytical derivations.

The second part details the numerical tools used all along the manuscript. Precisely, simulations, which aim to finely reproduce the experiments, are performed with the Particle-In-Cell code WARP+PXR, co-developed by the Lawrence Berkeley National Laboratory and the CEA Saclay. It is based on state-of-the-art pseudo-spectral Maxwell solver that I benchmark on plasma mirror simulations. As opposed to standard Maxwell solvers, the former greatly improve the simulation accuracy and render accessible 3D cases not possible otherwise. These large scale PIC simulations are also complemented by simulations carried out by a particle tracker code that I develop that significantly accelerates the time to solution, while giving thorough understandings of the processes at play.

The third part reports the first comprehensive numerical and experimental study of coupling mechanisms between laser and overdense plasma as a function of the plasma-vacuum interface at relativistic laser intensities. Our observations reveal a clear transition from a temporally *periodic* mechanism to a *chaotic* process as the interface becomes smoother.

The last part encompasses all numerical and theoretical works aimed at explaining thoroughly the key signatures of these two distinct regimes. First we discuss the acceleration of electrons in vacuum after their emission from the solid target. The principal features have already been published for simple laser configurations, but remain unknown in more complex situations. Second, thanks to numerical simulations, the chaotic mechanism responsible for electron ejection is fully characterized as well as its domain of validity in terms of laser-plasma parameters. Finally, because this mechanism is found to be almost independent of plasma collective effects, the dynamics of plasma particles can be described as if they were in vacuum. It allows us for reducing the equations governing the motion into well-known physical system, the pendulums. Similarly to free electrons in electromagnetic waves, these systems may or may not exhibit chaotic be-

haviours.

This work was subject to several publications and conference presentations listed at the end of the manuscript. Other articles will be also submitted in a near future.

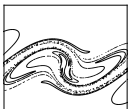

Part I

Introduction to Principal Physical Concepts

1 Introduction to Plasma Mirrors

When an intense femtosecond laser pulse is focused on a solid target, the electric field is sufficiently high to almost instantly ionize matter. It leads to a creation of a dense plasma, which expands towards vacuum. Due to the very short pulse duration and its high-contrast, the plasma barely expands during the interaction and forms a pre-plasma at the vacuum-plasma interface with a scale-length much smaller than the incident laser wavelength. Such a dense plasma reflects most of the incident light along the specular direction as if it were a mirror of high optical quality.
This introductory chapter is dedicated to the physics of the *plasma mirrors* from their creations to their fundamental use as particle and light sources with remarkable properties. In particular, are detailed several nonlinear couplings between light and matter responsible for electron emission and high harmonic generation (HHG).

Contents

1.1 Creation of a Dense Plasma Reflective for the Incidence Wave

1.1.1 Field ionization of matter

Described by Irving Langmuir as the fourth state of matter, a plasma is an ionized gas made of free electrons and positive ions. In contrast to other states of matter (solid, liquid or gas), it is highly electrically conductive to the point that long-range electric and magnetic fields dominate the behaviour of the matter. It exists a large variety of plasmas, classified according to their temperatures, densities or degrees of ionization: from cold and weakly ionized gas used in the industry to hot and fully ionized plasmas deep inside stars.

In this manuscript, the plasma is created by focusing an intense laser pulse on a solid target, composed of silica (SiO_2) or plastic (C and H). Electrons will be ejected from their parent atoms when they receive enough energy $\mathcal{E}_i$ to propel them from their bound state to the continuum (e.g., 11.2 eV for C to C^+ or 13.6 eV for H to H^+). It can be done either by absorbing a single high-frequency photon (such as XUV photons) or multiple lower frequency photons.

When using a Ti:sapphire laser, the photon energy is too weak to operate a direct photoionization (only ~ 1.5 eV per photon at 800 nm) but the concentration of light is such that multiphoton ionization is likely to happen. This phenomenon is illustrated in Fig. 1.1–a.

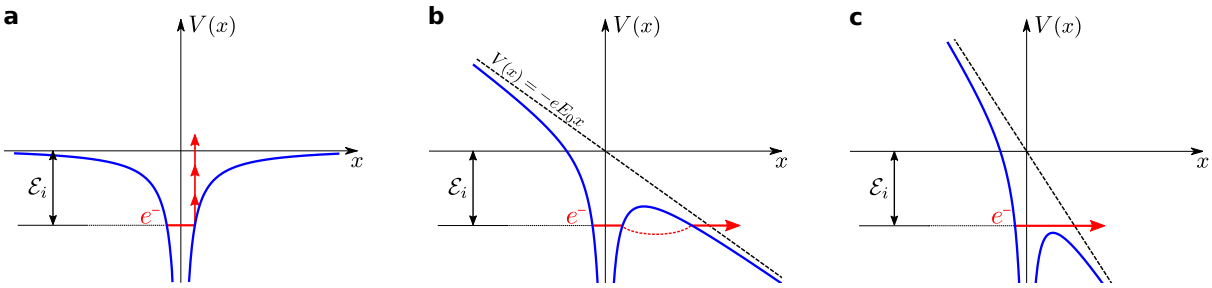

Figure 1.1: **Atom ionization by an external electric field** - For panel (a), the external electric field is weak. The potential is simply the Coulomb potential of the parent ion and the prevailing mechanism is multiphoton ionization. When the external field becomes stronger, it can disturb the binding potential. The different ionization processes are then (b): tunneling ionization or (c): over-the-barrier ionization.

When the intensity of the laser pulse becomes stronger, the laser field is able to distort the Coulomb field felt by the electron [Gibbon, 2005]. With E_0 the amplitude of the laser electric field, the new electric potential of the electron reads:

$$V(x) = -\frac{Ze^2}{4\pi\epsilon_0|x|} - eE_0x, \tag{1.1}$$

where Z is the charge of the parent ion, e the elementary charge and ϵ_0 the vacuum permittivity. Applying such an external laser field thus lowers the Coulomb barrier. It results that by quantum mechanics effect, the electron may tunnel through the barrier, with a non-zero probability (see Fig. 1.1–b). If the barrier falls below $\mathcal{E}_i$, the electron does even escape spontaneously. The last ionization mechanism is known as the over-the-barrier ionization (OBTI) and pictured in Fig. 1.1–c.

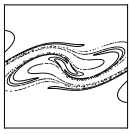

Quantitatively, it is possible to estimate the laser intensity required to suppress the ionization barrier by equating V and $\mathcal{E}_i$.
[Gibbon, 2005] gives a convenient expression for the threshold intensity I_{OBTI}:

$$I_{OBTI} = 4 \times 10^9 \left(\mathcal{E}_i\,[\mathrm{eV}]\right)^4 Z^{-2} \quad \mathrm{W.cm^{-2}}. \tag{1.2}$$

In particular, for the elements of interest (Si, O, H and C), several values of I_{OBTI} are listed in the following table.

Ions	Si^+	Si^{12+}	O^+	O^{7+}	H^+	C^+	C^{6+}
$\mathcal{E}_i$ [eV]	8.2	523	13.6	739	13.6	11.2	490
I_{OBTI} [$\mathrm{W.cm^{-2}}$]	2×10^{13}	2×10^{18}	10^{14}	2×10^{19}	10^{14}	6×10^{13}	6×10^{18}

Table 1.1: **Intensity thresholds for over-the-barrier ionization for Si, O, H and C.**

According to Tab. 1.1, an intensity of $I \sim 10^{13}$ $\mathrm{W.cm^{-2}}$ seems to be high enough to pull some electrons off carbon or silicon atoms. For 100 TW to multi-PW class laser pulses, the peak intensity I_0 is higher than 10^{19} $\mathrm{W.cm^{-2}} \gg 10^{13}$ $\mathrm{W.cm^{-2}}$ so the ionization occurs in the pedestal of the main pulse, i.e. well before the interaction between the peak of the pulse and the target. Considering that the laser temporal envelope evolves as a Gaussian function, the intensity of the electromagnetic wave varies as:

$$I(t) = I_0 \exp\left(-t^2/\tau_0^2\right) \tag{1.3}$$

with τ_0 the laser temporal duration. For $\tau_0 = 25$ fs and $I_0 = 10^{19}$ $\mathrm{W.cm^{-2}}$, the target starts to be ionized as soon as $I(t_i) \sim I_{OBTI}$, which gives $t_i \sim 400$ fs before the peak intensity. Therefore, the main pulse does not interact with a solid target but rather a plasma, probably almost fully ionized at that time (see Tab. 1.1).

Before the interaction with the main pulse, the resulting plasma expands in vacuum under thermal effects (mainly Coulomb collisions), creating an exponential density profile in front of the target surface [Kruer, 1988]. This profile is characterized by a scale length — L_g — called the *density gradient length*. L_g is found to be a crucial parameter of the interaction because most, if not all, couplings between light and solid target take place in this region, located at the interface between plasma and vacuum.

1.1.2 Propagation of an electromagnetic wave in a plasma

We now present the response of this plasma to an external electromagnetic wave. Maxwell's equations give the equation of propagation of the electric field in the medium:

$$\boldsymbol{\nabla}^2 \boldsymbol{E} - \frac{1}{c^2}\frac{\partial^2 \boldsymbol{E}}{\partial t^2} = \mu_0 \frac{\partial \boldsymbol{J}}{\partial t} + \frac{1}{\epsilon_0}\boldsymbol{\nabla}\rho, \tag{1.4}$$

with $\boldsymbol{E}$ the total electric field, $\boldsymbol{J}$ the current density vector, ρ the charge density, c the celerity of light and μ_0 the vacuum permeability.

For a transverse electromagnetic wave with angular frequency ω_0 — $\boldsymbol{E} = \widetilde{\boldsymbol{E}} \exp(-\mathrm{j}\,\omega_0 t)$ — propagating in a cold and non-collisional plasma, the electric field and current can be found using Ohm's law:

$$\boldsymbol{J} = -\mathrm{j}\epsilon_0 \frac{\omega_p^2}{\omega_0}\widetilde{\boldsymbol{E}}, \quad \text{where } \mathrm{j}^2 = -1. \tag{1.5}$$

We defined herein the *electron plasma frequency* ω_p:

$$\omega_p = \sqrt{\frac{n_e e^2}{m\epsilon_0}}, \tag{1.6}$$

where n_e is the electron density and m the electron mass. ω_p corresponds to the typical longitudinal quivering frequency of electrons, in response to a small charge separation. The dependency on the electron density can be physically explained: in denser parts of the plasma, particles will respond quicker to the perturbation as the electrostatic field induced by the space-charge separation, is higher.

Uniform plasma density. When the plasma density is uniform ($\boldsymbol{\nabla}\rho = 0$), the wave equation can be obtained by combining Eq. (1.4) and Eq. (1.5):

$$\boldsymbol{\nabla}^2 \widetilde{\boldsymbol{E}} + \frac{\omega_0^2}{c^2}\left(1 - \frac{\omega_p^2}{\omega_0^2}\right)\widetilde{\boldsymbol{E}} = 0. \tag{1.7}$$

Considering an electromagnetic mode $(\omega_0, \boldsymbol{k})$ such that $\widetilde{\boldsymbol{E}} = \boldsymbol{E_0}\exp(\mathrm{j}\,\boldsymbol{k}\cdot\boldsymbol{x})$, the wave dispersion relation reads:

$$k^2c^2 = \omega_0^2 - \omega_p^2. \tag{1.8}$$

Eq. (1.8) exhibits two distinct plasma regimes depending on ω_0:

- when $\omega_0 > \omega_p$, Eq. (1.8) admits a real solution for the wave vector k. The plasma behaves as a transparent medium for the incident wave characterized by a refractive index N_r:

$$N_r = \sqrt{1 - \omega_p^2/\omega_0^2} \leq 1. \tag{1.9}$$

- when $\omega_0 < \omega_p$, the wave vector becomes imaginary. The laser wave cannot propagate in the medium anymore and is reflected as if the plasma acts as a mirror.

The transition from one regime to the other occurs at a peculiar density — n_c — called the *critical density* obtained for $\omega_0 = \omega_p$ and defined by:

$$n_c = \frac{m\epsilon_0\omega_0^2}{e^2}. \tag{1.10}$$

It separates *underdense* plasmas ($n_e < n_c$) transparent for incident laser waves from *overdense* plasmas ($n_e > n_c$) opaque and reflective.

For Ti:Sapphire lasers for which $\lambda_0 = 800$ nm, $n_c \simeq 1.7 \times 10^{21}$ cm^{-3}. The critical density is lower than the solid density of our target ($n_e \sim 10^{23-24}$ cm^{-3}) by several orders of magnitude. A plasma created from a solid target is thus largely overdense. This plasma is then considered as a *plasma mirror* as it will reflect a large fraction of the incoming laser light.

Note that the above equations were derived in the classical regime ($I_0 < 10^{18}$ W.cm^{-2}) for which electron dynamics are not relativistic. When the laser intensity is higher ($I_0 \gtrsim 10^{18}$ W.cm^{-2}), [Lefebvre and Bonnaud, 1995; Guérin et al., 1996] point out the existence of a *relativistic transparency*. Due to relativistic effects, waves can propagate deeper into the plasma, up to a density $n_e = \gamma_0 n_c$, γ_0 being the Lorentz factor of the electrons related to the laser parameters:

$$\gamma_0 = \sqrt{1 + a_0^2}, \tag{1.11}$$

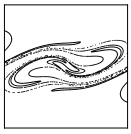

where a_0 is the normalized laser amplitude:

$$a_0 = \frac{eE_0}{m\omega_0 c} = \lambda_0[\mu\text{m}]\sqrt{\frac{I_0[\text{W.cm}^{-2}]}{1.37\times10^{18}}}. \tag{1.12}$$

This dimensionless parameter is particularly relevant to discriminate non-relativistic regimes ($a_0 \ll 1$) from the relativistic regime ($a_0 \gtrsim 1$). In this case, the electron quivering motion occurs at relativistic speeds. For a Ti:Sapphire lasers, this happens as soon as the intensity $I_0 \geq 2\times10^{18}$ W.cm^{-2}.

In any case, even by taking into account the relativistic transparency, a uniform solid target will ever stay a plasma mirror for realistic laser parameters. Indeed, a_0 must be as huge as 1000 to allow laser channeling by relativistic transparency. This corresponds to intensities as high as 10^{22-24} W.cm^{-2} at $\lambda_0 = 800$ nm, way beyond the scope of the present manuscript.

Plasma with a density gradient. Actually, due to plasma expansion after target ionization, the dense plasma rarely shows a perfect step-like density profile (Fig. 1.2–a) but rather exhibit an exponentially decaying density profile towards vacuum as shown in Fig. 1.2–b (for isothermal expansions). The electron density is dropping as it gets close to vacuum until ultimately falling below n_c. The total plasma layer is thus composed of an underdense part and an overdense part.

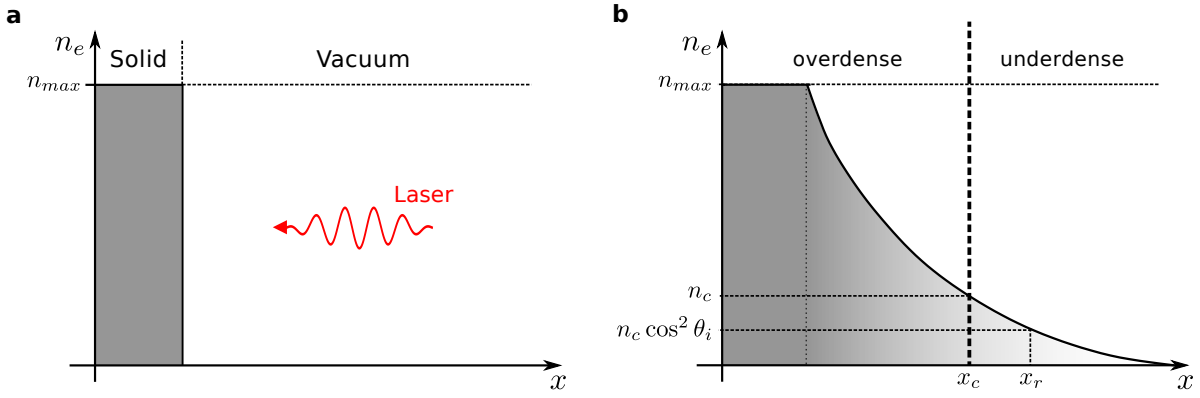

Figure 1.2: **Target density profile before and during interaction with the laser** - (a) Before interaction, the solid target is equally dense: $n_e = n_{max}(= 220\, n_c)$. (b) Under the laser light, a plasma is formed and expends in vacuum. The profile of this plasma covers two regions: one underdense ($n_e < n_c$) and one overdense ($n_e > n_c$).

Along the laser propagation in the underdense part of the gradient, the refractive index N_r(x) is continuously evolving accordingly to the local density. At oblique incidence, the local angle $\theta(x)$ between the wave vector $\boldsymbol{k}$ inside the plasma layer and the $\boldsymbol{x}$-axis is obtained by integrating the Snell-Descartes law: $\partial(N_r(x)\sin\theta(x))/\partial x = 0$. It comes that:

$$\sqrt{1-\frac{n_e(x)}{n_c}}\sin\theta(x) = \sin\theta_i, \tag{1.13}$$

where we introduce θ_i the laser angle of incidence. It appears that the density at which the laser is effectively reflected, n_r (obtained when $\theta = \pi/2$), is even lower than n_c:

$$n_r = n_c\cos^2\theta_i. \tag{1.14}$$

Note that for normal incidence ($\theta_i = 0$), we retrieve that the reflection occurs when $n_r = n_c$, as if the underdense part of the gradient plays no role.

Now that we have defined a plasma mirror, let us focus on the physical processes occurring during the laser plasma interaction.

1.2 Coupling Mechanisms between a Laser and a Dense Plasma

Since the laser pulse cannot penetrate into overdense regions of the plasma, the absorption of the laser energy can occur either in the undercritical part of the gradient or within the skin depth of the overcritical plasma, where the laser wave is evanescent. A fraction of this energy can be later transported into deeper plasma regions through energetic electrons. These may be generated during the interaction through several mechanisms.

At first, physicists initially anticipated the main mechanism of energy deposition to be *collisional absorption* [Kruer, 1988], where the electron-ion collisions disrupt the regular quivering motion of the plasma electrons in the light field, statistically leading to a net kinetic gain. However, in typical ultraintense laser-plasma interactions, electrons are accelerated up to MeV−GeV in tens of femtoseconds, while the time scales between collisions are usually longer than a picosecond. Given this time scale discrepancy, actual absorption mechanisms cannot rely on collisions between particles.

Nevertheless, even if we restrict the study to collisionless couplings between light and matter, the abundance of processes available in the literature is such that it would be too long and too tedious to describe them all here. For interested readers, a in-depth review of the topic can be found in [Gibbon, 2005] for example. Instead, we decide to narrow it down to three mechanisms at the center of this thesis: the resonance absorption, the vacuum heating (or Brunel absorption) and the less known in the solid target community stochastic heating.

1.2.1 Resonance absorption

Let us start this overview by presenting the *resonance absorption*[1] (RA), mechanism which is dominant for long gradient scale lengths. At oblique incidence, we have seen that the laser wave is reflected at the density $n_r = n_c \cos^2\theta_i$. However, if the incident pulse is p-polarized[2], some laser energy may tunnel up to the critical density n_c in the form of an evanescent wave, where it drives a resonant plasma wave (see Fig. 1.3–a). This wave will grow as the laser keeps providing energy until it is either being damped by collisional effects if the laser intensity is low, or by wave breaking, if it is higher [Albritton and Koch, 1975; Bergmann and Mulser, 1993].

This can happen only if the density gradient length L_g is long enough that the refractive index slowly varies over a laser wavelength [Ginsburg, 1964; Kruer, 1988]. It leads to a condition on L_g: $L_g k_0 \gg 1$, $k_0 = \omega_0/c$ being the laser wave vector. Physically, it means that L_g has to be much greater than the electrons quivering in the laser field. We will come back to this statement

[1] Freidberg et al., 1972; Estabrook, Valeo, et al., 1975; Forslund et al., 1975; Estabrook and Kruer, 1978; Kruer, 1988

[2] When the component of the laser electric field is parallel to the plane of incidence, the wave is termed to be p-polarized (p for parallel). If $\boldsymbol{E}$ is on the contrary perpendicular to this plane, the wave polarization is called s (s standing for *senkrecht*, the German world for perpendicular).

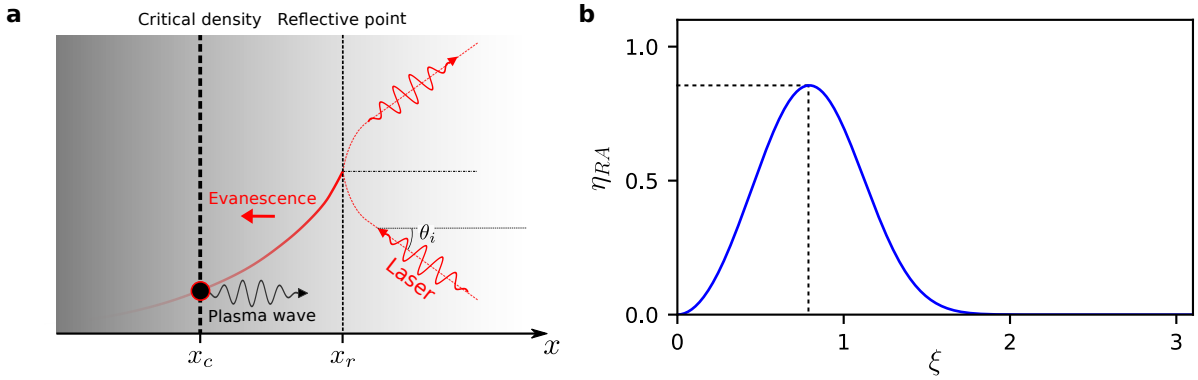

Figure 1.3: **Resonance absorption mechanism** - In panel (a), a laser is reflected by a plasma density gradient at the position x_r. Beyond x_r, some energy is delivered into the plasma in the form of an evanescent wave, which drives a resonance near the critical density. After some time, the resonance can lead to wave breaking or can be damped by Coulomb collisions. Panel (b) displays the dependence of the fraction of absorbed laser energy η_{RA} as a function of the parameter $\xi = (k_0 L_g)^{1/3} \sin\theta_i$.

in the next subsection.

According to [Denisov, 1957; Gibbon, 2005], for long density scale lengths, the fraction of absorbed laser energy η_{RA} is expressed as a function of a single parameter ξ depending on both the gradient length L_g and the laser incidence angle θ_i — $\xi = (k_0 L_g)^{1/3} \sin\theta_i$:

$$\eta_{RA} = \frac{1}{2}\Big(2.3\,\xi\,\exp\big(-2\xi^3/3\big)\Big)^2. \tag{1.15}$$

The profile of $\eta_{RA}(\xi)$ is plotted in Fig. 1.3–b. In certain conditions, the fraction of the energy stored in the plasma wave can reach 85% of the laser energy. This occurs when $\xi \simeq 0.79$, which gives $L_g \simeq \lambda_0/4$ at $\theta_i = 45°$.

Despite quantitative results, most analytical derivations describing the RA are based on perturbation theories, in which the whole density gradient is only weakly disturbed. In particular, they assume that the local densities are not modified by the laser pulse, which tends to be incorrect as soon as the laser intensity becomes too high. Also, the Lorentz gamma factor is often forgotten, implying that the electrons are not relativistic. Some efforts were proposed to include the relativistic effects [Drake and Y. C. Lee, 1976] but as we will see further ahead in the manuscript, resonance absorption is superseded by another mechanism at relativistic intensities ($a_0 \gtrsim 1$).

In any case, the necessary condition for resonance absorption is a density gradient that is long enough for the laser wave to propagate, regardless of its intensity. At very steep gradients, the RA will also cease to be dominant in favor of another collisionless coupling — the vacuum heating or Brunel mechanism.

1.2.2 Brunel mechanism

When the density gradient in front of the target is too sharp, the excursion amplitude of electrons in the laser oscillations — δ_x — becomes so large that it can exceed the gradient scale length itself. In an iconic paper, [Brunel, 1987] predicted a transition towards a new collisionless

mechanism, which he ironically called "not-so-resonant, resonant absorption". In this case, electrons at the plasma surface are first pulled out of the plasma by the laser field, when $E_\perp$ (the component of the electric field perpendicular to the target surface) points towards the target direction. As the laser electric field component changes sign, the same electrons will be pushed back into the plasma under the combined action of the laser and the electrostatic space charge fields. As soon as these so-called *Brunel electrons* have returned back to the plasma, they are not subject to any field so they further travel ballistically into the target at the velocity that they have acquired in vacuum. These particles never render their energy acquired in the laser and are responsible for energy absorption by the plasma.

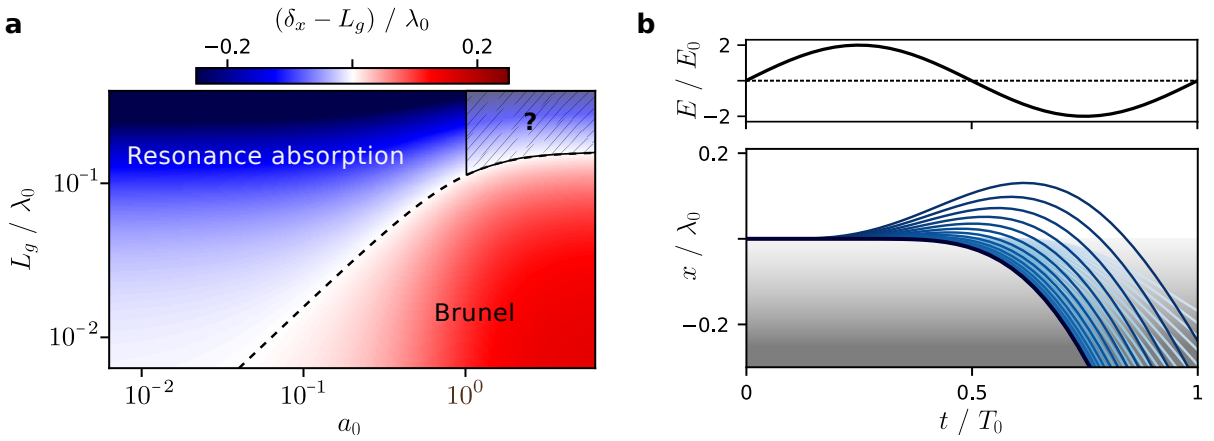

Figure 1.4: **A transition to Brunel mechanism for short gradients** - Panel (a) shows the evolution of the quantity $(\delta_x - L_g)$ as a function of a_0 and L_g. The black dashed curve indicates the particular location where $\delta_x = L_g$. The hatched area indicates that the whole diagram is not completely understood yet. In panel (b), we represent electrons trajectories $x(t)$. The different line colors correspond to different time of injection $t_i \in [0.08,\ 0.55]T_0$, from dark blue to white. On top of the figure is pictured the electric field profile along time.

Brunel's criterion to discriminate RA from his new mechanism is based on the relative values of δ_x and L_g. In a crude approximation, one can use $\delta_x \simeq v_{osc}/\omega_0$, where v_{osc} is the quivering velocity of electrons in the laser field. Thanks to the equations of motion, v_{osc} can be quantified and reads $v_{osc} \simeq eE_0/\gamma_0 m\omega_0 = a_0 c/\gamma_0$, with γ_0 the already defined Lorentz factor related to the laser intensity — $\gamma_0 = \sqrt{1+a_0^2}$. Overall, the resonance breaks down if the following condition is fulfilled:

$$L_g < \delta_x = \frac{a_0 \lambda_0}{2\pi\sqrt{1+a_0^2}}. \tag{1.16}$$

In Fig. 1.4–a is plotted the quantity $(\delta_x - L_g)$ as a function of a_0 and L_g. The black dash line highlights the locations where $\delta_x = L_g$ and delimits the transition between the two mechanisms. The Brunel absorption is found to be predominant in the bottom-right region, while the RA is expected to prevail upper the line. In addition,we indicate a hatched area in the top-right corner corresponding to high intensities and long gradients. The purpose of this manuscript will be to unearth the dominant mechanism at stake in this regime.

Mechanism at low intensity. Now, let us focus on the Brunel mechanism itself. We consider a p-polarized wave impinging on a steep plasma under oblique incidence with the angle θ_i. For a simple model, Brunel imposed few hypotheses beforehand:

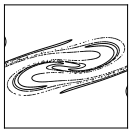

- the laser intensity is kept modest ($a_0 \lesssim 1$) and the particles are not relativistic ($\gamma = \gamma_0 = 1$). It implies that the magnetic field contribution is ignored and the magnetic Lorentz force $\boldsymbol{F_B} = -e\boldsymbol{v} \times \boldsymbol{B}$ is neglected.
- The plasma-vacuum interface is modeled as an initial step-like density profile: for $x > 0$, there is the vacuum where a standing electric wave is set up and for $x < 0$, there is the plasma considered as a perfect conductor, which can freely emit electrons.
- At the plasma surface, the transverse components of the electric field are canceling so the electrons only move along the normal direction. The Brunel mechanism is modeled in 1D.

At the interface, the driving electric field is given by:

$$E_\perp(t) = 2E_0 \sin\theta_i \sin(\omega_0 t). \tag{1.17}$$

As the field increases for $t > 0$, electrons are pulled out of the plasma in order to maintain a zero field on the conductor surface ($x = 0$). That creates an electrostatic field E_s along x. This field is given by the Gauss's law for the i^{th} electrons emitted at $t = t_i$:

$$E_{s,\,i}(t) = e\int_{x_i}^{+\infty} \frac{n_e(x)}{\epsilon_0}\mathrm{d}x. \tag{1.18}$$

Another fundamental hypothesis of the Brunel mechanism is that the electron trajectories never cross each other, so that the total charge in front of the i^{th} electron remains unchanged. The electrostatic field seen by this electron is constant over time: $E_{s,\,i}(t) = E_{s,\,i}$ and can be determined at the surface where the total field canceled:

$$0 = E_\perp(t_i) + E_{s,\,i} \quad \Leftrightarrow \quad E_{s,\,i} = -E_\perp(t_i). \tag{1.19}$$

The total electric field seen by the i^{th} electron at any time is then:

$$E(t) = E_\perp(t) - E_\perp(t_i) = 2E_0 \sin\theta_i\Big(\sin(\omega_0 t) - \sin(\omega_0 t_i)\Big). \tag{1.20}$$

The position $x_i(t)$ and velocity $v_i(t)$ of this electron can be obtained after integrating the equation of motion $m\mathrm{d}v_i/\mathrm{d}t = -eE(t)$ and read:

$$\begin{aligned} &\bullet\quad v_i(t) = v'_{osc}\Big(\cos(\omega_0 t) - \cos(\omega_0 t_i) + \omega_0\,(t - t_i)\sin(\omega_0 t_i)\Big),\\ &\bullet\quad x_i(t) = \frac{v'_{osc}}{\omega_0}\Big(\sin(\omega_0 t) - \sin(\omega_0 t_i) - \omega_0\,(t - t_i)\cos(\omega_0 t_i) + \frac{1}{2}w_0^2\,(t - t_i)^2\sin(\omega_0 t_i)\Big). \end{aligned} \tag{1.21}$$

with $v'_{osc} = 2v_{osc}\sin\theta_i$. The corresponding trajectories are plotted in Fig. 1.4–b in various shades of blue related to the time of emission t_i. Electrons that are emitted at late times return to the plasma also at late times but with a higher velocity. It induces a natural bunching of these particles as they penetrate the overdense part of the plasma, along a peculiar caustic displayed as a black line in the figure. It was shown by [Quéré et al., 2006; Thaury and Quéré, 2010] that the electron density peak in that region will excite plasma oscillations at different positions within the gradient and be responsible for an emission of harmonics up to the plasma frequency. This process of generation is called *Coherent Wake Emission*.

Mechanism at relativistic intensities. It is important to note that Brunel's electrons are always supposed to return back to the plasma. Therefore, no electron should be detected

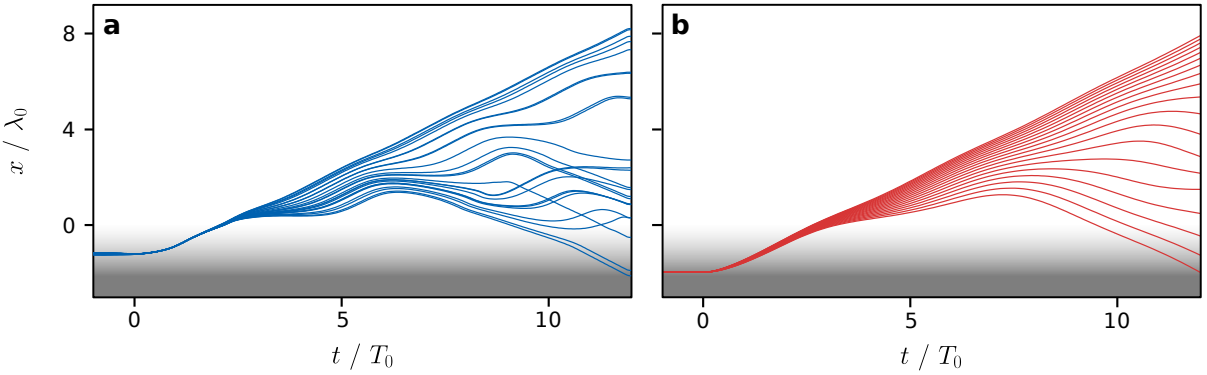

Figure 1.5: **Brunel mechanism in the relativistic regime** - [Image from [Thévenet, Vincenti, et al., 2016]]. Electron trajectories from (a) a numerical simulation and (b) the analytical model developed in [Thévenet, Vincenti, et al., 2016] for $a_0 = 8$, $L_g = \lambda_0/10$ and $\theta_i = 45°$.

in front of the target. However, when the laser intensity is heightened up to 10^{18-19} W.cm^{-2}, numerical simulations show that a fraction of surface electrons are emitted towards vacuum. It means that the initial hypotheses of Brunel are somehow violated. At high intensities, the gyromagnetic term of the Lorentz force becomes comparable to the electric term and cannot be neglected any longer. Brunel's electrostatic model has to be extended.

In [Thévenet, Vincenti, et al., 2016], the authors have enriched Brunel's model with relativistic and magnetic effects, as well as non-uniform fields that depend on the electron position. In Fig. 1.5 are plotted some particle trajectories obtained from a numerical simulation in blue and the new extended model in red. The electron dynamics end up to be more complex and intertwined. Moreover, clear jets of electrons are expelled in vacuum, which never return back. For convenience, we will also use the term *Brunel's electrons*, when designating this particular electron population, despite that it did not exist in Brunel's original model.

Note that at high laser intensities, Brunel mechanism can even happen at normal incidence, but this time the electrons are driven by the magnetic force rather than the electric force (the electric field is tangent to the plasma surface). This mechanism happens twice per laser period (because the Lorentz magnetic force oscillates at $2\omega_0$) and is commonly named as $\boldsymbol{J} \times \boldsymbol{B}$ heating [Kruer and Estabrook, 1985].

1.2.3 Stochastic heating

The last coupling mechanism between light and solid target presented here is called *stochastic heating* [Mendonça and Doveil, 1982; Mendonca, 1983; Rax, 1992]. It is in general less known in the solid target community than the two previous mechanisms, because it requires a large quantity of electrons in the underdense part of the gradient, not compatible with the plasma mirror regime. It should occur for long density gradients ($L_g \gtrsim \lambda_0$) and relativistic intensities, but the transitions from resonance absorption or Brunel mechanism remain unclear. In this regime, the electrons are found to behave chaotically while absorbing the laser energy.

This mechanism simply happens when free electrons are evolving in a combination of two non-collinear waves. In that case, the motion is in general non-integrable and can even become chaotic if the intensity of one of the two wave is sufficiently high (typically one with $a_0 > 1$

and one with $a_0 \sim 0.1$ [Z.-M. Sheng, Mima, Sentoku, et al., 2002]). The system ends up to be extremely sensible to initial conditions despite being deterministic *a priori*. More information related to chaotic systems will be treated in the next chapter.

This process is not limited to free electrons but may also take place in very tenuous plasma ($n_e \sim 10^{-2}\, n_c$), where electron motion is mainly governed by direct interactions with the laser pulse. Then, it did not take long to find evidences that stochastic heating is the mechanism at play when two intense lasers are interfering within a gas jet [P. Zhang et al., 2003; Z.-M. Sheng, Mima, J. Zhang, et al., 2004]. It was even theoretically proposed as a scheme to inject electron in laser wakefield acceleration[3]: a first intense laser drives plasma waves and a weak second pulse, sent in the opposite direction, will introduce a small perturbation propelling several electrons out of their regular trajectories. Some of them may be trapped into the wake. Experiments conducted during Rechatin's thesis [Faure, Rechatin, et al., 2006; Rechatin, 2009] proved the validity of the scheme. However, for evident problems of laser synchronization and alignment, experiments of stochastic heating in gas are particularly challenging and ended to be abandoned in favor of other much more reliable injection techniques [Esarey, Schroeder, et al., 2009].

Back to laser interactions on solid targets, as soon as in the 80s, [Mendonça and Doveil, 1982] first suspected that a small fraction of a laser pulse reflected by a plasma surface could provide an adequate perturbation to make the system non-integrable. This was later confirmed by [Sentoku et al., 2002], who, based on numerical simulations, demonstrated that electrons can gain energy through stochastic heating in the underdense part of a density gradient. Upon reflection, the combination of incident and reflected electromagnetic waves in the underdense part of the plasma layer produces a standing wave near the position of reflection x_r, corresponding to the density $n_r = n_c \cos^2\theta_i$ (see 1.2–b, page 13). The experimental setup becomes much more simple because it does not require an additional synchronized laser pulse anymore: the additional wave is directly created *in situ* by the overdense part of the gradient.

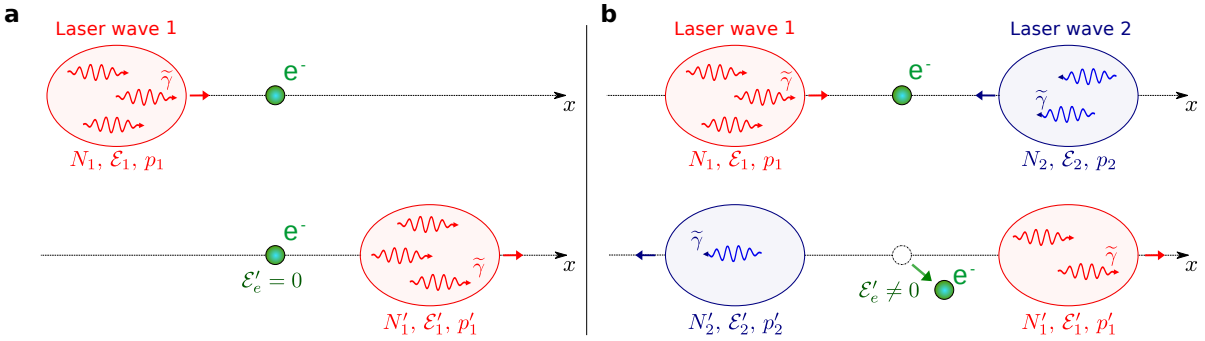

Figure 1.6: **Drawing of a simple model of photon absorption** - Panel (a) displays an interaction between a laser pulse (in red), carrying many photons $\widetilde{\gamma}$, and a single electron (in green). The top line corresponds to a state before interaction and the bottom line after interaction. In panel (b), a second laser pulse is added (in blue) colliding with the first pulse. Note that the different laser colors are not related to the actual laser wavelengths but are only rendered to help discriminating laser 1 from laser 2.

Model of photon absorption. An essential condition to stochastically heat electrons is the presence of a second wave. When a single laser beam (assumed to be a monochromatic plane wave) is present, photon absorption processes are hindered as they do not conserve both energy

[3] Umstadter et al., 1996; Esarey, Hubbard, et al., 1997; Fubiani et al., 2004; Rassou et al., 2014

and momentum of the total system. By contrast, if another beam traveling in the opposite direction is added to the system, the combined absorption of multiple photons simultaneously from both beams becomes allowed.

To illustrate why in practice the electrons are able to gain energy in two waves rather than in one, we derive a simple model of photon absorption for a single free electron. As displayed in Fig. 1.6–a, we consider that the incoming light is made of a coherent sum of N_1 photons (symbol $\widetilde{\gamma}$) with the same energy $\mathcal{E}_1$ and momentum $\boldsymbol{p_1} = p_1\boldsymbol{x}$. The electron is initially set at rest such that its energy $\mathcal{E}_e = mc^2$ and its momentum $p_e = 0$.

We also suppose that N_1 is sufficiently high to neglect all potential radiations created by electron-photon scattering — such as Compton scattering — over the laser light. In addition, we are strictly interested in the net kinetic energy gain after interaction and not how the electron energy can potentially evolve up and down in the middle of the interaction.

We are looking for the existence of a tuple $(N_1', \mathcal{E}_1', p_1')$, quantities related to the photons after interaction, which respects the conservation law of energy and momentum of the system, but allowing for a photon absorption by the electron. In other words, we aim to find an electron energy $\mathcal{E}_e'$ and momentum p_e' after the interaction, different from the initial state ($\mathcal{E}_e' \neq \mathcal{E}_e$ and $p_e' \neq 0$). Equating the whole energy and momentum of the system before and after the interaction reads:

$$\begin{aligned} \bullet \quad & N_1\mathcal{E}_1 + mc^2 &&= N_1'\mathcal{E}_1' + \mathcal{E}_e', \\ \bullet \quad & N_1 p_1 &&= N_1' p_1' + p_e'. \end{aligned} \tag{1.22}$$

For both photons and electron, energy can be related to momentum: for a photon $\mathcal{E}_1 = p_1 c$ and for an electron $\mathcal{E}_e' = \gamma mc^2$, with $\gamma = \sqrt{1 + \left(p_e'/mc\right)^2}$ being the electron Lorentz factor. Overall, after combining the two lines of Eq. (1.22):

$$\begin{aligned} & mc^2 = \gamma mc^2 - p_e' c, \\ \Leftrightarrow \quad & \gamma^2 = 1 + \left(\frac{p_e'}{mc}\right)^2 + 2\,\frac{p_e'}{mc}. \end{aligned} \tag{1.23}$$

The only solution of this equation is $p_e' = 0 = p_e$ and thus $\mathcal{E}_e' = mc^2 = \mathcal{E}_e$. There cannot be any photon absorption in this case.

Now, a second laser beam is added that travels in the opposite direction (see Fig. 1.6–b). In the same way, we define the tuples $(N_2, \mathcal{E}_2, p_2)$ and $(N_2', \mathcal{E}_2', p_2')$ to designate the number of photons related to the second laser, their energies and their momenta, before and after interaction with the electron. Defining α the ratio between the photon energy of the first and second laser, it comes that $\mathcal{E}_2 = \alpha\mathcal{E}_1$ and $p_2 = -\alpha p_1$ (and same equations for primed variables). The negative sign in the momentum comes from the counter propagation. In case of two waves, the energy balance becomes:

$$\begin{aligned} \bullet \quad & \left(N_1 + \alpha N_2\right)\mathcal{E}_1 + mc^2 &&= \left(N_1' + \alpha N_2'\right)\mathcal{E}_1' + \mathcal{E}_e', \\ \bullet \quad & \left(N_1 - \alpha N_2\right) p_1 &&= \left(N_1' - \alpha N_2'\right) p_1' + p_e' \end{aligned} \tag{1.24}$$

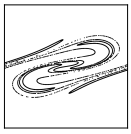

and

$$\begin{aligned} & 2\alpha N_2 p_1 c + mc^2 = 2\alpha N_2' p_1' c + \gamma mc^2 - p_e' c, \\ \Leftrightarrow \quad & \gamma = 1 + \frac{p_e'}{mc} + \frac{2\alpha}{mc}\Big(N_2 p_1 - N_2' p_1'\Big) = \sqrt{1 + \left(\frac{p_e'}{mc}\right)^2}, \\ \Rightarrow \quad & p_e' = -2\alpha\Big(N_2 p_1 - N_2' p_1'\Big)\frac{mc + \alpha\Big(N_2 p_1 - N_2' p_1'\Big)}{mc + 2\alpha\Big(N_2 p_1 - N_2' p_1'\Big)}. \end{aligned} \tag{1.25}$$

The exact value of p_e' does not matter much in practice, but more importantly, this formula ensures that solutions with $p_e' \neq 0$ exist for which both energy and momentum of the total system are conserved. By contrast to the case with one wave, the electron is able to absorb some photons from the two lasers and therefore be accelerated.

In this manuscript, we will extensively study the stochastic heating in laser plasma interactions in many laser configurations (e.g., laser polarization, incidence, intensity, etc.) as well as the transitions towards resonance and Brunel absorptions.

1.3 Plasma Mirrors as a Source of Particles and Light

1.3.1 High harmonic generation by the ROM mechanism

For more than a decade now, plasma mirrors have been subject of interest in the high power laser community. One of the main motivations that drive such studies is mainly fundamental, because they can provide bright electron and harmonic sources that are capable of probing the ultrafast dynamics of the matter at the attosecond scale [Tsakiris et al., 2006; Vincenti and Quéré, 2012; G. Ma et al., 2015]. More recently, [Vincenti, 2019] showed that they may also be used to reach extreme light intensities, never achieved in experiments yet, allowing to probe unexplored regimes of quantum electrodynamics.

Upon reflection on the plasma mirror surface, non-linear interactions between the laser and the plasma can lead to the production of a high harmonic comb, associated in the temporal domain to attosecond bunches. At high intensities ($I > 10^{18}$ W.cm^{-2}), the laser electric field drives periodic oscillations of the surface, making it move at relativistic velocities. These oscillations induce a Doppler shift that periodically distorts the reflected wavefronts and introduces new frequencies multiple of ω_0. This mechanism of generation is known as the *Relativistic Oscillating Mirror* or ROM [Lichters et al., 1996; von der Linde and Rzàzewski, 1996; Dromey et al., 2006].

Doppler effect. Before considering a relativistic oscillating mirror, we derive a simpler case, where a wave is reflected by a perfect mirror traveling at a constant velocity $v_M > 0$ along the $\boldsymbol{x}$ axis (see Fig. 1.7–a). For a stationary observer, the reflected wave will show an angular frequency ω_r different from the frequency ω_0 of the incidence wave: this is known as the relativistic *Doppler effect*.

Indeed, in a case of a normal reflection on the mirror, the electric fields of the two waves read:

$$\begin{aligned} &\bullet \quad E_i(x,t) = E_0 \cos\big(\omega_0(t + x/c)\big), \\ &\bullet \quad E_r(x,t) = E_0 \cos\big(\omega_r(t - x/c)\big). \end{aligned} \tag{1.26}$$

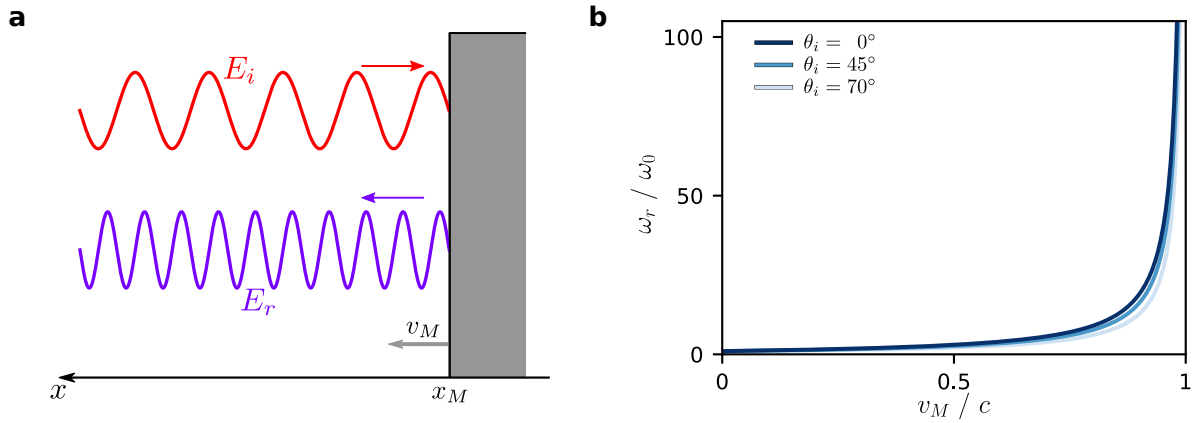

Figure 1.7: **Doppler effect with a relativistic drifting mirror** - On panel (a), an incident wave (in red) with an angular frequency ω_0 is reflected on a mirror drifting at the velocity $v_M \boldsymbol{x}$. After interaction, the reflected wave (in purple) shows an angular frequency $\omega_r > \omega_0$. Panel (b) shows the variation of ω_r/ω_0 as a function of the velocity v_M for three different laser angles of incidence θ_i.

At the surface of the perfect mirror ($x = x_M = v_M t$), the boundary condition for the electric field is simply $E_i(x_M, t) = -E_r(x_M, t)$. It comes that:

$$\omega_r = \omega_0 \frac{1 + v_M/c}{1 - v_M/c} = \omega_0 \left(1 + \frac{v_M}{c}\right)^2 \gamma_M^2, \tag{1.27}$$

where $\gamma_M = 1/\sqrt{1 - (v_M/c)^2}$ the Lorentz factor associated to the drifting mirror. Assuming that the mirror is traveling at ultra relativistic velocity: $v_M \to c$, the angular frequency of the reflected wave asymptotically scales as:

$$\omega_r = 4\,\omega_0 \gamma_M^2. \tag{1.28}$$

To convert ω_0 to high frequency, the velocity of the mirror must be close to the speed of light: for example if $v_M = 0.35\,c$, $\omega_r = 2\,\omega_0$, while if $v_M = 0.95\,c$, $\omega_r \simeq 40\,\omega_0$.

It is also possible to extend the model to oblique incidence with an angle θ_i, such as presented in [Einstein, 1905; Yeh, 1965]. In that case, the frequency shift becomes:

$$\omega_r = \omega_0 \gamma_M^2 \left(1 + \left(\frac{v_M}{c}\right)^2 + 2\left(\frac{v_M}{c}\right)\cos\theta_i\right). \tag{1.29}$$

In Fig. 1.7–b is displayed the variation of ω_r/ω_0 for different angles of incidence. This quantity depends only weakly on θ_i.

Relativistic Oscillating Mirror model by Lichters. In practice, the mirror is not traveling at constant velocity but is oscillating back and forth under the influence of the laser electric field. Its velocity is thus continuously varying from 0 to some $v_{M_{\max}} = v_{osc}$ during a laser period (see Sec. 1.2.2) and one should expect generating a comb of different harmonic orders rather than a single frequency ω_r.

The mechanism of generation based on a relativistic oscillating mirror was initially proposed by [Wilks, 1993] and [Bulanov et al., 1994], but [Lichters et al., 1996] was the first to derive a model

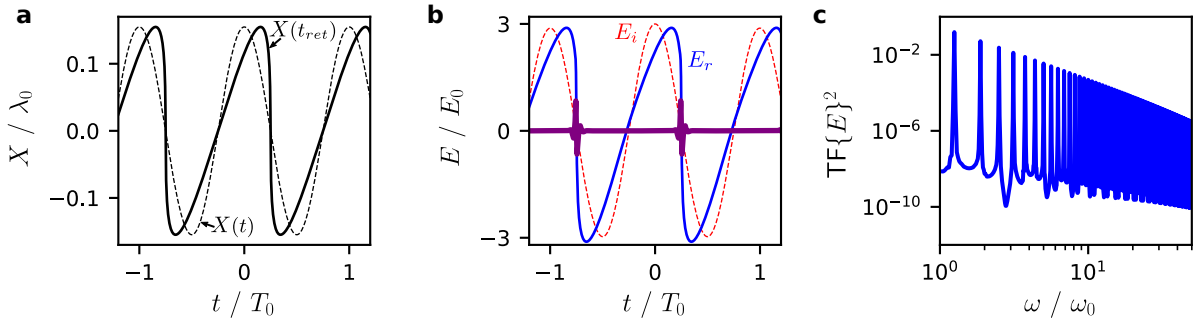

Figure 1.8: **The Relativistic Oscillating Mirror model by Lichters** - In panel (a) is pictured the position of the surface electrons under the combined action of incident and reflected fields: $X(t)$ is plotted in dash line and $X(t_{ret})$ ($X(t)$ at retarded times) in solid line. In panel (b), we plot the incident (red) and reflected (blue) electric fields as well as the reflected field filtered for harmonics 20 to 40 (purple). Finally, the whole spectrum of the electric field is displayed in panel (c) in log-log scale.

that gives the temporal shape of the reflected field. This model assumes that the plasma setup is the same as for Brunel mechanism (see Fig. 1.4–b, page 16): the $x < 0$ area is filled with a steep overdense plasma ($n_e \gg n_c$ and $L_g \ll \lambda_0$) and a p-polarized laser is impinging on this target with an angle of incidence θ_i. Ions are kept immobile and electrons located at the position $X(t)$ are oscillating under the action of the laser electric field. Considering the steepness of the skin depth — $l_s = c/\omega_p$ — at the interface vacuum-plasma, we suppose that the harmonic generation also takes place at $X(t)$.

According to [Lichters et al., 1996], the expression of $X(t)$ should not be simple, because the restoring force created by the space charge electrostatic field behaves differently in the plasma layer and in vacuum. This force can only be described by kinetic simulations, whereas Lichters' model bases on hydrodynamic equations. So, the authors assume that the surface should mainly be driven by the laser. That gives an analytical form for $X(t)$ pictured as a sine wave (or a more complicated periodic form, combination of different laser harmonics):

$$X(t) = \frac{v_{osc}}{\omega_0} \cos(\omega_0 t + \phi), \tag{1.30}$$

where v_{osc} reads at oblique incidence:

$$\frac{v_{osc}}{c} = \frac{2a_0 \sin\theta_i}{\sqrt{1 + (2a_0 \sin\theta_i)^2}}. \tag{1.31}$$

ϕ is the relative phase between the driving field and the surface oscillation. Recalling that the harmonic source is sharply localized at $X(t)$, the reflected electric field $E_r(x,t)$ is given by:

$$E_r(x,t) \simeq \mu_0 c \int J_{//}(X(t_{ret}), t_{ret})\, dx' \simeq \mu_0 c\, l_s\, J_{//}(X(t_{ret}), t_{ret}), \tag{1.32}$$

where $J_{//}$ is the current transverse to the plasma surface and

$$t_{ret} = t - (X(t_{ret}) - x)/c \tag{1.33}$$

is the retarded time that takes into account the temporal delay between the emission from the source and an observer located in x at a time t. Physically, $X(t_{ret})$ simply corresponds to the position of the surface as seen by this observer.

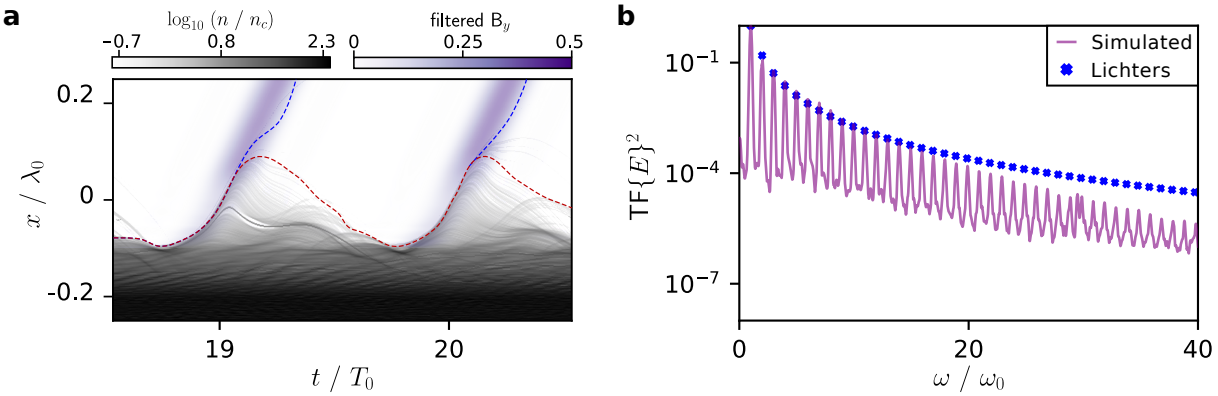

Figure 1.9: **Relativistic Oscillating Mirror in numerical simulation** - The data were extracted from a 1D Particle-In-Cell simulation. Panel (a) shows the temporal evolution of the plasma surface (in black), as well as the emitted attosecond pulses (in purple). The plasma surface is sketched in a red dash line as well as representative trajectories for ejected electrons in blue. In panel (b), the spectrum found in this simulation (purple solid line) is compared to the one predicted by Lichters' model (blue crosses). The y-axis is in log scale.

The electric field can be determined by evaluating $X(t_{ret}) = X(t - (X(t_{ret}) - x)/c)$, which corresponds to a fixed point problem $f(a) = a$. Because t_{ret} appears on both sides of Eq. (1.33), $X(t_{ret})$ is solved by using a recursive algorithm:

$$\begin{aligned} &\bullet \quad X_0 = X(t), \\ &\bullet \quad X_{k+1} = X(t - (X_k - x)/c), \end{aligned} \tag{1.34}$$

where $X(t)$ is given by Eq. (1.30).

The converged value of $X(t_{ret})$ is plotted in Fig. 1.8–a. From the point of view of the fixed observer, the retarded times distort the profile of the surface. Because of the Doppler effect due to the motion of the surface, the reflected electric field is distorted as well (see Fig. 1.8–b). It results that extra frequencies appear in the spectral domain (see Fig. 1.8–c). The time corresponding to the harmonic emission is obtained after filtering a certain range of harmonics (e.g., from the orders 20 to 40) and returning back into the temporal domain. As shown in Fig. 1.8–b, the harmonics are mostly generated when the laser wavefront is steep. The filtered field (purple line) is characterized by a train of attosecond bunches, each one separated by a laser period.

The principal results obtained with Lichters' model are now compared to Particle-In-Cell simulations (see Ch. 3, page 43 for more information on the Particle-In-Cell method). In Fig. 1.9–a, we plot the plasma density along time in black as well as the filtered field extracted from a 1D simulation. Similarly to the analytical derivation, the plasma surface (red line) oscillates in time and at every laser period, attosecond pulses are emitted towards vacuum. However, as shown in Fig. 1.9–b, the Lichters' model fails to perfectly reproduce the harmonic efficiency decay (even it well matches at lowest orders). This discrepancy might come from the principal assumption of the Lichters' model, which imposes a sine profile for $X(t)$.

More generally, the ROM model allows for a simple understanding of the physics at play and reproduces the main features of the reflected electric field waveform. However, it does not give any precise insights on the spatial properties of the harmonic beam or a possible harmonic cutoff. Since Lichters, many more authors have tried to extend the model of the oscillating

mirror [Baeva et al., 2006; Gonoskov et al., 2011; Debayle et al., 2015], but it seems that a universal model, capable of predict all right properties of the harmonic emission in any cases, has not been found yet.

1.3.2 Electron acceleration from plasma mirrors

Synchronized with the harmonic emission, plasma mirrors can also inject attosecond electron bunches into the intense reflected field. These electrons will undergo a direct interaction with the laser beam through a process called *Vacuum Laser Acceleration* or *VLA* [Thévenet, Leblanc, et al., 2016] and be continuously accelerated in vacuum. In fact, if an electron remains in a given optical laser cycle, it constantly gains energy through transverse acceleration imposed by the laser electric field, until it leaves the focal volume[4]. This scheme is promising because it relies on accelerating fields as high as 10 TV.m^{-1} that largely overcome the typical values observed in conventional accelerators ($\sim$ 50 MV.m^{-1}).

However, even if the process behind VLA has been known for a long time, experimental observations have largely remained ambiguous [Malka et al., 1997; Cline et al., 2013]. This is because VLA requires a controlled injection with specific initial conditions, which are found to be extremely challenging in actual experiments:

(i) the electron bunches must be narrow enough ($\ll \lambda_0$) that the whole is equally accelerated,

(ii) the electron bunches must be injected at relativistic velocities at the beginning of an accelerated cycle in order to maximize the gained energy. They must also leave the laser at a right time before entering a decelerated cycle.

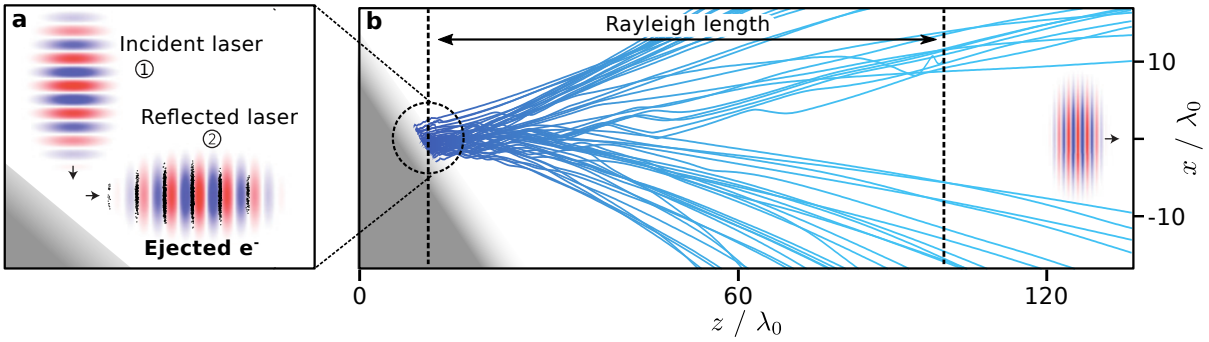

Figure 1.10: **Sketch of VLA with plasma mirrors** - [Image from [Thévenet, Leblanc, et al., 2016]] Panel (a) displays the injection of electrons (black dots) in the reflected field (blue to red). Electrons are grouped into attosecond bunches injected by the plasma mirror at each optical laser cycle. Panel (b) pictures the interaction of electrons in vacuum. Several electron trajectories are plotted in blue extracted from a 2D numerical simulation.

Electrons that are not properly injected in the laser beam tend to explore many different optical cycles, where they are accelerated and decelerated for an overall low gain of energy. This problem did stand during many years until it was finally solved in [Thévenet, Leblanc, et al., 2016], which proposes the first indubitable evidences of VLA by using plasma mirrors as electron injectors, which verify both above conditions. The general idea is presented in Fig. 1.10. In

[4]It implies that the laser cannot be a plane wave (see Sec. 1.2.3) but must present a finite spatial extension. The most common spatial envelop is the Gaussian waveform.

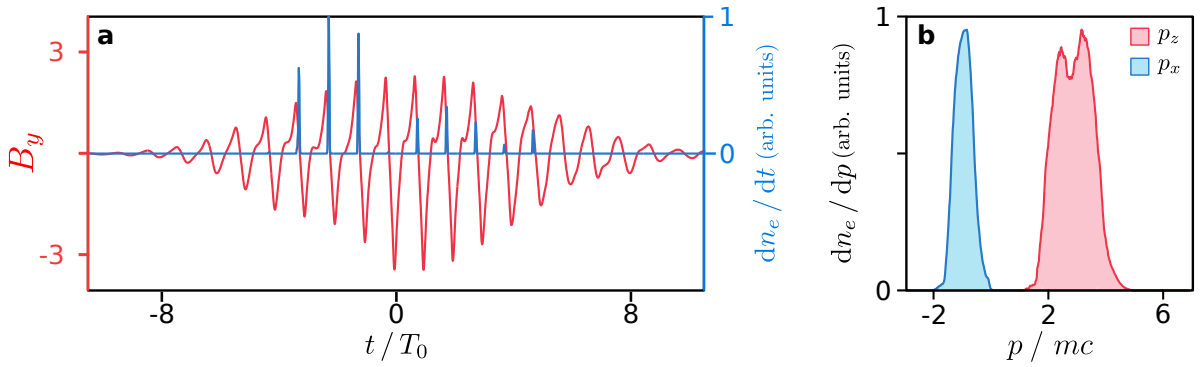

Figure 1.11: **Initial conditions of electrons ejected from plasma mirrors** - [Image from [Thévenet, Leblanc, et al., 2016]] Panel (a) illustrates the waveform of the laser magnetic field B_y reflected by the plasma mirror (red line) and the temporal density profile of the ejected electrons (blue line), obtained from a numerical simulation. Panel (b) shows the corresponding momentum distribution of these electrons, along the specular direction, p_z, and along the polarization direction of the reflected laser, p_x, taken from the same simulation.

the following, the whole process is dissociated in two steps: the injection (Fig. 1.10–a) and the interaction in vacuum (Fig. 1.10–b).

Electron injection in the reflected field. According to [Thévenet, Leblanc, et al., 2016], two parameters are crucial to operate a suitable injection: the phase in the laser field and the initial electron velocity (momentum). In [Geindre et al., 2010; Tian et al., 2012], it was noticed that electrons are expelled from a plasma mirror in the form of attosecond bunches once per laser period and at very precise phases, close to the nodes of the reflected laser field (see Fig. 1.11–a). For now, let us assume that the bunching primarily comes from the ROM harmonic generation: at each cycle, when an attosecond bunch of light is emitted towards vacuum by the surface electrons, some of these manage to escape the mirror and concurrently travel with the harmonic beam. Such electrons may be seen in numerical simulations (see the blue dash line in Fig. 1.9–a). Further ahead in the manuscript (see Sec. 6.1), we will introduce another mechanism which is also at play and helps rearranging electrons in bunches, right after the emission.

Regarding velocity, the electrons start their motion from the plasma surface at slightly relativistic energy ($\mathcal{E} \sim 1.5$ MeV) along the laser specular direction (see Fig. 1.11–b). The initial conditions are thus quite ideal for VLA.

Interaction in vacuum. To study the dynamics in vacuum, [Thévenet, Leblanc, et al., 2016] base their results on numerical simulations performed with a particle tracker code that solves motion equations along time using analytically imposed fields (see Ch. 4, page 65 for more information on the method). It appears that two electron populations can be discriminated depending on the number of optical cycles N_{oc} that they have experienced during their interaction with the laser:

- for low energy electrons, the dynamics in the laser are driven by a force depending on the waveform (e.g., Gaussian) and directed towards low-intensity regions: the ponderomotive force. The motion relies on a timescale separation, where every quantity f is written as $f = \bar{f} + \tilde{f}$ with $\bar{f}$ varying slowly and $\tilde{f}$ varying rapidly with respect to the laser period [Quesnel and Mora, 1998]. In general, the particle experiences fast oscillations in the laser

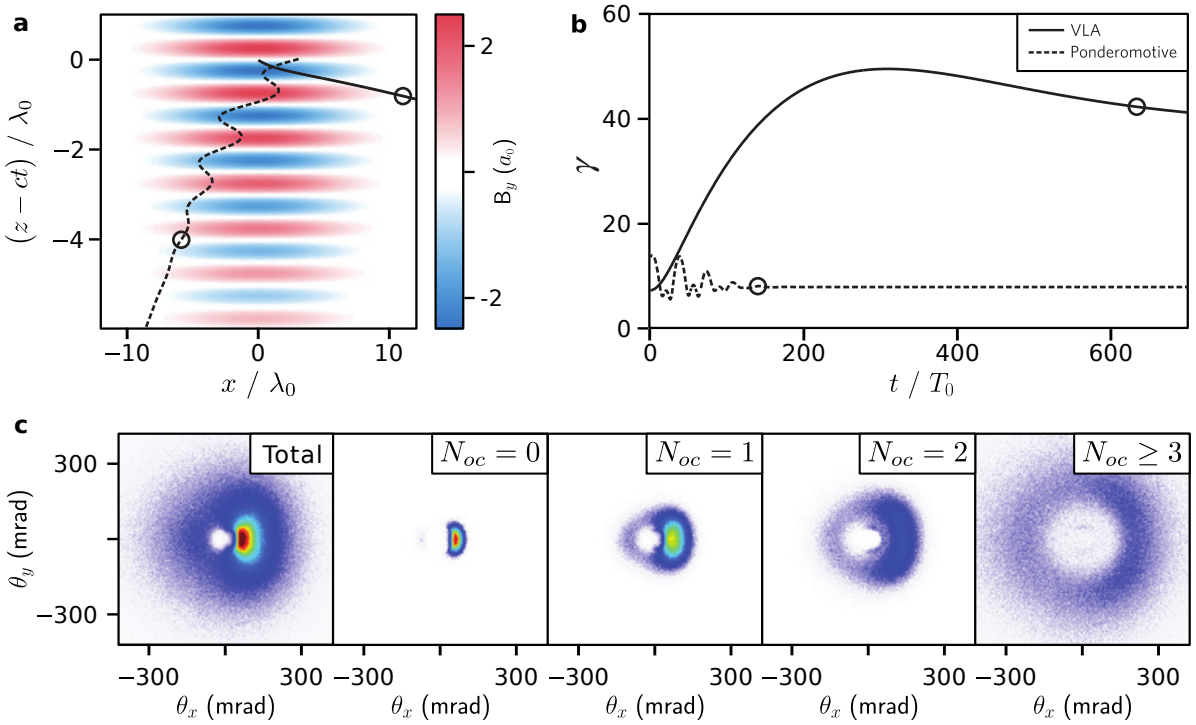

Figure 1.12: **Electron interaction in vacuum** - [Image from [Thévenet, Leblanc, et al., 2016]] On panel (a) are shown two trajectories corresponding to a ponderomotive electron (dash line) and VLA electron (solid line). The circles indicate the position of the electrons, as they escape the laser influence. On panel (b) are plotted the energy of the same two electrons along time. Finally, panel (c) pictures the angular distribution for various electron populations ($N_{oc} \in [0,\ 3+]$) as well as the whole distribution.

cycles and slow oscillations due to the variations of the pulse envelope in space. The general form of the ponderomotive force is obtained after averaging all quantities over the laser period and reads:

$$\frac{\mathrm{d}\bar{\boldsymbol{p}}}{\mathrm{d}t} = -\frac{e^2}{2m\bar{\gamma}} \boldsymbol{\nabla} \overline{|\tilde{A}_\perp^2|}, \tag{1.35}$$

where A is the vector potential of the wave. The force only depends on the gradient of the wave intensity and the direction of polarization plays no particular role. For a Gaussian beam, electrons tend to be radially expelled from the high intensity regions (center of the pulse).

Electrons, which explore several optical cycles ($N_{oc} > 3$) are called *ponderomotive electrons*. They are quickly propelled out of the laser volume at low energy in all directions (because of the isotropy of the ponderomotive force) (see Fig. 1.12–a, b).

- When an electron is highly relativistic, it tends to stay longer in one optical cycle as its speed is close to the phase velocity of the wave. It can gain energy all along its trajectory and escapes the laser before dephasing ($N_{oc} = 0$, see Fig. 1.12) after typical distances of the order of the Rayleigh length.

The transition from one extreme population to another is of course continuous and depends on the gamma of injection. In Fig. 1.12–c, we show how electrons are angularly distributed in the final angular distribution as a function of N_{oc}. Ponderomotive electrons form a ring-shaped beam centered on the laser propagation axis, whereas VLA electrons ($N_{oc} = 0$) tend to concentrate in

a bright peak on the edge of the ponderomotive hole, along the polarization direction. This peak is located on one side of the hole because electrons are ejected once every laser period and all surf the same half-cycle (in practice the one corresponding to negative values of the electric field).

Conclusion

When an intense laser pulse ($I > 10^{18}$ W.cm^{-2}) is focused on a solid target, the electric field is sufficiently powerful to completely ionize the target surface and create a dense plasma, which expands towards vacuum. The density profile in front of the target is observed to be exponential, characterized by the density gradient length — L_g.

When $L_g \ll \lambda_0$, the plasma behaves as a mirror of optical quality, which is able to completely reflect the incoming light in the specular direction: it becomes a *plasma mirror*. In this regime, the excursion amplitude of electrons in the laser oscillations becomes so large that it can exceed the gradient scale length itself. At every optical cycle, the surface electrons are first pulled out of the plasma by the electric field before being accelerated back to the target when its sign shifts. It is the Brunel mechanism.

Under the action of the laser, the plasma surface periodically oscillates in time and acts as a relativistic oscillating mirror capable of distorting the incident field by Doppler effect. This periodic temporal modulation is associated to a high harmonic content in the frequency domain or to a train of attosecond pulses, in the temporal domain. Synchronized with this harmonic emission, relativistic electrons are also emitted in the form of attosecond bunches that can be injected at the right phase in the reflected field. These electrons undergo Vacuum Laser Acceleration and gain energy by direct interaction with the laser in vacuum.

When $L_g \sim \lambda_0$, the laser can propagate in the underdense part of the plasma and be reflected at the density $n_c \cos^2 \theta_i$. At low intensity, some energy can be transfered to a resonant plasma wave, which grows near the critical density until eventually breaks. At higher intensities, the dominant absorption mechanism has not been evidenced so far and the transition from resonance absorption remains unclear. In this context, one objective of this PhD thesis will be to elucidate and model this "new" mechanism, called stochastic heating, for which particles are evolving chaotically inside the underdense part of the plasma layer.

2 Introduction to Chaotic Dynamics

Along this chapter, let us stand aside from the previously described framework to discuss on a more general topic in physics known as *system dynamics* [Strogatz, 2018]. It will be useful in the next chapters to describe stochastic heating. This topic encompasses all studies related to the temporal evolutions of a given physical system. It all started in the mid-1600s, when Newton discovered the basic laws of motion and explained celestial mechanics previously observed by Copernicus or Kepler. In particular, he put into equation and resolved the two-body problem, where two massive objects (e.g., the Earth and the Sun) move under the action of gravity.
From there, physicists tried to extend Newton's derivation to more complex systems, starting with the three-body problem (e.g., by adding the Moon in the previous Earth-Sun system) but it surprisingly turned out to be much more difficult to solve. After two hundred years, it was admitted that in fact this problem was fundamentally unsolvable, in a sense that no universal analytical solution should exist.
In the late 1800s, a breakthrough came from Henri Poincaré [Poincaré, 1892], who introduced a new topological approach for the dynamics. His method allowed for qualitatively understanding intertwined behaviours of most solutions of the three-body problem. He was also the first to recognize that such a system is extremely sensitive to small perturbations and that small differences in the initial conditions may lead to large variations over time [Poincaré, 1908]. His work has truly paved the way towards a new branch of dynamics later called *chaos theory*, defined by [Kautz, 2010] as "the science of predictable random motion".

During this chapter, we go through the first historical manifestation of chaos in a simple system observed by Lorenz in [E. N. Lorenz, 1963]. We then extend this work to another class of non-linear systems that we will widely manipulate in the following of the manuscript: the *pendulum*. Note that by choice, this overview does not involve any heavy mathematical formalism so that it can be read and understood by non-specialists of chaos theory.

Contents

2.1 Butterfly Effect from Lorenz

2.1.1 History

In the first part of the 20th century, the ideas developed by Poincaré actually stayed marginal. Physicists were indeed skeptical that strange mathematical behaviours could happen in actual physical systems apparently governed by a well-defined set of deterministic equations (i.e., without randomness). Everything changed with the development of computers in the 1950s. Thanks to this new tool, one was capable of solving differential equations over large time scales, without relying on tedious analytical derivations.

It was precisely on his personal computer — a Royal-McBee LGP-30 — that Edward Lorenz accidentally observed chaos for the first time in 1961, while performing weather prediction simulations [E. N. Lorenz, 1963]. At some point of his work, Lorenz had to repeat a past simulation, but to save some time, he chose not to restart from the beginning but from a set of intermediate values instead. To do so, he entered as a new input, a state from the previous simulation that he recovered from a *printout*. However, the weather predicted by the second simulation largely diverged from the earlier complete calculation.

This discrepancy actually comes from a rounding error introduced by Lorenz himself while rebooting. Indeed, the printout data was rounded to three decimals, whereas the computer was manipulating numbers with higher precision (in practice 6). So, when the computer restarted, the new simulation was slightly different from the original run. Considering the *simplicity* of his system, Lorenz expected that such a low variation would not perturb the final result. However, he discovered that his weather model was highly unstable and extremely sensitive to initial conditions.

To reach as many people as possible, Lorenz illustrated this sensitive dependence on initial conditions in weather prediction by a poetic metaphor: the *Butterfly effect* [E. Lorenz, 1972]. He asked the following question: *Does the flap of a butterfly's wings in Brazil set off a tornado in Texas?*. At first glance, this question might seem a bit puzzling, because a butterfly is obviously not able to create a tornado on its own. In fact, the proposition herein does not rely on if it may or may not create the tornado but rather whather a flap of its wings can sufficiently perturb the whole atmospheric system that at some point down the road, a tornado would appear in Texas.

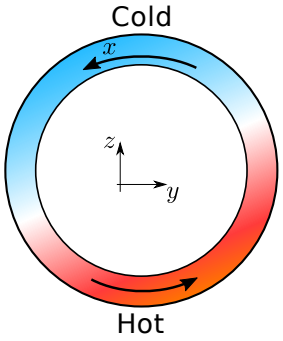

Figure 2.1: **Lorenz convection cell.**

It is actually impossible to answer Lorenz's question by direct weather observations. Of course the whole universe cannot reset and restart at a perfect state where everything remains identical but a flap of some butterfly wings. Nonetheless, as we will see later on, results from computational models of weather prediction tend to indicate that any perturbation produces results that diverge from each other at an exponential rate. Even some disturbance as imperceptible as a butterfly flap should eventually lead to great changes if one waits an adequate amount of time. The Butterfly effect exemplifies the difficulty to precisely predict weather at large time scales.

2.1.2 Lorenz's model for atmospheric convection

In 1961, the model that Lorenz developed was a simplified mathematical system for an atmospheric convection cell. Such a cell is displayed in Fig. 2.1. It is a ring tube where the atmosphere is heated in the bottom and cooled at the top. Because a warm air is rising up and a cold air is falling down, the fluid within the ring is always flowing. The system is highly imbalanced and there is no preferential sense for the direction of the fluid displacement. The fluid alternatively turns clockwise and anticlockwise as long as the heating and cooling systems are operating.

To model the system, Lorenz defined 3 variables $x(t)$, $y(t)$ and $z(t)$: x is somehow related to the rate of convection ($\sim$ the velocity of the fluid), y to the horizontal temperature gradient and z to the vertical temperature gradient. The Lorenz model can be written as followed:

$$\begin{aligned} \bullet \quad & \frac{\mathrm{d}x}{\mathrm{d}t} = \sigma(y - x), \\ \bullet \quad & \frac{\mathrm{d}y}{\mathrm{d}t} = R_a x - y - xz, \\ \bullet \quad & \frac{\mathrm{d}z}{\mathrm{d}t} = xy - bz, \end{aligned} \tag{2.1}$$

where σ, R_a and b are fixed parameters: σ is called the Prandtl number, R_a the Rayleigh number and $b > 0$ is related to the convection itself. In his original paper, [E. N. Lorenz, 1963] considered the case where $\sigma = 10$, $R_a = 28$ and $b = 8/3$.

In Fig. 2.2, we plot a solution along time in the 3D-space $(x,\ y,\ z)$. The trajectory remains bounded to a particular volume, which curiously also looks like a butterfly. It appears that the

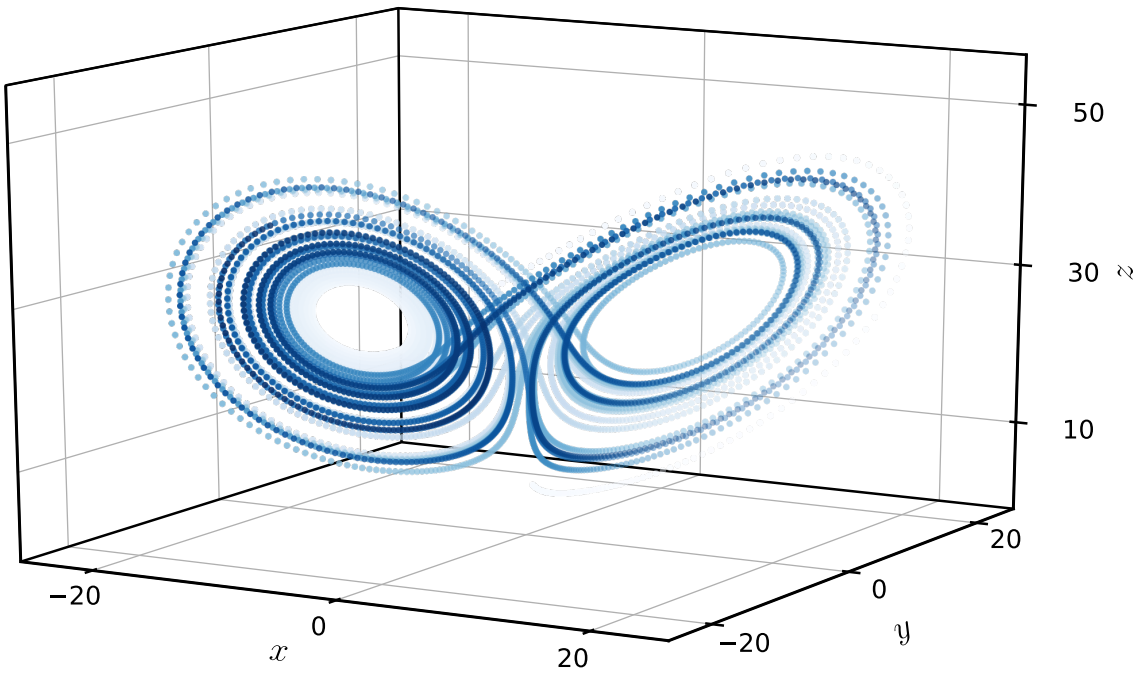

Figure 2.2: **Trajectory on Lorenz's strange attractor** - In this figure is plotted a 3D-trajectory of a solution of Eqs. (2.1) for $t \in [0,\ 40]$ from white ($t = 0$) to dark blue ($t = 40$). Here, we use $(\sigma,\ R_a,\ b) = (10,\ 28,\ 8/3)$ and $(x(0),\ y(0),\ z(0)) = (0,\ 1,\ 5)$.

curve is rolling over two points (located at $\sim [\pm 8.5,\ \pm 8.5,\ 28]$) but never stabilizes around one. Instead, the solution jumps from one wing to the other.

In dynamical systems, we call *attractor* an ensemble towards which a system tends to evolve. Most of the time, an attractor is simply a geometric subset of the whole space such as a fixed point (e.g. for the linear pendulum) or a limit cycle, sketching a succession of the same periodic set of values (e.g., the Van der Pol oscillator [Van der Pol, 1926]). Lorenz's system exhibits another class of attractors showing a complex structure that cannot be described by linear combination of geometric objects. Such attractors are called *strange attractors*. Starting from any initial state $(x(0),\ y(0),\ z(0))$, the resulting solution of Eqs. (2.1) will ultimately tend to the attractor and never depart from it.

The dimension of the Lorenz's attractor can be measured by mathematical derivations [Hausdorff, 1919; Grassberger and Procacia, 1983] and shows a non-integer value of ~ 2.05. The dimension is then slightly larger than the dimension of a surface but necessarily below 3, the dimension of the whole space.

2.1.3 Sensitivity to initial conditions

However, for now, even if the system behaviour is clearly anharmonic and nonlinear, it is not yet sufficient to claim that it is chaotic. To do so, we have to prove that the system is extremely sensitive to initial conditions. So, we intentionally repeat what Lorenz did by mistake: change slightly the initial state and see how the final result is being affected.

We decide to conduct this study by modifying the initial value of x, but note that changing y or z would lead to the same conclusions. So, let x_1 be the solution for $x(t)$ of the Lorenz's system plotted in Fig. 2.2 and x_2 a solution for $x(t)$ initialized arbitrary close to x_1 by a small amount $d(0)$, where $d(t) = |x_1(t) - x_2(t)|$. Several trajectories corresponding to different values of $d(0)$

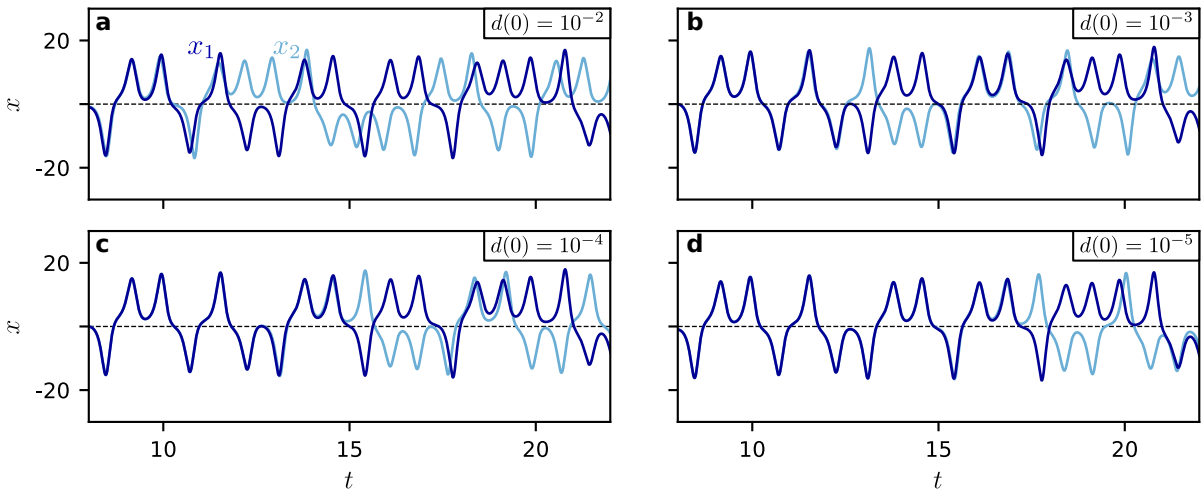

Figure 2.3: **Temporal evolution of the fluid velocity for different initial conditions** - On each panel, two trajectories are plotted: x_1 in dark blue considered as a baseline and x_2 a trajectory initially very close to x_1 by a small offset $d(0)$ given in labels. The Lorenz parameters are $\sigma = 10$, $R_a = 28$ and $b = 8/3$.

are reported in Fig. 2.3. Immediately, it comes that similarly to Lorenz, we found that x_1 and x_2 are separating after a short time. As expected, the smaller the offset, the longer it takes to perceive the effect of the initial deviation. However, for $d(0)$ as small as 10^{-5} the motion is grossly affected as early as $t = 17$ time units. Worse, dividing by a factor of 10 the offset only delays the time to separation by $\simeq 2$ time units. It seems that indeed the system is extremely sensitive to small perturbations.

The chaotic character of the dynamics can be further quantified by the calculation of the so-called *Lyapunov exponent* — λ_L. The Lyapunov exponent of a dynamical system is a mathematical quantity that characterizes the rate of separation of infinitesimally close trajectories. Quantitatively, two trajectories in a given space initially separated by $d(0)$ evolve along time at an exponential rate given by:

$$d(t) = |x_1(t) - x_2(t)| \approx d(0) \exp(\lambda_L t) . \tag{2.2}$$

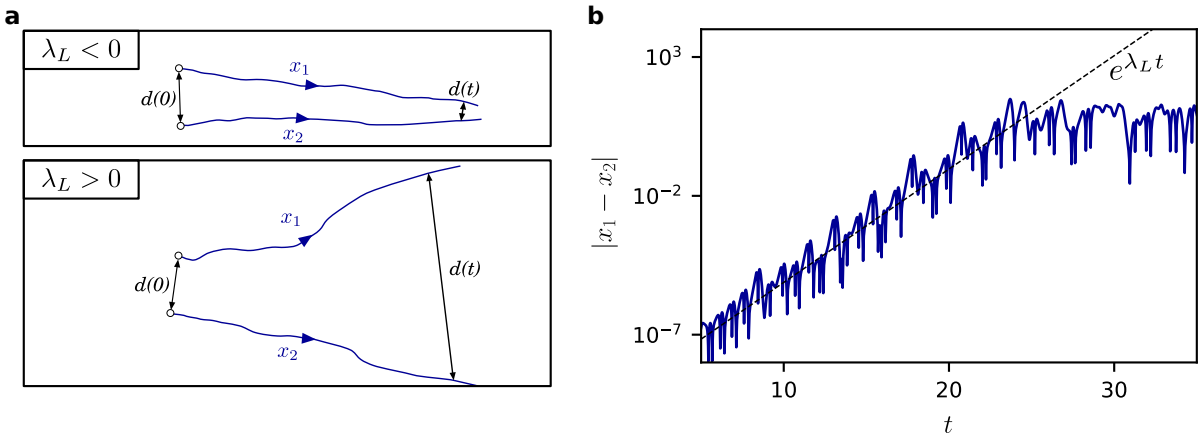

Figure 2.4: **Lyapunov exponent of the Lorenz's system** - Panel (a) displays a schematic drawing of the evolution of two trajectories x_1 and x_2 along time in function of the sign of the Lyapunov exponent λ_L: (i) in the upper part of the panel, $\lambda_L < 0$ and the trajectories tend to get closer to each other, (ii) when $\lambda_L > 0$, the system becomes chaotic and the trajectories diverge. On panel (b) is plotted in log scale the deviation $d(t) = |x_1(t) - x_2(t)|$ as a function of time for the Lorenz's model for an initial offset $d(0) = 10^{-7}$. We plot as well the curve $f(t) = \exp(\lambda_L t)$ as a dashed line. The Lorenz parameters are $\sigma = 10$, $R_a = 28$ and $b = 8/3$.

A schematic drawing of the trajectory separation in a general case is sketched in Fig. 2.4–a. The behaviour of the system evolves differently depending on the sign of λ_L:

- when $\lambda_L < 0$ (upper drawing of Fig. 2.4–a), the two trajectories gets closer to each other, the system is non chaotic and dissipative. Small perturbations do not affect the system.
- When $\lambda_L \approx 0$, $d(t)$ stays close to $d(0)$ at all time, the system is also considered as non chaotic but this time no more dissipative.
- when $\lambda_L > 0$ (lower drawing of Fig. 2.4–a), two trajectories even arbitrary close diverge, the system becomes chaotic.

In numerical computations, it is common to define the Lyapunov exponent between x_1 and x_2

as[1]:

$$\lambda_L(x_1,\, x_2) = \lim_{t\to\infty} \left(\frac{1}{t} \ln \frac{d(t)}{d(0)} \right). \tag{2.3}$$

For the Lorenz's system, we find $\lambda_L \simeq 0.94 > 0$. In Fig. 2.4–a, $d(t)$ is plotted along time in log scale and follows an exponential trend until $t \sim 25$ time units. However, at longer times, the separation between original and perturbed trajectories are no longer growing. According to [Kautz, 2010], the saturation comes from the system itself: the convecting fluid inside the cell cannot travel faster than a certain threshold. As shown in Fig. 2.3, the absolute velocity of the fluid $|x_1|$ is bounded by 18 units, so d cannot exceed 36 in the worst case scenario (when $x_2 = -x_1$). This highlights an interesting property of chaotic systems (at least those involving a strange attractor): they are locally unstable but yet globally stable. Two trajectories adopt an overall similar motion (stay confined within the attractor), while remaining forever distinct.

Lorenz's system is particularly interesting for those who discover chaos, for both historical and physical reasons. From very simple equations, it illustrates the main chaos properties that we will face again in the manuscript.

2.2 Chaos in Pendulums

2.2.1 Simple gravity pendulum

Another example of nonlinear systems that can sometimes exhibit chaotic behaviours are pendulums at large. As a reminder, a pendulum consists of a bob suspended by a rigid (and massless) rod to a pivot point. For now, we consider the simplest case of all, the *Simple gravity pendulum*, for which the pivot position has been fixed.

We define $\theta(t)$ as the angle between the rod and the vertical axis and $v_\theta(t) = \mathrm{d}\theta/\mathrm{d}t$ the angular velocity of the bob along time, as shown in Fig. 2.5–a. We define the so-called X and O points, respectively the top unstable ($\theta = \pi$) and bottom stable ($\theta = 0$) positions of the bob. Its temporal motion is governed by the following differential equation:

$$\frac{\mathrm{d}^2\theta}{\mathrm{d}t^2} + \nu \frac{\mathrm{d}\theta}{\mathrm{d}t} + \omega_0^2 \sin\theta = 0, \tag{2.4}$$

with ω_0 the angular frequency of the system and ν a friction coefficient. If $\nu \neq 0$, the pendulum motion is *damped*.

When $\nu = 0$, the position and velocity are related as follows:

$$\frac{\mathrm{d}^2\theta}{\mathrm{d}t^2} = -\omega_0^2 \sin\theta, \tag{2.5}$$

$$\frac{1}{2}\left(\frac{\mathrm{d}\theta}{\mathrm{d}t}\right)^2 = \omega_0^2 \cos\theta + C^{st},$$

$$v_\theta^2 = v_0^2 - 2\,\omega_0^2\,(1 - \cos\theta), \tag{2.6}$$

where we consider the initial conditions: $\theta(0) = 0$ and $v_\theta(0) = v_0$. In Fig. 2.5–b are plotted different bob trajectories for different values of v_0 in *phase space* $(\theta,\, v_\theta)$. Note that θ describes

[1] This particular formula in fact gives the *maximal* Lyapunov exponent. In practice, there are as many Lyapunov exponents as the dimension of the system (For Lorenz's, = 3), but for our purpose, the only knowledge of the maximal exponent is sufficient.

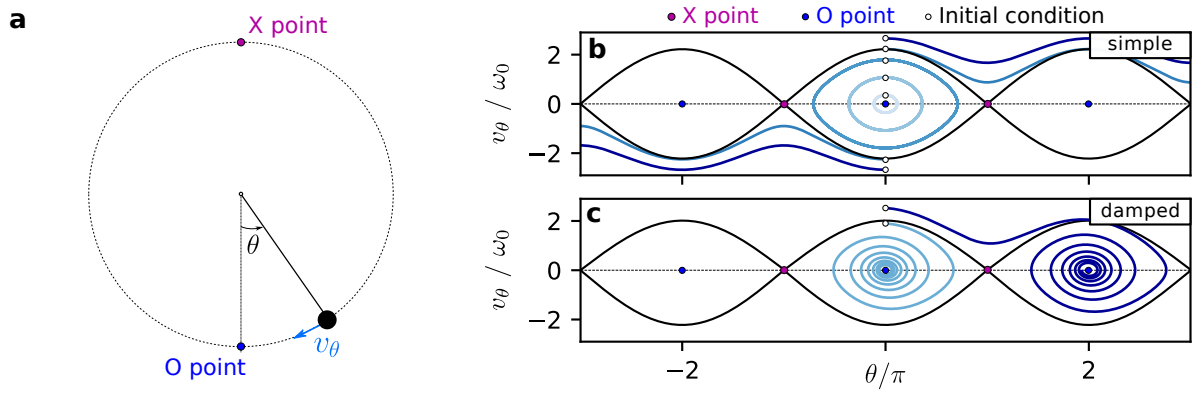

Figure 2.5: **Trajectories in phase space for a simple pendulum** - Panel (a) sketches a simple pendulum and highlights two positions of interest: the unstable X point and the stable O point. On panels (b) and (c) are plotted different trajectories in phase space, solutions of Eq. (2.4): (b) $\nu = 0$ and (c) $\nu = 0.1$. Each trajectory starts from a different initial state (displayed as white circles), which corresponds to $\theta(t) = 0$ and $v_\theta(0) = v_0$ from 0.3 to 2.5 ω_0. The O and X points are also pictured in this space.

angles defined between 0 and 2π radians, but we unwrap the θ-axis to keep track of potential gains (or losses) of turns, observed when the bob crosses the top X position. According to Fig. 2.5–b, the system exhibits two peculiar behaviours:

- when $|v_0|$ is low, the trajectories stay trapped. The pendulum mass is reaching a certain position $\theta_0 < \pi$ and then returns backwards. It permanently oscillates around the stable O point position, which is equivalent to describing a closed orbit in phase space. This orbit tends to an ellipse if the initial kick is so weak that the approximation $\sin\theta \simeq \theta$ is verified at all time.

- when $|v_0|$ is sufficiently large, the trajectories are not closed anymore and the mass is able to complete full rotations. Along its motion, it crosses the position of the unstable X point.

The orbit that crosses $\theta = \pi$ at zero velocity, delimits trapped and circulating trajectories and is called the separatrix (drawn in black in Fig. 2.5–b). It corresponds to $v_0 = 2\,\omega_0$.

When damping is taken into account ($\nu > 0$), the pendulum progressively slows down, while oscillating. A trajectory below the separatrix is not a closed ellipse anymore but rather a spiral that gets closer to the O point at each passings (see light blue line in Fig. 2.5–c). If the bob has started from a circulating orbit, its velocity decreases until being too weak to allow for a full rotation (dark blue line). As soon as the trajectory crosses the separatrix, it also becomes trapped and the mass is spiraling around the O point. For a damped pendulum, this fixed point is an attractor.

The (damped) simple pendulum does not show chaotic motions. The trajectories are analytically described when $\nu = 0$ and when $\nu > 0$, the pendulum tends to stop, no matter its initial velocity. A system was shown to be chaotic, if any two initially close trajectories diverge. Regarding the stated properties of the simple pendulum, finding chaos is unlikely.

2.2.2 Forced pendulum

As we did not find any chaos signatures for the simple pendulum, we complicate the system by imposing an external force oscillating at an angular frequency ω. In practice, the pivot point, which was previously fixed, is now connected to a driver that applies a sinusoidal torque (see Fig. 2.6–a). The equation governed the bob motion is thus being modified as follows:

$$\frac{\mathrm{d}\theta^2}{\mathrm{d}t^2} + \nu\frac{\mathrm{d}\theta}{\mathrm{d}t} + \omega_0^2 \sin\theta = a \sin\omega t, \tag{2.7}$$

where a is the amplitude of the driving force.

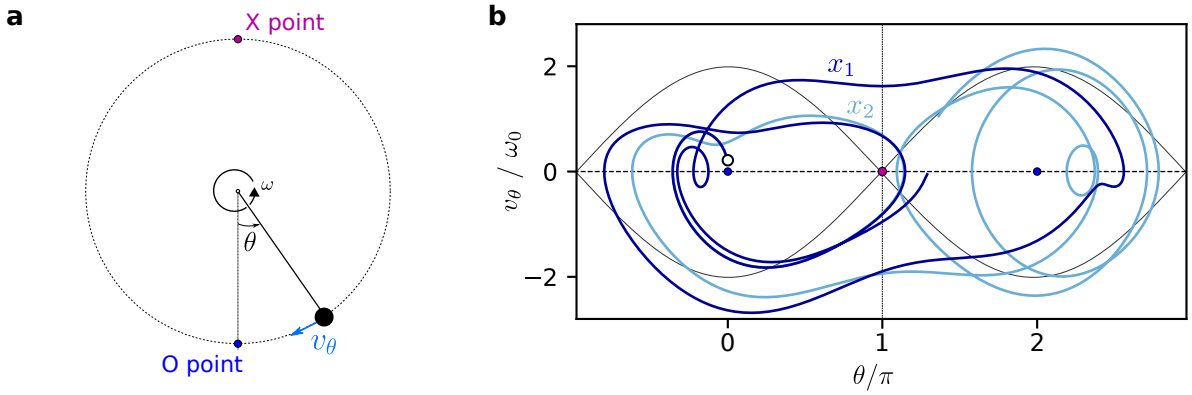

Figure 2.6: **Trajectories in phase space for a forced pendulum** - Panel (a) sketches a forced pendulum and highlights two positions of interest: the unstable X point and the stable O point. On panel (b) is plotted two trajectories in phase space, solutions of Eq. (2.7) for $\nu = 0.1$, $a = 1$ and $v_0 = v_\theta(0) = 0.2\,\omega_0$ for x_1 and $= 0.201\,\omega_0$ for x_2. The O and X points are also pictured in this space.

In Fig. 2.6–b, similarly to the simple pendulum, we plot two trajectories in phase space, with the slightly identical initial conditions $\theta(0) = 0$ and $v_\theta(0) = 0.205 \pm 0.005\,\omega_0$. Now, the resulting trajectories seem unpredictable. When the pendulum is forced, the bob motion becomes non-periodic and alternates times of oscillations and times of rotations, without any particular logic. Fig. 2.6–b also highlights the extreme sensitivity of the system to initial conditions: two trajectories x_1 and x_2, which are initially distant by a variation of $10^{-3}\omega_0$ on the angular velocity, end up separating after only 10 ω_0^{-1}.

2.2.3 Origin of chaos

When a pendulum is driven by an external force, chaos seems to arise. Its origin can be intuitively explained by the fundamental nature of the top unstable X point position.

In a case of a simple unforced pendulum, the X point discriminates closed and circulating trajectories, so that a small variation on the velocity reached near that point, can lead to two very different trajectories: one where the bob falls back and one where it effectively crosses the top position. In a sense, it means that the simple pendulum may be sensitive to initial conditions. However, since this behaviour remains exceptional, it does not make it chaotic. In general, most trajectories initially very close do not radically diverge.

This is illustrated in Fig. 2.7–a-c in a case of a damped pendulum. For each panel, two trajectories with similar initial conditions are plotted. In Figs. 2.7–a and c, the initial velocity is either far too low or far too high when the bob approaches the X point, so that the two trajectories remain almost superimposed. If the velocity is too low, the bob does not reach the X point and falls back to oscillate around $\theta = 0$. If the velocity is too high, the bob exceeds the X point with a large velocity and the pendulum ends up oscillating around $\theta = 2\pi$. By contrast, when the initial angular velocity is chosen very close to $2.2\,\omega_0$ (see Fig. 2.7–b), the bob mass almost pauses at the top position and it either falls down (dark blue trajectory) or crosses the X point (light blue trajectory). The two resulting trajectories are clearly separated.

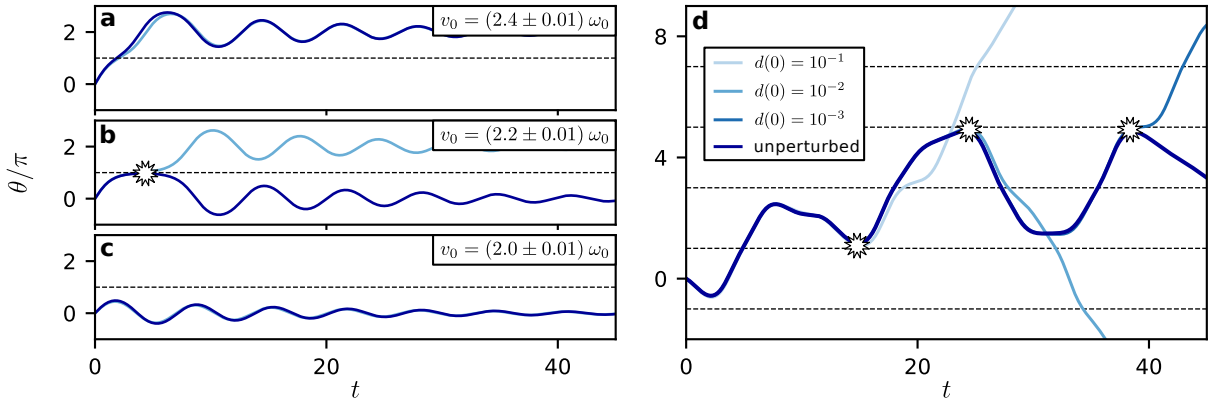

Figure 2.7: **sensitivity near the X point** - Panels (a-c) deal with the sensitivity to small variations for a damped simple pendulum. For each of these panels, two trajectories distant from $d(0) \sim 0.01$ are plotted. The initial velocities are chosen to approach an X point displayed in horizontal dashed line. On panel (d), the sensitivity is shown for a forced pendulum: a baseline trajectory is plotted in dark blue as well as three others shifted by an initial offset indicated in labels. For each trajectory, a white sun highlights the position, where it macroscopically differs from the baseline. The different horizontal dashed lines pictured different X point positions.

When the pendulum is forced with a sufficiently powerful driver, the crossing of the X point is repeated a large number of times. The divergence is no more limited to a single event but rather persists indefinitely. Each time the bob approaches the X point, there is a chance that neighboring trajectories diverge. Any trajectories, even very close initially, will eventually end up separating if one waits a sufficient amount of time.

This behaviour is displayed in Fig. 2.7–d, where four trajectories are plotted. One particular trajectory is chosen as a baseline and the three others are initialized with slightly different v_0. One can easily notice that the perturbed trajectories always diverge from the baseline when the bob is closed to the X point (pictured as horizontal dashed lines). This sensitivity to the X point is what makes the whole forced pendulum system chaotic.

2.2.4 Condition for chaos

In order to understand why chaos can only appear when the pendulum is forced, we now turn to mathematics. The first thing that brings chaos in a system is nonlinearities. Indeed, if a system is linear, a change of the input systematically leads to a proportional change of the output. It means that any initial small variations $d(0)$ does not grow in time, the system cannot be chaotic.

All the previously presented systems so far were actually nonlinear: the Lorenz's system involves two quadratic terms xz and xy and the gravitational force observed in pendulums depends on $\sin\theta$ rather than just θ. However, if nonlinearities are mandatory to exhibit chaos, they are not sufficient.

In particular, it is found that nonlinear systems of 2 variables can never be chaotic. This statement comes from a particular theorem intuited by H. Poincaré in 1881 and proved by I. Bendixson in [Bendixson, 1901]:

Theorem 1 *Given an autonomous*[2] *differential equation for a* ***two****-component vector* X — $dX/dt = f(X)$ — *with* f *a differentiable function from* $\mathbb{R}^2$ *to* $\mathbb{R}^2$*, then all solutions on a bounded support converge towards either a fixed point or a periodic function (= limit cycle).*

This theorem ensures that the only possible attractors in a 2D phase space are fixed points and limit cycles, both non chaotic. [Kautz, 2010] proposes a simple experiment to illustrate the Poincaré - Bendixson theorem (PBT), requiring only a pencil and a sheet of paper. There, the paper stands for a bounded 2D space and the pencil is used to draw a trajectory. The challenge is to find a trajectory that satisfies three conditions: (i) it must stay in the sheet domain, (ii) it cannot cross itself and (iii) it cannot pass arbitrarily close to itself when headed in the opposite direction (in order to preserve f differentiability). A simple try might convince the reader that the drawn trajectory can either stop to a point or be forced to approach a limit cycle.

For a simple pendulum, it is possible to rewrite Eq. (2.4) in the form expected by the PBT:

$$X = \begin{pmatrix} \theta \\ v_\theta \end{pmatrix} \quad \rightarrow \quad \frac{\mathrm{d}X}{\mathrm{d}t} = \begin{pmatrix} v_\theta \\ -\omega^2 \sin\theta - \nu v_\theta \end{pmatrix} = f(X). \tag{2.8}$$

Here, we verify that f is precisely a differentiable function. The orbit solutions of the system previously found are bounded. As you may recall θ designates an angle so $\theta \in [-\pi, \pi[$. The velocity is also bounded to $\pm v_0$ due to energy conservation (see Eq. (2.6)). Then, the PBT ensures that the system cannot exhibit any chaotic behaviours.

However, if the number of variables is higher than 2, the PBT cannot be applied and other kinds of attractors appear that allow chaotic dynamics. In Sec. 2.1, the atmospheric convection cell modeled by 3 time-dependent variables x, y and z (3D space) is chaotic within a strange attractor.

When a pendulum is forced, the applied torque imposes a third degree of freedom by explicitly adding t in the equation. It is possible to rewrite Eq. (2.7) as an autonomous system by introducing a new variable $\tilde{t} = t$, which reads:

$$X = \begin{pmatrix} \theta \\ v_\theta \\ \tilde{t} \end{pmatrix} \quad \rightarrow \quad \frac{\mathrm{d}X}{\mathrm{d}t} = \begin{pmatrix} v_\theta \\ -\omega^2 \sin\theta - \nu v_\theta + a \sin\omega\tilde{t} \\ 1 \end{pmatrix} = f(X). \tag{2.9}$$

As Lorenz's system, the dimension for X is also $3 > 2$, so the pendulum system may be chaotic (and actually is, see Fig. 2.6).

[2] An equation or a system of equations are called autonomous when they do not explicitly depend on the variable used in the derivatives. In this chapter, this variable is exclusively t.

Conclusion

Along this chapter, we endeavor to introduce the basics of chaotic dynamics for non-chaos specialists. To ensure accessibility, we choose the physicist's point of view (rather than the mathematician's) and propose intuitive clues on how and why some nonlinear system can behave chaotically.

The starting point of this overview was the remarkable Lorenz's model for atmospheric convection. From simple equations, it illustrates the extreme sensitivity to initial conditions in weather prediction, a phenomenon known as the butterfly effect. A small perturbation does not change the fundamental character of the fluid convective motion but it jumbles our ability to predict it.

Chaos can also be encountered in even simpler nonlinear systems, the pendulums. For these, the sensitivity to small variations is exclusively located near the top unstable position and a small variation on the velocity observed near this point can discriminate trapped and circulating orbits. When a pendulum is forced, the unreliability experienced near the X point is faced repeatedly, which gives rise to global chaotic behaviour for any trajectories.

This study might be found a bit unrelated to laser-plasma interaction. However, we will demonstrate further ahead that the equations of motion of free particles in plane waves can be in fact reduced into pendulum equations. Understanding how chaos can appear in such systems is essential to comprehend stochastic heating.

Part II

Numerical Tools

3 Particle-In-Cell Simulations for a full Kinetic Description of Laser-Plasma Interactions

Although some aspects of laser-plasma mirror interactions can be analytically resolved in the first chapter, many kinetic effects could not be efficiently captured without the support of numerical simulations, especially Particle-In-Cell (PIC) codes. In addition, they offer deeper insights on the interaction, not accessible in the experiments due to the extremely short time and length scales at play. This chapter mainly focuses on the PIC method. After explaining the general algorithm, we show typical diagnostics used in all simulations tackled in this manuscript. Then, we show that the standard PIC method employing finite-difference Maxwell solvers induce strong numerical noise, which can strongly affect the physical processes observed in laser-plasma mirror interactions. This has hindered the understanding of key phenomenons at the center of this thesis. These errors might be avoided using a dispersion-free solver, such as the recently developed pseudo-spectral solver, available in the WARP+PXR code.

Contents

3.1 Vlasov-Maxwell System

Being natural or artificial, the different plasmas are characterized by a large range of density n_e or temperature T_e, which span multiple spatio-temporal scales and particle interactions. Nevertheless, it is common to classify plasmas in two large categories based on the particle collision rate. For almost collisionless plasmas, two physical models are widely used: kinetic and hydrodynamic models. The last ones can be used to study laser-plasma interactions as long as kinetic effects (for instance particle trajectories crossing due to plasma wavebreaking) do not play a notable role. In this case, it makes sense to average kinetic equations in space and define typical fluid quantities such as density or mean velocity. These models are particularly interesting to study plasma flow, such as solar wind or plasma discharge. However, in UHI physics, the plasma dynamics are often much more complex and it is frequent to observe particles crossing, which invalidates by definition the fluid hypotheses. We would therefore prefer using a kinetic approach.

In a kinetic model, each particle species α (electrons or ions) is described as a distribution function $f_\alpha(\boldsymbol{r},\ \boldsymbol{p},\ t)$ in position-momentum space $(\boldsymbol{r},\ \boldsymbol{p})$, which verifies the so-called Boltzmann-Vlasov equation [Vlasov, 1968]:

$$\frac{\mathrm{d}f_\alpha}{\mathrm{d}t} = \frac{\partial f_s}{\partial t} + \frac{\mathrm{d}\boldsymbol{r}}{\mathrm{d}t}\cdot\frac{\partial f_\alpha}{\partial \boldsymbol{r}} + \frac{\mathrm{d}\boldsymbol{p}}{\mathrm{d}t}\cdot\frac{\partial f_\alpha}{\partial \boldsymbol{p}} = 0. \tag{3.1}$$

For relativistic particles with a charge q_α, it is possible to include the Lorentz force in the Vlasov equation through the equations of motion:

$$\frac{\mathrm{d}\boldsymbol{p}}{\mathrm{d}t} = q_\alpha(\boldsymbol{E} + \boldsymbol{v}\times\boldsymbol{B}) \text{ with } \boldsymbol{v} = \frac{\mathrm{d}\boldsymbol{r}}{\mathrm{d}t}, \tag{3.2}$$

where the electromagnetic fields $\boldsymbol{E}$ and $\boldsymbol{B}$ are given by the Maxwell's equations:

$$\begin{aligned}
&\bullet \quad \text{Maxwell - Gauss:} && \boldsymbol{\nabla}\cdot\boldsymbol{E} = \frac{\rho}{\epsilon_0},\\
&\bullet \quad \text{Maxwell - Gauss for magnetism:} && \boldsymbol{\nabla}\cdot\boldsymbol{B} = 0,\\
&\bullet \quad \text{Maxwell - Faraday:} && \boldsymbol{\nabla}\times\boldsymbol{E} = -\frac{\partial \boldsymbol{B}}{\partial t},\\
&\bullet \quad \text{Maxwell - Ampère:} && \boldsymbol{\nabla}\times\boldsymbol{B} = \mu_0\left(\boldsymbol{J} + \epsilon_0\frac{\partial \boldsymbol{E}}{\partial t}\right).
\end{aligned} \tag{3.3}$$

Solving the coupled Vlasov-Maxwell's equations can be done using two ways, defining two different types of codes: Vlasov codes and Particle-In-Cell codes. A Vlasov code discretizes these equations along the 6D phase space $(\boldsymbol{r},\ \boldsymbol{p})$ and advances them in time. However, in practice, solving in the 6D space is incredibly resource demanding (e.g., storing 1000 points per axis would require 10^{18} bytes or 1 exabyte!) and most of the time stringent simplifications are needed. In the following, we would prefer a Lagrangian formalism to describe the plasma: the Particle-In-Cell method, more tractable, even though not trivially solution to the Vlasov-Maxwell's system [Melzani et al., 2013; Grassi et al., 2016].

3.2 Particle-In-Cell Method

3.2.1 General overview

The kinetic resolution of plasma physics is often supported by Particle-In-Cell (PIC) codes. The PIC method relies on the Eulerian formalism for Maxwell's equations and the Lagrangian formalism for the Vlasov equation. The method itself is actually fairly old and was popularized in the late 1950s by Buneman, Dawson, Hockney, Birdsall, Morse among others[1]. Whereas, the particles can freely move all along the domain, electromagnetic fields and sources are discretized and computed on a grid via Maxwell's equations. The particles contribute to the electromagnetic sources by using an interpolation function, designated as *particle shape* [Hockney and Eastwood, 1988]. The same function is used to interpolate the fields on particles. There is no direct interaction between particles, which see each other through the grid but never directly.

Plasmas in nature contain millions to tens of billions of particles per Debye sphere, and relevant micro-physical phenomena spread over numerous Debye lengths: for example, a $5^3 \mu\text{m}^3$ cube of plasma at the solid density $n \sim 10^{23}$ cm^{-3} leads to more than 10^{13} particles to simulate! It would require too much computational resources to track these particles one by one.

Instead, simulated particles represent a certain number N_p of real particles, a statistical sample of a finite volume of the distribution function in phase space. These are called *super-particles* and present the same charge/mass ratio as real particles. They are treated as stiff bodies with a define momentum $\boldsymbol{p}_p$ but with a certain particle shape $S(\boldsymbol{r} - \boldsymbol{r}_p)$ for the particle-grid interpolation. S is a normalized function defined on a bounded support ($\int S(x)dx = 1$), centered around its average position $\boldsymbol{r}_p$. The common particle shape functions are pictured in Fig. 3.1. Increasing the particle shape order imposes more computational power but considerably reduces the numerical heating (finite-grid instability), which may drastically disturb the physics involved [Vincenti, 2011].

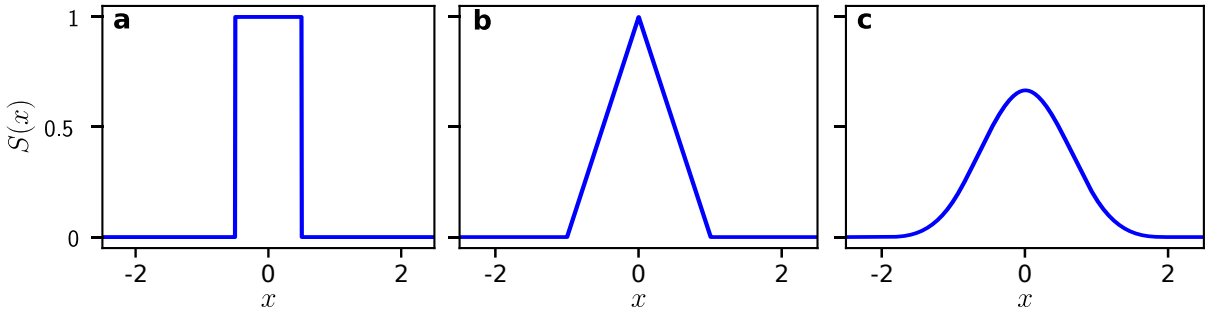

Figure 3.1: **Particle shape functions in 1D** - (a) the top hat-function, also called the Nearest Grid Point method (NGP), (b) the triangular function, also called Cloud-In-Cell (CIC), the convolution of (a) with itself and (c) a spline function, the convolution of (b) with itself

From now and in the whole manuscript, we will abusively skip the term *super-* and just speak about *particle* when designating a *super-particle*. Keep in mind that each of these *particles* can still represent 10^3 to 10^{13} real particles in typical UHI simulations.

[1] Evans and Harlow, 1957; Morse and Nielson, 1969; Dawson, 1983; Birdsall and Langdon, 1985; Arber et al., 2015.

3.2.2 Particle-In-Cell loop

After this general overview, let us see in details how the particles and fields are advanced at each time step. The general algorithm is called *Particle-In-Cell loop* and its principle is sketched in Fig. 3.2.

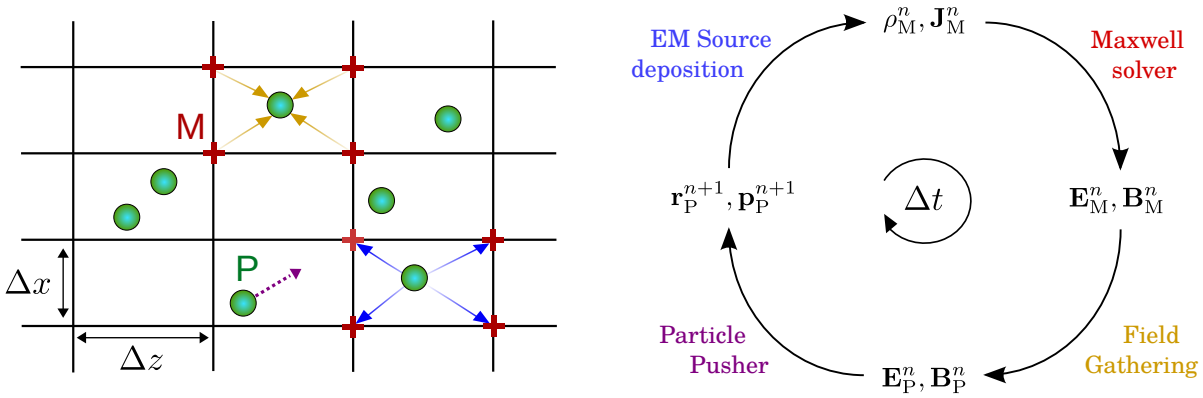

Figure 3.2: **Particle-In-Cell loop** - Schematic drawing of the PIC algorithm performed at every time step: (i) the particles (pictured as green disks, label P) contribute to electromagnetic sources, charge and current defined on grid nodes (red crosses, label M), (ii) the Maxwell's equations are solved on the grid nodes, (iii) the electromagnetic fields are gathered from grid nodes to particles and finally (iv) the particles are pushed according to equations of motion.

The method typically includes four steps detailed as follows:

(i) Current deposition from particle to mesh. Firstly, the electromagnetic sources, current $\boldsymbol{J}(\boldsymbol{r})$ and charge $\rho(\boldsymbol{r})$, have to be projected from particles to grid nodes, thanks to the particle shape S. On each mesh point M (see Fig. 3.2), they are defined as:

$$\rho(\boldsymbol{r}_{\rm M}) = \sum_p q_p S(\boldsymbol{r}_{\rm M} - \boldsymbol{r}_p) \quad \text{and} \quad \boldsymbol{J}(\boldsymbol{r}_{\rm M}) = \sum_p q_p \boldsymbol{v}_p S(\boldsymbol{r}_{\rm M} - \boldsymbol{r}_p), \tag{3.4}$$

with q_p and m_p, respectively the charge and the mass of a particle p and $\boldsymbol{v}_p$ its velocity defined as:

$$\boldsymbol{v}_p = \frac{{\rm d}\boldsymbol{r}_p}{{\rm d}t} = \frac{\boldsymbol{p}_p}{m_p \gamma_p} \quad \text{and} \quad \gamma_p = \sqrt{1 + (\boldsymbol{p}_p/m_p c)^2}. \tag{3.5}$$

In practice, the charge conservation law is not automatically verified, i.e., $\partial_t \rho + \boldsymbol{\nabla} \cdot \boldsymbol{J} \neq 0$. For this reason, it is common to use the Esirkepov algorithm [Esirkepov, 2001], which ensures a charge conserving deposition for any particle shape S for standard Maxwell solvers.

(ii) Maxwell solver on grid nodes. Secondly, the electromagnetic fields are advanced according to Maxwell's equations. Regarding the four equations, only the Ampere and Faraday equations do matter to describe the evolution of a dynamical system. The two others are not explicitly time-dependent and are verified all along the simulation assuming that they and the charge conservation law are satisfied at initialization. Then, from the two curl equations, the electromagnetic source are used to advance the fields $\boldsymbol{E}$ and $\boldsymbol{B}$ in time and space on the grid nodes (e.g., mesh point M in Fig. 3.2).

The most commonly used method for advancing Maxwell's equations on a grid was presented in [Yee, 1966] and is based on a second-order discretization in time and space on a staggered grid

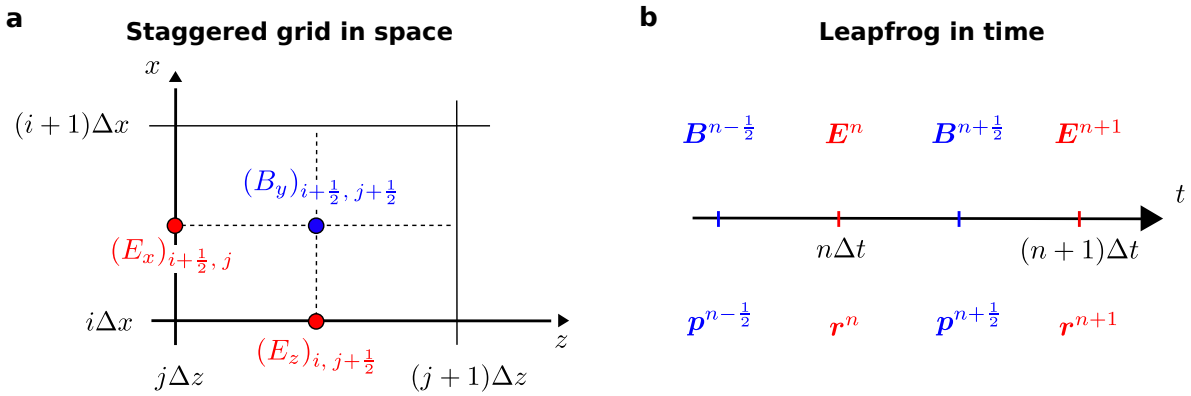

Figure 3.3: **The Yee solver and Boris pusher** - This figure displays at which position and time the electromagnetic field components are defined in 2D, when using the Yee Maxwell solver (panel (a)). In addition, the super-particle positions are defined at integer times $n\Delta t$ whereas their momentums are known at half-integer times $(n+1/2)\Delta t$ to ensure a second-order precision in the Boris pusher (panel (b)).

(see Fig. 3.3–a). The staggering actually ensures a second-order precision within one time step but the different field components are thus neither defined at the same position nor at the same time.

In practice, the way to solve the Maxwell's equations is crucial for an accurate simulation. In Sec. 3.4, we will study the impact of Maxwell solver discretization errors on typical plasma mirror simulations.

(iii) Field gathering from mesh to particles. The fields are interpolated from the grid nodes to each particle position using the S particle shape. We define $\boldsymbol{E}_p$ and $\boldsymbol{B}_p$, the corresponding fields on each particle (e.g., P in Fig. 3.2) by:

$$\boldsymbol{E}_p = \sum_{\mathrm{M}} \boldsymbol{E}_{\mathrm{M}} S(\boldsymbol{r}_{\mathrm{M}} - \boldsymbol{r}_p) \quad \text{and} \quad \boldsymbol{B}_p = \sum_{\mathrm{M}} \boldsymbol{B}_{\mathrm{M}} S(\boldsymbol{r}_{\mathrm{M}} - \boldsymbol{r}_p). \tag{3.6}$$

(iv) Particle pusher. Once the fields $\boldsymbol{E}_p$ and $\boldsymbol{B}_p$ are known, it is possible to update the particle positions and momenta through the relativistic equations of motion:

- $$\frac{\boldsymbol{p}_p^{n+1/2} - \boldsymbol{p}_p^{n-1/2}}{\Delta t} = q_p \left[\boldsymbol{E}_p^n + \left(\frac{\boldsymbol{p}_p^{n+1/2} + \boldsymbol{p}_p^{n-1/2}}{2 m_p \gamma^n} \right) \times \boldsymbol{B}_p^{n+1/2} \right], \tag{3.7}$$
- $$\frac{\boldsymbol{r}_p^{n+1} - \boldsymbol{r}_p^{n}}{\Delta t} = \frac{\boldsymbol{p}_p^{n+1/2}}{m_p \sqrt{1 + (\boldsymbol{p}_p^{n+1/2}/m_p c)^2}}, \tag{3.8}$$
- $$\gamma^n = \sqrt{1 + \left(\frac{\boldsymbol{p}_p^{n+1/2} + \boldsymbol{p}_p^{n-1/2}}{2 m_p c} \right)^2}. \tag{3.9}$$

The principal issue is to retrieve $\boldsymbol{p}_{\mathrm{p}}^{n+1/2}$, which appears in both sides of Eq. (3.7). The common resolution technique is based on a leap frog second-order explicit method, known as the *Boris pusher* [Boris, 1972]. This method is volume preserving. The Boris algorithm lies on three step and reads:

1. A first half electric acceleration,

2. the full magnetic rotation and middle γ calculation,

3. the second half electric acceleration.

This method was improved over time for different specific cases where the Boris pusher was not optimal. In particular, [Vay, 2008] found that it does not preserve the property of electric field and magnetic field cancellation. Assuming that a particle is submitted to constant nonzero electric and magnetic fields in such a way that their mutual contributions cancel, $\boldsymbol{E}+\boldsymbol{v}\times\boldsymbol{B}=0$, the particle should follow a ballistic motion. However, when using the Boris scheme, this equation admits a solution only if $\boldsymbol{E}=c\boldsymbol{B}=0$. It means that in the general case, where $\boldsymbol{E}\neq 0$ and $\boldsymbol{B}\neq 0$, the particle would experience a spurious force. A way to bypass this problem is to use the Vay pusher, which was specifically constructed to preserve the cancellation of electric and magnetic fields but at the expense of volume conservation.

Recently, [Higuera and Cary, 2017] also developed their own pusher, which might combine the benefits of Vay and Boris pushers, without any drawbacks.

In the following, we will extensively base our study on a self-developed particle tracker code (see Chapter 4). This code solves the equations of motion with one of the three different pushers without considering space charge effects. The fields are known via analytical formulas and are directly applied onto the particles without using any grid or interpolation functions.

Parallelization method. In plasma mirror simulations, accurately solving different harmonic orders requires a fairly high resolution, resulting in large simulation boxes and high number of particles (typically 10^{5-7} particles and grid points in 2D, 10^{8-10} in 3D). These simulations do not fit in memory of a single CPU (Central Processing Unit) core and cannot be performed in a reasonable amount of time. Instead, we distribute small subdomains across a certain number of cores. The PIC loop is executed independently on each subdomain. At the end of a time step, each core exchanges information with its nearest neighbours that can be escaping particles or points at the borders needed to advance Maxwell's equations. The communication between cores is operated via the Message Passing Interface (MPI).

Fig. 3.4 displays such an MPI exchange for the Yee solver. A simulated domain of 4×6 grid nodes is split among 4 MPI subdomains, each corresponding to a different color $\left(\text{phase } \textcircled{1}\right)$.

Solving Maxwell's equations on a given node with the Yee solver requires to know at least 2 other adjacent points per axis, or stencil. The stencil corresponding to the bottom-left blue node is highlighted in black and takes the form of a cross. After domain decomposition, the subdomain S2 cannot access to any nodes but its own. The PIC loop cannot be performed near boundaries by lack of information of the missing neighbouring points (see the blank nodes outside of S2). It is necessary to introduce an extra layer of nodes at the border of each subdomain called *guard region* or *guard cells*. At each time step, they are filled with copies of adjacent cells from another subdomain (orange or green dots into S2).

After the exchange $\left(\text{phase } \textcircled{2}\right)$, it becomes possible to solve Maxwell's equations everywhere and the PIC loop is performed on each enlarged subdomain independently. Note that in this particular example, the actually simulated domain is much larger than the initial domain (6×8 or 2 times larger). The speedup in time is balanced by a cost on extra allocated memory and it is

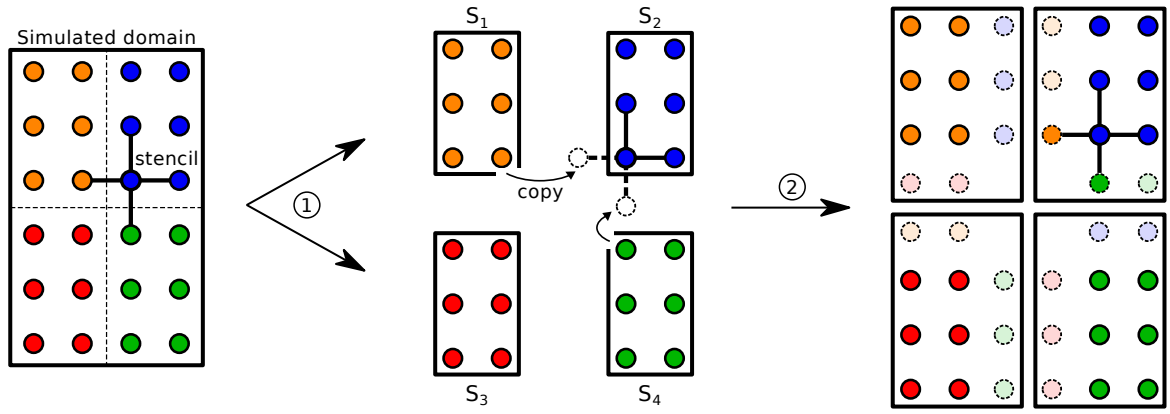

Figure 3.4: **MPI exchange for standard Maxwell solvers** - A large domain is split into four subdomains, each handling 2×3 nodes (colored dots). In order to resolve the Maxwell's equations with the Yee solver, it is mandatory to know the 4 direct adjacent nodes for any given node. This dependency is pictured as a black stencil for example for the bottom-left node of S2. At each time step, data from neighbouring subdomains are copied into extra nodes to compensate the lack of information near the boundaries. When all copies are performed, it results on an enlargement of the number of nodes handled by each subdomain.

sometimes better to keep reasonably large subdomains to avoid overly large memory duplication.

Now that we presented the basics of the PIC loop, let us focus on PIC simulation set-ups specifically designed to accurately study laser-plasma mirror interactions.

3.3 Typical PIC Simulations of Laser-Plasma Mirror Interactions

3.3.1 WARP+PXR code

During my whole PhD, I used the legacy PIC code – WARP – coupled with the high-performance library – PICSAR (for Particle-In-Cell Scalable Application Resource, abbreviated in PXR).

WARP[2] is an open-source 3D PIC code, which has been extensively developed at the Lawrence Livermore National Laboratory (LLNL) and the Lawrence Berkeley National Laboratory (LBNL) for over twenty years. It is written in a combination of Fortran for efficient implementation of computationally intensive tasks and Python for control of simulations and input-output interface. WARP is designed to simulate a rich variety of physical processes including laser-plasma interactions at high laser intensities. To do so, it allows the use of state-of-the-art numerical algorithms (most of them were actually developed by the WARP team) such as boosted frame [Vay, 2007], galilean frame [Kirchen et al., 2016; Lehe et al., 2016] or a large range of Maxwell solvers, we will detail furthermore.

Although it is possible to perform plasma mirror simulations with WARP alone, the time to solution is highly accelerated by coupling the code to the open-source library PXR[3]. PXR has

[2] http://blast.lbl.gov/blast-codes-warp
[3] https://picsar.net

been developed by J.L. Vay and H. Vincenti in close collaboration between the LBNL and the CEA to help porting PIC codes to future many-core machines up to exascale supercomputers. The PXR library includes numerous optimization strategies to fully benefit from the three levels of parallelisms (internode, intranode, and vectorization) offered by current and upcoming architectures. It can be coupled to WARP or other PIC codes[4] through a Python layer, which overwrites most of time consuming routines of the PIC loop. We nicknamed this code WARP+PXR.

All PIC simulations reported in this manuscript were performed with the WARP+PXR code either locally for 1D-2D simulations or on the supercomputer MIRA[5] in Argonne National Laboratory as part of an Innovative and Novel Computational Impact on Theory and Experiment (INCITE) award, mainly for 3D simulations.

3.3.2 1D Simulation setup

Ideally, studying laser-plasma mirror interaction would always require highly resolved 3D simulations for direct comparisons with experiments or phenomena that specifically requires 3D, e.g., harmonic focusing or laser diffraction. However, even if it starts to become reality to run such simulations [Vincenti, 2018; Chopineau et al., 2019], it is much more common for the community to rely on 1D or 2D simulations. The main reason is obviously the computational cost of 3D simulations but also because for relative large laser waist ($w_0 \gg \lambda_0$), 1D simulations of plasma mirror physics still bring satisfying insights (see Chapter 1). Then, changing the dimensionality is a trade-off between tractable simulations and realistic inputs.

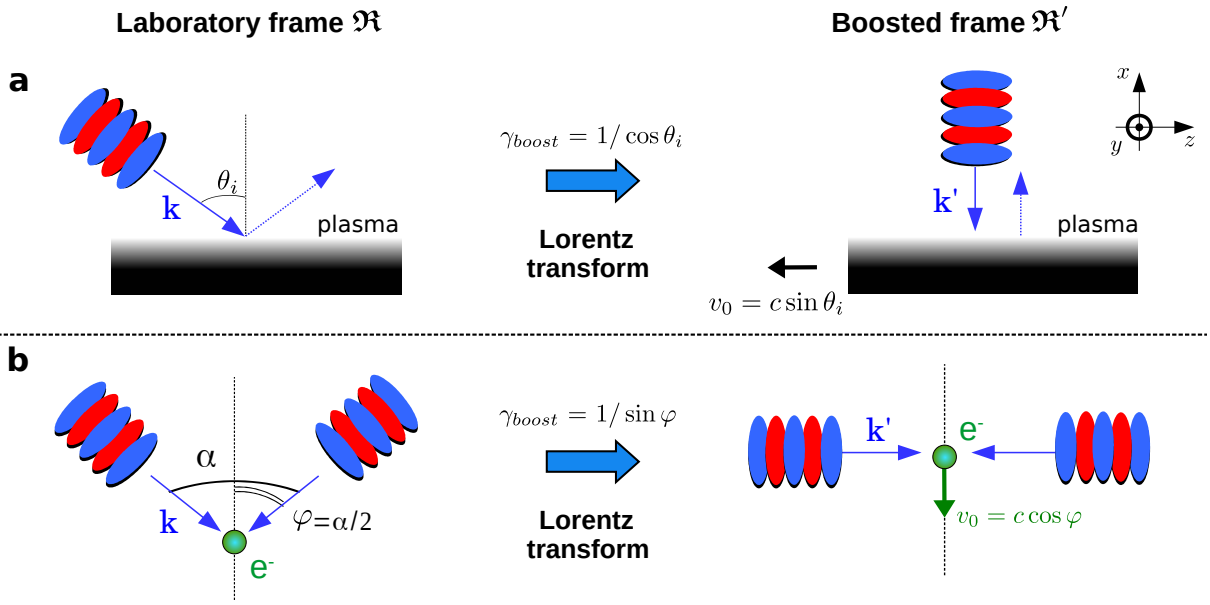

Figure 3.5: **Bourdier transformation for our two cases of interest** - Panel (a) shows the general setup for 1D PIC simulations: in the laboratory frame (left drawing), a plane wave is impinging on a plasma with an angle θ_i. In the boosted frame, the incidence is normal but the plasma is drifting at a velocity $v_0 = c\sin\theta_i$. The setup of panel (b) will be used mostly in Chapter 8 where two plane waves interfere with an angle $\alpha = 2\varphi$ in the laboratory frame. In the boosted frame, the two waves are counter propagating and the electron velocity is $v_0 = c\cos\varphi$.

[4]For example, it has been recently coupled to the SMILEI code as well by H. Kallala.
[5]https://www.alcf.anl.gov/alcf-resources/mira

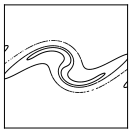

Bourdier frame transformation. It is possible to reduce a 2D geometry where a plane wave obliquely impinges on a solid target to a 1D geometry, where the laser incidence is normal to a drifting plasma. The method, introduced in [Bourdier, 1983], is based on a Lorentz transformation and sketched in Fig. 3.5–a.

Let the laser wave vector be $\boldsymbol{k} = k_0(-\cos\theta_i,\ 0,\ \sin\theta_i)$ and $\omega_0 = k_0 c$ in the laboratory frame $\mathfrak{R}(x,\ y,\ z)$, the idea is to find a *boosted frame* $\mathfrak{R}'(x',\ y',\ z')$ where the longitudinal component of the vector $\boldsymbol{k}$ in this new frame, named $\boldsymbol{k'}$, disappears, i.e., $\boldsymbol{k'} = k'_0(1,\ 0,\ 0)$. In this section, every primed variable is related to the boosted frame $\mathfrak{R}'$. One can show that a frame $\mathfrak{R}'$ which moves uniformly relative to $\mathfrak{R}$ along the z axis with a velocity v_0, is appropriate. The associated Lorentz factor of this transformation is $\gamma_{boost} = 1/\sqrt{1-(v_0/c)^2}$. The wavevector and spatiotemporal four-vectors become in $\mathfrak{R}'$:

$$\begin{aligned}
&\bullet\ x' = x, && \bullet\ k'_x = k_x = -k_0\cos\theta_i,\\
&\bullet\ y' = y, && \bullet\ k'_y = k_y = 0,\\
&\bullet\ z' = \gamma_{boost}\left(z - t v_0\right), && \bullet\ k'_z = \gamma_{boost}\left(k_z - \omega_0 v_0/c^2\right) = 0,\\
&\bullet\ t' = \gamma_{boost}\left(t - z v_0/c^2\right), && \bullet\ \omega' = \gamma_{boost}\left(\omega_0 - k_z v_0\right).
\end{aligned} \tag{3.10}$$

Since $k'_z = 0$ and $k_z = \omega_0 \sin\theta_i/c$ by definition, it comes:

$$v_0 = c\sin\theta_i \quad \text{and} \quad \gamma_{boost} = 1/\cos\theta_i. \tag{3.11}$$

Besides the previous four-vectors, the electromagnetic fields are also transformed. In $\mathfrak{R}$, they are defined as followed:

$$\boldsymbol{E} = E_0 \begin{pmatrix} \sin\theta_i \\ 0 \\ \cos\theta_i \end{pmatrix} \sin\psi \quad \text{and} \quad \boldsymbol{B} = B_0 \begin{pmatrix} 0 \\ 1 \\ 0 \end{pmatrix} \sin\psi, \tag{3.12}$$

with the phase $\psi = k_0 z \sin\theta_i - k_0 x \cos\theta_i - \omega_0 t$.

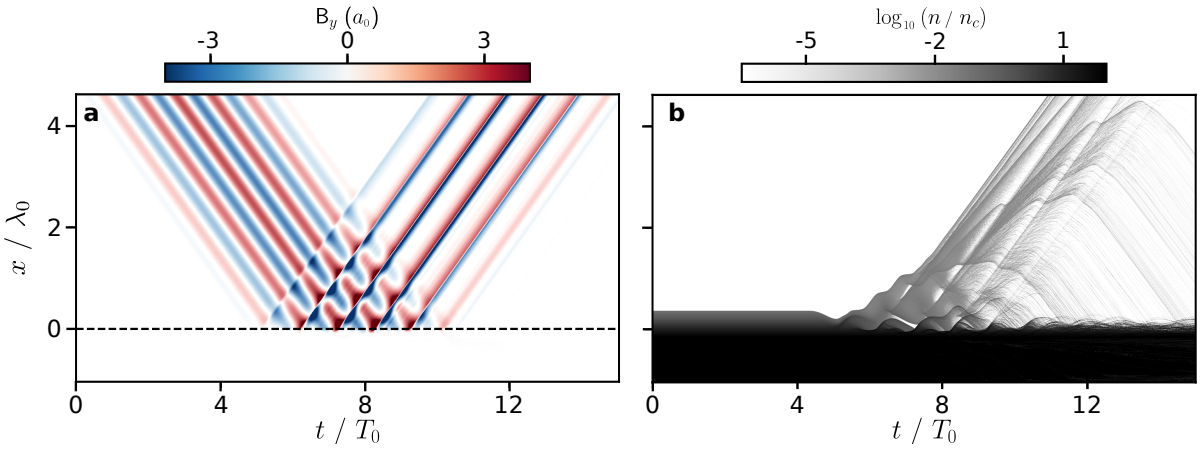

Figure 3.6: **Simulation set-up in 1D** - Temporal evolution of the y_{boost} component of the magnetic field (panel a) and of the electronic density (panel b) in the Bourdier frame. The simulation parameters were chosen in the laboratory frame such as $a_0 = 3$, $L_g = \lambda_0/10$, $\tau_0 = 5T_0$, $n_{max} = 100 n_c$ and $\theta_i = 45°$. The position of the critical density n_c is sketched in dashed line.

Using the expressions of x', z' and t' from Eq. (3.10), the phase is transformed such as:

$$\psi' = -k_0 x' \cos\theta_i - \omega_0 t' \cos\theta_i. \tag{3.13}$$

Then, from the electromagnetic boosted transformation equations, the fields in $\mathfrak{R}'$ read

$$\boldsymbol{E}' = E_0 \cos\theta_i \begin{pmatrix} 0 \\ 0 \\ 1 \end{pmatrix} \sin\psi' \quad \text{and} \quad \boldsymbol{B}' = B_0 \cos\theta_i \begin{pmatrix} 0 \\ 1 \\ 0 \end{pmatrix} \sin\psi'. \tag{3.14}$$

Note that the normalized vector potential, $a_0 = eE_0/\omega_0 mc$, remains unchanged.

The plasma parameters are also transformed. In particular, the plasma density n defined as the number $\delta^3 N$ of particles per unit volume is increased by a factor γ_{boost} in the boosted frame: $n' = \delta^3 N/(\delta x' \times \delta y' \times \delta z') = \delta^3 N/(\delta x \times \delta y \times \delta z \cos\theta_i) = n/\cos\theta_i$. In addition, the plasma, which was initially at rest in the laboratory frame, acquires a drift velocity $\boldsymbol{v_d} = -v_0\,\boldsymbol{z}$ in $\mathfrak{R}'$ in the boosted frame.

The setup pictured in Fig. 3.5–b will be used mostly for the stochastic heating study in Chapter 8 and is related to the setup of Fig. 3.5–a by considering $\varphi = \pi/2 - \theta_i$. The interaction between two lasers presenting an angle $\alpha = 2\varphi$, is thus transformed to a simpler counter-propagating case.

An example of a 1D-PIC simulation performed in the Bourdier frame is sketched Fig. 3.6 in the $(x,\ t)$ space. A laser, $a_0 = 3$ and pictured from blue to red in Fig. 3.6–a, is reflected by an overdense plasma, pictured in grey in Fig. 3.6–b. The incident angle θ_i is chosen in the laboratory frame as 45° and the corresponding Lorentz factor is thus $\gamma_{boost} = \sqrt{2}$. During the reflection occurring when $t \in [4.5, 9]\ T_0$, the laser drives periodic oscillations of the plasma mirror and a high harmonic comb is emitted (see the field deformation after reflection). Synchronized with this harmonic generation, electron jets are emitted towards vacuum.

3.3.3 2D/3D Simulation setup

However most of the time, 1D simulations do not entirely capture all physical phenomenons, such as laser focusing or electron ejection far from target. These effects start to be relevant when the laser pulse deviates significantly from a plane wave. In these cases, we need to run 2D or 3D simulations. In particular, 3D simulations allow for direct comparisons with all experimental observables.

In a high-dimensionality simulation (2D and *a fortiori* 3D), such as the 2D simulation presented in Fig. 3.7–a, the volume of dumped data can become very large. It becomes necessary to use diagnostics extracting the physically relevant subset of data from the simulation. Besides costly full grid and particle dumps, we are using two other diagnostics:

(i) Plane detectors which record the field and the particles along time on a streak line in 2D, or plan in 3D (see Fig. 3.7–a). We use it either near the focal spot on a plane normal to the target ($\mathcal{P}_1$) to study the dynamics of the surface or far from target ($\mathcal{P}_2$) to retrieve harmonic content in the reflected field or ejected electron distribution.

The high harmonic spectrum in the $(\omega,\ \boldsymbol{k}_\perp)$ space can be obtained after computing a Fast Fourier Transform of the reflected field recorded on $\mathcal{P}_2$ (see Figs. 3.7–a, b). $\boldsymbol{k}_\perp$ represents all

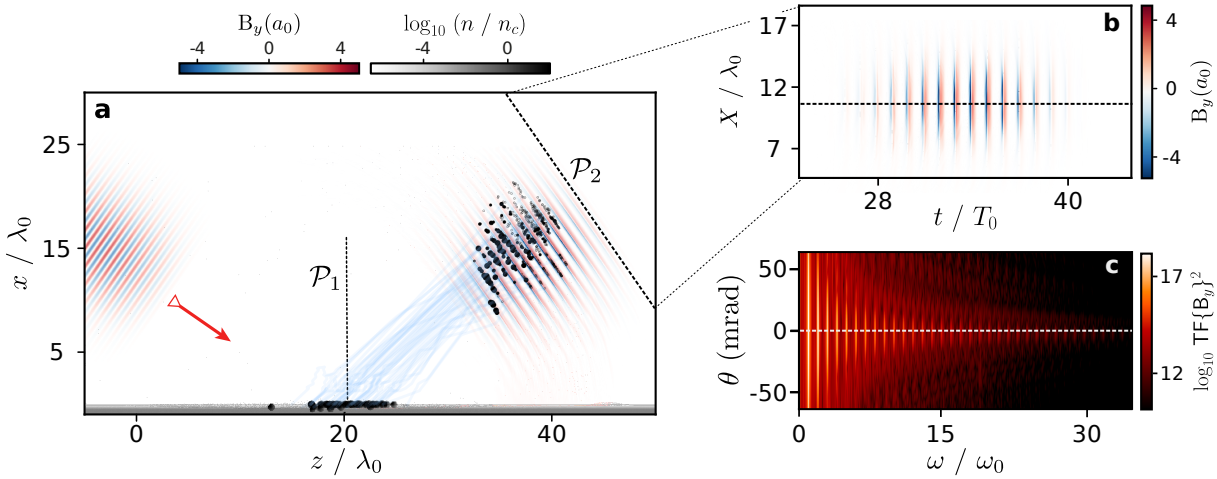

Figure 3.7: **Numerical set-up used for both 2D/3D simulations** - Panel (a), a laser (B_y pictured from blue to red), $a_0 = 4$, $w_0 = 5\lambda_0$, is impinging a grey and overdense target with an angle $\theta_i = 55°$. The exponential gradient in front of the target is characterized by a spatial scale length $L_g = \lambda_0/15$. Here, $\Delta x = \lambda_0/140$. After interaction, some electrons, pictured as black dots, are expelled from the surface and travel inside the reflected laser pulse. Their history after ejection is retrieved and displayed as blue trajectories. In addition, the reflected magnetic field is recorded along time on an oblique streak plane $\mathcal{P}_2$. The spatio-temporal evolution of this field is given on panel (b). Panel (c) shows the corresponding angularly-resolved harmonic spectrum in log color scale.

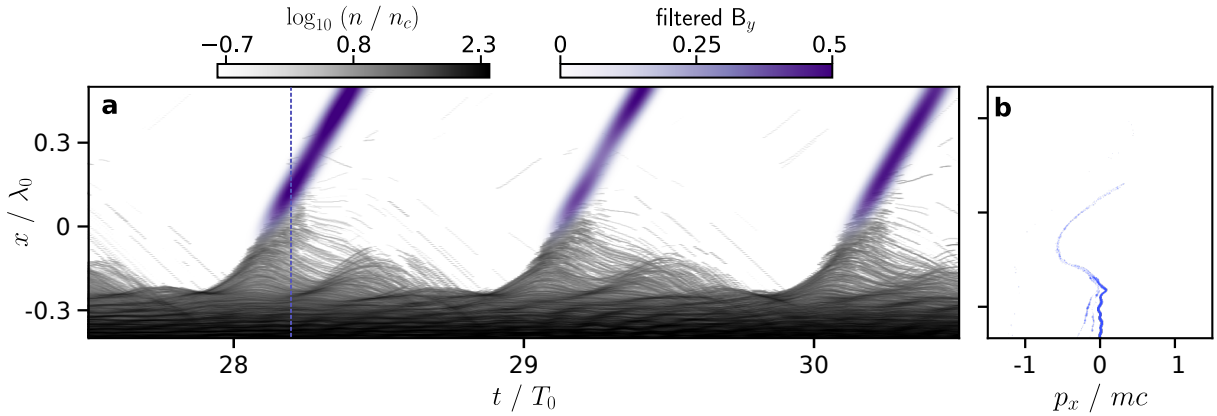

Figure 3.8: **Temporal dynamics of the plasma mirror using a plane detector in the plasma surface** - In panel (a), spatio-temporal plasma evolutions (in gray log color scale) are recorded on $\mathcal{P}_1$ (see Fig. 3.7–a) as well as the attosecond light pulses emitted during the interaction (harmonics 10-20). Panel (b) shows the electron distribution during the ejection in the (x, p_x) phase space at a time $t = 28.2\,T_0$ (blue dashed line). All physical and numerical parameters are kept the same as in Fig. 3.7.

vectors orthogonal to the reflected laser wavevector $\boldsymbol{k}_0$. An additional mathematical treatment [Vincenti, 2011] gives the angularly-resolved spectrum in the (ω, θ) space, such as plotted in Fig. 3.7–c.

An overview of results obtained on $\mathcal{P}_1$ is pictured in Fig. 3.8. In Fig. 3.8–a, the surface (in grey) is oscillating and an attosecond pulse (in purple) is emitting at every cycle. In addition, at

$t = 28.2\ T_0$ (purple dashed line), the different surface electrons are plotted in the (x, p_x) phase space (see Fig. 3.8–b), where x is the direction normal to the target surface.

(ii) Ejected particle diagnostics, which save the spatial distribution of ejected electrons at each time step. Only a small fraction of the total electrons are expelled from the plasma mirror, which represents a much lower and managable quantity of data. Before run time, a unique number or ID is associated to each particle, making possible the recovery of corresponding trajectories, as the ones pictured in blue in Fig. 3.7–a.

In the following, we will use these diagnostics to assess which Maxwell solver is the most accurate to model harmonic generation from plasma mirrors.

3.4 Influence of Maxwell solvers on Plasma Mirror Simulations

3.4.1 Dispersion relation in a numerical vacuum

Modeling of high-order harmonic generation with PIC codes is particularly challenging as it involves an accurate description of short wavelenghts radiations spanning many harmonic orders and broad emission angles. However, standard PIC codes currently fail to finely reproduce the good harmonic properties, because of numerical errors induced, in particular, by the Maxwell solver (step (ii) of the PIC algorithm in red in Fig. 3.2, page 46). Their mitigation would demand a numerical resolution so high that realistic 3D simulations have not been possible so far, even on the largest supercomputers worldwide.

The standard PIC method uses finite-difference time-domain (FDTD) Maxwell solvers on a staggered grid (part 3.2.2). Although it offers second order accuracy in time and space, the discretization inevitably introduces numerical artifacts, especially artificial numerical dispersion of electromagnetic waves in vacuum.

In vacuum, the dispersion relation, $\omega = kc$, ensures that any electromagnetic wave propagates at the speed of light c. Instead, the numerical vacuum simulated by FDTD solvers behaves as a dispersive medium, where waves with different frequencies do not travel with the same group and phase velocities. For plasma mirror simulations, the plasma surface, along which the harmonics are created, acts as an interface between two media – a perfect vacuum and a numerical vacuum of refractive index $n_r \neq 1$ – that deflects highest frequency waves according to Snell-Descartes law.

Dispersion relation for the Yee solver in 2D. For historical reasons, the Yee solver [Yee, 1966] is one of the most popular solvers, for which Maxwell's equations are discretized using a second-order finite difference scheme, where electromagnetic fields components are placed on a staggered grid (see Fig. 3.3–a, page 47). They read in 2D in vacuum:

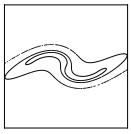

$$\begin{cases} \dfrac{(E_x)^{n+1}_{i+\frac{1}{2},\,j} - (E_x)^{n}_{i+\frac{1}{2},\,j}}{c\Delta t} = -\dfrac{(cB_y)^{n+\frac{1}{2}}_{i+\frac{1}{2},\,j+\frac{1}{2}} - (cB_y)^{n+\frac{1}{2}}_{i+\frac{1}{2},\,j-\frac{1}{2}}}{\Delta z}, \\ \dfrac{(E_z)^{n+1}_{i,\,j+\frac{1}{2}} - (E_z)^{n}_{i,\,j+\frac{1}{2}}}{c\Delta t} = +\dfrac{(cB_y)^{n+\frac{1}{2}}_{i+\frac{1}{2},\,j+\frac{1}{2}} - (cB_y)^{n+\frac{1}{2}}_{i-\frac{1}{2},\,j+\frac{1}{2}}}{\Delta x}, \\ \dfrac{(cB_y)^{n+\frac{1}{2}}_{i+\frac{1}{2},\,j+\frac{1}{2}} - (cB_y)^{n-\frac{1}{2}}_{i+\frac{1}{2},\,j+\frac{1}{2}}}{c\Delta t} = \dfrac{(E_z)^{n}_{i+1,\,j+\frac{1}{2}} - (E_z)^{n}_{i,\,j+\frac{1}{2}}}{\Delta x} - \dfrac{(E_x)^{n}_{i+\frac{1}{2},\,j+1} - (E_x)^{n}_{i+\frac{1}{2},\,j}}{\Delta z}, \end{cases} \tag{3.15}$$

where n is the current time step index and i and j are the mesh indices. As any EM wave can be decomposed in plane waves and Maxwell's equations are linear, we restrict the study to a single plane wave as follows:

$$(A)^{n}_{i,\,j} = Ae^{\mathrm{j}(k_x i\Delta x + k_z j\Delta z - \omega n\Delta t)}, \tag{3.16}$$

where $\mathrm{j}^2 = -1$. To avoid too heavy notations, we define:

$$\begin{cases} (E_x)^{n}_{i+\frac{1}{2},\,j} & \equiv & E_x, \\ (E_z)^{n}_{i,\,j+\frac{1}{2}} & \equiv & E_z, \\ (cB_y)^{n+\frac{1}{2}}_{i+\frac{1}{2},\,j+\frac{1}{2}} & \equiv & cB_y. \end{cases} \tag{3.17}$$

The stability of the system can be derived through a von Neumann stability analysis [VonNeumann and Richtmyer, 1950]. After simplification, the system of equations 3.15 becomes:

$$\begin{cases} \dfrac{\left(e^{-\mathrm{j}\,\omega\Delta t/2} - e^{\mathrm{j}\,\omega\Delta t/2}\right)}{c\Delta t} E_x = -\dfrac{\left(e^{\mathrm{j}k_z\Delta z/2} - e^{-\mathrm{j}k_z\Delta z/2}\right)}{\Delta z} cB_y, \\ \dfrac{\left(e^{-\mathrm{j}\,\omega\Delta t/2} - e^{\mathrm{j}\,\omega\Delta t/2}\right)}{c\Delta t} E_z = +\dfrac{\left(e^{\mathrm{j}k_x\Delta x/2} - e^{-\mathrm{j}k_x\Delta x/2}\right)}{\Delta x} cB_y, \\ \dfrac{\left(e^{-\mathrm{j}\,\omega\Delta t/2} - e^{\mathrm{j}\,\omega\Delta t/2}\right)}{c\Delta t} cB_y = \dfrac{\left(e^{\mathrm{j}k_x\Delta x/2} - e^{-\mathrm{j}k_x\Delta x/2}\right)}{\Delta x} E_z - \dfrac{\left(e^{\mathrm{j}k_z\Delta z/2} - e^{-\mathrm{j}k_z\Delta z/2}\right)}{\Delta z} E_x. \end{cases} \tag{3.18}$$

Changing $\left(e^{\mathrm{j}X/2} - e^{-\mathrm{j}X/2}\right)$ by $2\mathrm{j}\sin(X/2)$ and reducing the system give the numerical dispersion relation in vacuum for the Yee solver[6]:

$$\frac{1}{c^2\Delta t^2}\sin^2\left(\frac{\omega\Delta t}{2}\right) = \frac{1}{\Delta x^2}\sin^2\left(\frac{k_x\Delta x}{2}\right) + \frac{1}{\Delta z^2}\sin^2\left(\frac{k_z\Delta z}{2}\right). \tag{3.19}$$

[6]This equation can easily be extended to 3D:

$$\frac{1}{c^2\Delta t^2}\sin^2\left(\frac{\omega\Delta t}{2}\right) = \frac{1}{\Delta x^2}\sin^2\left(\frac{k_x\Delta x}{2}\right) + \frac{1}{\Delta y^2}\sin^2\left(\frac{k_y\Delta y}{2}\right) + \frac{1}{\Delta z^2}\sin^2\left(\frac{k_z\Delta z}{2}\right).$$

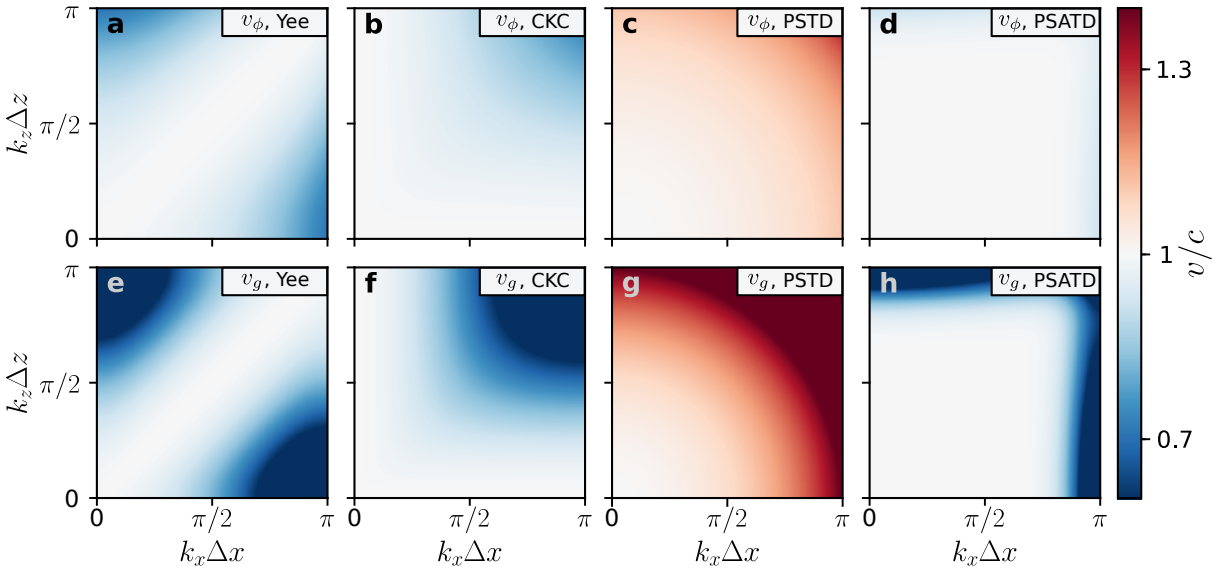

Figure 3.9: **Phase and group velocities for different Maxwell solvers in 2D in vacuum** - The panels (a) and (e) are respectively the phase and group velocity for the Yee solver, (b) and (f) same for Cole-Karkkainen-Solver, (c) and (g) same for the spectral solver PSTD and (d) and (h) same for the spectral solver PSATD. Both pseudo-spectral solvers are computed with a finite order 100. All these quantities were computed at the corresponding CFL condition. The areas, where the velocities are equal to c, are pictured in white. For the PSTD solver only, waves can be faster than c.

When $\omega\Delta t \ll 1$ and $k_x\Delta x$, $k_z\Delta z \ll 1$, Eq. (3.19) does converge to the right solution $\omega = kc$. However, even if the laser fundamental frequency ω_0 is resolved enough to mitigate numerical dispersion effects, it is not necessarily the case for the highest generated harmonics ($n\omega_0$ with $n \sim 20 - 30$), for which the resolution may need to be tens times higher to completely mitigate the deviation to the perfect dispersion equation.

Another consequence to this equation is that the time step cannot be arbitrary chosen. If $\Delta z = \Delta x$ (always the case in solid target simulations) and $\eta = c\Delta t/\Delta x$, it reads:

$$\sin^2\left(\frac{\omega\Delta t}{2}\right) = \eta^2\left[\sin^2\left(\frac{k_x\Delta x}{2}\right) + \sin^2\left(\frac{k_z\Delta z}{2}\right)\right] \leq 1. \tag{3.20}$$

This inequality must be verified anywhere to ensure the scheme stability and in particular near the Nyquist frequency, where $k_x\Delta x$, $k_z\Delta z \to \pi$. Then, η is bounded from above[7]:

$$\eta \leq 1/\sqrt{2}. \tag{3.21}$$

This is the condition of stability for the simulation, also named as the *Courant-Friedrichs-Lewy (CFL) condition* [Courant et al., 1928]. Beyond this limit, ω has a non-zero imaginary solution and the plane wave amplitude (Eq. (3.16), page 55) exponentially grows over time.

From the dispersion equation (Eq. (3.19)), it is possible to define the numerical phase velocity

[7] In 3D, $\eta \leq 1/\sqrt{3}$.

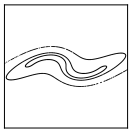

v_ϕ and group velocity v_g respectively equal to ω/k and $|\mathrm{d}\omega/\mathrm{d}\boldsymbol{k}|$, with $k = \sqrt{k_x^2 + k_z^2}$:

$$\begin{cases} v_\phi = \dfrac{\omega}{k} = \dfrac{2c}{\eta k \Delta x}.\sin^{-1}\left(\eta\sqrt{\mathrm{s}_x^2 + \mathrm{s}_z^2}\right), \\ \\ v_g = \left|\dfrac{\mathrm{d}\omega}{\mathrm{d}\boldsymbol{k}}\right| = \dfrac{c}{2}\sqrt{\dfrac{\sin^2\left(k_x\Delta x\right) + \sin^2\left(k_z\Delta z\right)}{\left(1 - \eta^2\left(\mathrm{s}_x^2 + \mathrm{s}_z^2\right)\right)\left(\mathrm{s}_x^2 + \mathrm{s}_z^2\right)}}, \end{cases} \tag{3.22}$$

with $\mathrm{s}_x = \sin\left(k_x\Delta x/2\right)$, $\mathrm{s}_z = \sin\left(k_z\Delta z/2\right)$ and $\sin^{-1}$ the inverse sine function. As pictured in Fig. 3.9–a, e, these two velocities are in fact lower than c for any k.

Note that at the CFL condition, when a wave is propagating along the grid diagonal, i.e., $k_x\Delta x = k_z\Delta z$, the solver does not present any dispersion. It is something to keep in mind when designing a simulation in order to maintain numerical artifacts as low as possible.

Dispersion equation for the Cole-Karkkainen-Cowan solver in 2D. Several decades after Yee, Cole and Karkkainen proposed a new type of FDTD solvers [Cole, 1997, 2002; Karkkainen et al., 2006], which are similar to Yee's scheme but for which the spatial derivative of the Maxwell-Faraday equation is discretized on more points, introducing a variable coefficient β in the expression of the finite difference stencil in space. In practice, it is possible to add even more coefficients in order to optimize the solver to a given problem [Vay, Geddes, et al., 2011; Blinne et al., 2018]. However, in this manuscript, we will limit ourselves to the particular case where $\Delta x = \Delta z$ and $\beta = 0.25$, discussed by Cowan in [Cowan et al., 2011]. With the same Von Neumann analysis, it is possible to find the corresponding numerical dispersion for the Cole-Karkkainnen-Cowan (CKC) solver:

$$\frac{1}{c^2\Delta t^2}\sin^2\left(\frac{\omega\Delta t}{2}\right) = \frac{A_x}{\Delta x^2}\sin^2\left(\frac{k_x\Delta x}{2}\right) + \frac{A_z}{\Delta z^2}\sin^2\left(\frac{k_z\Delta z}{2}\right), \tag{3.23}$$

with $A_x = (1-\beta) + \beta\cos(k_z\Delta z)$ and $A_z = (1-\beta) + \beta\cos(k_x\Delta x)$.

The numerical phase and group velocities corresponding to the CKC solver are displayed in Fig. 3.9–b, f. This solver is interesting because the CFL condition is equal to 1 and thus allows for larger time steps than the Yee solver: $c\Delta t = \Delta x\ (= \Delta z)$. It is also dispersion-free along the grid axes, i.e., when $k_x\Delta x = 0$ or $k_z\Delta z = 0$. It might be a good alternative to the Yee's scheme, e.g., for wakefield simulations, where a pulse is propagating along one axis during a large number of time steps.

Looking at Fig. 3.9, it seems that second-order finite-difference solvers present numerical dispersion in most of the spatial domain. In order to minimize it, we turn to higher order-p finite-difference solvers and their infinite order limit, pseudo-spectral solvers.

3.4.2 Introduction to pseudo-spectral solvers

When the order of a solver is increased, the discrete derivatives tend to their continuous values and we should expect numerical artifacts, such as numerical dispersion, to be mitigated. Then, using very high-order can significantly decrease the needed resolution and improve the overall stability for a given accuracy. This can enable realistic 3D PIC simulation studies that are otherwise not practical.

When the order p becomes very large, using spatial convolutions (e.g. FDTD) start to be extremely costly and must be replaced by Fast Fourier Transform (FFT)-based algorithms, where the fields are resolved in the spectral domain:

$$\begin{aligned} &\bullet \quad \mathrm{j}\boldsymbol{k}\cdot\widetilde{\boldsymbol{E}} = \widetilde{\rho}/\epsilon_0, && \bullet \quad \mathrm{j}\boldsymbol{k}\cdot\widetilde{\boldsymbol{B}} = 0, \\ &\bullet \quad \frac{\partial\widetilde{\boldsymbol{B}}}{\partial t} = -\mathrm{j}\boldsymbol{k}\times\widetilde{\boldsymbol{E}}, && \bullet \quad \mu_0\epsilon_0\frac{\partial\widetilde{\boldsymbol{E}}}{\partial t} = \mathrm{j}\boldsymbol{k}\times\widetilde{\boldsymbol{B}} - \mu_0\widetilde{\boldsymbol{J}}, \end{aligned} \tag{3.24}$$

where $\widetilde{\boldsymbol{F}}$ is the Fourier transform of the quantity $\boldsymbol{F}$. Solvers, which derive Maxwell's equation in Fourier space are called *pseudo-spectral* solvers.

However, despite significant advantages in terms of accuracy, high-order solvers have not been widely used so far because of their poor scalability to tens of thousands of cores [Habib et al., 2012]. Indeed, these solvers commonly use global FFTs, which require global communications all across the domain. In contrast, parallelizing low order solvers involves local communications with the neighbouring subdomains (as we have already seen in Fig. 3.4), which makes it easily scalable up to millions of cores .

In [Vay, Haber, et al., 2013], the authors proposed to apply the cartesian domain decomposition technique currently used with low order FDTD solvers to infinite order pseudo-spectral solvers. This new parallelization method is based on local FFTs on each subdomain and allows for a scaling almost as good as those obtained for FDTD solvers [Vincenti and Vay, 2018]. However, the deviation from global FFTs indubitably generates numerical errors, equivalent to a truncation of the (infinite) stencil in the spatial domain. Fortunately, these errors stay quantitatively small and localized near the guard regions, where the truncations are more likely to have impact.

The fundamental argument legitimating this method is that physical information cannot travel faster than the speed of light. Since the guard cells are rewritten at every time step, a large part of the errors do not have time to propagate inside the domain and end up to be erased.

Recently, [Vincenti and Vay, 2016] demonstrated that it is possible to strongly mitigate the truncation errors by replacing the infinite order stencil by one with a high but finite order. To do so, local FFTs are still performed on each subdomain but k is replaced in Eq. (3.24) by its discrete value at a p-order, k_p. It can be written thanks to the so-called Fornberg coefficients C_l^p defined in [Fornberg, 1990; Vincenti and Vay, 2016]:

$$k_p^2 = \sum_{X\,\in\,\{x,z\}} \left(\frac{2}{\Delta X} \sum_{l=1}^{p/2} C_l^p \sin\left(\frac{(2l-1)k_X\Delta X}{2} \right) \right)^2 . \tag{3.25}$$

In practice, for all simulations performed with a pseudo-spectral solver in this manuscript, $p = 100$. A more general and versatile domain decomposition method has been developed in [Kallala et al., 2018], as part of Haithem Kallala's PhD thesis to considerably reduce the allocated memory.

We now present two pseudo-spectral solvers implemented in WARP+PXR, which differ on how the time derivative are modeled: either analytically for the Pseudo Spectral Analytical Time Domain (PSATD) solver or using finite discrete derivatives for the Pseudo Spectral Time Domain (PSTD) solver.

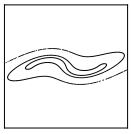

Class solver	Solver	CFL condition	Phase velocity
Finite Difference Time Domain	**Yee**	$\eta \leq 1/\sqrt{2}$	$\frac{2c}{\eta k \Delta x} . \sin^{-1}\left(\eta \sqrt{\mathrm{s}_x^2 + \mathrm{s}_z^2}\right)$
	CKC	$\eta \leq 1$	$\frac{2c}{\eta k \Delta x} . \sin^{-1}\left(\eta \sqrt{A_x \, \mathrm{s}_x^2 + A_z \, \mathrm{s}_z^2}\right)$
Pseudo-Spectral Time Domain	**PSTD**	$\eta \leq \sqrt{2}/\pi$	$\frac{2c}{\eta k \Delta x} . \sin^{-1}(\eta k/2)$
	PSATD	None	1
	PSATD-p	None	$\frac{c k_p}{k}$

Table 3.1: **Summary table of CFL conditions and phase velocities for several Maxwell solvers.**

The Pseudo Spectral Analytical Time Domain (PSATD) solver. In [Haber et al., 1973], the authors presented a pseudo-spectral solver that integrates analytically the solution over a finite time step, under the assumption that electromagnetic sources are constant over this period. The mathematical derivation can be found in [Vay, Haber, et al., 2013] and is not presented in detail in the manuscript.

The general idea is to separate the field components transverse and longitudinal to $\boldsymbol{k}$ in the Eq. (3.24). While the longitudinal equations are easy to solve (since the terms $\boldsymbol{k} \times \widetilde{\boldsymbol{F_L}}$ disappear), the transverse ones are much more complicated and the time integration is only possible by assuming that the sources remain constant along Δt. At the end, the total formulation for the PSATD solver for a staggered grid is:

$$\begin{cases} \widetilde{\boldsymbol{E}}^{n+1} = \widetilde{\boldsymbol{E}}^{n} + 2\mathrm{j}\, S_h\, \hat{\boldsymbol{k}} \times \widetilde{\boldsymbol{B}}^{n+1/2} - \dfrac{2\mathrm{j}\, S_h}{kc} \widetilde{\boldsymbol{J}}^{n+1/2} + \hat{\boldsymbol{k}} \left(\hat{\boldsymbol{k}} \cdot \widetilde{\boldsymbol{J}}^{n+1/2}\right) \left(\dfrac{2\mathrm{j}\, S_h}{kc} - \Delta t\right), \\ \\ \widetilde{\boldsymbol{B}}^{n+3/2} = \widetilde{\boldsymbol{B}}^{n+1/2} - 2\mathrm{j}\, S_h\, \hat{\boldsymbol{k}} \times \widetilde{\boldsymbol{E}}^{n+1} + \mathrm{j}\, \dfrac{1 - C_h}{kc}\, \hat{\boldsymbol{k}} \times \left(\widetilde{\boldsymbol{J}}^{n+3/2} - \widetilde{\boldsymbol{J}}^{n+1/2}\right), \end{cases} \tag{3.26}$$

with $S_h = \sin\left(kc\Delta t/2\right)$, $C_h = \sin\left(kc\Delta t/2\right)$ and $\hat{\boldsymbol{k}} = \boldsymbol{k}/k$.

Considering k_p instead of k, the resulting solver, named PSATD-p, is extremely accurate in the whole domain, regarding the phase and group velocities (see Fig. 3.9–d, h) and does not present any CFL condition. In addition, recent works show its excellent scalability to million CPU cores on MIRA [Vincenti and Vay, 2018]. Recent papers were published to show its advantages over FDTD solvers in many domains of UHI physics[8].

The Pseudo Spectral Time Domain (PSTD) solver. The last solver presented in this manuscript is the PSTD scheme [Liu, 1997]. This solver is the limit of order-p FDTD solvers when $p \to \infty$. In this scheme, the Maxwell's equations are solved in the Fourier space but the time advance is not performed using analytical integration as in PSATD but rather using a finite

[8] Lehe et al., 2016; Kirchen et al., 2016; Jalas et al., 2017; Blaclard et al., 2017; Vincenti and Vay, 2018; P. Lee and Vay, 2019.

difference integration. Looking at Fig. 3.9–c, g, the PSTD solver is dispersive, but presents an isotropic dispersion relation. It also imposes a stringent CFL condition, $c\Delta t/\Delta x = \sqrt{2}/\pi \simeq 0.45$ in 2D that severely increases the computation time. Unlike order-2 FDTD solvers, for which departing from the CFL condition ($c\Delta t < \eta\Delta x$) introduces more dispersion and noise to the simulation, the PSTD scheme tends to be dispersion-free, when the time step is reduced for a fixed spatial resolution. In fact, when $c\Delta t \to 0$, the PSTD solver converges to the PSATD solver. Its numerical dispersion equation is given by:

$$\frac{4}{c^2\Delta t^2}\sin^2\left(\frac{\omega\Delta t}{2}\right) = k^2. \tag{3.27}$$

In practice, this solver does not present any interest for HHG simulations. It has the same spatial complexity as the PSATD solver at each time step, while it introduces non physical dispersion and requires smaller time steps. Nevertheless, as one of the few purely superluminal solvers, where v_ϕ, $v_g > c$, see Fig. 3.9–c, g, we will use it as a comparison tool to see the effect of a positive dispersion on HHG simulations.

A summary of all important results related to the different Maxwell solvers presented in this section can be found in Tab. 3.1.

3.4.3 Effect of the numerical dispersion on harmonic generation

In the previous sections, it has been shown that the different Maxwell solvers introduce numerical dispersion leading to errors in the wave propagation. In order to study these non physical artifacts in HHG PIC simulations, we ran different cases with the numerical and physical inputs defined in the Tab. 3.2. For all cases, physical parameters were fixed. The spatial mesh was also fixed while the time step was varied using the corresponding CFL condition.

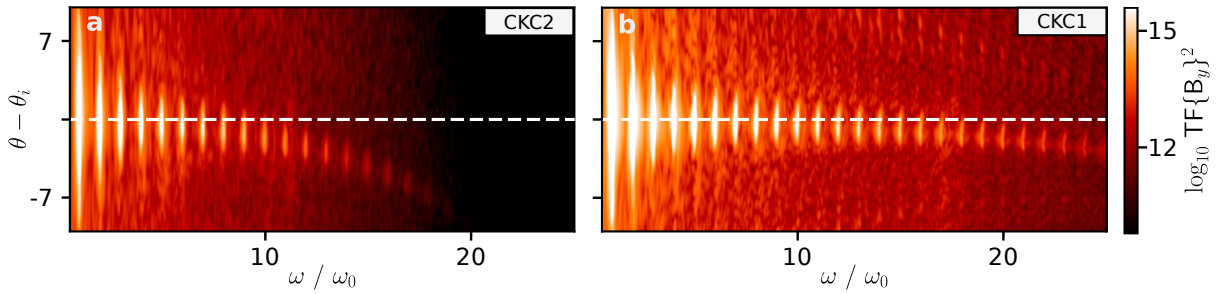

Figure 3.10: **Angularly resolved spectra for two different resolutions with CKC solver** - Panel (a) corresponds to the spectrum of the simulation `numdisp_CKC2`, where $\Delta x = \Delta z = \lambda/50$ and panel (b) to the simulation `numdisp_CKC1`, where $\Delta x = \Delta z = \lambda/100$. The relative angular deviation is expressed in degree. The harmonic comb seems to be deflected from the specular direction. This deflection is stronger at lower resolution.

Effect of numerical dispersion on the spatial properties of harmonic beams. In order to check the effect of a numerical artifact, one of the most natural solution consists to try different resolutions and compare the numerical convergence. We thus ran two simulations with the CKC solver — `numdisp_CKC2` and `numdisp_CKC1` — in the setup defined in section 3.3.3 but for two different resolutions, respectively $\Delta x = \lambda/50$ and $\Delta x = \lambda/100$. The two resulting angularly resolved harmonic spectra are displayed in Fig. 3.10.

Table 3.2: **Numerical and physical parameters for the benchmark of different Maxwell solvers on HHG simulations** - The physical parameters remain fixed but the solver is changed. In addition, we run two simulations with different resolutions with CKC. In order to ease the reading, we replace the duplicate values by dashes.

Simulation	solver	Δx, Δz	$c\Delta t$	a_0	w_0	L_g	θ_i
`numdisp_Yee`	**Yee**	$\lambda_0/100$	$\Delta x/\sqrt{2}$	8	$5\lambda_0$	$\lambda_0/15$	55°
`numdisp_PSTD`	**PSTD**	-	$\sqrt{2}\Delta x/\pi$	-	-	-	-
`numdisp_PSATD`	**PSATD**	-	Δx	-	-	-	-
`numdisp_CKC1`	**CKC**	-	Δx	-	-	-	-
`numdisp_CKC2`	**CKC**	$\lambda_0/50$	Δx	-	-	-	-

It is striking to notice the strong spectrum deflection, which depends on the harmonic order. Since the deflection depends directly on the numerical resolution, it is of course a pure numerical artifact. A converged simulation would present a perfectly straight spectrum.

This effect is in fact due to the numerical dispersion and we develop a simple toy model in [Blaclard et al., 2017] that can be used to predict the angular deviation of high-order harmonics based on the Maxwell solver and the spatio-temporal resolution of the simulation. This will allow us to further compute the best resolution that is needed to avoid angular dispersion effects for a given harmonic range. Our model is based on the numerical refractive index $n_r = c/v_\phi$ and the Snell-Descartes law and its principle is sketched in Fig. 3.11. As already seen in the previous sections, the numerical phase velocity in vacuum is different from c and depends on the angle and the frequency of each wave. We would expect such a dependence for the refractive index as well.

In experiments, Doppler harmonics are all generated at the laser-plasma interface and enter vacuum with an angle $\theta = \theta_i$ equal to the angle of incidence of the laser on the target. As har-

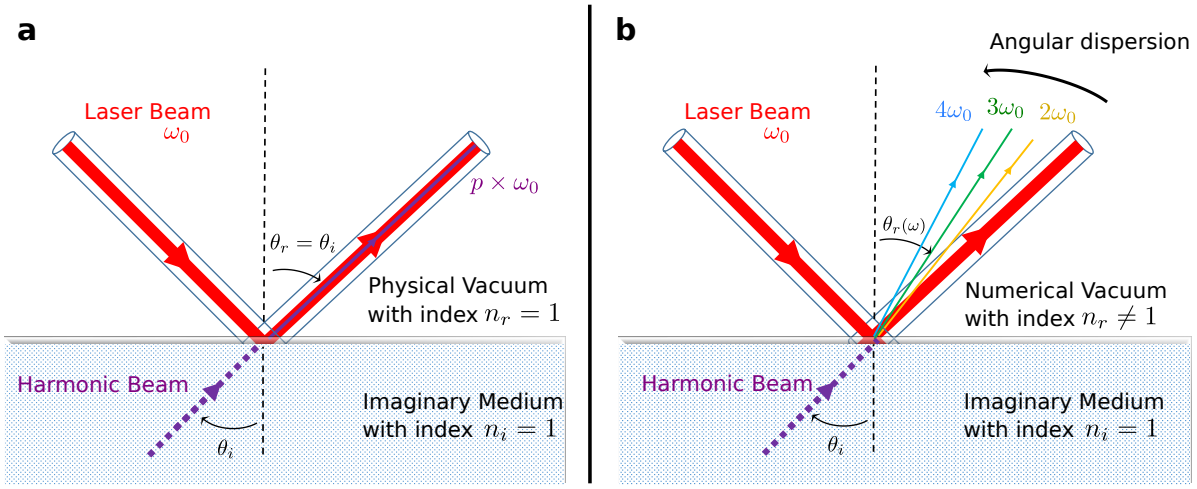

Figure 3.11: **Schematic drawing for harmonic angular deviation** - The harmonic beam, in purple, is modeled as an incident beam generated at the plasma-vacuum interface and entering in vacuum with an incidence angle $\theta = \theta_i$. (a) The physical case is represented. Because the vacuum index is 1, there is no dispersion and the harmonics are generated at the angle of specular reflection. (b) The transmission medium is numerical, therefore dispersive. Each frequency is deflected with an angle $\theta_r(\omega)$, which can be calculated with our simple model based on Snell's law.

monics are generated exactly at the plasma-vacuum interface with the same angle θ_i, one could see this situation as if each harmonic beam initially came from an *imaginary* non dispersive medium of index $n_i = 1$ and entered vacuum (see Fig. 3.11–a) with an angle of incidence θ_i. As *real vacuum* is a non dispersive medium of refractive index $n_r = 1$ for all frequencies, high-order harmonics will thus not be refracted and propagate in vacuum with the same angle $\theta_r = \theta_i$.

Oppositely, in PIC simulations, ROM harmonics are still generated at the laser-plasma interface but this time they enter a dispersive vacuum, which has a refractive index $n_r(\omega, \theta_r)$ (the brackets standing for the dependency on the frequency ω and on the propagation angle in the numerical medium θ_r). As a consequence, different harmonic orders will be refracted by the plasma-vacuum interface at different angles θ_r (see Fig. 3.11–b). The Snell's law presented below can be used to model this effect :

$$n_i \sin\theta_i = n_r(\omega, \theta_r) \sin\theta_r(\omega), \tag{3.28}$$

where $n_i = 1$ and θ_i is the laser angle of incidence. Notice that in this particular case, θ_r also depends on ω due to the anisotropy of the Maxwell solver. The unknown in Eq. (3.28) to be determined for each harmonic frequency ω is thus $\theta_r(\omega)$. The medium refractive index n_r is obtained from the numerical dispersion and is the inverse of the phase velocity displayed in Fig. 3.9.

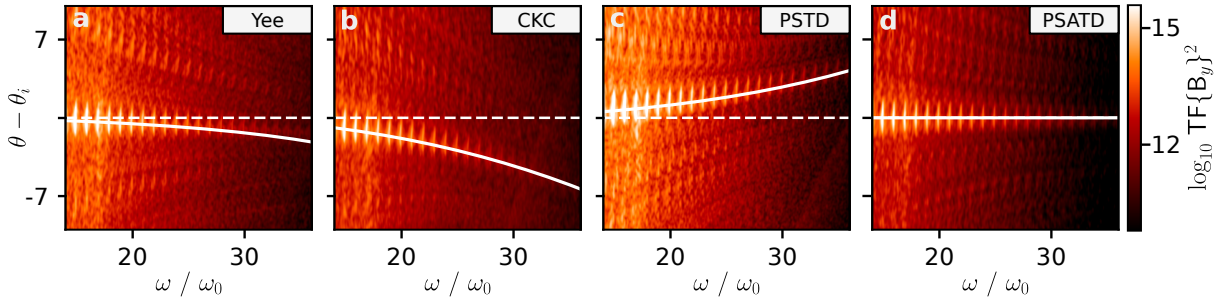

Figure 3.12: **Angularly resolved spectra (log-scale) for different Maxwell solvers in the range of $\omega_n/\omega_0 = 15$ to 35** - Panel (a): `numdisp_Yee`. Panel (b): `numdisp_CKC1`. Panel (c): `numdisp_PSTD`. Panel (d): `numdisp_PSATD`. The white solid line is the curve expected by the refraction model. For (a) and (b), $n_r > 1$ and the harmonics get closer to the normal at higher frequency with a negative angle of refraction (see Fig. 3.11). For (c), the PSTD solver numerical index $n_r < 1$ and the refraction angle is positive. The panel (d) shows a dispersion-free spectrum obtained with the PSATD solver.

With an iterative algorithm, it is easy to find the numerical value of θ_r for every frequency ω at a given resolution. Fig. 3.12 shows angularly resolved harmonic spectra obtained from PIC simulations for different Maxwell solvers. For each one, we overlap the angular deviation computed by solving Eq. (3.28) for each frequency (white line) to the angularly resolved harmonic spectra. For each case, our predictions do agree very well with the angular deviation observed in simulation.

For FDTD solvers such as Yee or CKC, the refractive index is always greater than 1 (i.e., $v_\phi \leq c$, see Fig. 3.9–a, b). As a consequence and because the refractive index increases with frequency, the highest harmonics are deflected closer to the normal to the plasma mirror surface (see. Fig. 3.12–a, b) as predicted by the Snell-Descartes law.

As opposed to FDTD solvers, the refractive index of vacuum for the PSTD solver is lower than 1 ($v_\phi \geq 1$ see. Fig. 3.9–c). As a consequence and because the refractive index decreases with

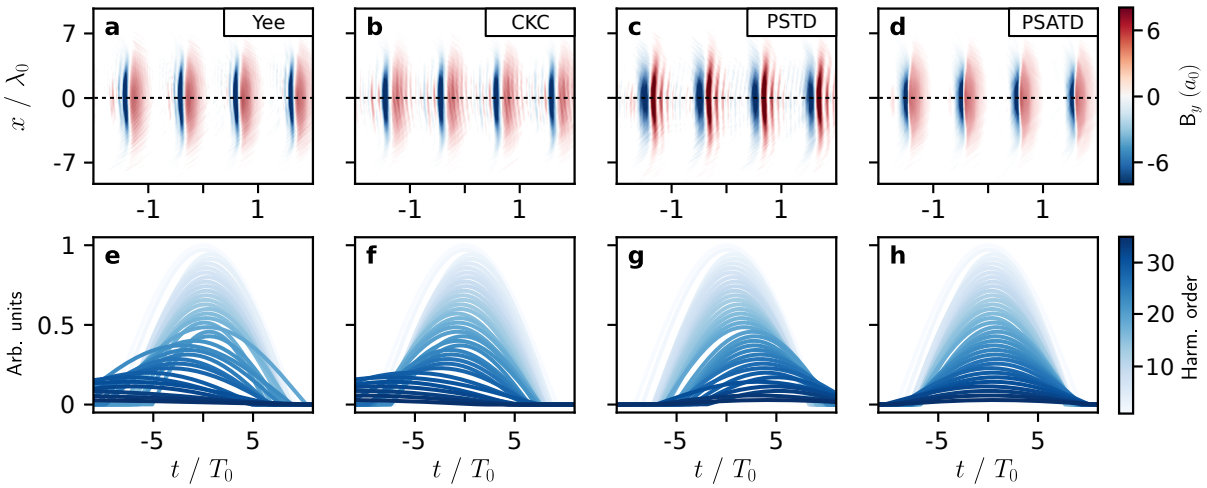

Figure 3.13: **Group velocity dispersion for different Maxwell solvers** - Panels (a)-(d) display the y component of the reflective magnetic field for the different simulations at a distance 55 λ_0 from target. Each simulation corresponds to a different solver: (a) `numdisp_Yee`, (b) `numdisp_CKC2`, (c) `numdisp_PSTD` and (d) `numdisp_PSATD`. In addition, panels (e)-(h) show the relative position of each fitted harmonic envelope in the total pulse for the same respective simulations. Every curve, pictured from white to blue, corresponds to a specific filtered harmonic order and the amplitude is arbitrary chosen. Only the PSATD solver does not present any group velocity dispersion, since all harmonic envelopes remain in phase.

frequency, the highest harmonics are deflected further from the normal towards the plasma mirror surface. Moreover, when light travels from a medium with a higher refractive index toward a medium with a lower refractive index, Snell's law indicates that for an angle of incidence greater than a certain limit angle θ_l, the wave should not pass through the interface and would be totally reflected. The reflective limit angle is obtained when $n_i \sin\theta_i = n_r$. In practice, the total reflection appears at grazing incidence (see [Blaclard et al., 2017]).

Effect of numerical dispersion on the temporal properties of attosecond pulses. In parallel to the phase velocity dispersion, the different Maxwell solvers also induce strong group velocity dispersion. It does not play a key role at generation but becomes clearly visible after some propagation in vacuum. Even if the different harmonic orders are refracted when they enter in the dispersive vacuum, they are still generated at the same time in the simulation, time given by the plasma surface dynamics and the ROM mechanism (see Sec. 1.3.1, page 21). It means that overall all harmonic orders are initially in phase in space and time. But after some iterations and because the group velocity depends on the frequency, the different harmonic orders are propagating at different speeds, leading to a temporal chirp and a stretch of the reflected field temporal envelope.

This harmonic temporal chirp can be seen in Fig. 3.13, where we recorded the reflective magnetic field on a plane detector (see Fig. 3.7, page 53) at 55 λ_0 from target. The pulse is propagating from left to right and each panel corresponds to a simulation performed with a different solver: (a) `numdisp_Yee`, (b) `numdisp_CKC1`, (c) `numdisp_PSTD` and (d) `numdisp_PSATD`. For sublumninal solvers such as Yee (Fig. 3.13–a, e) and CKC (Fig. 3.13–b, f), the highest harmonic orders are propagating slower than the fundamental frequency and one may notice high frequency signals behind each attosecond pulse. By contrast, for PSTD (Fig. 3.13–c, g), the highest-harmonic wave packets are drifting in front of the pulse. Finally, since the PSATD solver is dispersion-free, the attosecond pulses keep their entirety all along the propagation (Fig. 3.13–d, h).

This effect is increasing over time and can be quantified as a function of the resolution for a given distance or as a function of the distance for a certain resolution. Then, it can be used as another convergence criterion in addition to the numerical harmonic deflection.

Conclusion

To efficiently describe laser-plasma interactions, it is necessary to use kinetic codes such as Particle-In-Cell codes. These codes are particularly useful to access observables that are hard to follow in experiments and are thus crucial to interpret and guide future measurements.

However, most of Particle-In-Cell codes employ finite-difference Maxwell solvers, which introduce strong numerical errors, especially due to numerical dispersion. In this chapter, we characterized its effect on the properties (spatial and temporal) of the harmonic emission and it is safe to conclude that standard solvers fail to accurately describe the laser-plasma mirror interaction, at least at reasonable resolutions.

In the following and for all PIC simulations performed in this manuscript, we will use the massively parallel version of the PSATD solver, which completely mitigates the errors related to numerical dispersion. In particular, this solver allows for accurate solid target 3D-simulations, impossible otherwise.

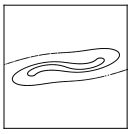

4 Particle Tracking Simulations for Laser-Matter Interactions without Collective Effects

In this manuscript, certain coupling mechanisms between light and particles do not necessarily have to be modeled with PIC simulations. Among others, we can cite Vacuum Laser Acceleration (VLA) or Stochastic Heating, both studied further ahead. In these cases, the dynamics of electrons are mainly governed by the interaction with the laser beam, while collective effects are minor if not completely negligible. Then, particles can be advanced in time by only considering the contribution of the laser fields in the Lorentz force. If these fields are known with analytical formulas at any time and space, one does not need to numerically solve the whole Maxwell-Vlasov system anymore. However, using a particle pusher code relies on few subtleties, in particular on how well modeled a laser field can be.

Contents

4.1 Presentation of our Particle Tracker Code

For specific applications, the dynamics of electrons can be efficiently captured without the need of PIC codes. To do so, some simulations are performed with reduced models, less costly in term of allocated memory as well as time to solution.

During my thesis, I developed and used a particle tracker (PT) code, specifically designed to push test particles in a given electromagnetic field in 3D space. More precisely, at each time step, the electromagnetic fields are first computed on exact particle positions thanks to analytical formulas. Then, the temporal motion of the particles is solved by using one of the three already presented 2nd-order accurate relativistic particle pushers: the Boris, the Vay and the Higuera pushers (step (iv) of the PIC loop, see Sec. 3.2.2). During the resolution, particles can be independently treated as they do not influence the evolution of the electromagnetic fields. As the code does not solve either Maxwell's equations or source deposition (steps (i) and (ii) of the PIC loop, see Sec. 3.2.2), there is no need for a spatial grid. Particles can freely move in the simulation.

The code is written in Python, fully open-source and available on GitHub[1]. The code was designed to be as complete as possible and it allows for an extensive choice of laser polarizations, incidence angles, spatial and temporal shapes, on and off focus, radiative effects... For the I/Os, similarly to the PIC code WARP+PXR, it adopts the OpenPMD standard[2] to store particle data. We can then reuse all viewer tools defined for this standard or data analysis scripts developed for WARP+PXR.

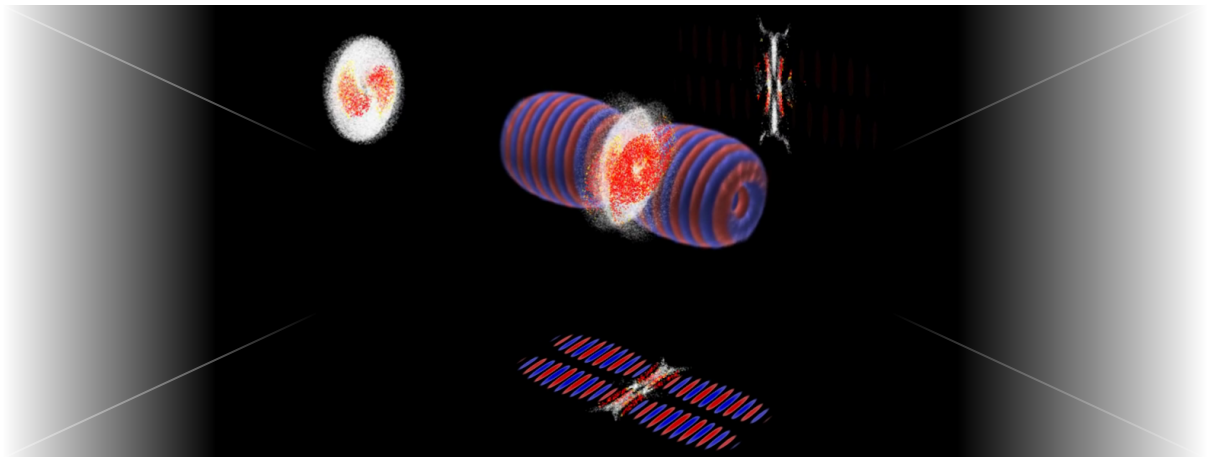

Figure 4.1: **Collision of two Laguerre-Gaussian beams in a cylindrically shaped electron cloud** - The rendering is performed with the 3D-visualization software VisIt. The fields are displayed from blue to red, while the particles are pictured from white to orange depending on their energy. Alongside the 3D image in the middle, are plotted three different slices taken in the middle of the interaction box.

In Fig. 4.1, we show an example of a simulation performed with this code and rendered with the 3D-visualization software VisIt, developed in Livermore [Childs et al., 2012]. There, two laser beams, carrying orbital angular momentum and modeled as Laguerre-Gaussian beams such as defined in [Allen et al., 1992], are interfering in an electron cloud. During the interaction, a

[1] `https://github.com/lidyl/particle_pusher`
[2] `https://github.com/openPMD/openPMD-standard`

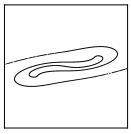

portion of the orbital angular momentum is transfered to the particles.

It exists a full video of this interaction uploaded on the Internet[3]. This video was actually presented at the EPS conference in Milan in 2019 and I was pleased to win the best video award with it.

4.2 Modeling Gaussian Pulses in Particle Tracker Simulations

In order to perform PT simulations as close as possible to experiments, it is required to model spatially shaped laser pulses, such as Gaussian beams. These are solutions to the Helmholtz equation combined with the paraxial approximation. As a reminder, for any electromagnetic waves[4] $\boldsymbol{U}$ polarized along $\boldsymbol{x}$ and propagating along $\boldsymbol{z}$, defined as:

$$\boldsymbol{U}(x,y,z,t) = u(x,y,z)\, e^{\mathrm{j}(\omega_0 t - k_0 z)}\boldsymbol{x}, \tag{4.1}$$

the Helmholtz equation is given by:

$$\nabla^2\left(u\, e^{-\mathrm{j}k_0 z}\right) + k_0^2\, u\, e^{-\mathrm{j}k_0 z} = 0. \tag{4.2}$$

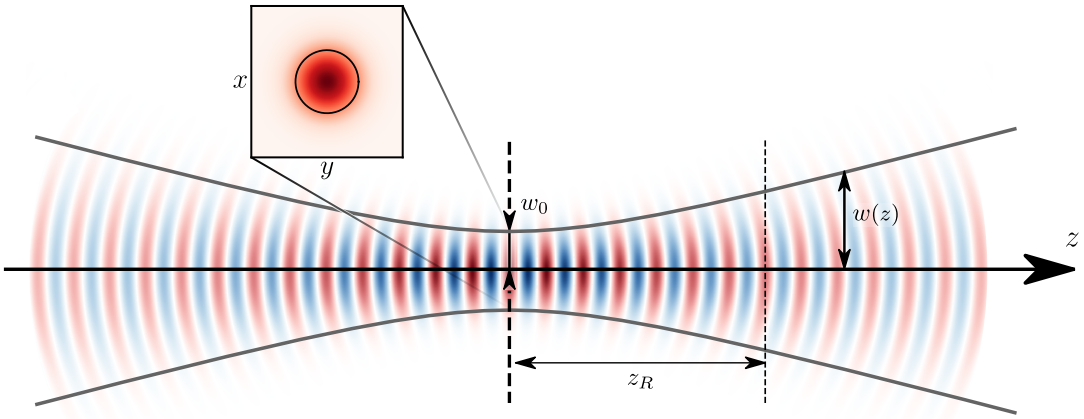

Figure 4.2: **Amplitude of the electric field for a monochromatic Gaussian beam near focus.**

The paraxial approximation is a small-angle approximation assuming that the propagation direction of light deviates only slightly from the beam axis. It means that the angle between $\boldsymbol{k}$ and $\boldsymbol{z}$ remains low. For the field $\boldsymbol{U}$, this approximation reads:

$$\left|\frac{\partial^2 u}{\partial z^2}\right| \ll \left|k\frac{\partial u}{\partial z}\right|. \tag{4.3}$$

Expansion and approximation yield the following equation:

$$\nabla_\perp^2 u = 2\mathrm{j}k_0\frac{\partial u}{\partial z}. \tag{4.4}$$

where the symbol $\perp$ stands for the transverse directions, i.e., $\boldsymbol{x}$ and $\boldsymbol{y}$. The spatial profile of a laser beam solution of Eq. (4.4), can be decomposed in cylindrical modes. The lowest-order is

[3] `https://www.epsplasma2019.eu/wp-content/uploads/2019/07/V2_Blaclard.mp4?_=2`
[4] $\boldsymbol{E} = \boldsymbol{U}$ or $\boldsymbol{B} = \boldsymbol{k}\times\boldsymbol{U}/ck_0$

precisely the Gaussian mode, for which u is defined as:

$$u(x,y,z) = U_0 \frac{w_0}{w(z)} \exp\left(-\frac{x^2+y^2}{w^2(z)}\right) \exp\left(-\mathrm{j}\left(k_0 \frac{x^2+y^2}{2R(z)} - \psi(z)\right)\right), \tag{4.5}$$

with $w(z) = w_0\sqrt{1+z^2/z_R^2}$ the laser beam width, $w_0 = w(0)$ the beam waist, U_0 the amplitude of the wave at origin, z_R the Rayleigh length, $R(z)$ the radius of curvature and $\psi(z) = \tan^{-1}(z/z_R)$ the Gouy phase. Such a beam profile is pictured in Fig. 4.2 around focus.

Since this solution relies on the paraxial approximation, it is not accurate for strongly diverging beams. In practice, the above form is valid as soon as $k_0 w_0 \gg 1$. In most simulations or experiments presented in this manuscript, $w_0 = 5\lambda_0$ and $k_0 w_0 = 10\pi \simeq 31.4 \gg 1$.

However, one can easily check that a field defined in Eq. (4.5) does not currently verify Maxwell's equations out of axis (for example, $\boldsymbol{\nabla}\cdot\boldsymbol{E} = \partial E_x/\partial x \neq 0$). As we will see later on, the particle dynamics within this field are found to be incorrect as well, even when $k_0 w_0 \gg 1$. It is then essential to correct the fields and properly model a Gaussian beam in our code. A solution can be found in [Quesnel and Mora, 1998], in which the authors proposed to expand Maxwell's equations near the paraxial solution as a power series of $\epsilon = 1/k_0 w_0 \ll 1$. They found in particular that at first order in ϵ, it is necessary to add extra 1^{st}-order longitudinal components E_z and B_z. The main components of the electromagnetic field, E_x and B_y, for a wave linearly polarized along x, are still being defined by Eq. (4.5). The real parts of the whole field up to first order become:

$$\begin{aligned}
&\bullet\ E_x = E_0 \frac{w_0}{w} \exp\left(-\frac{r^2}{w^2}\right) \cos\phi_0, && \bullet\ B_x = 0,\\
&\bullet\ E_y = 0, && \bullet\ B_y = \frac{E_x}{c},\\
&\bullet\ E_z = -2\epsilon E_0 \frac{x w_0}{w^2} \exp\left(-\frac{r^2}{w^2}\right) \sin\phi_1, && \bullet\ B_z = -2\epsilon \frac{E_0}{c} \frac{y w_0}{w^2} \exp\left(-\frac{r^2}{w^2}\right) \sin\phi_1,
\end{aligned} \tag{4.6}$$

with:

$$\begin{aligned}
&\bullet\ \phi_0 = \omega_0 t - k_0 z - z\frac{x^2+y^2}{z_r w^2} + \tan^{-1}\left(\frac{z}{z_r}\right),\\
&\bullet\ \phi_1 = \omega_0 t - k_0 z - z\frac{x^2+y^2}{z_r w^2} + 2\tan^{-1}\left(\frac{z}{z_r}\right).
\end{aligned} \tag{4.7}$$

One can easily verify that these fields satisfy Maxwell's equations at first order. The forms defined in Eq. (4.6) are precisely the ones implemented in the particle tracker code.

The corrections brought by [Quesnel and Mora, 1998] are fundamental to describe the proper electron trajectories in a realistic pulse. In a spatially shaped electromagnetic wave, particle undergo a force depending on the wave envelope and directed towards low-intensity regions: the ponderomotive force. The authors demonstrated in particular that corrections at first-order are sufficient to take account for ponderomotive effects.

As a reminder, the ponderomotive force is defined after averaging all particle and laser quantities over fast oscillations relatively to the laser period and reads:

$$\frac{\mathrm{d}\bar{\boldsymbol{p}}}{\mathrm{d}t} = -\frac{e^2}{2m\bar{\gamma}} \boldsymbol{\nabla} \overline{|\tilde{A}_\perp^2|}, \tag{4.8}$$

The force only depends on the gradient of the wave intensity and the direction of polarization plays no particular role. For a Gaussian beam, electrons tend to be radially expelled from the center of the pulse, where the fields show maximal intensities.

In order to illustrate ponderomotive effects on particles, we now run two simulations of a Gaussian pulse crossing an electron cloud initially at rest and spatially distributed within a cylinder. For the first simulation, the fields are expressed using the zeroth-order only, while for the second one, we add the first-order corrections defined in Eq. (4.6). The trajectories of a given electron and the final distributions are reported in Fig. 4.3.

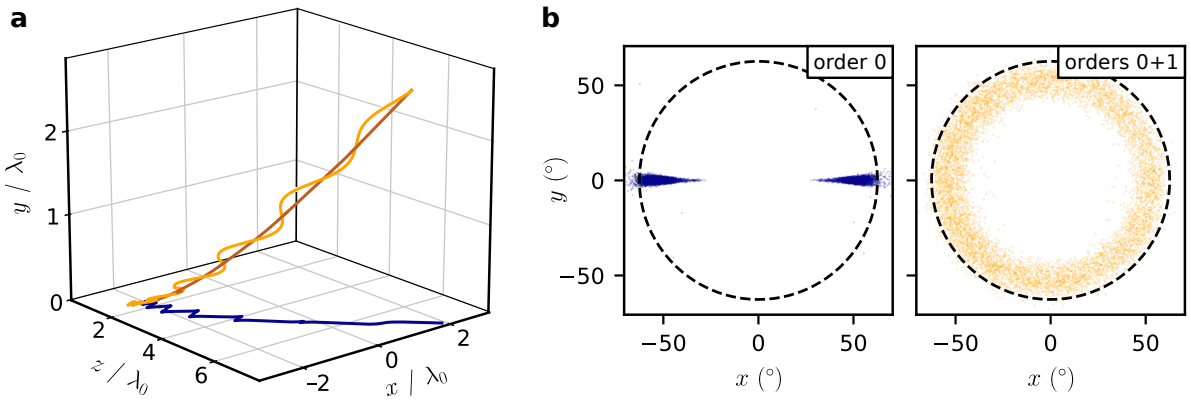

Figure 4.3: **Electron dynamics in Gaussian beam with and without first-order corrections** - On panel (a), three electron trajectories are plotted in the 3D-space (x, y, z): (i) in blue, with only considering zeroth-order fields, (ii): in orange, with fields corrected up to the first order and (iii) in brown, with ponderomotive force only (Eq. (4.8)). On panel (b) are plotted the final angular distributions without (blue) and with (orange) first-order field corrections. The black dashed circle just helps the reader for direct comparison between the two plots.

Without corrections, the particles (blue trajectory in Fig. 4.3–a and left panel of Fig. 4.3–b) are maintained in the plane (x, z) of polarization. It can be intuitively expected since the component of the Lorentz force along y is identically equal to zero at zeroth-order ($E_y = 0$ and $(\boldsymbol{v} \times \boldsymbol{B})_y = 0$). This description of a Gaussian field fails to reproduce the isotropic distribution expected by the definition of the ponderomotive force in Eq. (4.8).

When first-order corrections are taken into account, the particles now travel also in the y-direction. In Fig. 4.3–a, the brown line shows the trajectory of a particle only exposed to the long time scale ponderomotive force, while the yellow line shows the trajectory of the same particle in the full oscillating field. It is clear that this whole motion combines dynamics at slow and fast time scales and that the ponderomotive effects are well reproduced. Regarding the electron distribution (see right panel of Fig. 4.3–b), it is isotropic and shaped as a ring. The particle are correctly expelled in all transverse directions from the center of the pulse (corresponding to the point (0, 0)).

Effect of the laser temporal shape. In the previous discussion and for simple considerations, the pulse was supposed to be monochromatic and thus does not present a finite duration. When adding a time envelope to the laser pulse, the previous Gaussian beam solution is simply

multiplied by a function $g(t - z/c)$. The main component of the electric field becomes:

$$E_x = E_0 \frac{w_0}{w} \exp\left(-\frac{r^2}{w^2}\right) \cos\phi_0 \, g(t - z/c). \tag{4.9}$$

In most of the time, g is chosen to be either a Gaussian function or a cosine function and reads:

$$\begin{aligned} &\bullet \quad g(t - z/c) = \exp\left(-\frac{(t - z/c)^2}{\tau_0^2}\right), \\ &\bullet \quad g(t - z/c) = \cos\left(\frac{t - z/c}{\tau_0}\,\pi\right) \qquad \text{for } t - z/c \in \left[-\tau_0/2,\ \tau_0/2\right] \end{aligned} \tag{4.10}$$

with τ_0 the pulse duration. Similarly to the spatial envelope, such fields do not satisfy Maxwell equations in this form and may require corrections. Again in [Quesnel and Mora, 1998], the authors also studied the effects of the finite pulse duration and showed that they can be completely neglected as soon as $\tau_0\omega_0 \gg 1$. In practice, Ti:sapphire laser beam lines deliver few tens of femtosecond pulses and the condition is largely verified: for $\tau_0 = 25$ fs, $\tau_0\omega_0 \simeq 58 \gg 1$. Thus, the corrections related to the temporal shape are not taken into account in our PT code.

Conclusion

In this chapter, we presented a particle tracker code, specifically designed when collective effects do not play a significant role. It will be used in the following when the electron motion is mainly governed by the laser pulse.

Despite the code simplicity, few corrections were added to perform appropriate simulations, these mainly affecting the spatial shape of the laser beam. In particular, for Gaussian pulses, the ponderomotive force is wrongly modeled when only the zeroth-order components of the fields are considered. Only by introducing first-order corrections, electrons are expelled in all transverse directions, as expected by theoretical formulas.

Simulations performed with a PT code can obviously also be run with a PIC code, but a large amount of computing time would be wasted. For example a 3D simulation of Vacuum Laser Acceleration respectively costs hundreds of CPU hours with a PIC code, while barely 10 CPU minutes with the PT code. In addition, since particle data can be recorded at every time step, it is also easier to follow their trajectories one by one. All along this manuscript, it will be a powerful tool to dig into the physical processes at low cost, but obviously within the scope of its area of validity.

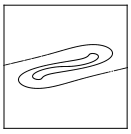

Part III

Signatures of the Coupling Mechanisms in Ultraintense Laser-Plasma Mirror Interaction

5 Effect of the Density Gradient Scale Length: Experimental and Numerical Investigations

The interaction of intense laser beams with plasmas created on solid targets involves a rich non-linear physics. Because such dense plasmas are reflective for laser light, the coupling with the incident beam occurs within a thin layer at the interface between plasma and vacuum. For very steep plasma surfaces, we expect the Brunel mechanism to be the mechanism at play but its validity range remains uncertain, especially when the plasma-vacuum interface becomes smoother in the relativistic regime.
The main results of this chapter were reported in [Chopineau et al., 2019], recently published in Physical Review X. The first section of this chapter focuses on the experimental setup used to control laser plasma mirror interactions in experiments. These experiments performed on the UHI100 TW laser at CEA Saclay outline a clear transition between two main mechanisms in function of the density scale gradient scale length L_g. The key signatures of these distinct regimes are then compared to PIC simulation results obtained with the WARP+PXR code.

Contents

5.1 Experiments on the UHI100 Laser at CEA Saclay

5.1.1 The UHI100 beam line

All experiments presented in this manuscript have been performed on the UHI100 laser located at CEA Saclay by the experimental team led by F. Quéré and consisting of A. Leblanc, L. Chopineau and A. Denoeud.

UHI100 is a Ti:sapphire laser, a commercial system developed by Amplitude Technologies, delivering an electromagnetic pulse with a temporal duration $\tau_0 = 25$ fs. The schematic drawing of the beam line is sketched in Fig. 5.1. Such laser emits in a near-infrared light around $\lambda_0 = 800$ nm and can be amplified to a peak power of 100 TW by the Chirped Pulse Amplification (CPA) technique in the compressor. [Strickland and Mourou, 1985] actually received the Nobel Prize in 2018 for the development of this technique.

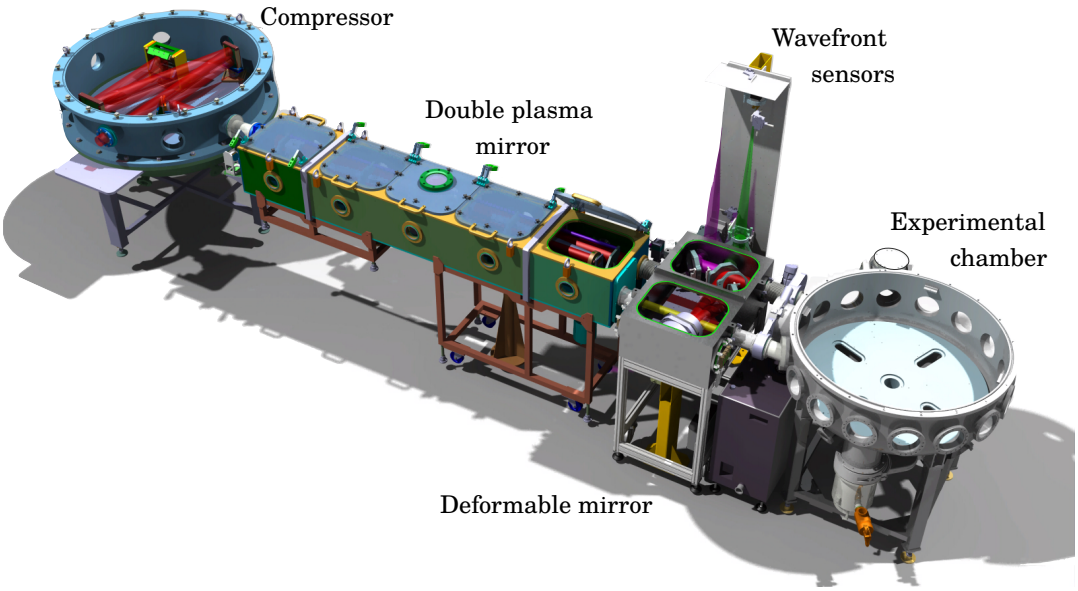

Figure 5.1: **The UHI100 beam line at CEA Saclay** - Starting from the left, the laser pulse is temporally compressed to a temporal duration $\tau_0 = 25$ fs. Then the temporal contrast is improved thanks to a double plasma mirror. The laser beam profile is improved *via* a set of deformable mirror and wavefront sensors and finally sent into the experimental chamber. *Courtesy of L. Chopineau.*

After temporal compression, the laser pulses generally presents a nanosecond pedestal before arrival of the main pulse. Induced mainly by Amplified Spontaneous Emission (ASE), this pedestal is typically 8 to 9 orders of a magnitude less intense than the main pulse. However, for ultra high intensities ($I \geq 10^{18-19}$ W.cm^{-2}), it becomes strong enough ($I \sim 10^{10-11}$ W.cm^{-2}) to start ionizing the target and creates a dense plasma. This plasma expands in vacuum during a nanosecond time scale, therefore leading to a long and largely uncontrolled exponential density profile in front of the target surface (characterized by a scale length L_g, see Sec. 1.1). This lack of precision complicates the interpretation of experiments and prevents high harmonic generation.

In order to avoid the premature creation of the plasma, UHI100 is equipped with a double plasma mirror system placed after the compressor [Lévy et al., 2007]. It increases the temporal

contrast by about 4 decades, thus reaching $\sim$ 13 orders of a magnitude for time delays $\gtrsim$ 100 ps before the main pulse. In addition, the laser wave fronts are corrected by an adaptive set of optical system (deformable mirror + wavefront sensors) to maximize the intensity on target in the experimental chamber. Such a high contrast ensures that no gradient scale length is induced before the main interaction. This is a prerequisite for the gradient control in experiments.

5.1.2 Gradient control in plasma mirror experiments

Now that the laser quality is sufficient, it becomes possible to perform plasma mirror experiments in a relativistic regime. To do so, the laser beam is focused by a parabola (focal length $f = 300$ mm) onto a glass target in the middle of the experimental chamber (see Fig. 5.2–a). The intensity at focus is around 10^{19} W.cm^{-2} or $a_0 \simeq 3$.

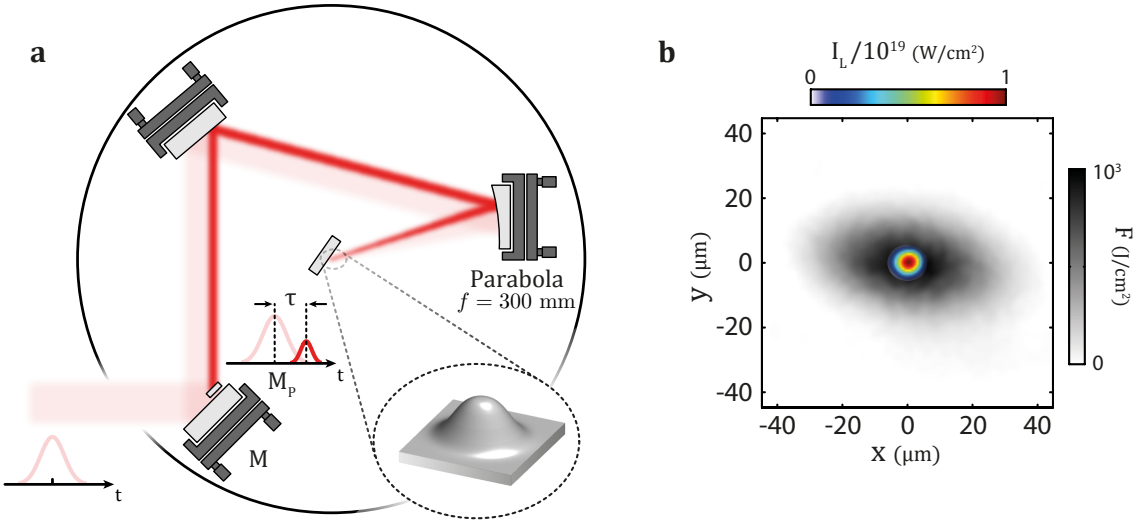

Figure 5.2: **Gradient control in plasma mirror experiments** - In panel (a), a prepulse is obtained from the main beam by simply adding a small mirror M_p placed in front of the mirror M, which introduces a temporal delay τ between the two pulses. This prepulse is focused on target using the same parabola as the main pulse. At focus, it ionizes the solid and creates a controllable gradient scale length by finely adjusting the delay τ. Panel (b) shows experimental focal spots for the prepulse (gray scale) and the main pulse (color scale). Because the prepulse spot is larger, the main pulse interacts with an almost homogeneous surface. *Courtesy of L. Chopineau*

In experiments, the density gradient scale length L_g in front of the target is controlled thanks to a *weak* prepulse traveling at an adjustable delay τ before the main pulse ($0 < \tau < 10$ ps). This prepulse can be simply created by a small mirror M_p placed on an edge of the main laser beam at a variable distance in front of a mirror M used for the transport of the main beam [Kahaly et al., 2013] (see Fig. 5.2–a). Its peak intensity is $I = 10^{16}$ W.cm^{-2}, which is high enough to strongly ionize the surface. Due to its smaller diameter before focusing, the prepulse produces a larger focal spot (pictured in gray scale in Fig. 5.2–b) than the main beam (in color). The density gradient that it creates can thus be considered as spatially uniform over the focal spot of the main laser pulse.

In the following, we systematically use $L_g(\tau)$ instead of just τ, since it gives direct information on the steepness of the surface. The evolution of the gradient scale length as a function of the delay can be measured in experiments using spatial domain interferometry [Bocoum et al., 2015].

5.1.3 Plasma mirror experiments

Studying signatures of harmonic or electron signals in typical plasma mirror experiments requires different experimental diagnostics that are presented in Fig. 5.3. As already seen before, the UHI100 laser is focused on a solid target and after interaction with an overcritical plasma, is reflected towards vacuum. The incident angle of the laser θ_i is chosen equal to 55°. The experimental team concentrates on two types of observables: the relativistic electron beam emitted by the target towards vacuum, and the beam of high-order harmonics generated around the specular reflection direction.

Two diagnostics are used for the electron beam:

- a LANEX screen which records by fluorescence the spatial profile of emitted electrons, at a distance of ~ 10 cm from the target.

- a new type of magnetic spectrometer for relativistic electrons [Chopineau et al., 2019], which provides the angularly-resolved kinetic energy spectrum of electrons in the plane of incidence (i.e. for $\theta_y = 0$).

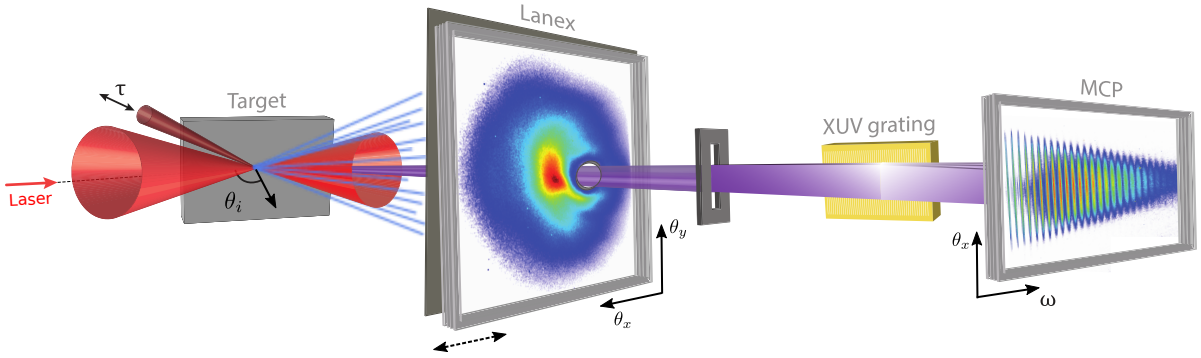

Figure 5.3: **Principle of a plasma mirror experiment** - The main laser beam as well as a controlled prepulse are impinging on a solid target. After reflection, harmonic and electron signals are recorded thanks to the following diagnostics: a LANEX screen for the measurement of the spatial profile of the high-energy electron beam, and the angularly-resolved XUV spectrometer.

The harmonic beam is characterized using an angularly-resolved extreme ultraviolet (XUV) spectrometer [Kahaly et al., 2013], equipped with a micro channel plate (MCP) detector. An example of an imaged harmonic signal is displayed at the right of Fig. 5.3. The harmonic spectrum and the electron beam spatial profiles can be measured simultaneously in a single shot, thanks to a small hole in the LANEX screen that lets the harmonic beam reach the spectrometer.

A simple additional diagnostic, requiring additional laser shots, consists of measuring the spatial profile of the reflected laser beam, by inserting a frosted glass plate that keeps only frequencies near the fundamental laser frequency. This is exploited to determine the plasma reflectivity for the incident laser beam.

5.2 Experimental Signatures of the Interaction

5.2.1 Gradient scale length influence

With this experimental setup, we aim to clearly identify the laser-plasma coupling mechanisms between light and plasma, when L_g varies from $L_g \ll \lambda$ to $L_g \sim \lambda$. The Fig. 5.4 summarizes the main findings of the experiment for a p-polarized incident laser for two extreme density gradient scale lengths $L_g = L_1 \sim \lambda/15$ and $L_g = L_2 \sim \lambda/1.5$. When L_g is increased from L_1 to L_2, the measured harmonic and relativistic electron signals radically change.

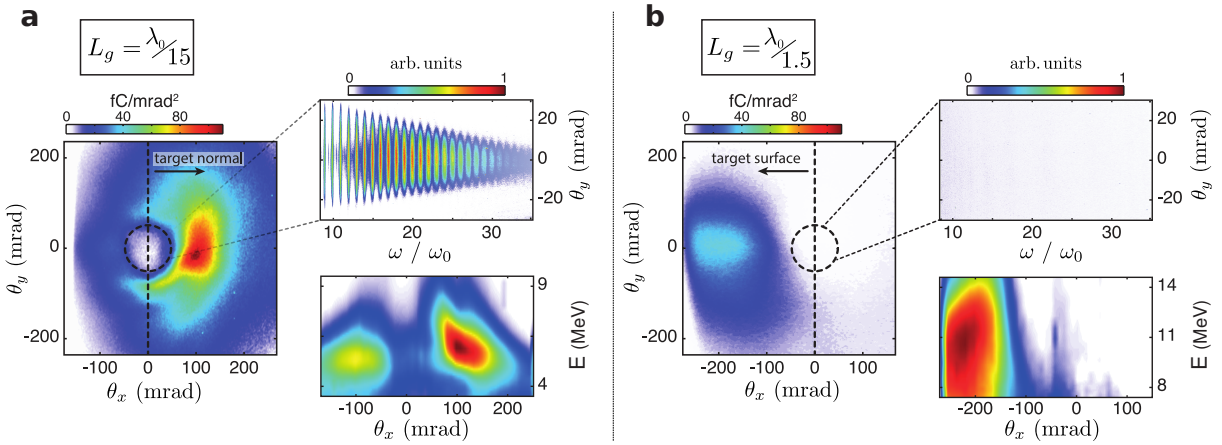

Figure 5.4: **Main experimental observables** - The main experimental findings for a p-polarized laser field are summarized: left images, angular emission pattern of relativistic electrons; bottom right images, angularly-resolved energy spectrum of electrons in the incidence plane ($\theta_y = 0$); top right images, angularly-resolved harmonic spectrum. Each panel corresponds to a different density gradient scale length L_g: (a) short gradient $L_g \sim \lambda/15$ and (b) long gradient $L_g \sim \lambda/1.5$.

Three main differences are observed:

- When $L_g = L_1 \ll \lambda$, the electron emission is predominantly peaked at $\theta_x \sim 100$ milliradians (mrad), close to the direction of laser specular reflection ($\theta_x = 0$ mrad), with a slight shift towards the target normal. As L_g is increased, it then switches to $\theta_x \sim -200$ mrad, a direction between specular direction and the tangent to the target surface ($\theta_x = -600$ mrad). It is also slightly broadened.

- Electrons reach energies about twice higher for large L_g (spectral peak around 10 MeV), with an angularly-resolved energy distribution (θ_x, E) that significantly changes. In the short gradient regime, a clear correlation is observed between emission angle θ_x and electron energy E, especially in the brightest part of the distribution ($0 \leq \theta_x \leq 200$ mrad): the electron energy increases as one gets closer to the specular direction. In contrast, in the long gradient regime, the electron spectrum hardly varies angularly: no significant correlation is observed on this angularly-resolved energy distribution.

- Harmonic emission is clearly observed for smallest gradient scale lengths, but it drops below the experimental detection threshold for large L_g.

The details of the transition between these two regimes are presented in Fig. 5.5, which displays the evolution with L_g of the electron beam angular profile in the incidence plane (Fig. 5.5–a),

and of the harmonic spectrum (Fig. 5.5–b). The most important point is the *quantitative* correlation, observed at short gradients, between the relativistic electron and harmonic signals (see plots in Fig. 5.5–c). As L_g is gradually increased, the electron signal S_{e1} around $\theta_x = 100$ mrad and the harmonic signal S_{ROM} reach a common optimum around $L_g = \lambda/15$, and then both quickly decrease. The electron signal S_{e2} on the other side of the specular direction then grows, but is not associated with any harmonic signal.

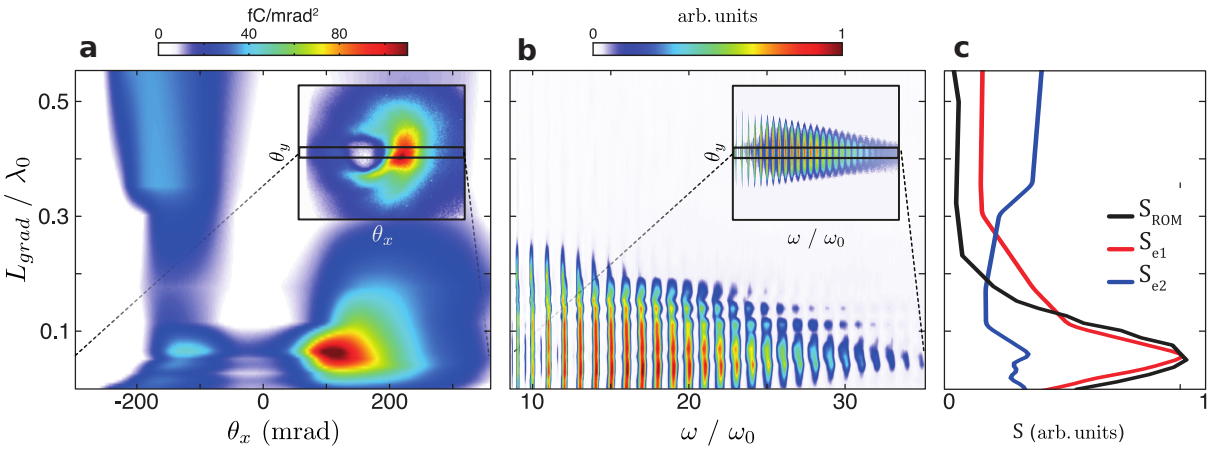

Figure 5.5: **Evolution of the experimental measurements with the density gradient scale length** - The angular profile of the relativistic electron beam (panel (a)), and the emitted harmonic spectrum (panel (b)) in the plane of incidence ($\theta_y = 0$) are plotted as a function of L_g, for a p-polarized laser field. Panel (c) shows different curves derived from these datasets: the harmonic signal integrated from the 20th to the 25th order (signal S_{ROM}), and the electron signals on the right (50 mrad $\leq \theta_x \leq$ 150 $mrad$, signal S_{e1}) and left sides (-250 mrad $\leq \theta_x \leq -150$ mrad, signal S_{e2}) of the specular direction, are plotted as a function of L_g.

These observations on the electron and harmonic beams clearly point to a complete change in the coupling mechanism between the laser field and the plasma, when L_g is increased. In the following, we will refer to these two interaction regimes as the short-gradient and long-gradient regimes for convenience.

5.2.2 Other experimental scans

Another important difference between these two interaction regimes is the dependence of electron signal on laser polarization, illustrated in Fig. 5.6. In the short gradient regime, the electron signal is totally suppressed when the polarization is switched from p to s. By contrast, for longer gradients, the electron signal is still observed for s-polarization, although it gets about five times weaker.

This transition is also visible for the plasma reflectivity: Fig. 5.7–a, b displays the spatial intensity profiles of the reflected laser beam in the two distinct coupling regimes. In the short gradient regime, a smooth beam is observed, which is almost unaltered compared to the incident laser beam: this is the so-called plasma mirror regime [Thaury, Quéré, et al., 2007], where the plasma acts as a high-quality mirror, specularly reflecting the incident light. By contrast, in the long gradient regime, the beam profile is strongly perturbed and starts exhibiting spatial structures that were not present on the incident beam. The term plasma mirror is thus no longer appropriate to this regime, although the laser field still interacts with a dense -and hence reflective-

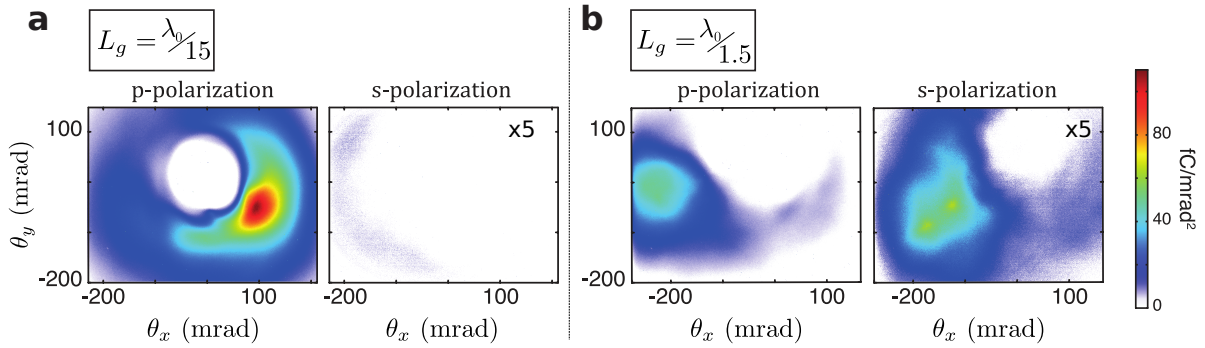

Figure 5.6: **Effect of the laser polarization on relativistic electron emission** - This figures shows the angular profiles of the relativistic electron emission in the two gradient regimes for p and s polarizations of the incident laser. In s-polarization, the signal amplitude is increased by a factor 5.

plasma. Experimentally, the spatial profile of the reflected laser beam might also be used as alternative signature of the transition in the laser-plasma interaction. By spatially integrating these images, the variation of the plasma reflectivity at the fundamental laser frequency as a function of L_g can be determined, and is displayed in Fig. 5.7–c, for both p and s-polarizations of the incident laser field.

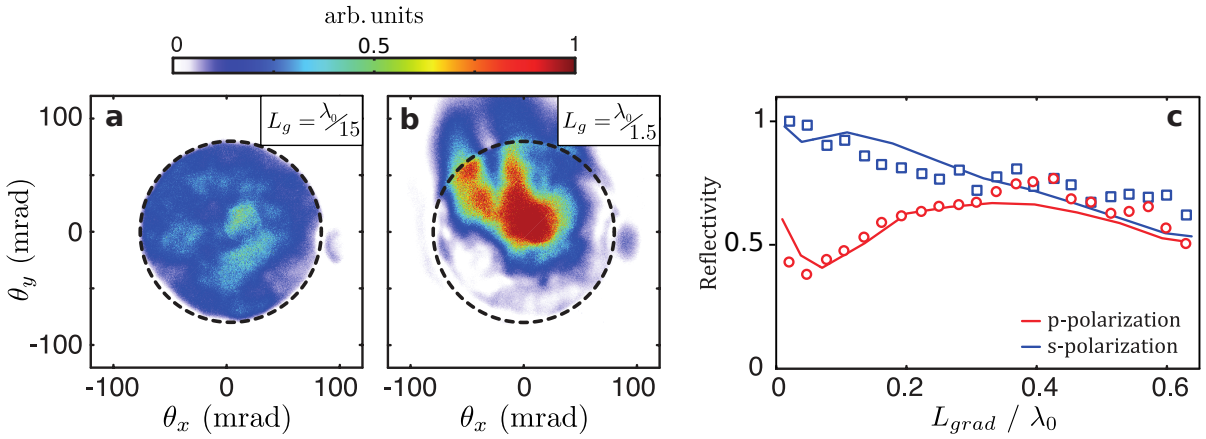

Figure 5.7: **Reflected fundamental beam and evolution of the plasma reflectivity** - The spatial intensity profile of the reflected laser beam are measured in the short (panel (a), $L_g \sim \lambda/15$) and long (panel (b), $L_g \sim \lambda/1.5$) density gradient regimes, for p-polarization of the incident laser. The black dashed circles indicate the initial divergence of the top-hat laser beam, before its interaction with the target. The evolution of the plasma reflectivity for the fundamental laser frequency is plotted in panel (c) as a function of L_g for both s and p polarizations (squares and circles). The lines show the corresponding results of 2D PIC simulations.

5.3 Numerical Observations of the Two Mechanisms

5.3.1 3D-Particle-In-Cell simulations in the experimental regimes

To understand these experimental observations, we use PIC simulations in the setup defined in Sec. 3.3.3 (page 52). First, we have to verify that these simulations are well performed in the actual physical conditions of the experiment and if they are reliable to properly reproduce

the key experimental findings. To check these two critical points, full 3D simulations of the interaction are carried out, so that we can directly confront the numerical and experimental results quantitatively, especially the full angular pattern of the electron emission, which is only accessible by 3D simulations.

The 3D simulations reported here require 6.3 millions computing hours each on the MIRA[1] cluster at ALCF and are performed in the same conditions as the experiments. All numerical and physical parameters remain the sames but the density gradient scale length that varies from $\lambda_0/15$ (`3D_short_gradient`) to $\lambda_0/1.5$ (`3D_long_gradient`) as precised in Tab. 5.1.

Simulation	solver	Δx, Δy, Δz	$c\Delta t$	a_0	w	L_g	θ_i	polar
`3D_short_gradient`	PSATD	$\lambda_0/70$	Δx	3	$5\lambda_0$	$\lambda_0/\mathbf{15}$	55°	p
`3D_long_gradient`	-	-	-	-	-	$\lambda_0/\mathbf{1.5}$	-	-

Table 5.1: **Numerical and physical parameters for the 3D simulations** - The physical parameters are chosen as close as possible to the experiments and were performed on the supercomputer MIRA. The only difference between the two cases is the density gradient scale length.

From these simulations, we extract the exact same observables as those measured in the experiments: the angular profiles and angle-energy distributions of the emitted electron beam, as well as the angularly-resolved harmonic spectra, displayed in Fig. 5.8. The harmonic spectra are recorded on a streaking line defined at a distance $d_s = 21\lambda_0$ from target (see Fig. 3.7, page 53).

For the emitted electrons, the measure of the numerical angular distribution is particularly tedious as they keep interacting in the laser pulse in vacuum over large distances (the experimental screen is placed in near field at ~ 10 cm from target). It is far too time consuming to perform the vacuum propagation with a PIC code, especially in 3D. Instead, as presented earlier in the manuscript (see Sec. 1.3.2), the problem is treated with a PT code. The use of such a code is valid since collective effects are negligible for relativistic electrons in vacuum. As a reminder, the interaction is solved in three steps: (i) the emitted electron profile is first recorded in PIC simulations close to the target, (ii) it is injected in the reflected field at the right phase and with the right properties in the PT code and (iii) we let it evolve in vacuum over distances of the order of the Rayleigh length. It ensures that most of electrons have escaped the laser volume at the end of the PT simulation.

Comparison with the Fig. 5.4 (page 77) shows that these simulations very well reproduce the two distinct interaction regimes found experimentally for all these observables. The only difference lies on the profile of the harmonic spectrum for `3D_short_gradient` which does not seem perfectly resolved. For these physical parameters, the spatio-temporal resolution has to be at least twice higher on each axis [Blaclard et al., 2017] to reach convergence. The corresponding simulation has thus not been possible at the current state so far. Note that in contrast the electron trajectories are supposed to be converged at this resolution [Vincenti and Vay, 2018].

These 3D benchmark simulations demonstrate both the reliability of PIC simulations, as well

[1] https://www.alcf.anl.gov/alcf-resources/mira

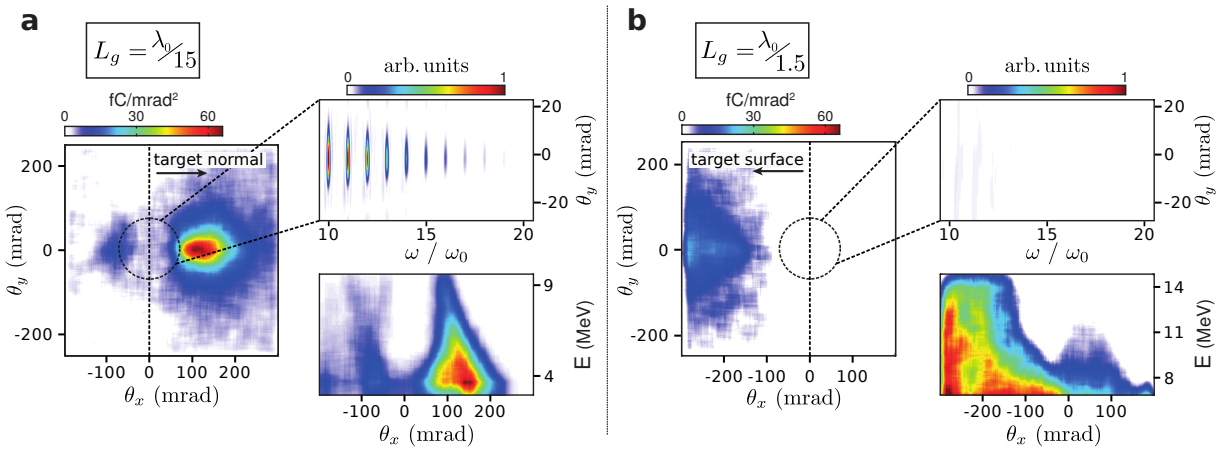

Figure 5.8: **3D PIC simulations of the laser-plasma interaction for two different density gradient scale lengths** - The physical conditions of these simulations are matched to the estimated experimental conditions of the shots shown in the Fig. 5.4 (page 77): panel (a) corresponds to a density gradient $L_g = \lambda_0/15$ (`3D_short_gradient`) and panel (b) to $L_g = \lambda_0/1.5$ (`3D_long_gradient`), while all other physical parameters remain the same. From these simulations, we extract the same observables as those measured in the experiment: the angular profile of the high-energy electron beam expelled in vacuum (left image in each panel), the (θ_x, E) distribution of these electrons (bottom right image in each panel), and the angularly-resolved harmonic spectrum (top right image in each panel).

as the excellent control of the interaction conditions in the experiments performed on UHI100. However, 3D simulations are rather hard to tract and we will prefer to rely on 2D simulations to get deep insights on the physical processes underlying these two distinct regimes.

5.3.2 Spatio-temporal properties of the electron emission

Now, that we ensured that simulations and experiments were performed in the same range of parameters, we dig deeper in the simulations. We are looking for clear spatio-temporal signatures of coupling mechanisms between light and plasma (see Sec. 1.2, page 14) that could be responsible for experimental observables. To do so, we run four 2D PIC simulations for different $L_g = \lambda_0/15$ and $\lambda_0/1.5$ and different laser polarizations. The other physical and numerical parameters remain the same and are presented in Tab. 5.2. The temporal dynamics of the plasma surface during interaction are first investigated. In a second time, we will discuss on spatial properties of the emitted electron beam.

Temporal dynamics of the plasma surface. The clear correlation observed between the high-energy electron and the harmonic signals for short gradients and a *p*-polarized wave (see Fig. 5.5–c, page 78) suggests that in this regime, the relativistic electrons are involved in the harmonic emission. Then, generating a highly-contrasted harmonic comb would be an indication that this electron emission is periodic in time, being locked to the driving laser field.

To support this idea, we consider the 2D PIC simulation `2D_short_gradient_p` performed with a short density gradient $L_g = \lambda/15$. In this simulation, the surface dynamics, displayed in Fig. 5.9–a, present a temporal periodicity, characteristic of the Brunel mechanism. Electron emission occurs in the form of bunches that are initially extremely short (in the attosecond range), emitted once every optical period. For $a_0 > 1$, these electrons reach relativistic velocities when they escape the plasma, and thus induce a periodic Doppler effect on the reflected laser field: this

Simulation	solver	Δx, Δz	$c\Delta t$	a_0	w	L_g	θ_i	polar
`2D_short_gradient_p`	PSATD	$\lambda_0/350$	Δx	3	$5\lambda_0$	$\lambda_0/\mathbf{15}$	55°	***p***
`2D_long_gradient_p`	-	-	-	-	-	$\lambda_0/\mathbf{1.5}$	-	***p***
`2D_short_gradient_s`	-	-	-	-	-	$\lambda_0/\mathbf{15}$	-	***s***
`2D_long_gradient_s`	-	-	-	-	-	$\lambda_0/\mathbf{1.5}$	-	***s***

Table 5.2: **Numerical and physical parameters for the 2D simulations** - The physical parameters are chosen as close as possible to the experiments. For these four simulations, we chose 2 gradient scale lengths, $\lambda_0/15$ and $\lambda_0/1.5$, and 2 laser polarizations, p and s.

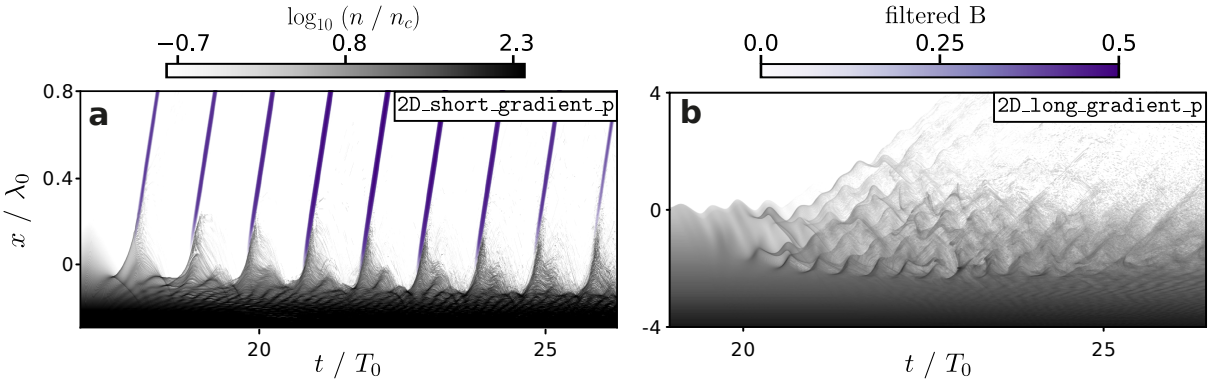

Figure 5.9: **Plasma surface evolution in the two distinct regimes for a *p*-polarized laser** - These data are obtained from 2D PIC simulations with different density gradients L_g – (a): `2D_short_gradient_p` and (b): `2D_long_gradient_p` (see Tab. 5.2). The temporal evolution of the plasma electron density (gray-scale color map, in log scale) is spatially-resolved along the normal to the target surface (see surface probe diagnostics, Sec. 3.3.3, page 52). The emitted attosecond pulses are superimposed to this density map in purple. They are clearly visible in panel (a), but are too weak to be observed in panel (b).

results in the generation of a comb of high-order harmonics of the laser frequency associated to a train of attosecond light pulses, spaced by one laser period, clearly observed in Fig. 5.9–a. This well-identified mechanism is the Relativistic Oscillating Mirror (ROM) mechanism, presented in Sec. 1.3.1. This is the origin of the harmonic signal observed in the experiments on UHI100. As emitted electrons are also responsible for the harmonic generation, this explains the clear experimental correlations observed between harmonic and electron signals at the short gradient regime.

As described earlier in this chapter, the harmonic signal is observed to collapse for longer density gradients L_g. One possible interpretation can be that the electron emission ceases to be periodic in time. And indeed, PIC simulations for longer density gradients (such `2D_long_gradient_p` shown in Fig. 5.9–b) strikingly show that, in contrast to the Brunel mechanism, electron emission is no longer periodic in this regime. The absence of harmonic signal in conjunction with the relativistic electron emission can thus be considered as a signature of the transition to another coupling mechanism, associated to a very different plasma temporal dynamics observed Fig. 5.9. This mechanism will be fully studied and is commonly known as *stochastic heating*.

Switching the laser polarization to s (see Fig. 5.10) kills also the harmonic generation but this time for both short and long density gradient regimes. It is expected that the Brunel mechanism is no longer at play for s-polarization: the electric field component normal to the target that drives Brunel electrons is being suppressed. Instead, the surface dynamics are driven by the magnetic component of the Lorentz force, which becomes non-negligible for $a_0 > 1$. Because this force is the product of two quantities oscillating at the laser frequency ω_0 – $\boldsymbol{p}$ and $\boldsymbol{B}$ –, the plasma surface oscillates twice faster, perfectly shown in Fig. 5.10–a. We have already seen (see Sec. 1.2.2) that this mechanism is an extension of Brunel mechanism at high intensity when the normal component of the magnetic force supersedes the electric force (e.g., p-polarized laser at normal incidence or s-polarization) and is commonly called $\boldsymbol{J} \times \boldsymbol{B}$ heating [Kruer and Estabrook, 1985]. For the intensities achieved in experiments, the corresponding electron quivering is however too weak to generate any train of attosecond light pulses and no harmonic signal was observed either in experiments or in simulations.

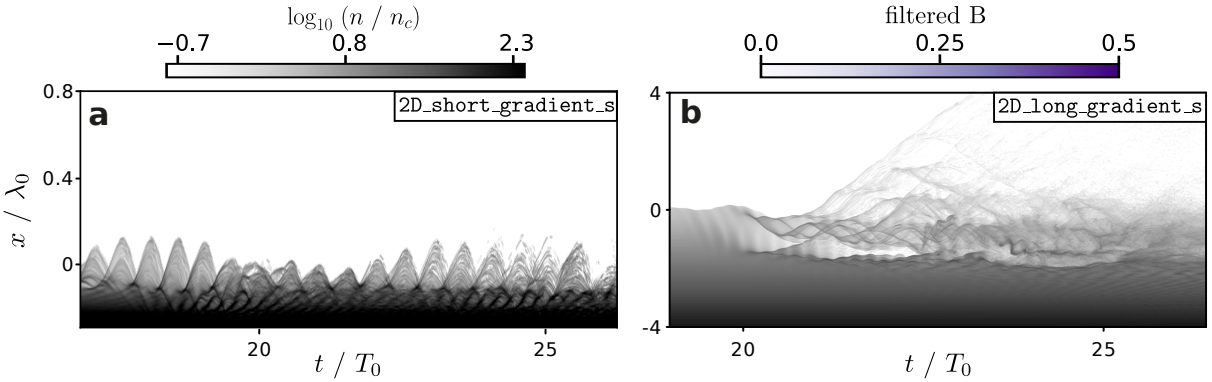

Figure 5.10: **Plasma surface evolution in the two distinct regimes for a s-polarized laser** - This figure is similar to the Fig. 5.9 but the laser polarization is switched from p to s: (a) `2D_short_gradient_s`, and (b) `2D_long_gradient_s` (see Tab. 5.2). In this configuration, the emitted attosecond pulses are too weak to be observed with the same color scale as in Fig. 5.9.

For longer L_g, the ejection mechanism seems very similar to the one observed for a p-polarized laser (see Fig. 5.9–b versus Fig. 5.10–b). It supports the previous experimental observations, reported in Fig. 5.6–b, where the electron angular profiles looked very much alike when $L_g = \lambda_0/1.5$. In fact, this new mechanism is found to be weakly dependent on laser polarization (details can be found in Sec. 8.5).

In addition, it discards the resonant absorption at this point: initially it was a good candidate at play in the long gradient regime, but is supposedly suppressed in case of s-polarization. We would thus expect a completely different behaviour after switching the laser polarization. In Sec. 7.3.1 (page 112), we show that the resonant absorption indeed appears for long gradient plasmas but at much lower intensities (when $a_0 \ll 1$).

Spatial structure of the electron emission. We now discuss the spatial properties of the outgoing electron beams after reflection, illustrated in Fig. 5.11 for the two p-polarized cases. In the short gradient regime, this structure is mostly determined by the interaction of expelled electrons with the reflected laser field in vacuum, while in the long gradient regime, it is rather imposed by their lifetime within the interference field.

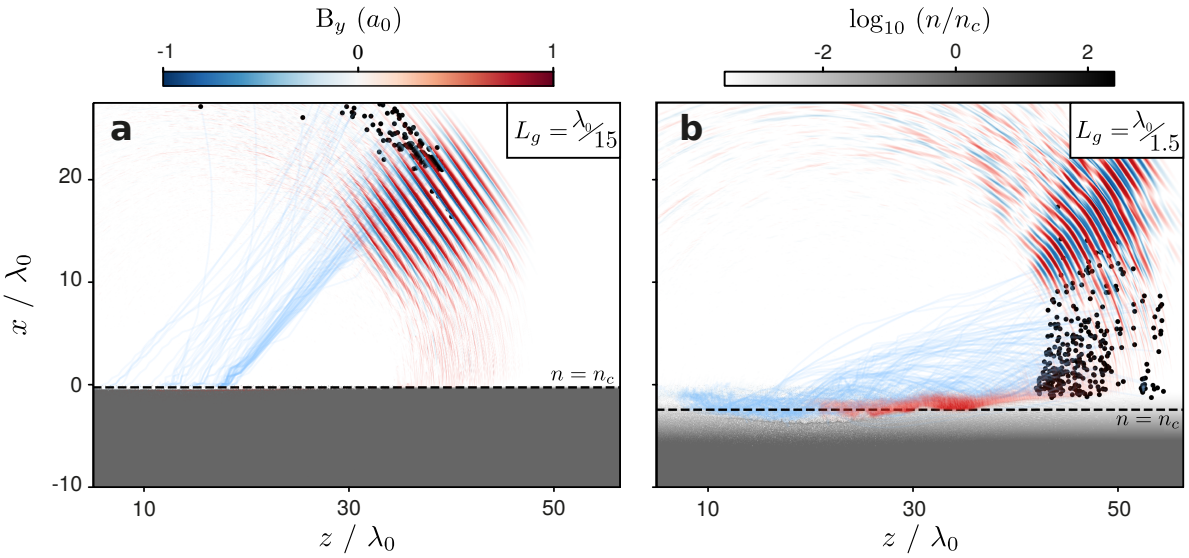

Figure 5.11: **2D PIC simulations in the two gradient regimes after reflection** - These two snapshots show the electron ejection after interaction for the two different density gradients L_g – (a): `2D_short_gradient_p` and (b): `2D_long_gradient_p` (see Tab. 5.2). The complete trajectories of a selected set of expelled high-energy test electrons are displayed in blue lines, as well as the y-component of the magnetic field (blue to red color map) at a given time after the laser-plasma interaction. The plasma density profile is indicated in a gray log scale.

In the case of short density gradients, the peculiar angular structure of the electron beam has recently been analyzed experimentally and theoretically in [Thévenet, Leblanc, et al., 2016] for simple regimes, where the harmonic content inside the reflected field was neglected. In the Brunel regime, electrons are expelled from the plasma as a very laminar beam, with relativistic velocities initially quasi-parallel to the direction of specular reflection (Fig. 5.11–a). These relativistic electrons thus co-propagate with the intense reflected laser field, with which they interact in vacuum over a distance of the order of the Rayleigh length. This interaction always results in the ejection of electrons out of the laser beam by ponderomotive scattering, and therefore forms a hole in the electron beam, centered on the specular direction, as observed in experiments Fig. 5.4–a (page 77) or 5.6–a (page 79).

Recalling the introductory section on Vacuum Laser Acceleration (VLA) (Sec. 1.3.2), there are two typical scenarios for this ejection, depending on the electron exact initial conditions, as they are expelled from the plasma into vacuum. Some electrons explore multiple optical cycles of the laser pulse, and thus oscillate in the field. Then, they get expelled from the laser focal volume by the so-called ponderomotive effect, isotropically and with a limited energy gain [Malka et al., 1997; Quesnel and Mora, 1998]. They form the ring-shaped halo observed on the electron beam. However, a large fraction of electrons actually remains around a given phase of the reflected field and rather 'surf' a single wavefront. They thus escape the laser beam laterally along the laser polarization direction, and form the bright peak observed next to the specular direction. The side on which this peak forms is determined by the laser phase at which electrons are expelled from the plasma into vacuum: the observation of a peak on one side only of the 'ponderomotive hole' (between the specular direction and the target normal) is an indication that electrons are ejected periodically *once* every laser period, when the laser field drags them out of the plasma, in the form of a sub-optical cycle bunches.

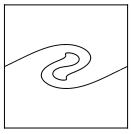

This second set of electrons experiences a quasi-constant E-field from the laser in vacuum until they escape the focal volume, leading to a greater energy gain than in ponderomotive scattering: this VLA process accounts for the observed asymmetry of the (θ_x, E) distribution (see Fig. 5.4–b), where higher energies are observed on one side of the hole (mostly VLA electrons) than on the other (ponderomotive electrons), as well as for the angle-energy correlations on this distribution [Thévenet, Vincenti, et al., 2016]. An important consequence is that the Doppler upshift factor induced by outgoing electrons on the reflected field, which leads to the generation of high-order harmonic (ROM mechanism), cannot be directly deduced from the electron spectra measured experimentally. Indeed, electrons keep gaining energy after they escaped the target and emitted high-order harmonics before being detected. For instance, simulations show that in experiments, the electron Lorentz factor typically varies from $\gamma \sim$ 2-3, as they are ejected from the plasma, to $\gamma \geq 15$ after interaction with the reflected laser field [Thévenet, Leblanc, et al., 2016], when they are detected.

The spatial properties of the electron beam observed in the long-gradient regime described here have not been elucidated in detail before [Chopineau et al., 2019]. The electron trajectories displayed in Fig. 5.11–b show that the conditions of electron ejection from the plasma are already very different in the short and long gradient regimes. In the second case, the expelled electron beam is no longer laminar, and rather has a complex velocity distribution. As shown in the next chapter, this feature can be attributed to the chaotic character of the electron heating mechanism leading to ejection from the plasma.

Furthermore, these 2D PIC simulations show a spatial degradation of the reflected laser beam wavefronts in the long gradient regime right after interaction (Fig. 5.11–b), while the beam wavefront is preserved in the short gradient regime (Fig. 5.11–a). This is qualitatively consistent with experimental observations (Fig. 5.7–a, b), where the laser beam intensity profile far from the target is observed to become degraded for long gradients. Along the non-linear propagation near the plasma critical density, a laser beam is partially depleted, and thus provides a possible interpretation for the degradation of the reflected laser wavefronts (see Sec. 7.3.2, page 114).

Conclusion

The combination of experiments and PIC simulations has provided strong evidence for a transition from Brunel absorption to another mechanism occurring when the density gradient scale length L_g is increased. This regime is no more periodic in time but rather chaotic as it involves complex trajectories within the interference field. In addition, it seems to persist after switching the laser polarization, in contrast to Brunel or resonant absorptions.

In the next chapters, we will endeavor to describe this new mechanism in details through both simulations (see Ch. 7, page 99) and theory (see Ch. 8, 119). However, before that, we want to bring some new insights regarding Vacuum Laser Acceleration that aims to complete and clarify the existing studies.

Part IV

Theoretical Analysis of Coupling Mechanisms in High-Power Laser-Plasma Mirror Interaction

6 Acceleration of Particles in Vacuum in the Short Gradient Regime

In the short gradient regime, electrons are emitted from the target in the form of attosecond bunches and then travel in the laser reflected wave. During their joined propagation with the laser beam, a fraction of electrons can gain energy by a Vacuum Laser Acceleration (VLA) over a distance of the order of the Rayleigh length. The remaining electrons get expelled radially from the laser focal volume by ponderomotive effect and form a isotropic distribution shaped as a ring.
Despite that [Thévenet, Leblanc, et al., 2016] characterized the principal features of VLA, some important points still have to be clarified. In particular, just after the emission, the electrons are crossing a standing wave resulting from the superposition of incident and reflected field and located in vacuum on top of the target. The dynamics inside this wave might not be simple and should be investigated.
Another important point is the influence of the laser wavefront on the electron distribution. [Thévenet, Leblanc, et al., 2016] decided to model the reflected field with a monochromatic Gaussian beam, whereas it actually shows a high harmonic content. We thus propose to complete their initial work and study how the electron distributions evolve in more complex laser configurations.

Contents

6.1 Electron Filtering on Top of a Solid Target

We start this chapter by analyzing the electron evolution in the interference field on top of solid targets. This happens in step (2) in Fig. 6.1 just after the ejection from the surface but before vacuum laser acceleration in the reflected field. Based on (1D-)models dealing with high harmonic generation on plasma mirrors such as [Thévenet, Vincenti, et al., 2016] and according to the Brunel mechanism, electron ejection is synchronized with the harmonic emission. Then, one would expect electrons to follow nearly ballistic motion from the emission time and be injected directly in the laser at the right phase. Hence, no one in literature has never questioned if it stays that simple at higher dimensions.

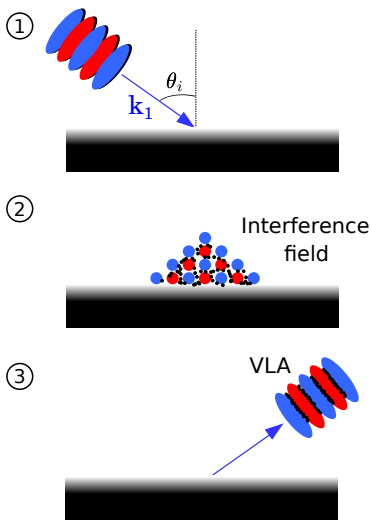

Figure 6.1: **Drawing of the electron emission.**

However in practice in 2D or 3D spaces, emitted particles first travel through an interference field, combination of both incident and reflected laser pulses. Their motion in this field is far from being simple but surprisingly tends to end up regular. It actually results in a better injection inside the wave. As we will see, all trajectories, initially not suitable for VLA, are either corrected or completely deflected.

PIC simulations. In Fig. 6.2, we display simulation results, performed with a PIC code at first. Multiple electrons are observed to be expelled and injected in the interference field. At $t = 30\,T_0$, they are not particularly locked at a specific laser phase (see Fig. 6.2–a).

Thanks to plane detectors, such as presented in Sec. 3.3.3 (page 52), we manage to record all emitted electrons along time at given x positions. The ensuing distribution are reported on Figs. 6.2–b, c for $x = 0.5$ and $4.5\,\lambda_0$. At close distance from the surface (Fig. 6.2–b), electrons located in front of the laser pulse are arranged into planes ($t < 35\,T_0$ or $z < 12\,\lambda_0$). However, the distribution quickly becomes blurry as electrons are emitted later on. Especially, those traveling in the tail of the pulse ($t > 40\,T_0$ or $z > 15\,\lambda_0$) are no more disposed in a regular manner.

By contrast, when the detector is placed after the interaction with the interference field, the recorded distribution is far less noisy and the different layers are clearly visible all along the pulse (see Fig. 6.2–b). Two consecutive layers are separated by a laser wavelength. It is fully consistent with the distribution found from 1D -simulation by [Thévenet, 2016].

Note also that a significant fraction of the charge is lost between the two planes. For this simulation, we find[1] 675 pC for the distribution of Fig. 6.2–c but only 155 pC for the one of Fig. 6.2–b. The interference field seems to act as a filter, which eliminates most of electrons and shapes the remaining ensemble making it suitable for a proper injection in the reflected laser field and for subsequent VLA.

[1]Since the simulation is performed in a 2D space, the 3D charge is obtained by multiplying the 2D charge by a factor equal to the laser waist, $w_0 = 5\,\lambda_0$.

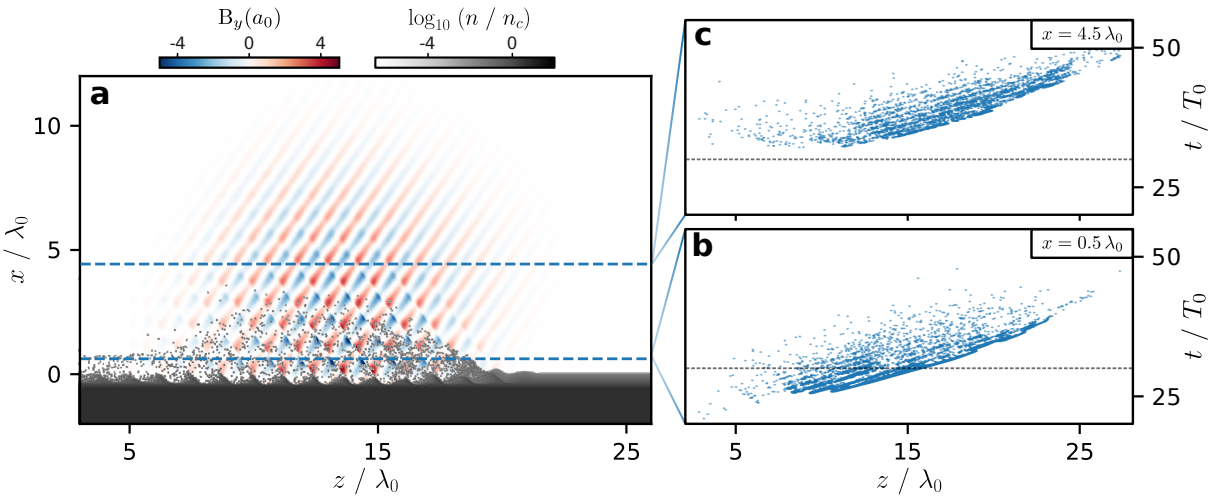

Figure 6.2: **Particle injection in an interference field in PIC simulations** - Panel (a) shows a typical PIC simulation of laser plasma-mirror interaction, where a laser pulse (blue to red color scale) is reflected by a plasma surface pictured in grey scale. Here, $\Delta x = c\Delta t = \lambda_0/100$. The snapshot is taken at $t = 30\,T_0$. During the interaction, ejected electrons are expelled towards vacuum and evolve in an interference field. These electrons are recorded along time on various planes located at different x-positions: (b) $x = 4.5\,\lambda_0$ and (c) $x = 0.5\,\lambda_0$.

PT simulations. Now, we will try to understand what happens in the interference field through PT simulations. As particles evolve directly in the electromagnetic field in vacuum, the dynamics can be efficiently captured with a PT code. It is then easier to track particles one by one and to follow their motion all along.

The main pitfall here relies on the design of the simulation since there is no plasma and thus no laser reflection. Instead, as presented in the drawing located on the top-right corner of Fig. 6.3–a, two laser pulses will cross each other in the electron cloud, ultimately leading to an interference field. Throughout the manuscript. we will keep using two laser waves to emulate a plasma reflection in PT simulations. In addition, to model the introduction in this field, all particle initial momenta are positive, i.e., p_x, $p_z > 0$. There is no preferred phase of injection: particles are continuously introduced in the interference field, without considering Brunel mechanism.

We perform such a simulation and report the electron distribution as well as the laser field on Fig. 6.3–a. Although their initial injection was uniform, it is striking how electrons are reordered into planes and that each plane is separated from one another by one laser wavelength. The interference field really rearranges particles, even in PT simulations.

Inside the interference field, the electrons are considerably shaken and their motion is far from ballistic. In Fig. 6.3–a, we highlight in blue a typical electron trajectory and it shows rotations and cusps. This can be explained *via* the magnetic field, which changes the direction of the particle near high-intensity regions.

In order to illustrate this statement, we superimpose, in Fig. 6.3–b, a quiver plot of the electron displacement on the magnetic map extracted from Fig. 6.3–a, for $5 < z\,/\,\lambda_0 < 9$. Each particle is pictured as a black arrow, which points towards its direction of propagation. It is clear that some paths are favored over others and that particles alternatively turn in different directions

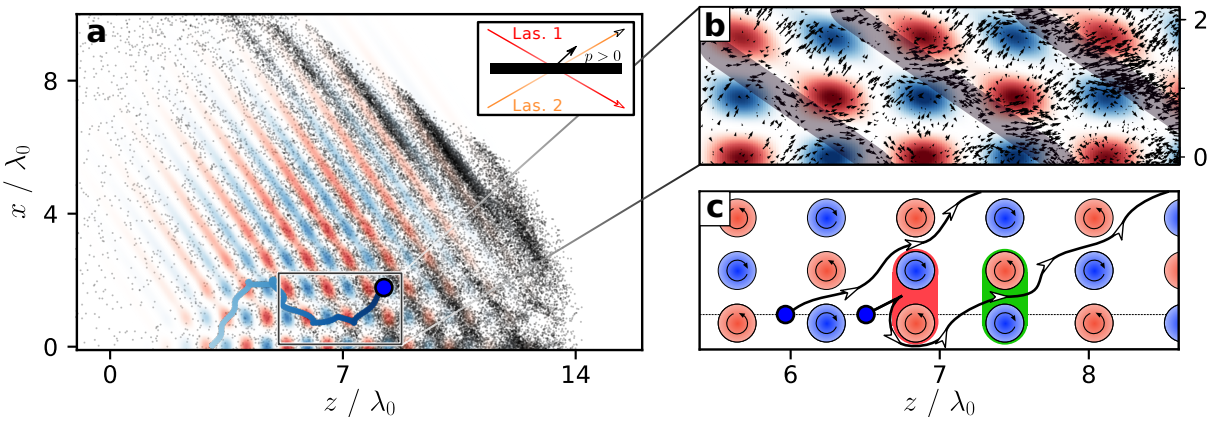

Figure 6.3: **Particle injection in an interference field in PT simulations** - Panel (a) illustrates the same simulation as in Fig. 6.2 but with the PT code. The reflection is modeled with two laser pulses and all particles show $p_x,\ p_z > 0$ (see inset in the top-right corner). A typical trajectory in these fields is highlighted in blue. In panel (b), we superimpose the magnetic field map extracted from panel (a), with a quiver plot of the electron displacement. In panel (c), the same map is sketched and we indicate the direction of rotation (curved black arrows) of electrons in such magnetic field. We let then evolve two particles within these fields. A forbidden *gate* (see text) is pictured in red, while a permitted gate is rendered in green.

depending on the sign of the nearest magnetic field node: in the anticlockwise direction near positive-magnitude regions and in the clockwise direction near negative-magnitude regions.

Studying the different trajectories is easier with the drawing of Fig. 6.3–c. It reproduces the magnetic map of Fig. 6.3–b, but we keep only information related to the direction of rotation around magnetic nodes. There, let us follow the trajectories of two particles injected at two consecutive field zeros (separated by a distance of $\lambda/2$). One has to remind though that in PIC simulations, only one of these electrons should exist as the injection is governed by the Brunel mechanism, which occurs only once per laser period.

Just by considering the sign of rotation near the different nodes, the left particle is allowed to travel upstream, while the right particle is forced to go back first. For further considerations, we name *gate* a group of two consecutive vertical magnetic nodes. In Fig. 6.3–c, two gates are displayed:

- a green gate, which is composed of a positive node on the top and a negative node on the bottom. A particle approaching this gate is allowed to cross it, because both nodes attract the particle towards its center.
- A red gate, which is composed of a negative node on the top and a positive node on the bottom. It is forbidden for a particle approaching this gate to cross it, because the nodes tend to push the particle out of its center.

The electron in the right cannot cross the red forbidden gate but still shows a positive p_z, so it drifts along z until it can travel through a permitted gate. After it crosses it, its motion becomes similar to the one of the left particle. This process is repeated for all particles and it explains why the motion seems to be regularized. Each trajectory is rather complex by itself but in average all particles are following similar paths, through the same gates.

In Fig. 6.3–b, we confirm that our two trajectories are consistent with the vector map and that particles are likely to be found within a green gate or near a border of a red gate. Then, the structure of oblique planes at every wavelength appears by itself (see the black oblique planes which encompass most of electrons in Fig. 6.3–b). It persists even after the interaction.

Thanks to the PT code, we are able to clarify the electron arrangement as planes observed in PIC simulations. The particles do not necessarily have to be periodically ejected to end up in layers separated by a laser wavelength. The evolution in the magnetic interference field alone is sufficient to explain the resulting distribution.

6.2 Vacuum Laser Acceleration

Now that we clarified the electron dynamics before injection in the laser pulse, we propose to tackle the logical follow-up: the Vacuum Laser Acceleration (VLA). The theory behind VLA was presented earlier in this manuscript (see Sec. 1.3.2, page 25) and will not be derived again. Instead, we continue the work started in [Thévenet, 2016] in two more complex cases: (i) in a pulse showing a harmonic content and (ii) when the laser reflection occurs out of focus. To do so we again combine PIC and PT simulations to efficiently retrieve the angular distributions of ejected electrons measured in experiments.

6.2.1 Influence of the harmonic content

In his thesis manuscript, [Thévenet, 2016, p. 137] extracted the electron conditions of injection (positions in the wave and momenta) from PIC simulations and inserted them into a PT code. From 1D-PIC simulations, he found the initial conditions reported in Figs. 6.4–a, b. In particular, the electrons are disposed in narrow planes near field nodes at every laser period.

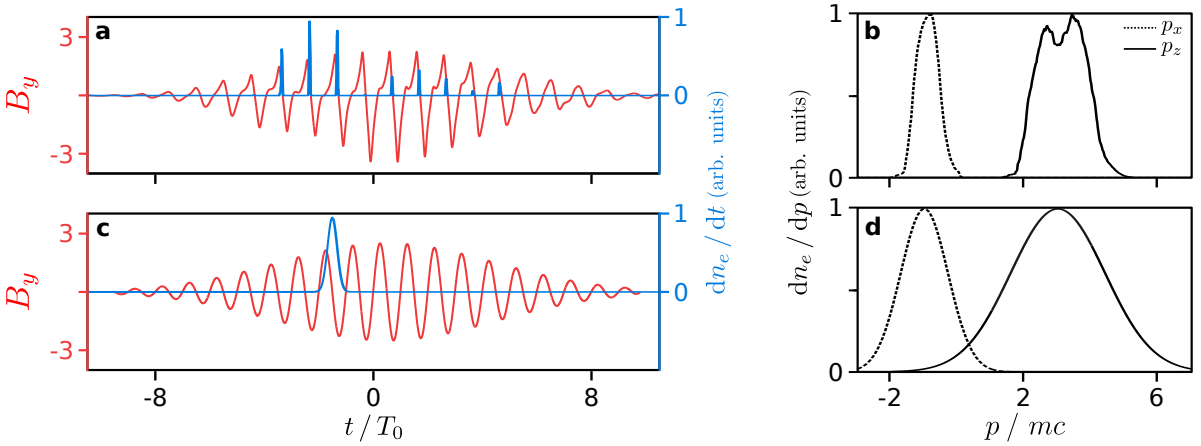

Figure 6.4: **Initial conditions of electrons ejected from plasma mirrors according to M. Thevenet** - [Image from [Thévenet, 2016, p. 137]] Panel (a) illustrates the waveform of the laser magnetic field B_y reflected by the plasma mirror (red line) and the temporal density profile of the ejected electron bunches (blue line), obtained from PIC simulations. Panel (b) shows the corresponding momentum distribution of these electrons, along the specular direction (p_z) and along the polarization direction of the reflected laser (p_x) taken from a 1D-PIC simulation. On panels (c) and (d) are reported the initial conditions as injected in Thevenet's PT code.

In order to find the same angular distributions as in experiments, the quantities injected in its PT code has however been considerably smoothed. These are reported in Figs. 6.4–c, d. In particular, he considered only one electron bunch in the reflected field (corresponding to ejection in a single laser period) and increased the width of position and momentum distributions. He also neglected the harmonic content of the reflected pulse and modeled it as a monochromatic Gaussian wave. We now try to go further and study the effect of the harmonics on the angular distribution of electrons.

Reflected field reconstruction The starting point of our analysis is to correctly model a pulse with a harmonic content. As the reflected field is rather complex, we assume that it is a perfect superposition of Gaussian waves (see Eq. (4.6), page 68), each wave oscillating at a frequency multiple of ω_0. Assuming that the different temporal and spatial envelopes are all equivalent, we are looking for the amplitude and the spectral phase of each individual harmonic.

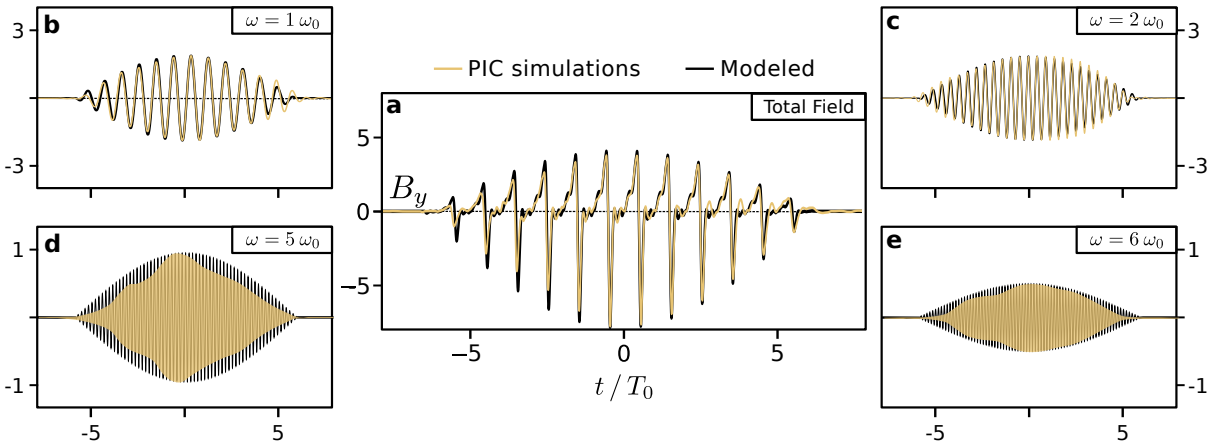

Figure 6.5: **Reflected field reconstruction in PT simulations** - In panel (a), we report in yellow the total field after reflection by a plasma mirror, extracted from a 3D-PIC simulation. This field shows a high harmonic content. Each frequency is filtered in the spectral domain and plotted in the temporal domain, e.g., on panels (b) to (e) (see labels for the orders). Note the different amplitude scales used in the different panels. For PT simulations, we regularize each different frequency by fitting the envelopes by a cosine shape (black curves). After summation up to the 10th harmonic, it gives the total field injected in the PT code (in black on panel (a)).

In the literature, theoreticians have proposed along time multiple models for the harmonic efficiency decay law. Let m be the harmonic order, [Baeva et al., 2006] first found a "universal" $m^{-8/3}$ law. However, it was then disputed by [Boyd and Ondarza-Rovira, 2008] in which the authors observed a weaker decline — between $m^{-7/3}$ and $m^{-5/3}$. Recently, [Vincenti, 2018] considered a m^{-2} law in the PetaWatt regime.

As there does not seem to exist an universal law, the proper harmonic amplitudes are directly extracted from a 3D-PIC simulation. This particular run costed 500k CPU hours on Mira, the spatial grid resolution was $\Delta x = c\Delta t = \lambda_0/50$ and the configuration was the one presented in Sec. 3.3.3. The reflective field is recorded on an oblique plane detector far from target (see $\mathcal{P}_2$ in Fig. 3.7–a, page 53) and its profile is reported in Fig. 6.5–a as an orange line. The waveform is distorted implying the presence of a high harmonic content. Note that this profile is also strongly dissymmetrical, this coming from the relative phase between harmonics, i.e., all frequencies are not perfectly in phase with the fundamental frequency.

As we do not have direct access to the analytical formula of the whole field, each harmonic is independently treated. We first select each frequency one by one in the spectral domain and deal with the corresponding filtered field in the time domain. In Figs. 3.7–b to e, four filtered frequencies are displayed in yellow (1st, 2nd, 5th and 6th orders). The temporal envelopes of the two first harmonics (Figs. 3.7–b, c) are close to the initial input (cosine shape) but as the harmonic order raises, they become distorted (Figs. 3.7–d, e).

Influence of the harmonic content on electron distributions. Now, let us use the modeled reflected field and see how it changes the final angular distribution in comparison to the ones obtained with a monochromatic wave. The result can be intuitively guessed by the form of the reflective wave and in particular how it varies close to the position of injection.

According to PIC simulation results (see Fig. 6.4–a, page 93), electron bunches are peaked near field nodes. Still, electrons from a same bunch can experience very different fields, as the waveform varies rapidly around zeros. For a monochromatic wave, its slope is much smoother (see Fig. 6.4–c) and the width of the electron density profile has to be increased to cover the same range of field magnitude. That is probably why [Thévenet, 2016] did broaden the temporal distributions in his simulations.

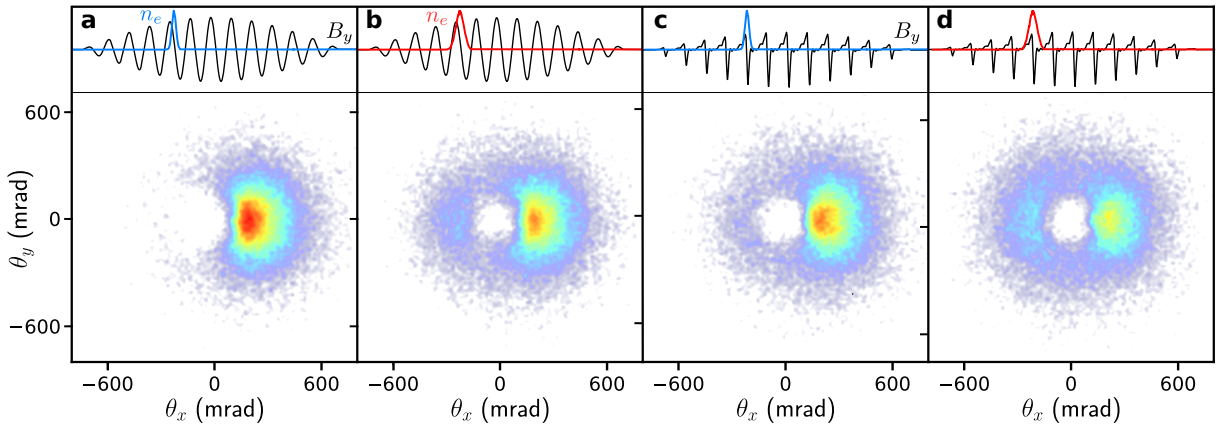

Figure 6.6: **Angular distributions of electrons with or without harmonic content** - All of these distributions are results of PT simulations performed in the similar way as in [Thévenet, 2016]. In our cases, a population of 50 000 electrons are recorded after the laser has traveled a distance equal to 3 z_r. Each panel corresponds to a different simulation performed with a narrow/broad initial temporal density profile of electrons (pictured in blue or red) and a different laser waveform (monochromatic or extracted from PIC simulations) as shown in top panels: (a) narrow/monochromatic, (b) broad/monochromatic, (c) narrow/PIC and (d) broad/PIC.

In order to confirm this hypothesis, we now run 4 different simulations with two different initial density profiles and two laser waveforms (extracted from PIC simulations and monochromatic). We report the final angular electron distributions for each case in Fig. 6.6. As a reminder, in experiments as in [Thévenet, Leblanc, et al., 2016], the final electron distribution presents two main characteristics: a hole devoid of particles in the center, which indicates that the electrons were expelled from the laser volume (similarly to Fig. 4.3), and a bright beam on one side of the hole along the polarization direction, constituted on fast electrons that surfed on a single half laser cycle.

For the two center panels (Figs. 6.6–b, c), the angular distributions are akin to the one observed experimentally. They precisely correspond to either the original Thevenet's simulation (Fig. 6.6–b) or to a simulation initialized with the field and electron profiles extracted from PIC simulations (Fig. 6.6–c).

When the initial density profile is narrow and the pulse monochromatic (Fig. 6.6–a), particles are subject to the same field amplitude, to a certain extent. In that case, most electrons undergo a similar motion in the laser pulse, which results in a brighter beam than observed in experiments. The hole is not clearly visible and very few particles show $\theta_x < 0$.

Oppositely, when the initial density profile is large but the pulse contains a harmonic content (Fig. 6.6–d), the electrons are distributed over radically different laser fields. They experience very different motions, which tend to standardize the final distribution. The electron beam is much weaker than in the last three cases and a second beam appears on the left part of the hole. It is constituted by particles that have surfed on the other half laser cycle.

When a reflected wave showing a high harmonic content is replaced by a monochromatic wave, the electromagnetic field near the position of injection varies less rapidly. In this condition, the initial density profile of electrons has to be enlarged to maintain the same initial field environment. That is why, despite using a laser without any harmonic content, [Thévenet, 2016] found quantitative results close to experiments.

6.2.2 Influence of laser focusing on electron distribution

Another interesting survey is the study of the impact of laser focusing on VLA, more precisely, how the angular distribution of electrons evolve when the laser focal spot is located behind or ahead the surface target. We decide to focus on three different conditions of electron injection. All of them are illustrated in Fig. 6.7: (i) when the laser focal spot is located at z_r before the target, (ii) when at focus and (iii) when at z_r behind the target. In all cases, the electron density profile is kept centered around a field zero and the laser is chosen as a monochromatic wave (and then the density profile is enlarged accordingly).

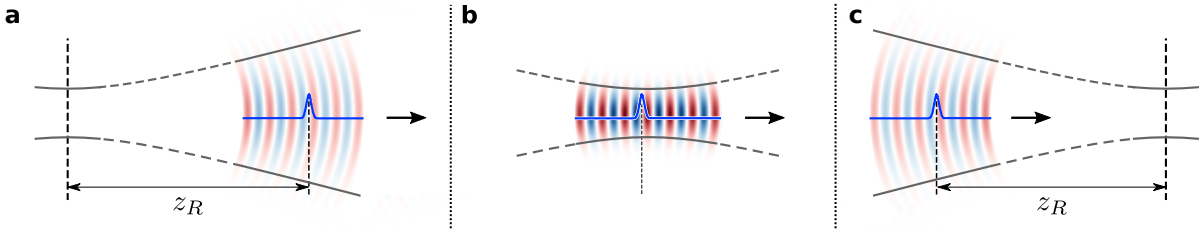

Figure 6.7: **Initial conditions of electron injection in a laser at focus and out of focus** - Each panel matches a case presented in the text: (a)→(i), (b)→(ii) and (c)→(iii). The initial electron density profile is pictured in blue and the laser from blue to red.

The influence of laser focusing on VLA was subject to an experimental campaign at CEA, not yet published in the literature. The experimental setup did not differ from the one presented earlier in this manuscript in Fig. 5.3 (page 76). Simply, one has to change the laser focal point

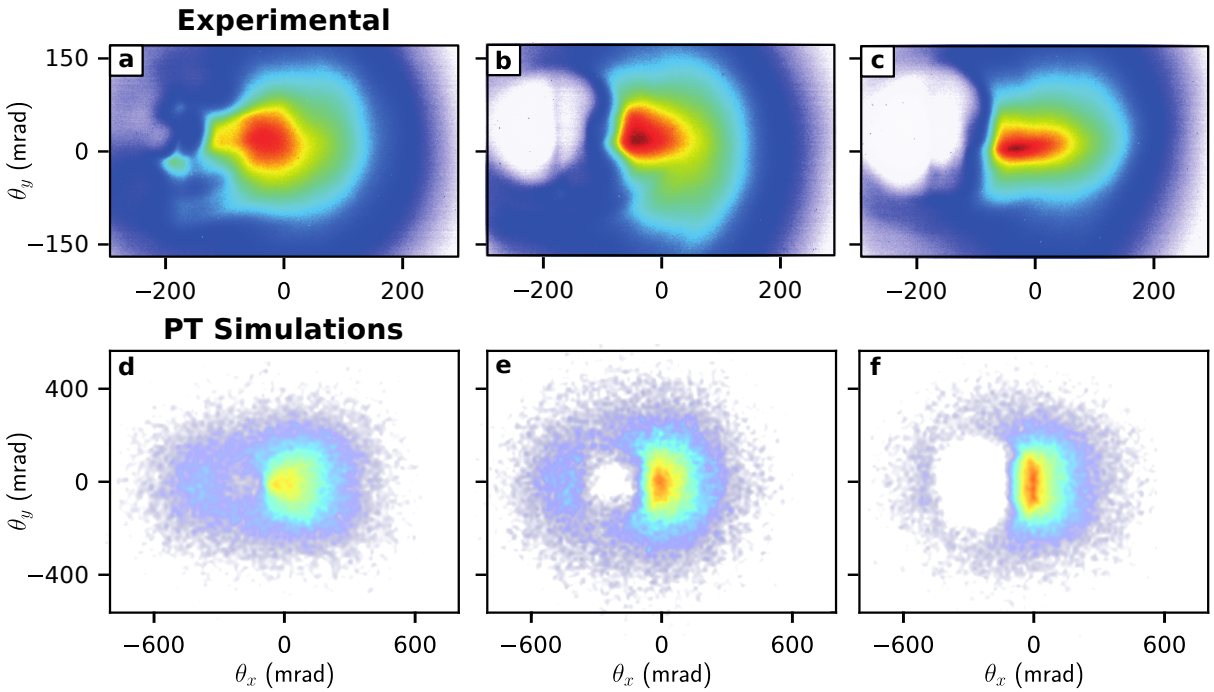

Figure 6.8: **Angular distributions of electrons at focus and out of focus** - Panels (a)-(c) picture experimental angular distributions of ejected electron. Each panel corresponds to a different shot, where the position of the focal point was displaced: (a): $+z_r$, (b): 0 and (c): $-z_r$. Panels (d)-(f) display the same observables but from PT simulations. Note that here, as the specular direction is not known with certainty in experiments, the position of $\theta_x = 0$ is defined by the position of the electron beam.

position along the specular direction without displacing either the target or the diagnostics. The main observed change concerns the final angular distributions of ejected electrons. These are pictured for each case in Figs. 6.8–a-c.

The focusing seems to play a role on the size of the ponderomotive hole. When the laser focal spot is located ahead the surface plane (see Figs. 6.8–a), the hole shrinks until completely disappears. By contrast, when the laser is focused behind the target (see Figs. 6.8–c), the hole seems to expand. Regarding the bright electron beam, the focusing does not play a significantly role and the differences observed in the three figures are related to shot to shot fluctuations rather than true focusing effects.

In order to validate these results, we run a set of PT simulations in the same condition of injection. The final angular distributions of electrons are reported in Figs. 6.8–d-f and we quantitatively reproduce the same evolution of the hole size. It also confirms that this effect is mainly introduced during the laser propagation and not at time of injection. As the hole is formed by ponderomotive effects by electrons escaping the laser volume in all transverse directions, it should also be ponderomotive effects that are responsible for its narrowing and expansion, when the laser focal spot is displaced.

In case (i), the laser intensity starts weak and because the focal spot is behind the initial position, it gets only weaker and weaker (see laser amplitudes in Fig. 6.7–a). Consequently, the ponderomotive force is never as intense as in the case (ii) (Fig. 6.7–b) and fewer electrons are ejected from the laser volume. Thus, the ponderomotive hole is smaller (until completely absent).

In case (iii), the laser intensity also starts weak but now the pulse begins by converging. Then, the ponderomotive force magnitude will increase up to the focus and decrease again afterwards as in cases (i) and (ii). The electrons will spend more time in strong field regions and be more accelerated in the radial direction. Thus, the ponderomotive hole is larger.

Conclusion

In this chapter, we endeavored to track electron dynamics after their emission from a dense plasma when the density gradient at the plasma-vacuum interface is short. Just after their ejection towards vacuum, they first encounter a standing wave formed by the combination of incident and reflected field. That field acts as a filter that eliminates too slow electrons and structures the remaining particles suitable for their injection in the reflected field.

From there, electrons undergo vacuum laser acceleration in the reflected field. Based on the work started in [Thévenet, Leblanc, et al., 2016], we studied VLA in two more complex cases: (i) when the laser beam shows a harmonic content and (ii) when it is out of focus. In both cases, we understood the final angular distribution of electrons thanks to PT simulations.

7 Coupling Mechanism in the Long Gradient Regime

After setting aside to tackle VLA, we come back to the coupling mechanisms between light and matter occurring in the density gradient. According to experiments and preliminary PIC simulations performed in the relativistic regime, increasing the density gradient scale length L_g in front of a plasma mirror allows for switching from Brunel's mechanism to another coupling mechanism. The purpose of this chapter is to completely characterize this new mechanism through Particle-In-Cell simulations.
When $L_g \sim \lambda_0$, electron ejection is observed to be no longer periodic but rather complex and disorganized. The reason is that electrons located in the underdense part of the plasma layer behave chaotically. The chaotic motion is driven by the standing wave formed by the incident and reflected laser waves. This mechanism is identified to be stochastic heating.
Along the chapter we will present the stochastic heating mechanism and prove that it is indeed at play in this regime. Then, we will see that despite occurring in the underdense part of the plasma layer, plasma collective effects may impact the electron emission. Finally, we focus on its domain of validity in terms of laser-plasma parameters.

Contents

7.1 Electron Heating Mechanism in the Long Gradient Regime

7.1.1 Introduction to stochastic heating

Let us start this chapter by recalling the basics of stochastic heating. First, we consider a free electron exposed to two non-collinear ultraintense laser beams. Using a quantum description of the field as an ensemble of photons provides a simple way to understand that this electron can gain more energy than when exposed to a single laser beam.

When a single laser beam (assumed to be a plane wave) is present, it is well-known that photon absorption processes are hindered because they do not enable to conserve both energy and momentum of the total system. By contrast, when two non-collinear beams are present, the combined absorption of multiple photons *simultaneously from both beams* is allowed, because the availability of photons with different **k** vectors makes it possible to conserve both energy and momentum of the total system (see Sec. 1.2.3, page 18).

For large field amplitudes, the laser field can be treated classically, and many previous studies in the literature have shown that electron dynamics in these combined non-collinear fields is not integrable and gets chaotic for high enough laser amplitudes (typically $a_0 \gtrsim 0.15$ for at least one of the two beams). This results in large energy gains, and this efficient regime of energy absorption by electrons is known as stochastic heating[1] - although the name chaotic heating would probably be more appropriate here, since the system is perfectly deterministic and involves no stochastic process.

This effect is obviously not restricted to isolated free electrons: it can equally occur for electrons

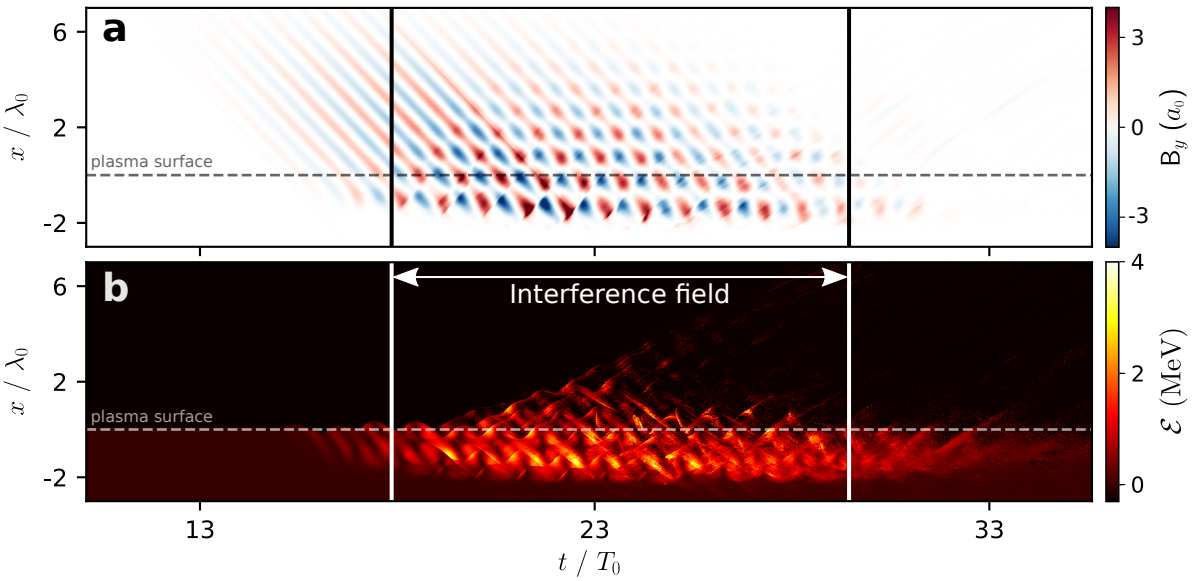

Figure 7.1: **Stochastic heating in the interference field in 2D simulation** - The two panels correspond to the same simulation (`2D_long_gradient_p` defined in Tab. 5.2). The panel (b) highlights the mean electron energy (pictured from black to yellow) gained in the interference field (in blue to red panel (a)).

[1] Mendonça and Doveil, 1982; Mendonca, 1983; Rax, 1992; Z.-M. Sheng, Mima, Sentoku, et al., 2002; Bourdier et al., 2005; Patin et al., 2006; Kemp et al., 2009; Paradkar et al., 2012; Krygier et al., 2014.

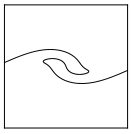

in an underdense plasmas, leading to an energy absorption process where neither collisions nor collective plasma effects play any major role. Such a coupling of the plasma with multiple laser beams has been studied experimentally in [P. Zhang et al., 2003] by exposing an underdense plasma to two laser beams. It is also known to play a role in electron injection in laser-driven plasma wakefield accelerators by the colliding pulse scheme [Faure, Rechatin, et al., 2006; Rassou et al., 2014].

To the best of our knowledge, [Mendonça and Doveil, 1982] were the first to point out that *one of the simplest situations in which an electron can behave stochastically consists of a non-uniform plasma submitted to the influence of an incident monochromatic wave. The small fraction of wave field reflected by the plasma inhomogeneity provides the perturbation which makes the particle Hamiltonian non-integrable.*. Also, [Sentoku et al., 2002] was the first to show it with the support of PIC simulations.

In our case, the required second non-collinear laser beam results from the reflection of the single input beam by the dense plasma. Electrons in the underdense plasma are then exposed to the standing wave formed in front of the overcritical part by the superposition of the incident and reflected beams, and can gain energy. This is precisely how we interpret the experimental results of chapter 5 (page 73) in the long gradient regime.

This heating is illustrated in Fig. 7.1, where we plot side by side magnetic field and electron energy along time. It is striking to notice that the plasma energy mostly increases, when the interference field exists (time range delimited by the two vertical bold lines). When the laser leaves the target, the whole underdense part of the plasma remains homogeneously hot.

7.1.2 Numerical proof of stochastic heating

With the help of simulations, we now support that the heating indeed occurring in the long gradient regime comes from chaotic processes. To do so, just as we proceeded when we studied the Lorenz system (see Sec. 2.1, page 30), the chaotic character of the electron dynamics is exhibited by the calculation of the *Lyapunov exponent* of plasma electrons. As a reminder, the Lyapunov exponent of a dynamical system is a mathematical quantity that characterizes the rate of separation of infinitesimally close trajectories. Quantitatively, two trajectories in phase space with initial separation $d(0)$ diverge at a rate given by:

$$d(t) \approx d(0) \exp(\lambda_L t), \tag{7.1}$$

where λ_L is the Lyapunov exponent.

A schematic drawing of the separation is shown in Fig. 7.2–a, where we consider two trajectories (x_1 or x_2 for example) initially very close in the phase space at $t = 0$. The trajectories evolves differently considering the sign of λ_L:

- when $\lambda_L < 0$ (upper drawing of Fig. 7.2–a), the two trajectories gets closer to each other, the system is non chaotic and dissipative,
- when $\lambda_L > 0$ (lower drawing of Fig. 7.2–a), the two trajectories diverge, the system becomes chaotic.

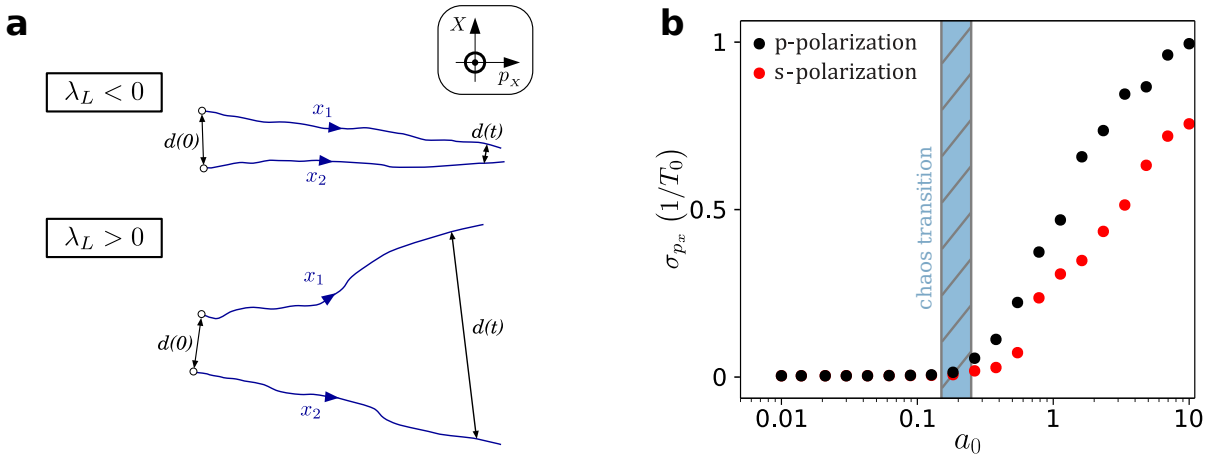

Figure 7.2: **Evolution of the Lyapunov exponent in 2D plane wave PIC simulations in the case A** - Panel (a) displays a schematic drawing of the evolution of two trajectories along time in phase space in function of the sign of the Lyapunov exponent λ_L: (i) in the upper part of the panel, $\lambda_L < 0$ and the trajectories x_1 and x_2 tend to get closer to each other, (ii) when $\lambda_L > 0$, the system becomes chaotic and the trajectories diverge. In panel (b), we plot the evolution of $\lambda_L(p_x)$ (the Lyapunov exponent for the quantity p_x) in function of the laser amplitude for both p (black dots) and s (red dots) polarizations. The chaos threshold is highlighted by a blue hatched area.

In simulations, it is possible to define the maximal Lyapunov exponent between two trajectories x_1 and x_2 as:

$$\lambda_L = \lim_{\substack{t\to\infty \\ d(0)\to 0}} \left(\frac{1}{t} \ln \frac{d(t)}{d(0)} \right), \tag{7.2}$$

for $d(0)$ as small as possible. We also define the maximal Lyapunov exponent $\lambda_L(V)$ for a given single phase space variable V considering d_V the distance between the two trajectories projected on the variable axis (e.g., X in Fig. 7.2–a). If $\lambda_L(V) > 0$ for at least one variable then the system will be chaotic. Typically, we run two simulations with the same initial conditions except for V and we compare how a same particle has evolved in both cases. This treatment is iterated on every particle of the simulation and averaged to get the total Lyapunov exponent.

The Lyapunov exponent $\lambda_L(p_x)$ for the p_x variable, obtained from 2D plane wave PIC simulations is displayed in Fig. 7.2–b, as a function of the incident laser amplitude and different laser polarizations. The exponent is very close to zero at low intensity, and gets strictly positive when $a_0 \gtrsim 0.15$ (the blue hatched area), thus pointing to chaotic dynamics. This threshold in laser intensity is consistent with early theoretical investigations of stochastic heating [Mendonca, 1983; Z.-M. Sheng, Mima, Sentoku, et al., 2002].

Note that the chaos seems to be more intense for p-polarization, this results will be explained in detail in Sec. 8.5, page 147.

7.1.3 Importance of the reflected laser field and underdense plasma layer

In introduction of this chapter, we stressed the importance of a second wave to seed stochastic heating. We thus run on a set of 2D plane wave PIC simulations for three different physical configurations displayed in Fig. 7.3 (numerical and physical parameters defined in Tab. 7.1):

Simulation	solver	Δz	a_0	L_g	θ_i	n_{max}	Nb waves
A: `reflect_plasma_mirror`	PSATD	$\lambda_0/350$	3	$\lambda_0/1.5$	55°	$200n_c$	1
B: `reflect_under_two_waves`	-	-	-	-	-	$0.4n_c\cos^2\theta_i$	2
C: `reflect_under_one_wave`	-	-	-	-	-	$0.4n_c\cos^2\theta_i$	1

Table 7.1: **Numerical and physical parameters for 2D-plane wave simulations performed in this section** - The laser and plasma parameters are the same for all three configurations defined in Fig. 7.3. However, for cases B and C the plasma maximal density has been truncated for $n > 0.4n_c\cos^2\theta_i$, allowing the laser to cross the plasma. In the case B, a second beam is coming from the other part of the plasma.

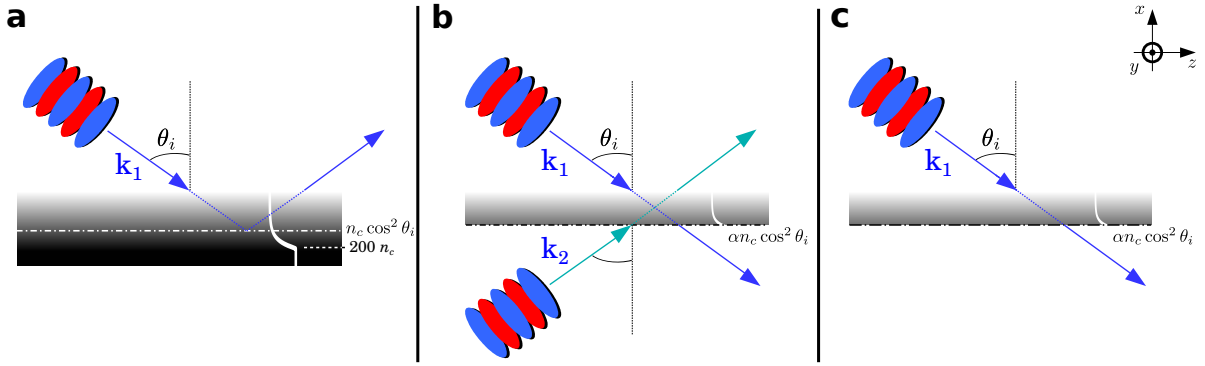

Figure 7.3: **Schematic drawing of three physical configurations aiming to exhibit the role of the reflected field** - In panel (a), it is the classical laser plasma mirror interaction in the long gradient regime, where the laser wave is reflected by an overdense target. For panel (b) and (c), the plasma profile has been truncated for densities $n > \alpha n_c\cos^2\theta_i$ ($\alpha = 0.4$) allowing the laser beam to cross. For panel (b), an other laser beam is added, coming from the other side of the plasma.

- the first configuration (simulation `reflect_plasma_mirror` or case A) corresponds to the interaction of an ultraintense laser pulse with a dense plasma in the long gradient regime. It is the general setup of the experiments.
- In the second configuration (simulation `reflect_under_two_waves` or case B), now the plasma profile has been truncated for densities $n > 0.4n_c\cos^2\theta_i$, i.e. keeping only the underdense part of the plasma, such that there is hardly any reflection of the incident laser by the plasma. This underdense plasma layer, surrounded by vacuum on both sides, is irradiated by the same laser beam as before, but also by a second beam, symmetrically arriving from the other side of the plasma (see Fig. 7.3–b). The role of this second laser is to emulate the beam reflected by the dense part of the plasma in case A.
- The last configuration (simulation `reflect_under_one_wave` or case C) is similar to case B but the truncated plasma layer is irradiated by one laser beam only.

Their key results are summarized in Fig. 7.4, and shed light on the role of the reflected field for driving stochastic heating. This figure displays the temporal evolution of the plasma electron density (Fig. 7.4–a-c), and the $x - p_x$ phase space distribution of electrons (Fig. 7.4–d-f) at the time when electron ejection from the plasma is observed to start (blue dashed line in

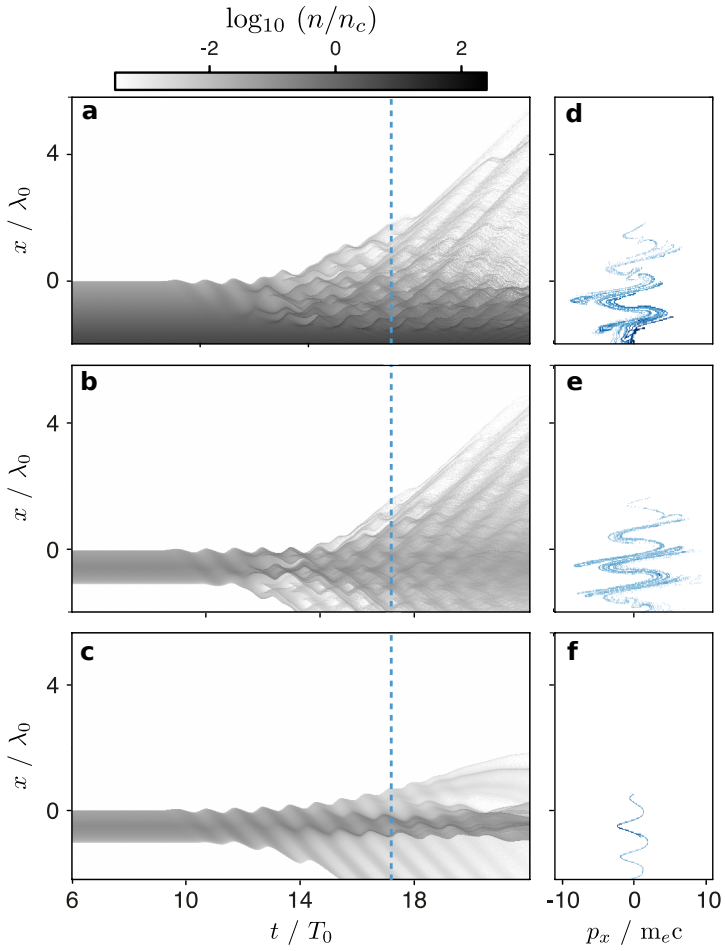

Figure 7.4: **Set of 2D-plane wave PIC simulations carried out to reveal the role of the laser field reflected by the plasma** - Each line corresponds to a different physical case presented in the drawing Fig. 7.3:
- A: `reflect_plasma_mirror`
- B: `reflect_under_two_waves`
- C: `reflect_under_one_wave`
(see Tab. 7.1 for numerical and physical parameters). In these three cases, panels (a)-(c) show plots of the temporal evolution of the plasma electron density in gray log color scale and panels (d)-(f) display snapshots of the $x - p_x$ phase space distribution of electrons in blue log color scale, taken at the time indicated by the blue line in panels (a)-(c) when $t = 17.3\ T_0$.

Fig. 7.4–a-c).

The upper panels correspond to the case A and the middle panels t the case B. The key point here is that both the temporal dynamics of the plasma density profile and the electron phase-space distributions look very similar for cases A and B.

By contrast, if the truncated plasma layer is irradiated by one laser beam only (lower panels), the plasma dynamics become totally different. More specifically, while similar upward electron ejections are observed in cases A (corresponding to the electron signal observed in our experiment) and B, this electron emission is strongly reduced in case C: less electrons are emitted, and they have much weaker velocities.

This toy-model study leads to two important conclusions:

- the comparison of cases A and B indicates that in the long gradient regime, the coupling mechanism leading to electron ejection mostly occurs in the underdense part of the density gradient,
- the comparison of cases B and C indicates that the overdense part of the plasma nonetheless plays a key role, by producing a reflected beam. When crossing and interfering with the incident beam, this strongly modifies the dynamics of electrons in the underdense plasma

layer.

These different electron dynamics in the underdense plasma layer can be also observed in phase space (see Fig. 7.4–d-f). When a single laser beam is present (case C), electrons are observed to simply oscillate non-linearly in the laser field, leading to a smooth and regular phase space distribution (Fig. 7.4–f). In striking contrast, in cases A and B, electron dynamics in the standing wave resulting from the superposition of two non-collinear laser beams are complex: the key point is that we observe a very strong local *stretching and folding* effect on the phase-space distribution, around each node of the standing wave.

Such a stretching and folding effect results in very different trajectories for particles that are initially very close in phase space: this is known to be one of the most typical routes to chaotic dynamics [Strogatz, 2018]. This repetitive stretching and folding eventually results in a highly-structured, multilayered phase space distribution (see Fig. 7.4–d, e), where electrons at a given spatial position have a complex momentum distribution. The striking contrast between these highly-structured phase space distributions, and the smooth distribution observed in case C again demonstrates the impact of adding a second wave on electron dynamics in the underdense part of the plasma.

7.2 Influence of Plasma Collective Effects

7.2.1 Influence of the underdense plasma layer density

Electron stochastic heating happens in tedious media, because laser waves must propagate. However, does the electron density of the media matter for the mechanism ? In order to answer this question, we propose yet another toy model, where a tenuous plasma recovers a perfect mirror as illustrated in Fig. 7.5. The tenuous part is composed of a front density gradient up to a tunable maximal density $n_{max} < n_c \cos^2 \theta_i$, so that the laser can always reach the perfect mirror, where it is reflected. The maximal density is varied from 5×10^{-3} n_c to 0.3 n_c. The purpose of the study is to observe how the electron dynamics are being affected.

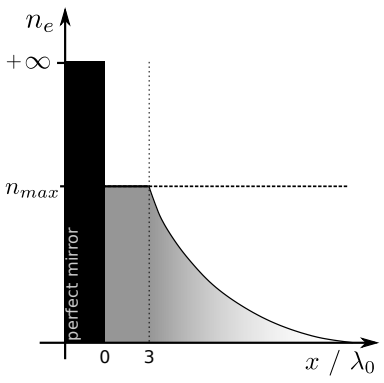

Figure 7.5: **Schematic drawing of the simulated density profile combining a tenuous plasma and a perfect mirror.**

We run a set of 2D simulations for three different maximal densities and plot in Figs. 7.6–a-c a snapshot of the plasma density profile as well as the magnetic field after reflection. It immediately comes that the spatial distribution of electrons are completely different in all three cases. When the density is extremely low (Fig. 7.6–a), most of electrons are expelled from the target in any directions ; some of them are even injected inside the reflected field. By contrast, at highest density (Fig. 7.6–c), the density gradient is strongly perturbed but not completely wiped out.

The spatial profile of the reflected field also highly depends on the density. In Fig. 7.6–a, the reflected wavefront is almost identical to the incident wavefront, while in Fig. 7.6–c it is

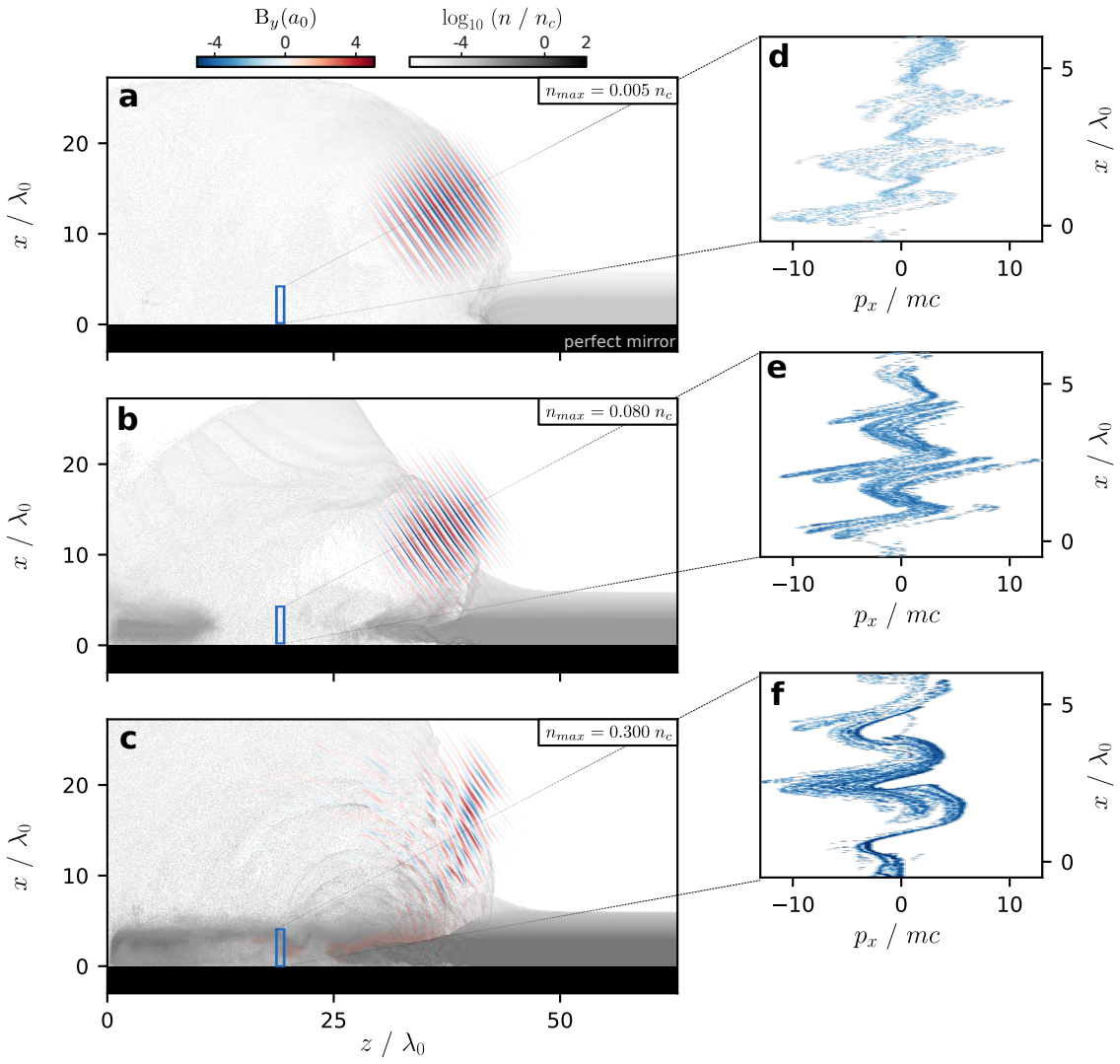

Figure 7.6: **2D PIC simulations of the interaction between a laser and a target combining a tenuous plasma and a perfect mirror** - The first three panels (a)-(c) show the electron ejection (grey color scale) and the field profile (blue to red color scale) after interaction ($t = 60\ T_0$) for three different maximal density: (a) $n_{max} = 0.005\ n_c$, (b) $n_{max} = 0.08\ n_c$ and (c) $n_{max} = 0.3\ n_c$. Panels (d)-(f) display snapshots of the $x - p_x$ phase space distribution of electrons in blue log color scale, taken at the time of interaction indicated by the blue square in panels (a)-(c) at $t = 37\ T_0$.

completely degraded. As suspected in Sec. 5.3.2, the spatial degradation observed in the long gradient regime comes from non-linear couplings between the light and near-critical plasmas.

Now, let us focus on the electron dynamics inside the underdense plasma layer during interaction displayed in Figs. 7.6–d-f for the same set of simulations. Surprisingly, the electron profiles in phase space are heavily similar. We observe each time a strong stretching and folding effect that mixes the electron distributions. According to the extremal values of p_x, the possible energy gained by stochastic heating is comparable. It is a clear evidence that this mechanism is only weakly dependent on the electron density.

Nevertheless, plasma collective effects still play an important role on the electron emission after heating. To quantify their impact, we looked at the angularly resolved distributions far from the target that are pictured in Figs. 7.7–a-c for the same simulations. Starting again at low

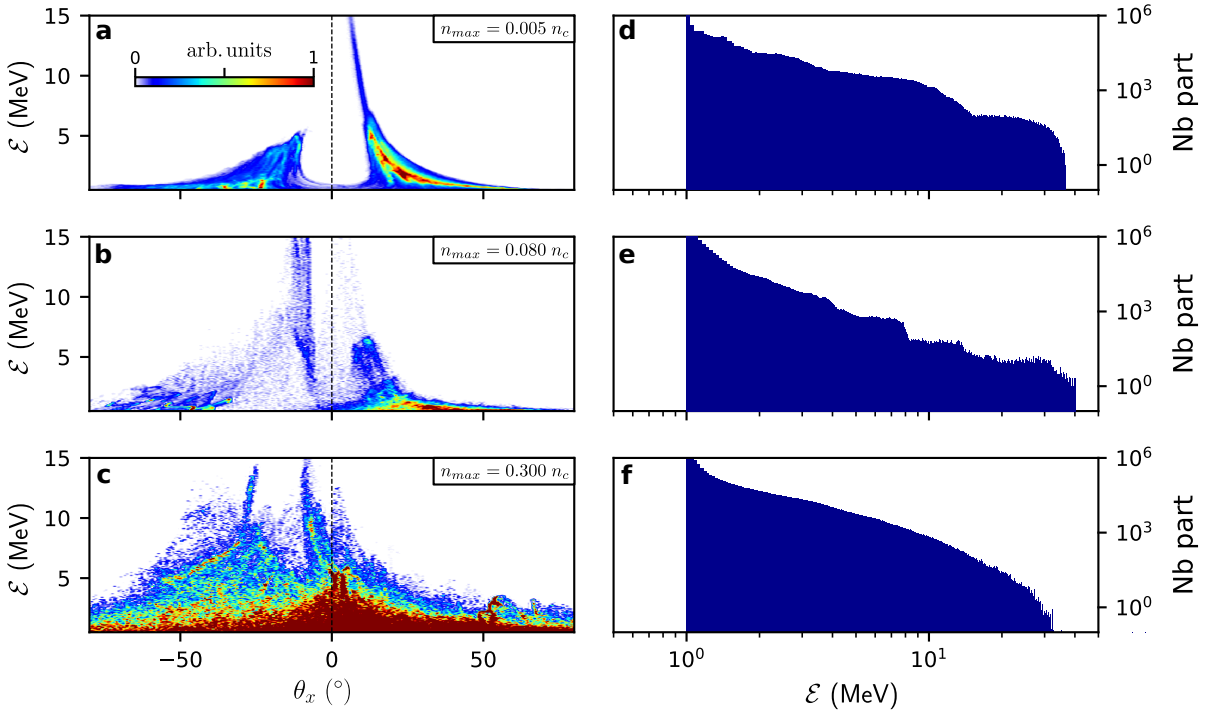

Figure 7.7: **Energy distributions far from the target after interaction between a laser and a target combining a tenuous plasma and a perfect mirror** - The fist three panels (a)-(c) display the angularly resolved energy profiles of emitted electrons expelled into vacuum extracted from the same simulations as in Fig. 7.6. In panel (d)-(f), these profiles are integrated along the angle axis and plotted in log-log scale.

densities (Figs. 7.7–a), a clear correlation is observed between the angle of emission and the energy: the electron energy is high close to the specular direction and decreases as one deviates from $\theta_x = 0$. This profile strongly resembles to a distribution found in the short gradient regime, when particles undergo VLA in the reflected field (see Fig. 5.4–a, page 77 for example).

It might seem unsettling to find such distribution here. However, let us recall that in the short gradient regime, free emitted electrons are first crossing an interference field as well that shapes the distribution into electron planes (see Sec. 6.1, page 90). In particular, we were able to create electron attosecond bunches in PT simulations, where particles were continuously introduced in the interference field at non-zero velocities, without considering Brunel mechanism. A same process happens here: the fastest electrons are emitted in the form of bunches into the reflected field, the only difference is that the initial kick is given by stochastic heating.

For higher density (Fig. 7.7–c), we retrieve the main features of the long gradient regime: less and less electrons are injected into the reflected field and most of the distribution is concentrated between specular direction and target surface ($\theta_x < 0$). In addition, there is no significant correlation observed between angle and energy. The collective plasma effects are mainly responsible for the direction of emission after electron heating. That can be explained by the strong space charge fields that retain electrons close to the target. These fields appear because a large fraction of electrons are expelled from the focal volume during interaction, while ions practically stay immobile at the considered time scales.

In Figs. 7.7–d-f, we plot the integrated energy distribution far from target and we verify that

it barely varies with the density. That reinforces our previous guess that stochastic heating itself hardly depends on the plasma density. These profiles are all three thermal distributions, which legitimates the use of *heating* in stochastic heating. By theoretical considerations, we will characterize the distribution of particle energy in the next chapter.

To summarize, the emission direction of electrons is strongly dependent on the underdense plasma density but the stochastic heating not so much. It legitimates the following study performed with a particle tracker code and free electrons.

7.2.2 Stochastic heating with a particle tracker code

As electron energy gain does not seem to depend on the plasma density, it may not be necessary to compute the whole dynamics with a PIC code. It may be possible to study stochastic heating in the interference field directly with the particle tracker (PT) code. The underdense plasma layer would be simulated by a whole of free electrons, where no collective effects are at play.

To validate the use of such a code over a full PIC code, we directly compare the results of a same 2D simulation performed in the configuration B defined in Fig. 7.3–b. A snapshot of the interaction is illustrated in Fig. 7.8–a. As a reminder, when two laser beams are interfering in the middle of an underdense plasma, the temporal dynamics of the plasma density profile are very close to the one obtained after interaction between a single ultra intense laser pulse and a plasma mirror in the long gradient regime.

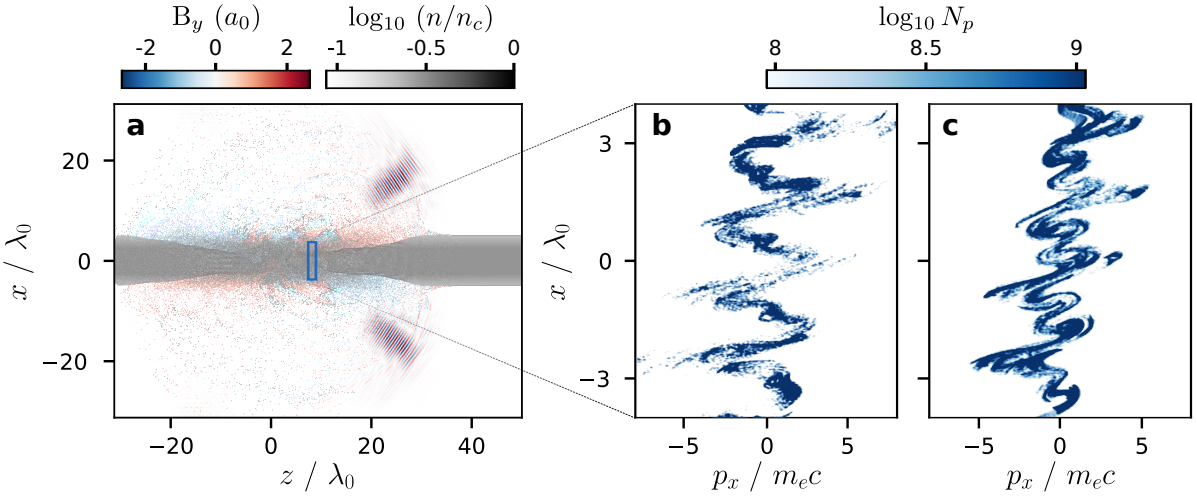

Figure 7.8: **Comparison between 2D PIC and PT simulations in the setup defined in Fig. 7.4–b** - Panel (a) displays a snapshot after the interference of two beams (pictured from blue to red) in the middle of an underdense plasma (in the gray log color scale). In panels (b) and (c) is plotted the $x - p_x$ phase space distribution in in blue log color scale for a subset of electrons located in the blue rectangle panel (a), when the beams are interfering. Panel (b) corresponds to a simulation performed with a PIC code, while panel (c) to a simulation performed with a PT code, with the same particle initialization ($\sim 10^7$ particles).

For both simulations, we set the particles at the exact same initial position at rest. The phase space distributions $(x,\ p_x)$ at time of interaction are shown for both PT and PIC simulations in Fig. 7.8–b, c. The two phase portraits look very much alike. Especially, the amplitude and

periodicity of the stretching and folding envelop ($-5 \lesssim p_x \,/\, m_e c \lesssim 5$) are well reproduced with the PT code.

Note that in a particle tracker code the concept of *super-particle weight* – N_p defined in Ch. 3 (page 43), which represents a certain number of real particles per super-particle– does not fundamentally exist. In motion equations, only the ratio charge over mass (independent from the weight) does matter to describe the species displacement. However, it is possible to assign a dummy weight for each particle, which does not impact the electron dynamics but emulate a plasma density. It becomes possible to quantitatively compare electron distributions with PIC simulations.

Fig. 7.9 represents histograms of momentum and energy distributions after the laser has passed, in blue for the PIC code and in red for the PT code. First thing to notice is the general good agreement between the results of the two codes:

- the p_x distribution in log scale (Fig. 7.9–a, d) seems symmetrical around zero and varies from $p_x \sim -20 m_e c$ to $p_x \sim 20 m_e c$,
- the p_z distribution in log scale (Fig. 7.9–b, e) is strongly asymmetrical and most of the electrons travel towards large z.

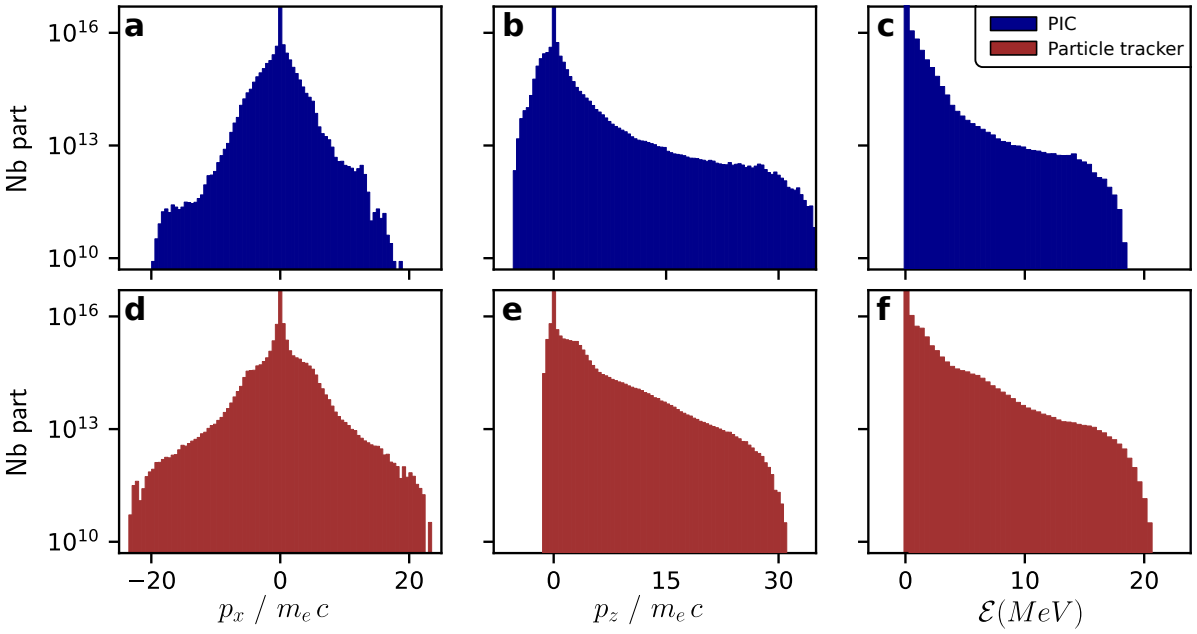

Figure 7.9: **Momentum and energy distributions for simulations performed with a PIC code and a PT code** - In panels (a)-(c), the different quantities —the momenta p_x, p_z and the energy $\mathcal{E}$— are obtained with a PIC code. In panels (d-f), the exact same quantities are obtained with a PT code. All of these histograms are expressed in log scale. For the particle tracker code, a dummy weight was attributed to the electrons allowing for direct comparison with the PIC code.

Looking at these results, a particle tracker code seems to offer a good alternative to PIC codes in the context of stochastic heating and interaction between laser and electrons without collective effect. It allows for predictive values of plasma energy and behaviour in a much shorter time to solution. Thus, it seems to be the perfect choice for having a better understanding on stochastic heating at a fundamental level, subject of the upcoming chapter.

7.2.3 Magneto-static fields on top of the surface

Besides stochastic heating, another specificity of the long gradient regime is the presence of quasi-static fields (QF) on top of the plasma surface (see Fig. 5.11b, page 84). These grow during the laser-plasma interaction, reach an amplitude typically of the same order of magnitude as the laser magnetic field, and then persist even after the laser pulse has been reflected by the plasma.

Such surface quasi-static fields have already been reported in multiple studies of the interaction of intense lasers with dense plasmas[2], and can be induced by a variety of physical processes[3]. In the present case, our simulations indicate that their development can be attributed to the 'fountain effect' described in [Sudan, 1993] where they originate from the cold return current inside the plasma that compensates for the lateral charge ejection from the laser focal volume.

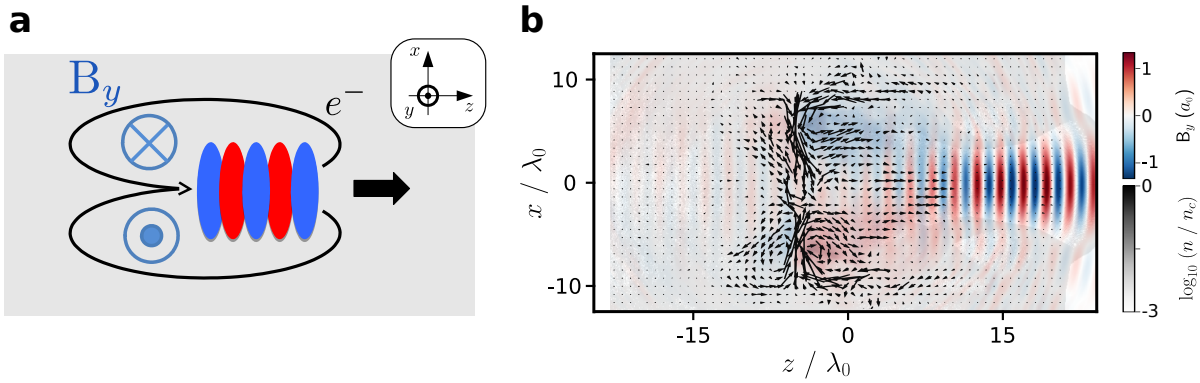

Figure 7.10: **Fountain effect in drawing and simulation** - A laser is going through an underdense plasma layer in a setup close to Fig. 7.11–a. Panel (a) is a drawing of the mechanism: the electrons are firstly expelled from the pulse by ponderomotive effect and cycle back thus generating a toroidal magnetic field (light blue) which co-propagates with the laser. Panel (b) shows the corresponding 2D PIC simulation, where the black arrows stand for the electronic displacement averaged over a time step.

In order to understand the fountain effect, it is easier to use the configuration of a laser traveling inside an underdense plasma layer. We will see just after that this effect can be generalized on solid targets. During the propagation the laser expels electrons by ponderomotive effect, which cycle back generating the QF (Fig. 7.10–a). In simulations, it is possible to have access to the return current by averaging in time the electron motion and smoothing fastest dynamics. The return current is mainly carried by cold electrons and locally weaker than the one generated by fast electrons but more persistent in time. The electronic displacement is pictured as a quiver plot in Fig. 7.11–b and the black arrows are pointing in the same direction as in Fig. 7.11–a: electrons on the side are circulating backwards until they loop behind the pulse. The signs of the generated fields are coherent with the Ampère's right-hand grip rule regarding the electron directions of rotation.

The quasi-static fields presented herein are extensively discussed in [Bulanov, 2005] in the context of ion acceleration *in a Dipole Vortex*. The authors noticed that a high-power laser propagation in a gas target ($n \sim 0.1 - 0.5 n_c$) generates quasi-static magnetic fields associated to an electron

[2] Ruhl et al., 1999; Tatarakis et al., 2002; Bulanov, 2005; Li et al., 2006; Pérez et al., 2013; Nakatsutsumi et al., 2018

[3] Fabbro and Mora, 1982; Sudan, 1993; Thaury, Mora, et al., 2010; Kumar et al., 2018

vortex structure. When the laser escapes the plasma, these fields are persisting and an extended region with a quasi-static electric field is formed, in which the ions can be accelerated. The configuration they found as optimal to maximize the field magnitude is the configuration presented in Fig. 7.10.

The QF shape of this configuration are then compared with two other cases: (i) when the laser is reflecting on a plasma mirror target with a long gradient $L_g = 1.5\lambda$ in normal incidence for Fig. 7.11–b and (ii) with an oblique incidence ($\theta_i = 55°$) for Fig. 7.11–c.

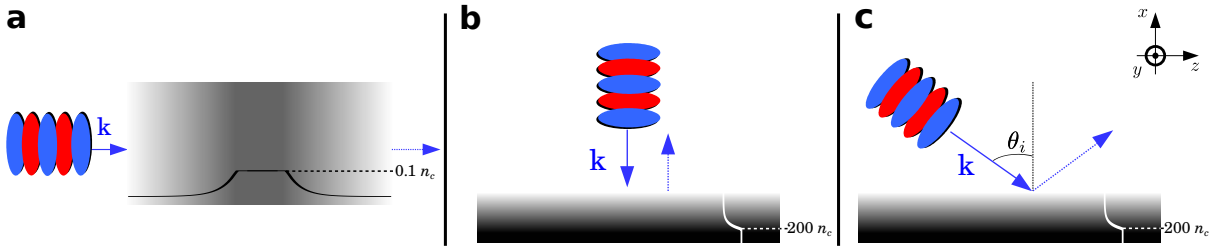

Figure 7.11: **Schematic drawing of three different laser interactions with a long gradient plasma leading to quasistatic fields** - In panel (a), the laser beam is crossing an underdense target presenting density gradients in front and back. In panel (b) and (c), the laser is reflecting on a plasma mirror with a long gradient $L_g = 1.5\lambda$ in normal incidence (b) and with an angle θ (c).

The results of 2D PIC simulations corresponding to these three cases are pictured in Fig. 7.12. It is particularly striking to notice how close the QF look alike in the first two cases (Figs. 7.12–a, b) in term of amplitude and shape. Typically, their amplitude reaches a magnitude equivalent to 0.8-1 in a_0 magnetic unit (while the laser amplitude is initially $a_0 = 3$) across 3-5λ_0. This indicates that a substantial portion of the energy of the incident laser pulse is converted into these fields (in practice $\sim 15\%$).

In addition, in Fig. 7.12–a, as observed in [Bulanov, 2005] a plasma channel spans all across the plasma layer. During a time significantly longer than the ones presented in the manuscript, the channel size is actually growing and cavities -area empty of electrons and ions- start to appear in the middle of the plasma.

Reflecting with an angle (Fig. 7.12–c) does not fundamentally change the physics at play and the QF still persist. However, there is now a asymmetry between the absolute amplitude of the surface fields. In fact, one can barely see the left and blue negative part of the surface fields while the positive part seems more intense than before. This asymmetry comes from the difference of density observed on both sides of the field, while traveling in the plasma. During the interaction, the laser field is surrounded by low densities near the surface and high densities (near-critical) at the point of reflection. Electrons are expelled by ponderomotive force from the focal volume in all spatial directions but more electrons are pulled back from highest densities to compensate the loss. They contribute to larger return currents and thus larger QF. The QF span also a broader surface area because the interaction surface itself increases in oblique incidence (as $\tan\theta_i$ typically).

The fountain effect is obviously dependent on the laser waist as it is a ponderomotive effect. When using a Gaussian pulse with a finite waist, e.g., $w = 5\lambda_0$, QF emerge in normal incidence

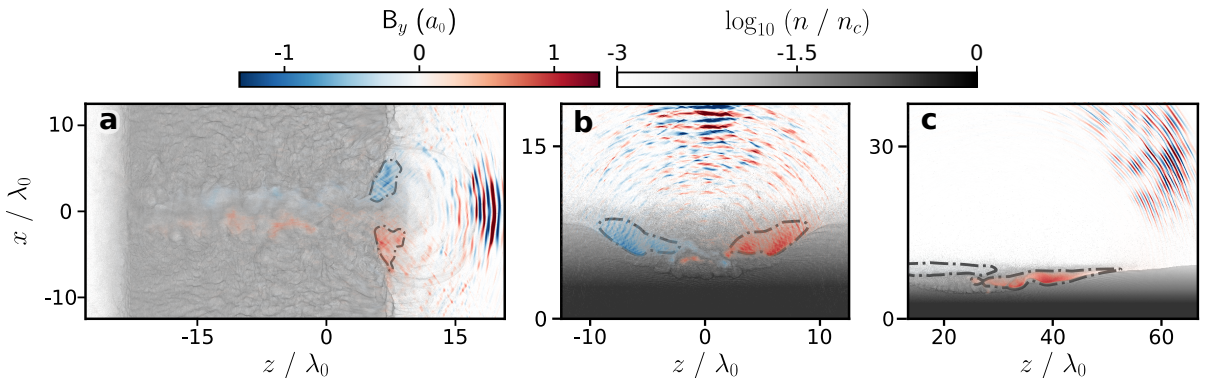

Figure 7.12: **Evolution of the surface static fields in three different configuration with a long gradient plasma leading to quasistatic fields** - In all the three cases, we display a snapshot of the B_y field and the plasma density (log scale) at the end of the interaction. The static fields are highlighted by a gray dot-dash line.

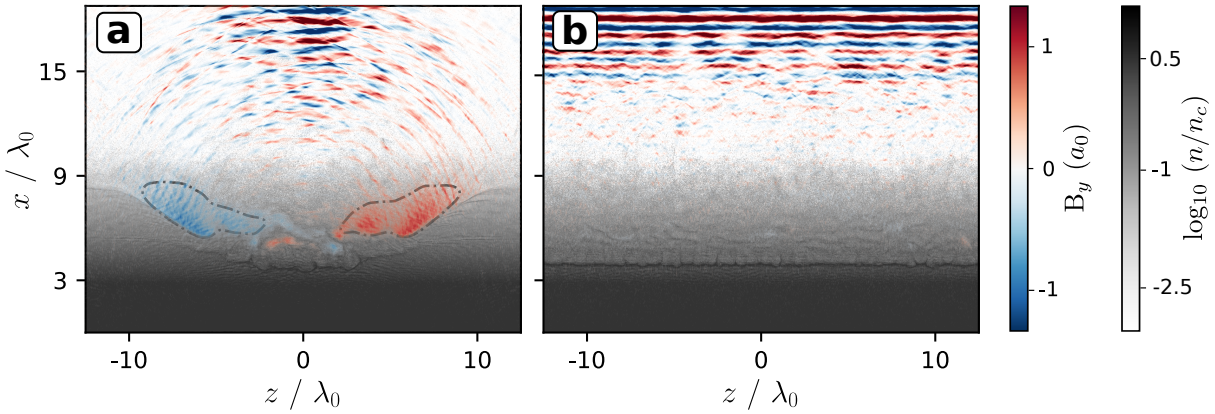

Figure 7.13: **Reflection in normal incidence for a Gaussian beam and a plane wave in the long gradient regime in 2D** - For both panels, the magnetic field is plotted in color scale, while the plasma is plotted in gray log scale. The static fields are highlighted by a gray dot-dash line.

(Fig. 7.13–a). When the plasma surface is homogeneously illuminated by a plane wave, the surface fields tend to completely disappear, as illustrated in Fig. 7.13–b.

To summarize, the quasi-static fields needs two conditions to appear in the long gradient regime: (i) the crossed plasma density has to be sufficiently high to drive large return currents and (ii) the laser waist has to be sufficiently small to maximize the ponderomotive force. In experimental conditions, these two conditions are full filled and such surface fields can be indeed measured [Tatarakis et al., 2002].

7.3 Validity Domain of Stochastic Heating

7.3.1 Threshold in intensity from resonance absorption to stochastic heating

Now that the mechanism in the long gradient regime is well understood, let us find the validity domain of stochastic heating in term of gradient and intensity.

As a reminder, in Sec. 1.2.2, we saw that resonance absorption is supposed to be the mechanism

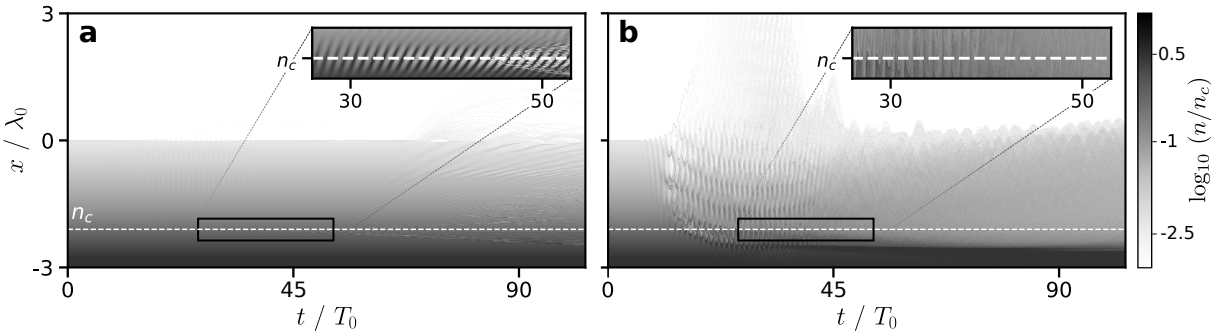

Figure 7.14: **2D-plane wave PIC simulations in the long gradient regime for two different laser amplitudes in *p*-polarization** - In both cases, the simulations are performed in the setup A defined in Tab. 7.1, page 103. The gray log scale represents the temporal evolution of the plasma electron density profile for (a) $a_0 = 0.1$ and (b) $a_0 = 3$. The insets represent zooms centered around the critical electron density of the initial plasma profile $n = n_c$ (materialized with the white dashed line).

at play at low intensity, when the gradient scale length was sufficiently long. Then, it may be possible to find a transition from resonance absorption to stochastic heating, when the intensity is increased. In addition, Fig. 7.2–b (page 102) showed that for lower laser amplitudes $a_0 \ll 1$, the Lyapunov exponent λ_L is very close to zero, suggesting that stochastic heating is no more the leading mechanism at play.

This is supported by the results of Fig. 7.14 obtained for PIC simulations performed in the case A (see Fig. 7.3–a page 103) for two different laser amplitudes $a_0 = 0.1$ and $a_0 = 3$. At a lower laser intensity (Fig. 7.14–a), a resonant excitation of plasma waves is observed around the critical density $n = n_c$. The resonant growth of these plasma waves eventually lead to wave breaking and subsequent ejection of hot electrons after the interaction. The underdense part of the plasma gradient ($n < n_c$) is only very weakly perturbed in this case.

However, for larger laser amplitudes, $a_0 = 3$, Fig. 7.14–b shows that the resonant growth of plasma waves at $n = n_c$ vanishes. As opposed to the *classical* case ($a_0 \ll 1$) where all resonance absorption models assumed an initially unperturbed plasma density profile, the electron density profile in the relativistic case is highly perturbed and the laser reflects on a density much higher than n_c (by relativistic transparency). This prevents the growth of any resonant waves near the critical density. Instead and as previously described, the interference pattern produced by the incident and reflected fields within the underdense part of the density gradient is responsible for stochastic heating of electrons, and results in a homogeneously heated underdense plasma layer.

When the laser polarization is switched, resonance absorption is supposed to disappear but not stochastic heating (see Fig. 5.10–b on page 83). This is perfectly illustrated in Fig. 7.15, at $a_0 = 0.1$ (Fig. 7.15–a) and $a_0 = 3$ (Fig. 7.15–b). At lower intensity, the plasma is barely perturbed by the laser and we observe no resonance near n_c. At higher intensities, in coherence with Fig. 5.10–b, stochastic heating appears and the electron density profile looks like the one obtained with a *p*-polarized wave.

The transition from resonance absorption to stochastic heating is detailed in a smoother way in Fig. 7.16 for 4 different laser intensities, $a_0 = 0.1,\ 0.5,\ 1$ and 5 and two laser polarizations in the setup A.

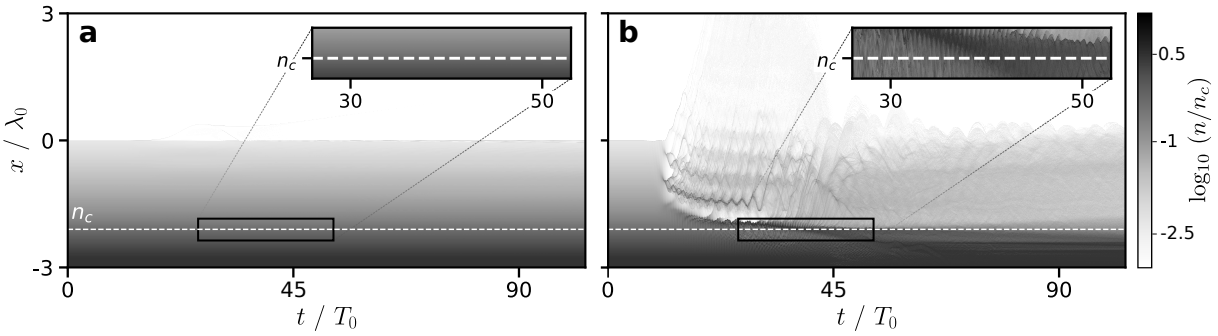

Figure 7.15: **2D-plane wave PIC simulations in the long gradient regime for two different laser amplitudes in *s*-polarization** - Same as in Fig. 7.14 but the laser polarization was switched. This time there is no resonance absorption at low intensity (panel (a)).

According to Fig. 7.2–b, the chaos appears for $a_0 \gtrsim 0.15$ and consequently there is no sign of stochastic heating in Fig. 7.16–a, e (where $a_0 < 0.15$). Then, for the six other panels, the intensity becomes high enough to allow stochastic heating to grow. Again, at a given intensity, the two density profiles for both polarizations look very much alike, in term of ejection but also in term of laser penetration, which increases by relativistic transparency.

Also for *p*-polarization, resonance absorption does not disappear immediately after passing the chaos threshold. It still coexists with stochastic heating for moderate intensities, such as $a_0 = 0.5$ and 1 (see the wave breaking near n_c in Figs. 7.16–b, c, but absent in Fig. 7.16–f, g). However, at some point the laser intensity becomes so high that the beam is reflecting on a density higher than n_c preventing the resonance absorption to exist (Fig. 7.16–d).

It is possible to theoretically estimate this limit. By recalling relativistic transparency, a high power laser does not reflect on a density $n = n_c \cos^2\theta_i$ anymore but on a density $n = \gamma_0\, n_c \cos^2\theta_i$ instead, with γ_0 the equivalent Lorentz factor for the laser beam defined as:

$$\gamma_0 \equiv \sqrt{1 + a_0^2}. \tag{7.3}$$

However, resonance absorption still occurs at the point on the density profile, where $\omega_p = \omega_0$ (see Figs. 7.16–a-c). Then, if the point of the reflection is deeper than the position of n_c, it prevents the growth of the resonance:

$$\begin{aligned} & \gamma_0\, n_c \cos^2\theta_i > n_c, \\ \Leftrightarrow \quad & a_0 > \frac{\sqrt{1-\cos^4\theta_i}}{\cos^2\theta_i} \simeq 2.87 \text{ for } \theta_i = 55°. \end{aligned} \tag{7.4}$$

In experiments, a_0 is roughly equal to 3 (> 2.87) and no resonance absorption signatures could be observed in this regime *a priori*.

7.3.2 Evolution with gradient scale lengths

We already know that a too short density gradient scale length prevents the stochastic heating to grow in favor of Brunel mechanism, because the laser does not propagate in a large enough underdense plasma layer. At very long gradient scale lengths ($L_g \gtrsim 3\text{-}5\lambda_0$), we would also expect the stochastic heating to disappear, since the reflection becomes continuous. In the plasma

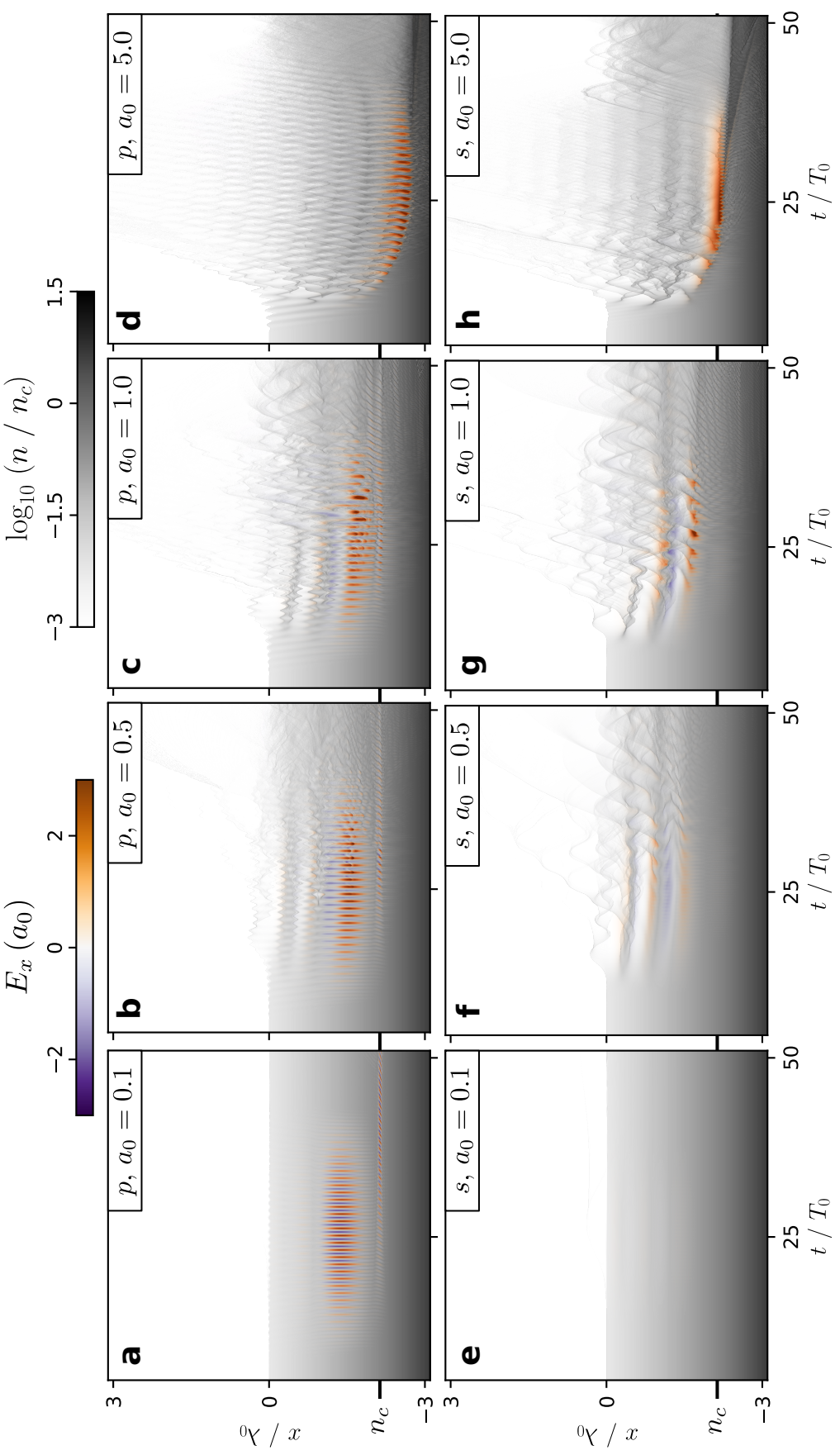

Figure 7.16: **Transition from resonance absorption to stochastic heating in 2D-plane wave PIC simulations** - For all of these cases, we represent the electronic density in gray log scale and the transverse electric field in color scale in the setup A defined in Tab. 7.1, page 103. The upper row (panels (a-d)) corresponds to a p-polarized incident wave, while panels (e-h) were obtained with a s-polarized laser. The different columns stand for different laser intensities: panels (a)/(e): $a_0 = 0.1$, (b)/(f): $a_0 = 0.5$, (c)/(g): $a_0 = 1$ and (d)/(h): $a_0 = 5$. For panels (b) and (c), the stochastic heating and the resonance absorption coexist (see the resonance near the n_c position).

layer, the laser wave is continuously turning inside the plasma layer (k_x varies with z), without creating a standing wave, combination of incident and reflective fields. This standing wave is mandatory for stochastically heating the plasma.

Reflection at low intensity. The reflection is indeed continuous when the laser intensity is low as illustrated Fig. 7.17 with a drawing (Fig. 7.17–a) and through 2D-simulation at $a_0 \ll 1$ and $L_g = 5\lambda_0$ (Fig. 7.17–b). The plasma layer is almost unperturbed along the wave propagation. Also, the wave self-focuses in the near-critical part of the plasma and thus presents a smaller waist.

Reflection at relativistic intensity. We now run the same simulation as in Fig. 7.17 but for $a_0 = 3$. The results are shown in Fig. 7.18 at different time steps. At higher intensities, non linear effects start happening (mainly non-linear self-focusing) and the laser is actually depleted during its propagation in the plasma. Looking at the B_y field in **k**-space in Fig. 7.18–e-h, the laser wavevector is turning in a continuous way along the propagation in the plasma but its footprint in Fourier space broadens. This indicates that the laser fails to keep its initial waveform and that its energy is spread over a wide range of angles.

In the spatial domain, Fig. 7.18–a-d shows that the laser is scattered in multiple filaments and almost fully absorbed before leaving the plasma: in this simulation only 21.6% of the laser initial energy is emitted toward vacuum as a highly deformed beam (Fig. 7.18–d). By ponderomotive effect, the different laser filaments draw channels and overdense regions.

Laser absorption by an overdense plasma was particularly studied in the 90s in a context of inertial fusion[4]. There, lasers are mostly picosecond to nanosecond and the interaction on a near critical plasma leads to strong parametric instabilities, in particular stimulated Raman scattering (SRS) or stimulated Brillouin scattering (SBS).

The incident laser light generates a scattered electromagnetic wave and a longitudinal wave that

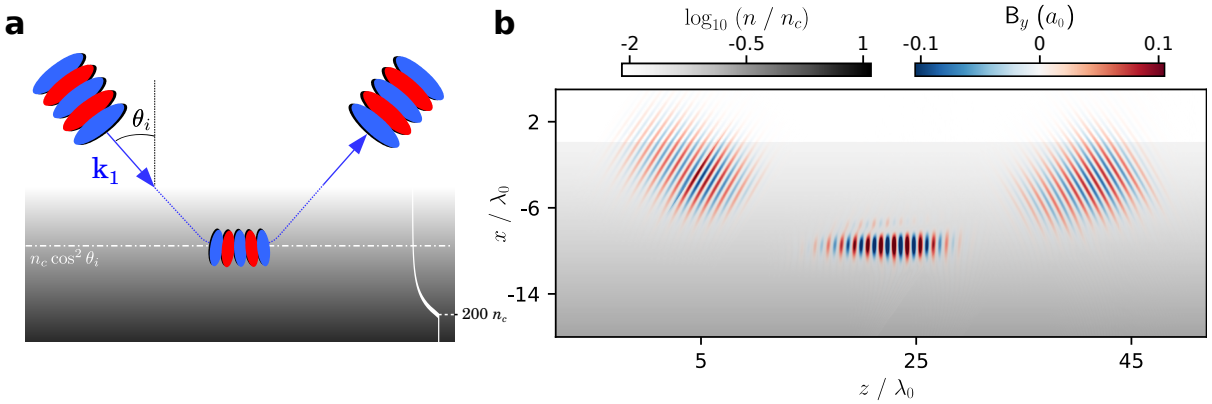

Figure 7.17: **2D-Reflection on plasma mirror with a very long density gradient at low intensity** - Panel (a) is a schematic drawing of this reflection where as always the laser pulses are pictured in blue and red and the plasma in gray. Panel (b) is the simulation performed in the same setup as panel (a) at low intensity ($a_0 = 0.1$ and $L_g = 5\lambda_0$) and is the combination of three snapshots, respectively taken at $t = 27T_0$, $t = 49.5T_0$ and $t = 72T_0$.

[4] Sakharov and Kirsanov, 1994; Decker et al., 1996; Quesnel, Mora, et al., 1997; Eliseev et al., 1998; Barr et al., 2000; Young et al., 2001

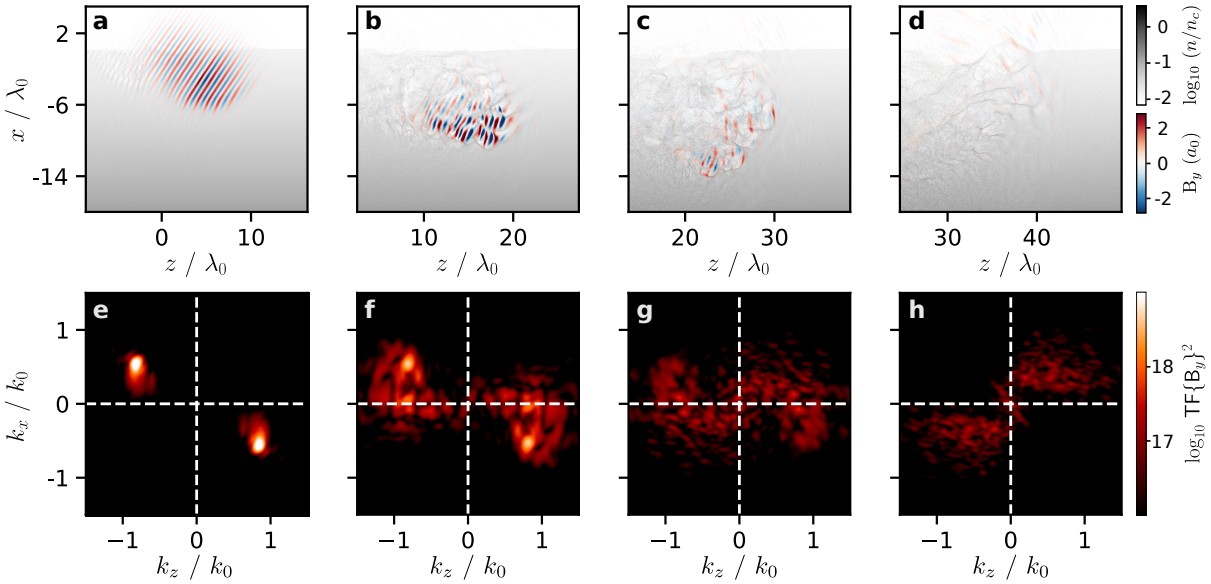

Figure 7.18: **2D-Reflection on plasma mirror with a very long density gradient at relativistic intensity** - The four upper panels are snapshots of the interaction of the laser ($a_0 = 3$ in color scale) on a very long gradient plasma ($L_g = 5\lambda_0$ in gray log scale) at respectively $t = 27T_0$, $t = 40.5T_0$, $t = 54T_0$ and $t = 67.5T_0$. The lower panels display the Fourier transform of the B_y field in log scale at the same times.

can be either an electron plasma wave in the case of SRS or an ion sound wave in the case of SBS. For ultrashort pulses, the interaction spans only over tens of laser periods during which the ion dynamics are mostly negligible. The SBS is thus unlikely. The absorption may be a combination of SRS and filamentation instabilities. Unfortunately, extra time would be needed to completely describe this regime, particularly rich in plasma physical processes and instabilities.

Conclusion

At relativistic intensities, the interaction between an ultra intense laser and a plasma mirror in the long gradient regime had not been fully studied in the literature so far. However, in most of experiments on solid targets, a poor beam contrast can often lead to density gradient scale lengths relatively long (typically the order of magnitude of the laser wavelength) for which a new mechanism happens.

This mechanism was found to be stochastic heating, where electrons in the underdense part of the plasma gain energy in the standing wave formed by the interference of incident and reflected field. In order to find such heating in the underdense layer, the overdense part is nevertheless important as it creates the secondary wave.

We also investigated the dependency on the underdense layer density. It was found that the energy gained by the electrons is relatively independent from the density, which legitimates the following chapter based on analytical motion of free electrons in two waves. However, the electron emission towards vacuum is strongly dependent from the density In addition to the stochastic heating, in 2D/3D simulations, we noticed that the laser expels electrons out of the focal volume, generating quasi-static fields along surface. These fields present a magnitude equivalent to the incident laser pulse and persist after the laser has passed.

The stochastic heating emerges at a specific laser intensity and below this threshold the resonance absorption is dominant (at least for p-polarization). At very long gradients, there is no clear interference field as the laser is continuously turning into the plasma. That should be an upper limit for stochastic heating. In this regime, strong parametric instabilities seemed to dominate the general behaviour at relativistic intensities but were not explored extensively in this manuscript.

8 Stochastic Heating in Plane Waves

The acceleration of free electrons in multiple electro-magnetic waves is a subject of interest for many fields of physics specifically in magnetic nuclear fusion or laser-plasma interaction. For many years, the theory behind stochastic heating has been studied with advanced mathematical derivations such as the super-Hamiltonian formalism [Mendonca, 1983; Bourdier et al., 2005] or the quasilinear theory [Rax, 1992; Rechatin, 2009]. Despite fair quantitative conclusions, these theories fail to provide an intuitive physical understanding of the processes at play.
In this chapter, we propose a different approach based on the equations of motion and temporal evolution of particles in phase space. The idea is to develop an alternative formalism, made of simple physical concepts, that will be easily understandable by non-specialists of chaos theory or Hamiltonian formalism and that allows to very quickly derive very accurate values of chaos thresholds as a function of laser parameters.
We will at first write the equations of motion in two counter-propagating waves in the form of pendulum equations, which are extensively studied dynamical systems, known to exhibit chaos in some cases. Then, we will show that this formalism is useful to describe particle diffusion, chaos threshold or electron trajectories. Finally, this chapter is closed by introducing an angle of incidence between the two waves, which makes the mechanism more complex but allows for direct comparisons with PIC simulations and experiments.

Contents

8.1 Electron Motion in an Electro-Magnetic Field

8.1.1 Equation of motion and canonical momentum conservation

In the previous chapters, we saw that PIC simulations can capture most of the physical processes at play to finely reproduce the experiments. Nevertheless, because of their complexity, it is sometimes extremely challenging to extract quintessential concepts among the large amounts of data produced. Studying stochastic heating does not require to consider collective dynamics. We would prefer using reduced models, which provide quantitative results, while being highly tractable. In this whole chapter, we run only particle tracker simulations, where plane waves propagate and interfere in a medium exclusively composed of free electrons. The simulated results are supported by a theoretical study based on equations of motion.

Let us start by deriving the electron motion in a given electro-magnetic field in the relativistic regime. The equation of motion for a single electron reads:

$$\frac{\mathrm{d}\boldsymbol{p}}{\mathrm{d}t} = -e\Big(\boldsymbol{E} + \boldsymbol{v}\times\boldsymbol{B}\Big) \quad \text{and} \quad \boldsymbol{p} = m\gamma\boldsymbol{v}. \tag{8.1}$$

It is interesting to introduce the vector potential, defined as:

$$\boldsymbol{E} = -\frac{\partial \boldsymbol{A}}{\partial t} \quad \text{and} \quad \boldsymbol{B} = \boldsymbol{\nabla}\times\boldsymbol{A}. \tag{8.2}$$

As a single electron is considered here, V does not appear in Eq. (8.2). The equation of motion becomes:

$$\begin{aligned}\frac{\mathrm{d}\boldsymbol{p}}{\mathrm{d}t} &= -e\Big(-\frac{\partial \boldsymbol{A}}{\partial t} + \boldsymbol{v}\times(\boldsymbol{\nabla}\times\boldsymbol{A})\Big)\\ &= -e\Big(-\frac{\partial \boldsymbol{A}}{\partial t} + \boldsymbol{\nabla}(\boldsymbol{v}\cdot\boldsymbol{A}) - (\boldsymbol{v}\cdot\boldsymbol{\nabla})\boldsymbol{A}\Big).\end{aligned} \tag{8.3}$$

Now, let us consider only plane waves propagating along the $\boldsymbol{x}$-direction. The polarization directions are then the $\boldsymbol{y}$ and $\boldsymbol{z}$ axes. As the electro-magnetic fields are invariant by translation along the transverse directions, it comes that:

$$\begin{aligned}&\bullet\quad \boldsymbol{\nabla}(\boldsymbol{v}\cdot\boldsymbol{A}) = \left(v_y\frac{\partial A_y}{\partial x} + v_z\frac{\partial A_z}{\partial x}\right)\boldsymbol{x} = \left(\boldsymbol{v}_\perp\cdot\frac{\partial \boldsymbol{A}_\perp}{\partial x}\right)\boldsymbol{x},\\ &\bullet\quad (\boldsymbol{v}\cdot\boldsymbol{\nabla})\boldsymbol{A} = v_x\frac{\partial A_y}{\partial x}\boldsymbol{y} + v_x\frac{\partial A_z}{\partial x}\boldsymbol{z} = v_x\frac{\partial \boldsymbol{A}_\perp}{\partial x},\end{aligned} \tag{8.4}$$

where the symbol $\perp$ stands for the transverse components. It leads to two equations:

- projection along $\boldsymbol{x}$: $$\frac{\mathrm{d}p_x}{\mathrm{d}t} = -e\left(\boldsymbol{v}_\perp\cdot\frac{\partial \boldsymbol{A}_\perp}{\partial x}\right), \tag{8.5}$$
- projection along $\perp$: $$\frac{\mathrm{d}\boldsymbol{p}_\perp}{\mathrm{d}t} = e\left(\frac{\partial}{\partial t} + v_x\frac{\partial}{\partial x}\right)\boldsymbol{A}_\perp = e\frac{\mathrm{d}\boldsymbol{A}_\perp}{\mathrm{d}t}, \tag{8.6}$$

where we recognize the total derivative of $\boldsymbol{A}_\perp$. The Eq. (8.6) is the so-called *canonical momentum conservation* equation:

$$\boxed{\frac{\mathrm{d}}{\mathrm{d}t}\Big(\boldsymbol{p}_\perp - e\boldsymbol{A}_\perp\Big) = 0 \quad \Leftrightarrow \quad \boldsymbol{p}_\perp - e\boldsymbol{A}_\perp = \mathrm{C}^{\mathrm{st}}.} \tag{8.7}$$

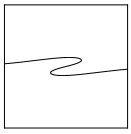

$\boldsymbol{p}_\perp - e\boldsymbol{A}_\perp$ is found to be a motion invariant. A particle initially at rest cannot gain any energy in transverse directions, when it interacts with an electromagnetic pulse.

Using the conservation of the transverse canonical momentum in Eq. (8.5), it is possible to find the differential equation in p_x:

$$\frac{\mathrm{d}p_x}{\mathrm{d}t} = -e\left(\frac{\boldsymbol{p}_\perp}{m\gamma}\cdot\frac{\partial \boldsymbol{A}_\perp}{\partial x}\right) = -\frac{e^2}{2m\gamma}\frac{\partial A_\perp^2}{\partial x}, \tag{8.8}$$

where $A_\perp^2 = A_y^2 + A_z^2$. The right-hand side of the equation is the so-called *ponderomotive force*. Let us now derive an equation for the position. To do so, we differentiate the particle velocity:

$$\begin{aligned}\frac{\mathrm{d}v_x}{\mathrm{d}t} &= \frac{1}{m\gamma}\frac{\mathrm{d}p_x}{\mathrm{d}t} - \frac{p_x}{m\gamma^2}\frac{\mathrm{d}\gamma}{\mathrm{d}t}\\ &= -\frac{e^2}{2m^2\gamma^2}\frac{\partial A_\perp^2}{\partial x} - \frac{v_x}{\gamma}\frac{1}{2\gamma m^2c^2}\left(\frac{\mathrm{d}p_\perp^2}{\mathrm{d}t} + 2p_x\frac{\mathrm{d}p_x}{\mathrm{d}t}\right)\\ &= -\frac{e^2}{2m^2\gamma^2}\frac{\partial A_\perp^2}{\partial x} - \frac{e^2 v_x}{2\gamma^2 m^2c^2}\left(\frac{\mathrm{d}A_\perp^2}{\mathrm{d}t} - v_x\frac{\partial A_\perp^2}{\partial x}\right).\end{aligned} \tag{8.9}$$

Finally, with $\dot{x} = \mathrm{d}x/\mathrm{d}t = v_x$ and the formula for the total derivative of $A_\perp^2$, the equation of motion in the relativistic regime reads:

$$\boxed{\frac{\mathrm{d}^2x}{\mathrm{d}t^2} + \frac{e^2}{2m^2\gamma^2}\left(\frac{\partial}{\partial x} + \frac{\dot{x}}{c^2}\frac{\partial}{\partial t}\right)A_\perp^2 = 0,} \tag{8.10}$$

where the red color highlights the relativistic terms. In the classical limit, i.e., $\gamma \to 1$ and $|\dot{x}| \ll c$, it simply becomes:

$$\frac{\mathrm{d}^2x}{\mathrm{d}t^2} + \frac{e^2}{2m^2}\frac{\partial A_\perp^2}{\partial x} = 0. \tag{8.11}$$

Eq. (8.10) is valid for any superposition of laser plane waves propagating along x. In the next sections, we will expand $A_\perp^2$ for different wave configurations and exhibit the main properties of the resulting particle dynamics.

8.1.2 Electron dynamics in a single plane wave

Firstly, let us start with the simplest case: the electron dynamics in a single plane wave linearly polarized along the z-axis. In this configuration, the vector potential reads:

$$\boldsymbol{A} = A_0\sin(k_0x - \omega_0t)\boldsymbol{z}, \tag{8.12}$$

with $A_0 = a_0mc/e$. In this configuration, it is possible to derive the fully relativistic orbits of electrons. This was presented for example in [Hartemann et al., 1995]. In this case, the system admits an additional motion invariant $mc\gamma - p_x$:

$$\begin{aligned}mc\frac{\mathrm{d}\gamma}{\mathrm{d}t} &= -\frac{e}{c}\boldsymbol{v}\cdot\boldsymbol{E} = \frac{e}{\gamma mc}p_z\frac{\partial A_z}{\partial t}\\ &= \frac{e^2}{2\gamma mc}\frac{\partial A_z^2}{\partial t}\\ &= -\frac{e^2}{2\gamma m}\frac{\partial A_z^2}{\partial x},\\ &= \frac{\mathrm{d}p_x}{\mathrm{d}t}\end{aligned}$$

$$\frac{\mathrm{d}}{\mathrm{d}t}\Big(mc\gamma - p_x\Big) = 0. \tag{8.13}$$

There are 3 independent motion invariants (two from Eq. (8.7) and $mc\gamma - p_x$) in a 3D space, which makes the system integrable in the Liouville sense. Therefore, the system cannot exhibit any chaotic behaviour.

In our case, the equations of motion in the classical regime are sufficient to give a physical insight of the electron dynamics. They can easily be derived from Eq. (8.11):

$$\frac{\mathrm{d}^2 x}{\mathrm{d}t^2} + 2a_0^2 c^2 k_0 \sin\left(2(k_0 x - \omega_0 t)\right) = 0. \tag{8.14}$$

We define a new variable $\xi \to 2(k_0 x - \omega_0 t)$, position of the electron in its co-moving frame. ξ satisfies the following equation:

$$\frac{\mathrm{d}^2 \xi}{\mathrm{d}t^2} + 4a_0^2 \omega_0^2 \sin\xi = 0. \tag{8.15}$$

We recognize there the well-known equation of a *simple gravity pendulum*. The oscillation period of this pendulum would be $T = \pi/a_0\omega_0$ and the solution can be expressed using elliptic integrals. The total particle motion along the x-axis is then a combination of a periodic behaviour related to the pendulum and a drift towards $x > 0$.

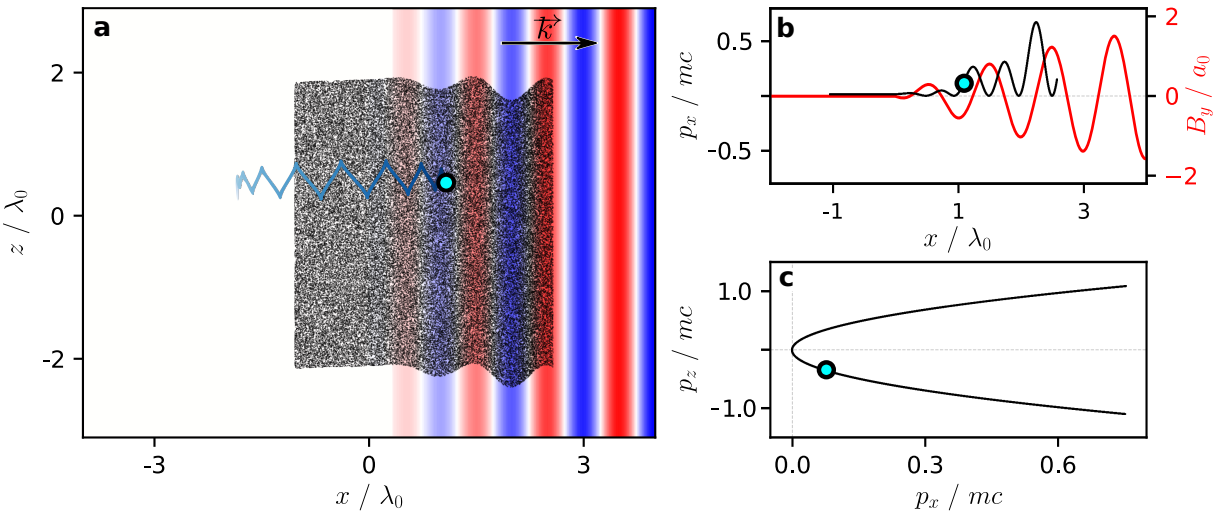

Figure 8.1: **Electron dynamics in a single linearly polarized wave** - In panel (a), a laser pictured from blue to red is traveling towards positive x through an electron cloud pictured as black dots. One particle is highlighted as a blue dot and its orbit as a blue line. At the same time step, we also display the electron distribution in different spaces: (b): (x, p_x) and (c): (p_x, p_z). To assist the reader, the magnetic field is plotted in panel (b) as well.

In order to illustrate this statement, we picture in Fig. 8.1–a a plane wave, propagating towards positive $\boldsymbol{x}$ and impinging on an electron cloud initially at rest and laid out randomly within a square: $-2\,\lambda_0 \leq\ x_{t=0},\ z_{t=0}\ \leq 2\,\lambda_0$. One electron of this population is highlighted in blue and its trajectory along time is pictured as the blue line in Fig. 8.1–a.

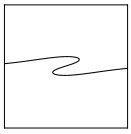

When the particles are inside the wave, they oscillate along the polarization direction, as one can see in Fig. 8.1–a in the ($x > 0$)-half space. But after the wave has passed, the global form of the distribution returns to a square. The final state is comparable to the initial one but slightly shifted towards positive x (see the ($x < 0$)-half space). The drift is clearly visible on the blue trajectory. The corresponding particle has traveled around $3\,\lambda_0$ since the beginning of the simulation.

Regarding the distributions in phase space (see Figs. 8.1–b, c), the system is again very simple. Starting from the formulas leading to motion invariants, it is possible to express all momentum components in term of A_z only. For p_y and p_z, Eq. (8.7) gives instantly $p_y = 0$ and $p_z = eA_z$ because the initial distribution is at rest. For p_x, we use the last invariant (see Eq. (8.13)):

$$\begin{aligned} & mc\gamma - p_x = mc \\ \Leftrightarrow \quad & m^2c^2 + p_x^2 + p_y^2 + p_z^2 = (mc + p_x)^2 \\ \Leftrightarrow \quad & 2mc\,p_x = p_z^2 = e^2A_z^2. \end{aligned} \tag{8.16}$$

It results that every momentum component is known at all time and at every position across space. From Eq. (8.16) in particular, we found that p_x is always positive and oscillates at twice the laser frequency (see Fig. 8.1–b). It is coherent with the particle drift towards positive $\boldsymbol{x}$. In addition, it also comes that the relation between p_z and p_x is an equation of a parabola as illustrated in Fig. 8.1–c. During its propagation in phase space (p_x, p_z), an electron would just travel along the parabola. At the end of the interaction, A_z returns to zero and so do p_x and p_z. As previously stated, this shows that particles cannot gain energy in a single plane wave (see Figs. 7.4–c, f, page 104 for example).

In the following, we add a second laser pulse and show how it affects the electron motion.

8.2 Electron Dynamics in Two Counter-Propagating Plane Waves

8.2.1 Equations of motion

We have already seen in PIC simulations (Sec. 7.1.3 page 102) that when a second laser wave is added, the electron dynamics in the interference field may become chaotic and particularly complex after few laser cycles. In fact, the chaotic nature of the system can be directly evidenced, even in a non relativistic regime, through the classical equations of motion. These can be written as different equations of simple or forced pendulums — dynamical systems known to exhibit chaos (see Ch. 2).

Starting from Eq. (8.10) (page 121) in the classical limit − i.e., without the red terms −, we write the equations of motion for two different cases: (i) two circularly polarized waves and (ii) two waves linearly polarized in the same direction. For now, these two waves are counter-propagating to one another along the $\boldsymbol{x}$ direction. This would correspond to studying electron dynamics in the interference pattern of incident and reflected fields occurring inside the underdense part of the target in the long gradient regime (see chapters 5 and 7). In all the following, the two waves will feature the same amplitude a_0 and angular frequency ω_0 to emulate the reflective wave produced by the overdense layer of the solid target.

Equations of motion in two circularly polarized waves. In this case, the transverse vector potential $A_\perp$ for each wave reads :

$$\begin{cases} \boldsymbol{A}_1 = & A_0\big(\cos(\omega_0 t - k_0 x)\boldsymbol{y} + \sin(\omega_0 t - k_0 x)\boldsymbol{z}\big)/\sqrt{2}, \\ \boldsymbol{A}_2 = & A_0\big(\cos(\omega_0 t + k_0 x)\boldsymbol{y} \pm \sin(\omega_0 t + k_0 x)\boldsymbol{z}\big)/\sqrt{2}, \end{cases} \tag{8.17}$$

where $\boldsymbol{A}_1$ corresponds to the wave propagating towards positive x and $\boldsymbol{A}_2$ the one propagating towards negative x. The first laser is chosen to be right-handed circularly (RHC) polarized but the second one can either be RHC polarized (negative sign) or left-handed circularly (LHC) polarized (positive sign).

In the classical limit, we only need to compute the spatial partial derivative of $A_\perp^2 = A_y^2 + A_z^2$ to explicit Eq. (8.10), which reads:

$$\frac{\partial A_\perp^2}{\partial x} = \frac{A_0^2}{2}\frac{\partial}{\partial x}\Big(\Big[\cos(\omega_0 t - k_0 x) + \cos(\omega_0 t + k_0 x)\Big]^2 + \Big[\sin(\omega_0 t - k_0 x) \pm \sin(\omega_0 t + k_0 x)\Big]^2\Big). \tag{8.18}$$

After developing the inner brackets, we get:

$$\frac{\partial A_\perp^2}{\partial x} = \begin{cases} A_0^2\,\dfrac{\partial}{\partial x}\Big(1 + \cos\left(2\omega_0 t\right)\Big) = 0 & \text{if } \boldsymbol{A}_2 \text{ is RHC}, \\ A_0^2\,\dfrac{\partial}{\partial x}\Big(1 + \cos\left(2k_0 x\right)\Big) = -2\,A_0^2\,k_0\,\sin\left(2k_0 x\right) & \text{if } \boldsymbol{A}_2 \text{ is LHC}, \end{cases} \tag{8.19}$$

where we used the following trigonometric formulas:

$$\forall(\varphi,\ \psi) \in \mathbb{R}^2, \quad \left\| \begin{array}{l} \bullet\ \ \cos^2\varphi + \sin^2\varphi = 1, \\ \bullet\ \ \cos\varphi\cos\psi \pm \sin\varphi\sin\psi = \cos(\varphi \mp \psi). \end{array} \right. \tag{8.20}$$

Back to Eq. (8.10), we find:

$$\frac{\mathrm{d}^2 x}{\mathrm{d}t^2} = \begin{cases} 0 & \text{if RHC}, \\ a_0^2 c^2 k_0\,\sin(2k_0 x) & \text{if LHC}. \end{cases} \tag{8.21}$$

We define a new variable $\theta \to \pi + 2k_0 x$, its temporal evolution is given by:

$$\boxed{\begin{array}{ll} \dfrac{\mathrm{d}^2\theta}{\mathrm{d}t^2} = 0 & \text{if RHC}, \\ \dfrac{\mathrm{d}^2\theta}{\mathrm{d}t^2} + \underbrace{2\,a_0^2\,\omega_0^2}_{\omega^2}\,\sin\theta = 0 & \text{if LHC}. \end{array}} \tag{8.22}$$

When the two lasers are both RHC polarized, the first line of Eq. (8.22) shows that electrons do not undergo any force along the $\boldsymbol{x}$ direction. If particular, when $v_{x|t=0} = 0$, one can note that they never move along the longitudinal direction. This statement stays valid even in the relativistic regime because the relativistic equation of motion, Eq. (8.8), (page 121) simply becomes $\mathrm{d}p_x/\mathrm{d}t = 0$. Of course, the transverse dynamics still exist, since the motion is constrained by the canonical momentum conservation (Eq. (8.7), page 120). Overall, the motion is known at whole time: $p_x = 0$ and $\boldsymbol{p}_\perp = \boldsymbol{A}_\perp$ and only presents a limited interest. Then, it will not be discussed further ahead.

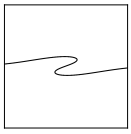

When the two laser waves present opposite circular polarizations, we find that the equations of motion can be written again as an equation of a simple gravity pendulum. The longitudinal dynamics can be expressed using elliptic functions. The swing period of the corresponding pendulum would be $T = 2\pi/\omega = \sqrt{2}\pi/a_0\omega_0$ and its proper angular frequency ω is linearly depending on a_0. It means that the higher the laser amplitude, the faster the pendulum. Note also that when $a_0 = 1/\sqrt{2}$, the pendulum oscillates at the laser frequency ($\omega = \omega_0$).

The system is again fully integrable even in the relativistic regime and we find a third motion invariant, which is simply γ:

$$\begin{aligned} mc\frac{\mathrm{d}\gamma}{\mathrm{d}t} &= \frac{e^2}{2\gamma mc}\frac{\partial A_\perp^2}{\partial t} \\ &= \frac{e^2}{2\gamma mc}\frac{\partial}{\partial t}\Big(1+\cos\left(2k_0x\right)\Big) = 0 \end{aligned} \tag{8.23}$$

The electrons cannot gain any energy in this configuration. p_x and $\boldsymbol{p}_\perp$ are still evolving in time but the kinetic energy does not vary. Because the system is integrable in the Liouville sense, the electron motion is completely predictable and there cannot be any chaotic behaviour.

Equations of motion in two linearly polarized waves. This time, both laser waves show a linear polarization along the same direction − e.g., $\boldsymbol{z}$. In the following, we refer to this configuration as two p-polarized wave case (or just p/p case)[1]. It will matter however in Sec. 8.5, when the angle of incidence between the two waves will be introduced. Nevertheless, for two counter-propagating and similarly linearly polarized waves, the transverse vector potential $\boldsymbol{A}_\perp$ for each wave reads:

$$\begin{cases} \boldsymbol{A}_1 = A_0\sin(\omega_0 t - k_0 x)\boldsymbol{z}, \\ \boldsymbol{A}_2 = A_0\sin(\omega_0 t + k_0 x)\boldsymbol{z}. \end{cases} \tag{8.24}$$

and the spatial partial derivative of $A_\perp^2$:

$$\begin{aligned} \frac{\partial A_\perp^2}{\partial x} &= A_0^2\frac{\partial}{\partial x}\Big(\Big[\sin(\omega_0 t - k_0 x) + \sin(\omega_0 t + k_0 x)\Big]^2\Big) \\ &= 4A_0^2\frac{\partial}{\partial x}\Big(\cos^2(k_0 x)\sin^2(\omega_0 t)\Big) \\ &= -8A_0^2 k_0\sin^2(\omega_0 t)\ \sin(k_0 x)\ \cos(k_0 x) \\ &= -2A_0^2 k_0\sin(2k_0 x)(1-\cos(2\omega_0 t)), \end{aligned} \tag{8.25}$$

where we used the following trigonometric formulas:

$$\forall(\varphi,\ \psi)\in\mathbb{R}^2,\quad \left\|\begin{array}{l} \bullet\quad \sin\left(\varphi-\psi\right)+\sin\left(\varphi+\psi\right) = 2\sin\varphi\cos\psi, \\ \bullet\quad 2\sin\varphi\cos\varphi = \sin 2\varphi, \\ \bullet\quad 2\sin^2\varphi = 1-\cos 2\varphi. \end{array}\right. \tag{8.26}$$

The equation of motion becomes:

$$\frac{\mathrm{d}^2x}{\mathrm{d}t^2} - a_0^2c^2k_0\sin\left(2k_0x\right)\left(1-\cos\left(2\omega_0 t\right)\right) = 0. \tag{8.27}$$

[1]The use of p here is an abuse of language, because for two counter-propagating waves, there is indeed no difference between p or s-polarizations.

Again, we define $\theta \to \pi + 2k_0 x$ and its temporal evolution after a time shift ($t \to t + \pi/2\omega_0$) is given by:

$$\boxed{\frac{\mathrm{d}^2\theta}{\mathrm{d}t^2} + \underbrace{2\,a_0^2\,\omega_0^2}_{\omega^2}\sin\theta(1+\cos(2\omega_0 t)) = 0.} \tag{8.28}$$

This equation is the equation of a pendulum commonly known as *Kapitza's pendulum* [Kapitza, 1951,1951]. In the 50's, Kapitza studied the properties of a rigid pendulum in which the pivot point (a.k.a., the attached point) quivers in the vertical direction, up and down. In particular, Kapitza demonstrated that under certain conditions based on the frequency of the vertical oscillations, the stable position appears to be above its attachment point. In contrast to the gravity pendulum, the stable position now lies above the pivot, while the position below the pivot, is no longer stable. In this regard, the term of *inverted pendulum* is also widely popular in the literature.

In the general case, the equation governing the bob motion for a Kapitza's pendulum is given by:

$$\frac{\mathrm{d}^2\theta}{\mathrm{d}t^2} + \frac{g}{l}\sin\theta\left(1 + \frac{a\,\nu^2}{g}\cos\nu t\right) = 0, \tag{8.29}$$

with a and ν respectively the amplitude and the frequency of the vertical oscillations, g the free fall acceleration and l the length of the pendulum. It is possible to write Eq. (8.28) in a similar form as Eq. (8.29) thanks to the following changes of variable:

$$\begin{aligned} g/l &\longleftrightarrow \omega^2 = 2a_0^2\omega_0^2, \\ \nu &\longleftrightarrow 2\omega_0, \\ a\,\nu^2/g &\longleftrightarrow 1. \end{aligned} \tag{8.30}$$

Note that in all Kapitza's studies, the variable parameters were a and ν, quantities imposed by the external oscillator. However, in our equations, among a_0 and ω_0, only the laser amplitude can be varied in experiments, which directly changes the proper angular frequency ω of the mathematical pendulum. It would be equivalent for a Kapitza's pendulum to change the length l.

For this type of forced pendulum, the stability of the upper position is ensured if the suspension point is vibrating with small amplitudes $a \ll l$ and with a frequency much higher than the proper frequency $\nu \gg g/l$. These two inequalities give the same general condition on the laser amplitude:

$$a_0 \ll 1/\sqrt{2} \simeq 0.707. \tag{8.31}$$

Beyond this threshold, the upper position is *a priori* no longer stable and it means that a transition toward a non predictable regime should be expected. Indeed, we have already seen in PIC simulations (see Sec. 7.1.2, page 101) that chaotic behaviour starts appearing at relatively low intensity ($a_0 \gtrsim 0.15$)

In the classical limit, the system is analogous to a forced pendulum, system known to exhibit chaos in some cases (see Sec. 2.2, page 34). In order to understand chaos origin and properties, it is unnecessary to consider the relativistic terms, which make the equations of motion fundamentally non-linear and complicate the analytical derivations. Actually, as we will see further ahead, introducing relativistic terms rather unexpectedly tends to stabilize the system,

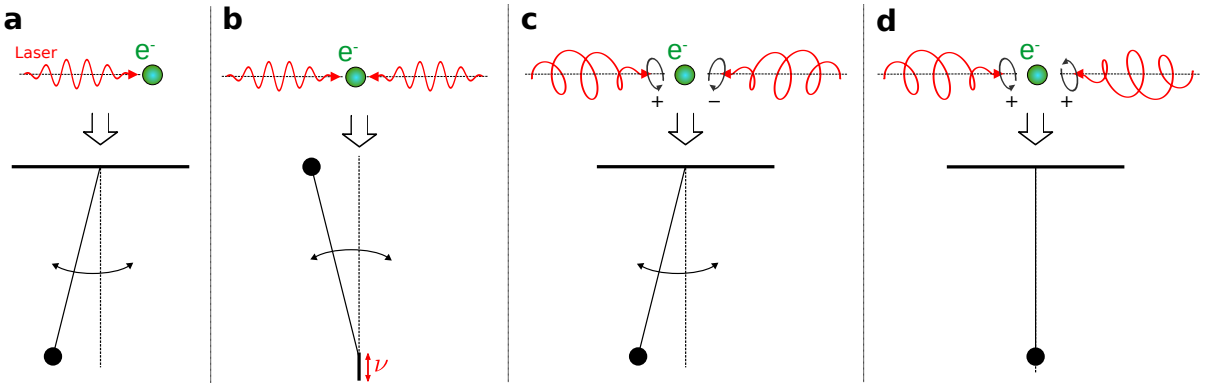

Figure 8.2: **Summary drawing of the comparison electron dynamics-pendulum** - The different panels present a different laser electron interaction setup: (a) one linearly polarized wave, (b) two linearly polarized waves, (c) one RHC and one LHC polarized waves and (d) two RHC polarized waves. For each case, we recall its equivalent pendulum: (a) and (c): simple gravity pendulum, (b) Kapitza or inverted pendulum and (d) pendulum *at rest*.

because the particle velocities remain bounded to c. Also, the magnitude of the ponderomotive force is lowered by a factor γ^2 in comparison to its classical value (see Eq. (8.10), page 121). Highly energetic particles would experience less influence of different laser fields and would not be accelerated as much as they would have without relativistic effects.

In Fig. 8.2, we have summarized the various configurations of laser wave polarizations discussed herein. Based on the inherent forms of the pendulum equations, it is possible to discriminate non-chaotic and chaotic configurations. So far, only the setup with two linearly polarized waves does introduce potential chaotic behaviour.

8.2.2 Numerical analysis of electron dynamics in two waves

At this point, one cannot go any further in the analytical derivation and we propose to study the dynamics thanks to PT simulations. This section aims to lay the foundation of a new formalism and to introduce the different observables important to understand the following. We start by giving a descriptive overview of the electron dynamics in the two different configurations of interest: RHC/LHC and p/p.

In all of these simulations, 10^5 electrons are initially located along the x-axis in the range $[-\lambda_0, \lambda_0]$, with zero longitudinal velocity ($p_{x|_{t=0}} = 0$). The electromagnetic waves are considered infinite in time and space, which imposes that all particles are directly initialized within the interference field. To ensure the verification of the conservation of the transverse canonical momentum at any time (Eq. (8.7), page 120), the particle transverse momenta need to be initialized to the corresponding transverse vector potentials at their positions: $\boldsymbol{p}_{\perp|_{t=0}}(x) = e\boldsymbol{A}_{\perp|_{t=0}}(x)$.

Dynamics in two circularly polarized waves. For monochromatic plane waves, the combination of a RHC and a LHC polarized waves defined in Eq. (8.17) (page 124) leads to the following interference electromagnetic field:

$$\begin{cases} \boldsymbol{E} = +\sqrt{2}\, E_0 \cos(k_0 x)\, (\sin(\omega_0 t)\, \boldsymbol{y} - \cos(\omega_0 t)\, \boldsymbol{z}), \\ \boldsymbol{B} = -\sqrt{2}\, B_0 \sin(k_0 x)\, (\sin(\omega_0 t)\, \boldsymbol{y} - \cos(\omega_0 t)\, \boldsymbol{z}), \end{cases} \tag{8.32}$$

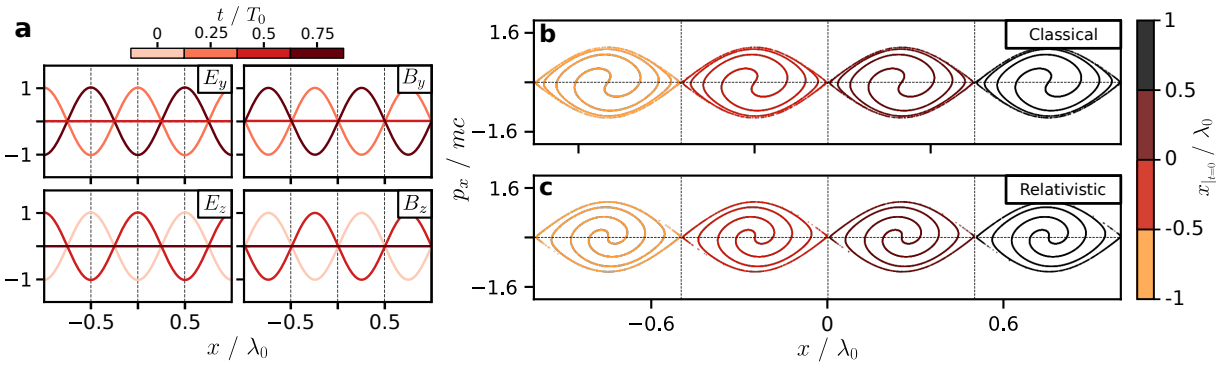

Figure 8.3: **Electron dynamics in RHC/LHC configuration** - Panel (a) shows the shape of the interference field in space, created by 2 counter-propagating RHC polarized and LHC polarized waves. Each line color corresponds to a different time within a laser period. In addition, the magnetic field nodes are highlighted as black dash lines. In panels (b) and (c), we represent the electron distributions in phase space after $2T_0$ in the fields of panel (a) for $a_0 = 0.8$, when using the classical (b) and relativistic (c) forms of the equations of motion. The discrete color scale depends on the different buckets, in which particles were initially located.

This interference field is displayed in Fig. 8.3–a in space at different times within a laser period (see the red color scale). It forms a standing wave, where time and space are decoupled. The electric field is seen to show nodes for each $k_0 x = \pi/2 + n\pi$ ($\forall n \in \mathbb{Z}$) and the magnetic field for each $k_0 x = n\pi$.

The electron distribution after 2 laser periods in this field is pictured in Fig. 8.3, when using the classical (Fig. 8.3–b) and relativistic (Fig. 8.3–c) forms of the equations of motion. In the remainder of this chapter, the color scale of particle markers in phase space is related to the electron initial position $x_{|t=0}$ and expressed as a set of 4 discrete colors corresponding to a different initial *magnetic field bucket*, i.e., the area between two magnetic field nodes, delimited by black dash lines. Each bucket is centered around an electric field node. From the different profiles of Figs. 8.3–b, c, one can infer three important points:

- the distributions look like simple pendulum phase portraits, where all the trajectories are trapped. The particles are simply rotating around fixed points on a close elliptical orbit. It happens that these fixed points exactly coincide with electric field nodes.
- the different colors do not mix, meaning that the particles are staying in their initial bucket all along the interaction.
- There is barely no difference between classical and relativistic regimes except for the slight change of amplitudes of the inner ellipses. In fact, the relativistic terms tends to damp p_x, forcing the particles to get closer to the electric field nodes at every pendulum proper period $T = 2\pi/\omega \simeq 0.88T_0$.

As stated in the previous subsection, the electron dynamics in two circularly polarized waves can be related to simple pendulum dynamics. In this case, the system seems to keep its simplicity in both classical and relativistic regimes.

Dynamics in two linearly polarized waves. When the laser polarizations are switched to linear, we showed that the laser particle interaction was similar to a Kapitza's pendulum, which is no more predictable when $a_0 \gtrsim 1/\sqrt{2}$. We should thus expect some clear signatures of chaos,

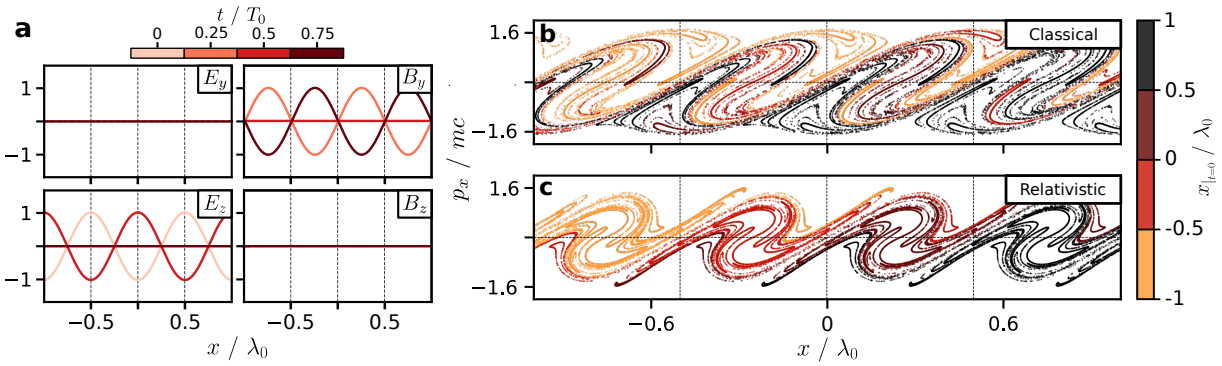

Figure 8.4: **Electron dynamics in *p*/*p* configuration** - Similar to Fig. 8.3 but for two p-polarized lasers.

when looking at the particle distribution in phase space for a laser amplitude $a_0 = 0.8 > 1/\sqrt{2}$. In this configuration, the interference field reads:

$$\begin{cases} \boldsymbol{E} = -2\,E_0 \cos(k_0 x)\cos(\omega_0 t)\,\boldsymbol{z}, \\ \boldsymbol{B} = +2\,B_0 \sin(k_0 x)\sin(\omega_0 t)\,\boldsymbol{y}. \end{cases} \tag{8.33}$$

This particular field is displayed in Fig. 8.4–a. Again the electric field presents nodes for each $k_0 x = \pi/2 + n\pi$ ($\forall n \in \mathbb{Z}$) and the magnetic field for each $k_0 x = n\pi$. In this configuration, the full magnetic and electric fields are in quadrature in space but also in time.

The electron distributions in this interference field are pictured in Figs. 8.4–b, c at $t = 2\,T_0$. We again perform the same simulation with either the classical or the relativistic equations of motion. However, this time, the two profiles present noticeable differences that are explained below:

- first, the particles can now migrate between buckets and the different colors are thus mixing along time. The associated particle diffusion is particularly strong in Fig. 8.4–b because the particles are allowed to be faster than the speed of the light. In the classical regime, we find that $v_{x,max} = p_{x,max}/m \simeq$ 1.6-1.7c and after only $2\,T_0$, the whole distribution is all mixed up. When the relativistic effects are taken into account (Fig. 8.4–c), the electron velocity is bounded to the speed of light. In the relativistic regime, we find $v_{x,max} = p_{x,max}/\gamma m \simeq 0.8c$ and fewer particles have left their initial bucket for this short time.

- The general form of the relativistic distribution of Fig. 8.4–c was already presented in the previous chapters as a typical *stretching and folding* pattern (see Fig. 7.4–e, page 104 or Fig. 7.8–c, page 108 for example). This effect is responsible for multi-layered structures especially near the magnetic field nodes (interface of the buckets). However, similarly to the circular polarization, the electric field nodes keep behaving as fixed points around which the whole distribution is rolling.

- The magnitude of the particle momentum is higher than the RHC/LHC configuration.

In the following, we stop using the classical equations of motion in simulation, which overestimate the heating and diffusion. However, for all analytical derivations, we continue to neglect relativistic terms. We now try to explain the temporal evolution of the electron distribution. In particular, we provide a clear physical explanation of the *stretching and folding* in phase space and why it can lead to chaos.

8.3 Stretching and Folding in Two Waves

8.3.1 A two-step mechanism leading to chaos

In this manuscript, we saw several times that the electron phase space distribution in two linearly polarized waves evolves in a peculiar fashion that we called *stretching and folding* (S&F). As its name suggests, it is a two-step mechanism combining a first step where the electron distribution is straighten (stretching phase) and a second one where it rotates around a fixed position (folding phase). Such a mechanism is actually fairly common in the culinary domain, when one wants to quickly distribute ingredients in a solid dough or introduce a multi-layer structure. Two famous examples are presented below:

- American candies called *Taffy*, a chewy candy obtained after a long pulling in a specific machine designed to stretch and fold the candy paste. The puller most in use today was firstly patented in [Richards, 1905] and a picture of such puller is displayed in Fig. 8.5–a. In his patent, the author drew several diagrams of taffy pulling in action. These drawings are reported in Fig. 8.5–b. These machines are also subject of interest in mathematics as in [Thiffeault, 2018], where taffy machines are described as topological toruses and compared to find the "best taffy puller in a mathematical case".

- Another examples is the puff pastry (or *pâte feuilletée*), a French dough presenting dozens of thin layers obtained by rolling out and folding a regular dough with fat. For a salted dough, it is possible to drop a single salt pinch on top before starting the process. Then, thanks to its chaotic motion, the salt will diffuse and be equally distributed inside the paste.

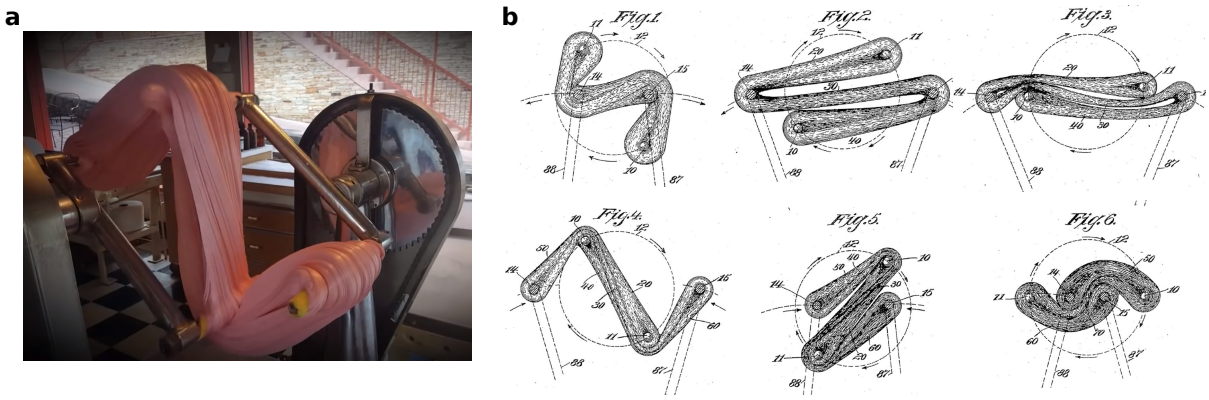

Figure 8.5: **A machine designed to stretch and fold candies: the taffy puller** - Both panels show a design presented in [Richards, 1905] with four rotating rods set on two axles. Panel (a) is a picture found on the Internet (**Source:** `https://www.youtube.com/watch?v=XnndSkcjlBw`), while panel (b) displays drawings directly imported from Richards' patent. In the picture of panel (a), the machine is found to be in the "Fig. 4" state of panel (b).

In the case of electrons in two waves, the stretching and folding occurs naturally, when the ponderomotive force evolves in time. As a reminder, the ponderomotive force reads in the two cases of interest (see Sec. 8.2, page 123 for the derivation):

- $-\partial_x A_\perp^2 = 2\,A_0^2 k_0\,\sin\left(2k_0 x\right)$ if RHC/LHC, (8.34)
- $-\partial_x A_\perp^2 = 2\,A_0^2 k_0\,\sin\left(2k_0 x\right)\left(1-\cos(2\omega_0 t)\right)$ if p/p. (8.35)

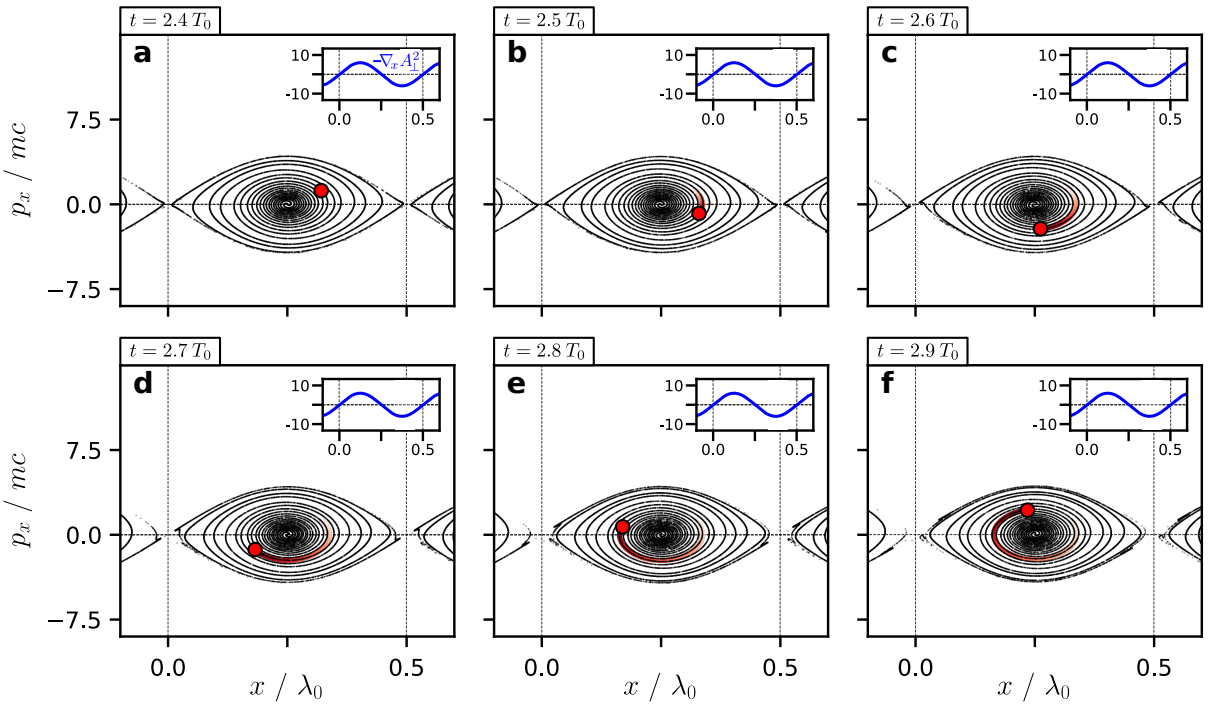

Figure 8.6: **Temporal evolution of the electron phase space distribution in the RHC/LHC case** - This figure illustrates different snapshots of the electron distribution in phase space at different times labeled on top of each panel. Here, the laser intensity is $a_0 = 3$. A typical particle is highlighted as a large red dot and its trajectory as the red trail. In the top-right corner of each panel, we plot the spatial profile of the ponderomotive force at each time.

S&F in the RHC/LHC configuration. In this case, the ponderomotive force is independent of time and just varies along the spatial direction. It constrains the electrons to follow the same motion during all the simulation.

In Fig. 8.6, we plot the evolution of the distribution of electrons at different times within half a laser period ($2.4\,T_0 \leq t \leq 2.9\,T_0$) in two oppositely circularly polarized lasers, with $a_0 = 3$. The plots are focused on a single magnetic bucket. A typical particle is highlighted in red and follows a trajectory on a close orbit, similarly to a simple gravity pendulum. Along this orbit and in the classical regime, the velocity is bounded:

$$\frac{\mathrm{d}^2\theta}{\mathrm{d}t^2} = -2\,a_0^2\,\omega_0^2\,\sin\theta \tag{8.36}$$

$$\frac{1}{2}\left(\frac{\mathrm{d}\theta}{\mathrm{d}t}\right)^2 = 2\,a_0^2\,\omega_0^2\,\cos\theta + C^{st}$$

$$v_\theta^2 = 4\,a_0^2\,\omega_0^2\,(\cos\theta - \cos\theta_0) \tag{8.37}$$

with θ_0, the initial position and v_θ the velocity of the particle in the θ-space. For small θ, Eq. (8.36) reduces into an equation of a harmonic oscillator and the trajectories close to the electric nodes, such the one of the red particle, are almost elliptical. The orbit defined with $\theta_0 = \pi$ delimits trapped and circulating particles and is called the separatrix. For a population initially at rest, all particles are located below the separatrix.

S&F in the p/p configuration. In this case, the force is now also oscillating in time (see Eq. (8.35)). The important thing to notice is that the temporal term — 1 – cos($2\omega_0 t$) — is

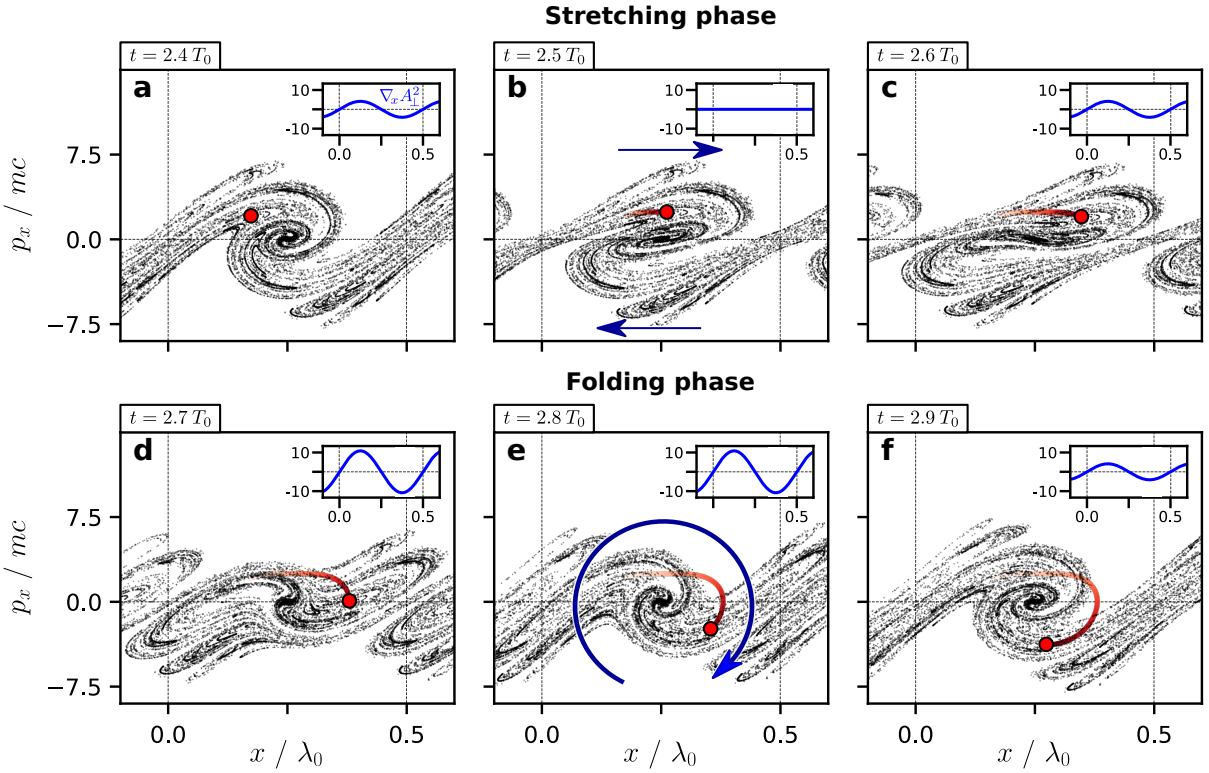

Figure 8.7: **Temporal evolution of the distribution of electrons in the p/p case** - Same figure as Fig. 8.6 for two p-polarized waves. This time the ponderomotive force evolves in time and the distribution undergoes two steps: (a-c) stretching phase with a longitudinal elongation illustrated by two blue arrows and (d-f) folding phase with a rotation around an electric field node illustrated by the curved blue arrow.

always positive, so the sign of the total force is given by the sign of $\sin(2k_0x)$. It means that simililarly to the RHC/LHC case, around an electric field node (e.g., $x = 0.25\,\lambda_0$), the force will always be positive on the left part ($x \leq 0.25\,\lambda_0$) and negative on the right part ($x \geq 0.25\,\lambda_0$). The consequence is that electrons are always attracted towards electric field nodes even in the p/p case.

Now, let us decompose the temporal electron dynamics in the interference field. Starting again at $t = 2.4\,T_0$, Fig. 8.7 exhibits two phases:

- $\mathbf{2.4\ T_0 \leq t \leq\ 2.65\ T_0}$ (Figs. 8.7–a-c): the ponderomotive force stays close to zero, letting the particles free from any force. Thus, they follow a ballistic motion, illustrated by the blue arrows in Fig. 8.7–b: all particles located in the upper part of the plot ($p_x > 0$) are traveling towards the positive x at constant velocity. Similarly, particles located in the lower part of the plot ($p_x < 0$) are traveling towards the negative x. The trajectory of the red particle in Fig. 8.7–c is almost straight and horizontal. The full distribution is extended on both sides of the x-axis, this is the **stretching phase**.

- $\mathbf{2.65\ T_0 \leq t \leq\ 2.9\ T_0}$ (Figs. 8.7–d-f): the ponderomotive force is strong and looks like the one obtained in the RHC/LHC case. Then, the electron motion is similar to Fig. 8.6, for which the particles were rotating around the electric field node. The rotation is illustrated with the blue curved arrow in Fig. 8.7–e. This arrow always points in a clockwise direction because the ponderomotive force keeps the same sign on both sides of an electric node along

time. The red trajectory describes a circular arc between Figs. 8.7–d and 8.7–f. The full distribution rotates around the electric field node, this is the **folding phase**.

S&F in a simplified model. The transition from one phase to the next is continuous since the ponderomotive force varies as a cosine of $2\omega_0 t$. As a toy model, we approximate the temporal term by a square signal to clearly dissociate the stretching from the folding. The temporal term is now a constant piecewise function[2] equal to 0 during the whole first $T_0/4$ period and 2 during the whole second $T_0/4$ period:

$$-\partial_x A_\perp^2 \quad \sim \quad \begin{cases} 0 & \text{for } t \in [0,\, T_0/4], \\ 4\, A_0^2 k_0 \, \sin\left(2k_0 x\right) & \text{for } t \in [T_0/4,\, T_0/2]. \end{cases} \tag{8.38}$$

This type of equation is known as the nonlinear Meissner's equation [Meissner, 1918] and is still widely studied in mathematics [A. P. Markeev, 2011; A. Markeev, 2015; Burov and Nikonov, 2019]. Using this formulation, it is easy to separate the two phases. It instantly comes that the particles follow a ballistic motion for $t \in [0,\, T_0/4]$ and a simple pendulum-type of motion for $t \in [T_0/4,\, T_0/2]$ (same form as the RHC/LHC case in Eq. (8.34), page 130). The electron dynamics in such an interference field is pictured in Fig. 8.8.

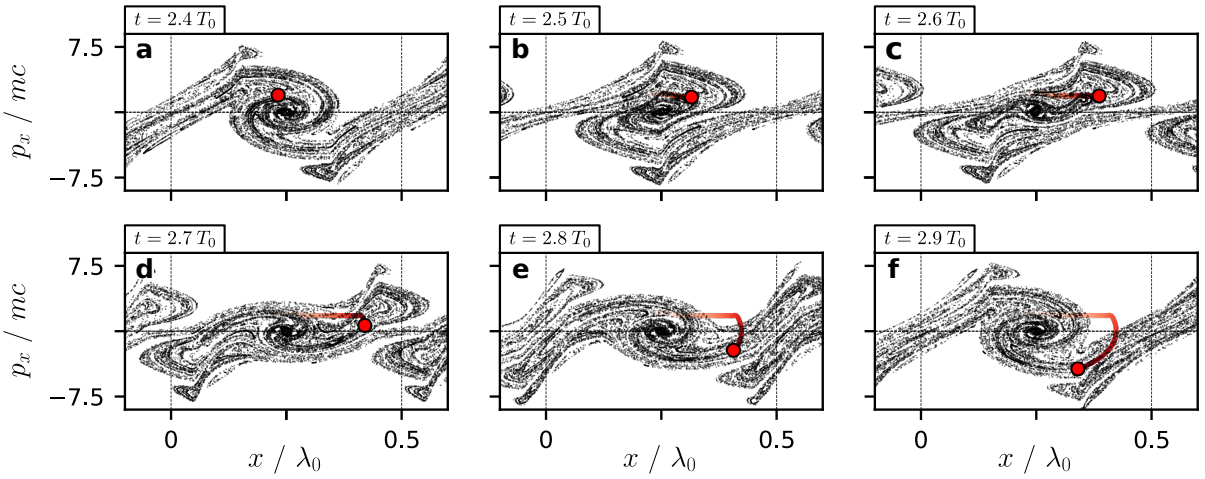

Figure 8.8: **Temporal evolution of the distribution of electrons in the simplified *p*/*p* case** - Same figure as Figs. 8.6 and 8.7 but when the ponderomotive force is modeled by a constant piecewise function defined Eq. (8.38) in order to clearly see the two different phases.

The red electron trajectory exhibits an unambiguous transition from a straight, and thus ballistic, motion (e.g., in Figs. 8.8–c) to a elliptical motion (e.g., in Fig. 8.8–f). The electron distribution looks like the one given by Fig. 8.7, even though the approximation of approaching the sinusoidal temporal term by a step function seemed strong *a priori*.

This simplified case is interesting because the equations of motion are solvable on both time intervals. This will be helpful in further calculations.

8.3.2 Criterion for the onset of chaos

One of the interests of studying the stretching and folding mechanism in detail is that it allows to derive a very simple geometrical for the onset of chaos that proves to be as accurate

[2] at $t = 0$, $\cos(2\omega_0 t) = 1$ so $1 - \cos(2\omega_0 t) = 0$ and at $t = T_0/4$, $\cos(2\omega_0 t) = -1$ so $1 - \cos(2\omega_0 t) = 2$.

as more complex Lyapunov calculations.

Switching to the pendulum analogy, it is natural to define the so-called *X* and *O points*, respectively the top unstable and bottom stable positions of the bob (see Fig. 8.9–a). When the bob is exactly located at the X point, it can either drop towards the left or towards the right depending on its velocity at that moment. Small discrepancies on the velocity can lead to two very different trajectories: one where the bob falls back and one where it crosses the X point. In particular, small uncertainties on the initial velocity can lead to important divergence to the analytical solution. In numerical simulations, these uncertainties mainly come from round-off errors, introduced by using finite precision floating point numbers on computers.

Each time the bob approaches the X point, some neighboring trajectories diverge rapidly (see Sec. 2.2, page 34). For a forced pendulum, the crossing of the X point is repeated a large number of times and two trajectories, even very close initially, will eventually end up diverging at an exponential rate very quickly. This sensitivity to initial conditions is what makes a system chaotic. Being able to distinguish two trajectories would require infinite precision, which is never achievable in real physical systems or in the numerical resolution of the corresponding equations on computers.

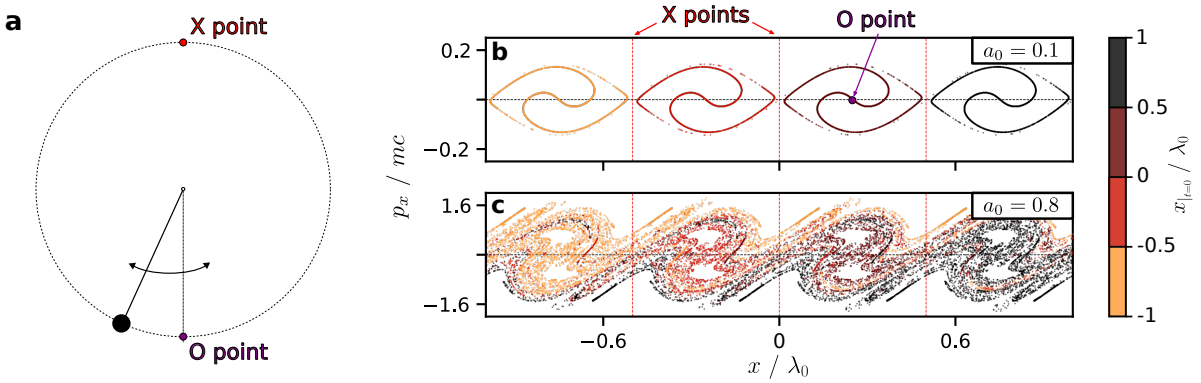

Figure 8.9: **Metastability for a pendulum and for electron dynamics** - Panel (a) shows a sketch of a forced pendulum highlighting the 2 points of interest: the unstable X point and the stable O point. In panels (b) and (c), we represent the distribution of electrons in phase space after $4\,T_0$ for two p-polarized lasers, below the chaos threshold ($a_0 = 0.1$, panel (b)) and beyond ($a_0 = 0.8$, panel (c)). The O and X points are also shown in this configuration.

For electron dynamics in an interference field, the electric field nodes stand for O points, while the magnetic field nodes play the same role as X points. In Sec. 8.2.2, we discriminated the chaotic regimes from the predictable, when the different particle colors, corresponding to their respective initial bucket, started to mix. This indicates that particles crossed X points at some moment of their lifetime and that the system is becoming chaotic.

In case of two circularly polarized waves (analog to a simple gravity pendulum), the particles travel along close orbits within a bucket and do not have any opportunity to cross an X point. For two linearly polarized waves, the electrons follow the same motion during the folding step and remain trapped. However, during the stretching phase, the particles do not feel any field influence and experience a ballistic motion, characterized by a constant velocity. If a particle is fast enough or sufficiently close to a boundary, it can possibly cross an X point during that time before being trapped again.

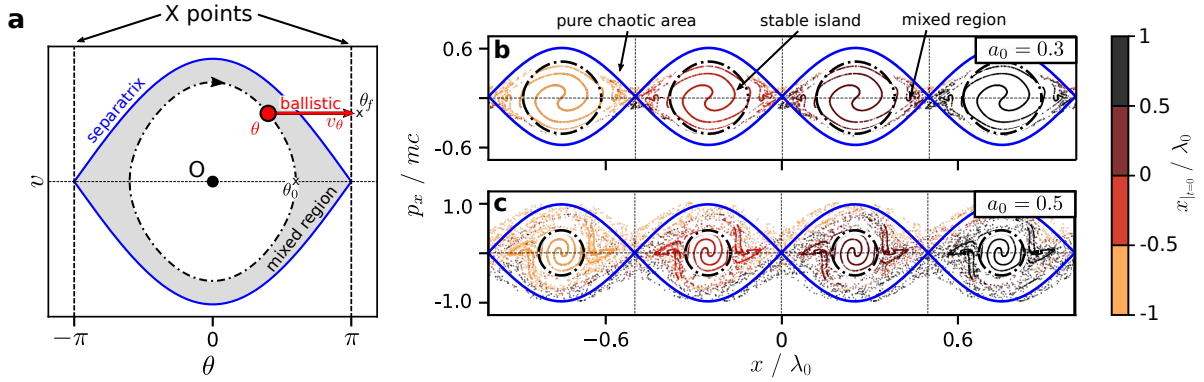

Figure 8.10: **Electron dynamics in the p/p case during the transition to chaos** - In panel (a), a particle (in red) previously on a trapped orbit (black dot-dash line) follows a ballistic motion from (θ_1, v_1) to (θ_2, v_1) during the stretching phase. If it is fast enough or sufficiently close to the boundary, it can cross an X point along the way. In all the grey area (mixed region), particles are able to change buckets. In panels (b) and (c), we represent the distribution of electrons in phase space after $4T_0$ for two laser amplitudes: (b) $a_0 = 0.3$ and (c) $a_0 = 0.5$. The blue envelope is the separatrix and the black dot-dash lines are the limit orbit obtained with the analytical model presented in the text. This orbit separates the distribution into two areas: stable islands and chaotic mixed region.

This simple physical insight shows that the value of the particle velocity, when the stretching phase starts, is key, as it remains constant during this whole step. If the laser intensity is low, most if not all particles are too slow to leave their bucket and the distribution in phase space looks like the stable circular case (Fig. 8.9–b). For a high enough laser amplitude on the other hand, the particles cross the buckets and pass through X points, which leads to chaos and particle diffusion (Fig. 8.9–c).

In between these two extreme regimes, the phase space shows a chaotic zone, which expands gradually from the separatrix to the electric node. We call it *mixed region* and display it in grey in Fig. 8.10–a. When in this area, particles follow closed orbits considered as trapped (below the separatrix) but which admit at least one position allowing for escapes during the stretching phase. In Figs. 8.10–b, c, we represent the distribution of electrons for two moderate amplitudes: $a_0 = 0.3$ and 0.5. It is clear that both regimes are chaotic, since particles are exchanged between buckets. However, they present central zones, where the particle distribution remains stable and looks like the one of Fig. 8.9–b. We call these areas *stable islands*, they are shrinking when a_0 is increased.

We now derive an analytical formula for the boundary of the mixed region. To do so, we consider the simplified form of the stretching and folding defined in Eq. (8.38) (page 133) and $\theta = \pi + 2k_0 x$. Here, we only use the classical form of equations of motion (and velocity instead of momentum), because we consider only moderate laser amplitudes ($0.1 < a_0 < 0.8$), for which relativistic effects do not play a major role. Using the reduced model, the classical equations of motion read:

$$\begin{cases} \dfrac{\mathrm{d}^2\theta}{\mathrm{d}t^2} + 4\,a_0^2\,\sin\theta = 0 & \text{for folding,} \\ \dfrac{\mathrm{d}^2\theta}{\mathrm{d}t^2} = 0 & \text{for stretching.} \end{cases} \tag{8.39}$$

During the folding phase, the particles are rotating around an electric field node along a closed

orbit. Then, let us consider a single particle located on a closed orbit identified by the point (θ_0, 0), where θ_0 is the position of the particle, when it has zero velocity. Such an orbit is pictured as a black dot-dash line in Fig. 8.10–a. At the end of the folding step, this particle (pictured in red) is located at a position in phase space (θ, v_θ). As a reminder, along its orbit, θ and v_θ are not independent and are bound by the following formula (see Eq. (8.37), page 131 for the RHC/LHC case):

$$v_\theta = 2\sqrt{2}a_0\sqrt{\cos\theta - \cos\theta_0}. \tag{8.40}$$

During the stretching phase which lasts π in θ-space, the velocity v_θ is kept constant all along. The particle leaves its initial bucket if it crosses an X point during that time, located at $\pm\pi$ (see Fig. 8.10–a). After the ballistic motion from (θ, v_θ) lasting π, a new point is reached (θ_f, v_θ), with θ_f the absolute position at the end of the stretching phase. A particle has escaped its bucket if θ_f is beyond the X point, which reads:

$$\theta_f = \theta + \pi v_\theta > \pi. \tag{8.41}$$

Replacing v_θ by its value, it comes:

$$a_0 > \frac{\pi - \theta}{2\sqrt{2}\pi\sqrt{\cos\theta - \cos\theta_0}}, \tag{8.42}$$

or

$$\theta_0 > \cos^{-1}\left(\cos\theta - \left(\frac{\pi - \theta}{2\sqrt{2}\pi a_0}\right)^2\right), \tag{8.43}$$

where $\cos^{-1}$ is the inverse cosine function.

In Fig. 8.11–a, the amplitude a_0 is pictured as a function of θ_0 and θ. The whole bottom-right part of the figure is forbidden since $\theta \leq \theta_0$ by definition of the orbit. An orbit is located in the

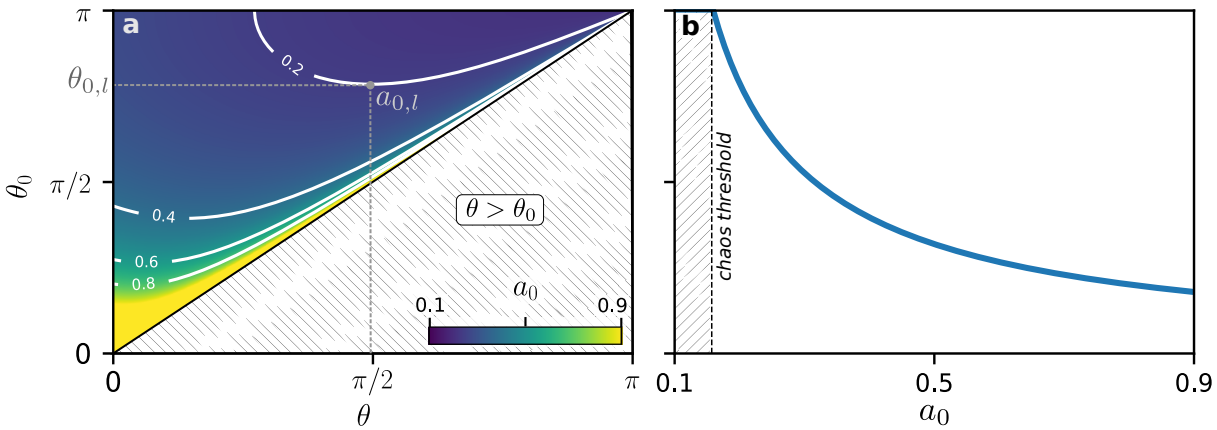

Figure 8.11: **Evolution of the limit orbit as a function of the laser amplitude** - In panel (a), the amplitude a_0 is pictured as a function of θ_0 and θ according to Eq. (8.42). θ is always smaller than θ_0 so the bottom-right part is forbidden. In addition to the color scale, we represent, as plain white lines, different isocontours corresponding to $a_0 = 0.2$, 0.4, 0.6, 0.8. For a given amplitude (e.g. $a_0 = 0.2$), the limit orbit θ_l is obtained after minimizing θ_0 along the right isocontour. Then, θ_l is reported in panel (b) and plotted as a function of a_0. Below the chaos threshold ($a_0 \sim 0.159$), the function is not defined.

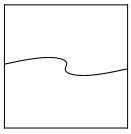

mixed region of the phase space displayed in Fig. 8.10–a, if it exists some positions θ, which allow the particle to leave its buckets. We are looking for the limit orbit $\theta_{0,l}$, along which strictly one value for θ exists. This limit orbit results from balance between a small distance to boundary ($\theta \to \pi$) but a sufficiently large velocity ($v_\theta \gg 0$).

As white lines, we highlight isocontours of a_0 in (θ, θ_0) space. The limit orbit is found where only a single θ is allowed, that corresponds to the minimum of θ_0 along the isocontour. For example, we show in Fig. 8.11–a, how we find $\theta_{0,l}$, when $a_0 = 0.2$.

For all orbits $\theta_0 > \theta_{0,l}$, there are multiple positions θ along the orbit allowing particle diffusion. For $\theta_0 < \theta_{0,l}$, all the particles remain trapped since they do not have a sufficient velocity to cross an X point during the stretching phase (stable islands). In Figs 8.10–b, c, the limit orbits found with the model for both laser amplitudes are pictured as a black dot-dash line and separate recognizable chaotic and non-chaotic simulated zones.

Another interesting point is that the function $\theta_{0,l} = f(a_0)$ (plotted in Fig. 8.11–b) is not defined at lowest intensities (hatched zone). It is possible to find laser intensities for which strictly zero particles are diffusing, even those exactly located on the separatrix and describing the orbit identified by (π, 0):

$$a_0 > \frac{\pi - \theta}{2\sqrt{2}\pi\sqrt{\cos\theta + 1}}. \tag{8.44}$$

The quantity is minimal when $\theta \to \pi$. It is possible to find the exact value of the limit thanks to the Taylor series of cosine near π:

$$\cos\theta \underset{\theta\to\pi}{\sim} \cos\pi - \frac{(\pi-\theta)^2}{2}\cos\pi = -1 + \frac{(\pi-\theta)^2}{2}. \tag{8.45}$$

It comes that:

$$\boxed{a_0 > \frac{1}{2\pi} \simeq 0.159} \tag{8.46}$$

By using a simple geometric and analytical approach, we can guess a threshold for chaos onset based only on the laser amplitude. The value of a_0 is nearly identical to the numerical observations obtained through PIC simulations in Sec. 7.1.2.

8.3.3 Loss of predictability after few cycles

When a particle crosses multiple times an X point, small variations on its initial value of momenta/positions can lead to completely different trajectories. The most common way to show this behaviour is through the Lyapunov exponent such as presented in Sec. 7.1.2 (page 101): two trajectories arbitrarily chosen very close in phase space at the beginning of the simulation eventually end up far away from each other.

In this section, we show that numerical errors, as small as the machine epsilon 10^{-16} for double-precision floating-point (float64), can still be large enough to observe a divergence to the converged solution. As there is no formula for the converged solution, a different strategy consists in trying to guess the initial position of each particle from its final position. To do so, we perform some simulations back and forth: first, the simulation is run with a positive time step but after a certain time, we shift its sign and perform the same number of iterations backwards.

The equations of motion are reversible and the dynamical system is expected to return at its exact initial state. However in case of chaotic systems and because of truncation errors, some particles will be observed to end up at positions largely different from their initial ones.

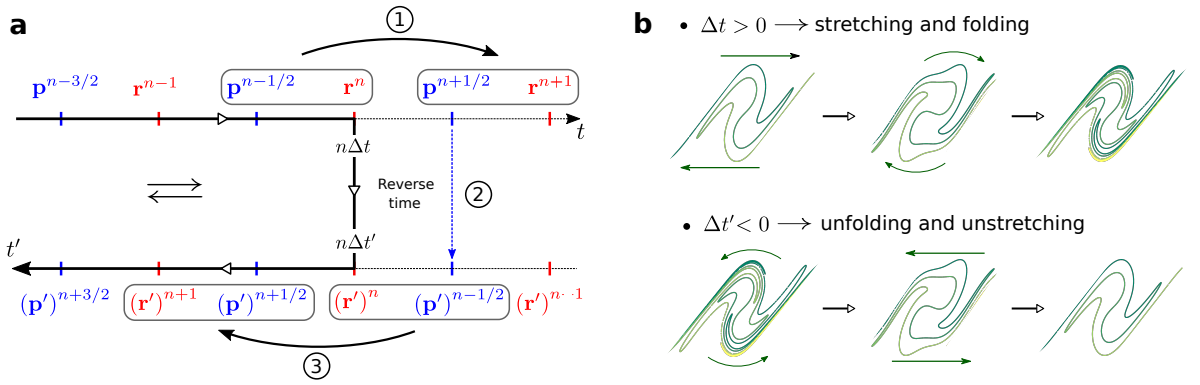

Figure 8.12: **Schematic drawing of the reverse time algorithm** - The panel (a) displays how the time is reversed in the Boris pusher to keep a second-order accuracy: step 1: regular Boris push with Δt, step 2: time inversion and correspondence between each quantity and its prime equivalent, step 3: regular Boris push with $\Delta t'$. On panel (b), we show simulated distributions evolving under positive and negative time steps: when it is positive, the stretching and folding tends to create a multi-layer pattern and when it is negative, an *unfolding and unstretching* removes the different layers.

The reverse time algorithm. Running back and forth simulations requires to carefully treat the sign inversion of the time step. For the Boris algorithm, positions and momenta are staggered in time with positions always ahead of momenta. Switching the sign of the time step without caution breaks the staggering and introduces a large error. This error dominates any other source of errors in the simulation.

In order to ensure the second-order accuracy of the pusher algorithm, the position is kept constant during the inversion process. A sketch of the algorithm is presented in Fig. 8.12–a. After n time steps, the current variables are $\mathbf{r}^n$ and $\mathbf{p}^{n-1/2}$. At step (1), we regularly perform the Boris pusher:

$$(1) \quad \| \quad (\mathbf{p}^{n-1/2},\ \mathbf{r}^n) \xrightarrow[\Delta t]{} (\mathbf{p}^{n+1/2},\ \mathbf{r}^{n+1}). \tag{8.47}$$

Then at step (2), the time is reversed. We define the variables after the time inversion with a prime. The subtlety here relies on the fact that $\mathbf{r}^{n+1}$ is not taken into account in order to guarantee that position is ahead of momentum at any time even after the shift:

$$(2) \quad \| \quad \begin{array}{lcl} \Delta t' & = & -\Delta t, \\ (\mathbf{p}')^{n-1/2} & = & \mathbf{p}^{n+1/2}, \\ (\mathbf{r}')^{n} & = & \mathbf{r}^{n}. \end{array} \tag{8.48}$$

Finally at step (3), we again perform the Boris algorithm but this time with $\Delta t'$:

$$(3) \quad \| \quad \left((\mathbf{p}')^{n-1/2},\ (\mathbf{r}')^{n}\right) \xrightarrow[\Delta t']{} \left((\mathbf{p}')^{n+1/2},\ (\mathbf{r}')^{n+1}\right). \tag{8.49}$$

This 3-step algorithm ensures keeping the second order accuracy of the scheme. For a simulation with two p-polarized waves, after time inversion, we observe that the electron distribution

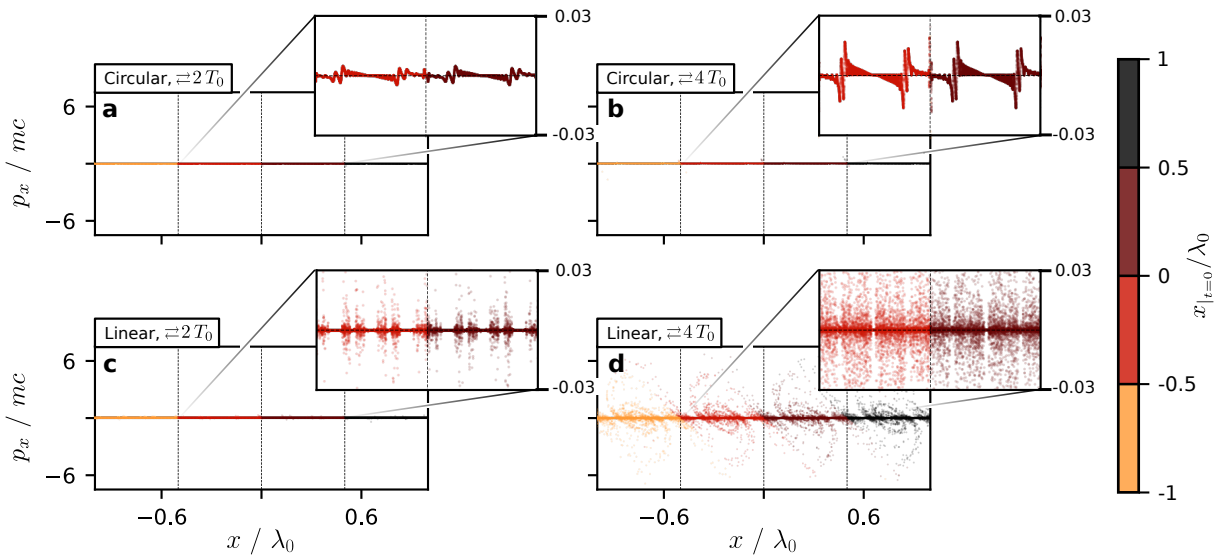

Figure 8.13: **Final electron distributions after back and fourth simulations in different cases** - On each panel, we plot the distribution of electrons in phase space after $\rightleftarrows NT_0$: panels (a)/(c): $N = 2$ and (b)/(d): $N = 4$ in the RHC/LHC (panels (a-b)) and p/p configurations (panels (c-d)). $a_0 = 3$. The insets in the top right corner are zooms close to $p_x = 0$ for $-\lambda_0/2 < x_{|_{t=0}} < \lambda_0/2$.

is *unfolded and unstretched* in phase space (see Fig. 8.12–b). Unlike the stretching and folding, which adds extra layers to the distribution at each period, running the simulation backwards removes these layers and simplifies the distribution of electrons.

In the following, we will use the notation $\rightleftarrows NT_0$ to designate simulation, with N laser periods performed forward and N laser periods backwards. The total duration of the simulation is thus $2\,NT_0$.

Comparison between initial and final distributions. Starting from the usual initial distribution ($-\lambda_0 < x_{|t=0} < \lambda_0$ and $p_{x|t=0} = 0$), we should expect to retrieve the exact same one after $\rightleftarrows NT_0$. In Fig. 8.13, we display the final distributions for different cases: $N = 2$, 4 and the two polarization configurations — RHC/LHC and p/p at relativistic intensity.

The first thing to notice is that the exact initial distributions fail to be *perfectly* reproduced, no matter the laser polarization. However, as expected for the circular case (Figs. 8.13–a, b), p_x remains quantitatively close to zero even after $\rightleftarrows 4T_0$.

On the contrary, for two p-polarized laser waves (Figs. 8.13–c, d), the deviation from the initial distribution is particularly strong: some particles do not even return to their initial bucket and for example, some red particles end up in the yellow bucket. In any cases, the deviation is larger when the simulation is longer. For longer simulations, the particles cross X points more frequently, which makes the converged trajectory harder to follow.

In order to quantify the deviation, we define in phase space an error radius $\mathcal{R}$ for each particle, defined as:

$$\mathcal{R} = \sqrt{\left(\frac{x_{|\rightleftarrows NT_0} - x_{|t=0}}{\lambda_0}\right)^2 + \left(\frac{p_{x|\rightleftarrows NT_0} - p_{x|t=0}}{mc}\right)^2}, \tag{8.50}$$

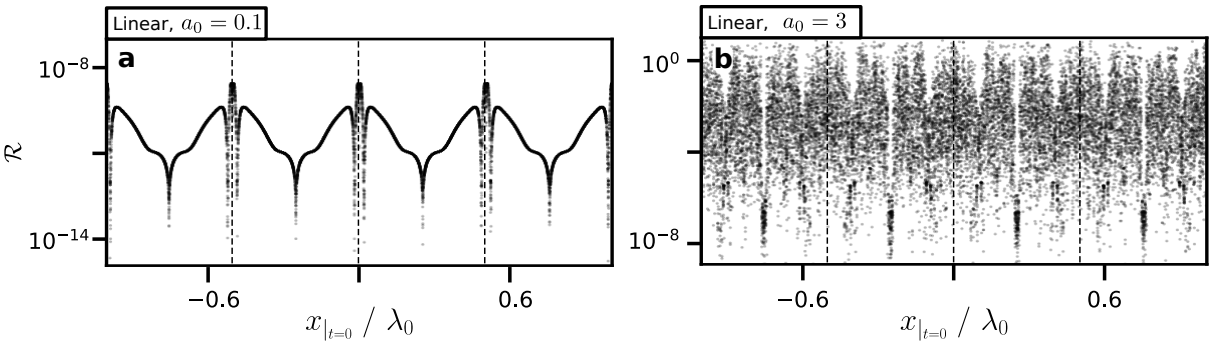

Figure 8.14: **Error radius $\mathcal{R}$ as a function of the initial position** - The electron distribution is represented in the space $(x_{|t=0}, \mathcal{R})$ in the p/p case at low ($a_0 = 0.1$, panel (a)) and high ($a_0 = 3$, panel (b)) intensities after $\rightleftarrows 4T_0$. Note the different scales for $\mathcal{R}$. The machine epsilon is roughly equal to 10^{-16} for these simulations performed in float64.

where $x_{|\rightleftarrows NT_0}$ and $p_{x|\rightleftarrows NT_0}$ are respectively the position and the momentum of the particles at the end of a $\rightleftarrows NT_0$ simulation. If $\mathcal{R}$ is lower than the machine epsilon, the particle is considered to have returned at its initial position in phase space. $\mathcal{R}$ is of course strongly dependent on the particle initial position and if the particle crosses or not an X point during the simulation. We should expect a large $\mathcal{R}$ when a particle is initialized near an X point and a low $\mathcal{R}$ when it is initialized near an O point.

$\mathcal{R}$ also depends on the precision of the floating point system. In our simulations, we choose double-precision floating-point format (float64) for which the machine epsilon is $2^{-53} \sim 10^{-16}$.

In Fig. 8.14, we plot the particle distributions in the space $(x_{|t=0}, \mathcal{R})$ in the p/p case for two laser amplitudes: $a_0 = 0.1$ and 3 after $\rightleftarrows 4T_0$. At low intensity (Fig. 8.14–a), there is a clear correlation between the error radius and the initial position: for one value of $x_{|t=0}$ corresponds one value of $\mathcal{R}$ and the distribution looks like a plot $\mathcal{R} = f(x_{|t=0})$. This means that the system is not sensitive to small variations by contrast to a chaotic system. This is true in most of the space as far as $x_{|t=0}$ is not too close to an X point. Near an X point, we have already seen that the trajectories tend to rapidly diverge. Then, for two initially adjacent particles, $\mathcal{R}$ can take multiple values near magnetic field nodes (look at the distinct dots near the bucket boundaries).

Beyond the chaos threshold, the particles are free to diffuse and thus cross multiple times an X point. This also worsens, when the simulation is run backwards forcing the particles to recross X points also on their way back. In Fig. 8.14–b, we observe now a completely different distribution, comparable to a random noise without any correlation. Knowing $\mathcal{R}$ for a particle does not give any indication on its initial position. Besides particles exactly initialized near an O point, the memory of the particle initial position is completely lost after few laser periods.

Influence of the temporal resolution on $\mathcal{R}$. We can go further and gauge how the accuracy of the simulation influences the $\mathcal{R}$ quantity. We run a set of simulations with different time durations and different time steps in the RHC/LHC and p/p cases. The different results are reported in Fig. 8.15 in log-log scale in the space $(T_0/\Delta t, \overline{\mathcal{R}})$, where $\overline{\mathcal{R}}$ is the average value of $\mathcal{R}$ over all simulated particles. Different shades of blue correspond to various simulation durations from $\rightleftarrows 1T_0$ to $\rightleftarrows 8T_0$.

The cases displayed in Figs. 8.15–a-c are all three non-chaotic because they are associated

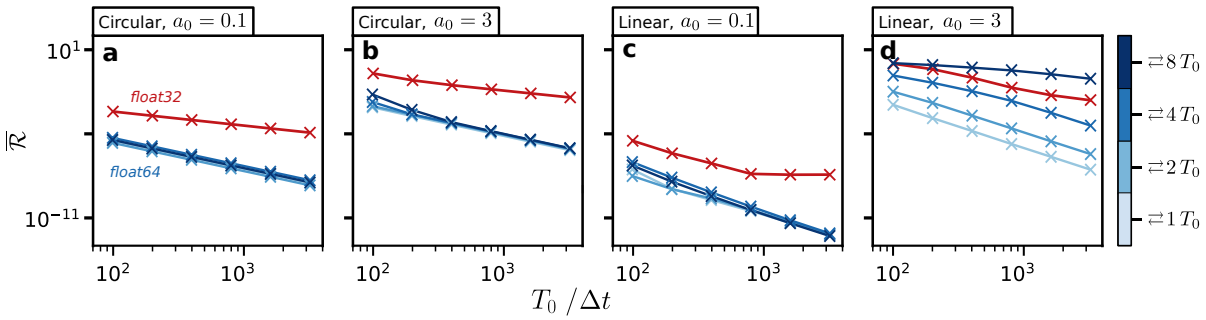

Figure 8.15: **Evolution of $\overline{\mathcal{R}}$ as a function of the simulation time step** - The average value of $\mathcal{R}$, $\overline{\mathcal{R}}$, is plotted as a function of the temporal resolution of the simulation. Each shade of blue corresponds to a different simulation length from $\rightleftarrows 1T_0$ to $\rightleftarrows 8T_0$. In addition, a set of simulations lasting $\rightleftarrows 4T_0$ but using the single-precision floating-point format (float32) is performed and the corresponding results reported as red curves.

to dynamics in circularly polarized waves or in linearly polarized waves but below the chaos threshold. Thus, the different plots present the same specificities:

- first, $\overline{\mathcal{R}}$ barely depends on the different length of simulations and the four curves are superimposed. Because very few particles are crossing X points (namely the ones initialized very close to a bucket boundary), most electrons follow a close orbit and their motion is entirely predictable. Since the system is not sensitive to small variations (see Fig. 8.14–a), trajectories do not diverge even for long simulations and it is always possible to retrieve the initial position.

- Second, $\overline{\mathcal{R}}$ evolves as a power law of $T_0/\Delta t$ with a negative exponent coefficient. In all of these cases, its absolute value tends to 2. In $\overline{\mathcal{R}}$, is encompassed contribution of all errors obtained by running numerical simulations instead of using the converged solution. It includes round-off errors but also discretization errors introduced by the numerical scheme — the Boris algorithm — which precisely vary as Δt^2. In such predictable systems, the major source of discrepancy to the converged solution is thus given by the discretization and not truncation errors.

The fourth case (Fig. 8.15–d) is much more interesting, because it involves chaotic trajectories. This time, the four blue curves are clearly separated and the power coefficient tends to 0 for the longest simulations. After $\rightleftarrows 8T_0$, $\overline{\mathcal{R}}$ is almost independent from the time step as the power coefficient equals -0.5. This is an evidence of chaotic behaviour, where the truncation errors introduced by the particle diffusion now generates an error much greater than the discretization error. It means that it is extremely delicate to reduce the value of $\overline{\mathcal{R}}$ by playing on the temporal resolution of the simulation. The longer the simulation, the more particles cross X points along their trajectory and the smaller initial variations lead to great divergences.

A solution to lower $\overline{\mathcal{R}}$ would be to change the overall precision of digits. We now perform a set of $\rightleftarrows 4T_0$ simulations, for which all quantities are encoded in the single-precision floating-point format (float32). For this digital representation, the truncation errors are larger than before and the machine epsilon equals 6×10^{-8}. The corresponding curves are displayed in red in Fig. 8.15. For all panels, $\overline{\mathcal{R}}$ is significantly larger by at least 3 orders of magnitude when using single-precision instead of double-precision.

In Fig. 8.15–c, the red curve follows a law in Δt^{-2} for large time steps but stabilizes at high temporal resolution. The value of the saturated points happens to be close to the machine epsilon. It indicates that we have reached the minimal possible error and that increasing the resolution even more would not improve the accuracy of the simulation.

Beyond the chaos threshold, we saw that truncation errors are the main source of discrepancies to converged trajectories. By reducing the digital precision, their amplitude is even heightened. Then, when using single-precision, the time step even has no influence on $\overline{\mathcal{R}}$. Consequently, the red curve in Fig. 8.15–d decreases less rapidly than the blue ones (power coefficient equal to -1.5 in float32 versus -2.2 in float64 for $\rightleftarrows 4T_0$ simulations).

In order to confirm that increasing the significant precision would allow for a better accuracy, even beyond the chaos threshold, I had originally planned to run extra simulations with the quadruple-precision floating-point format (float128). However, not all Python packages seemed to properly handle the format and the results were not compelling. Such simulations would probably require an explicitly typed language, e.g., C or Fortran.

Overall, it seems to be a vain effort to perfectly approach the converged trajectories in numerical simulations. In particular, the sensibility near X points is such that one cannot predict for sure if a particle would cross or not a boundary. Instead, we now consider the crossing in a probabilistic manner, where the knowledge of the accurate position and velocity is no more mandatory. The resulting probabilistic model would give insights on the particle diffusion and heating.

8.4 Random Walk and Diffusion

Beyond the chaos threshold, the particles move freely across space and explore many different buckets, sometimes far from their initial position. This diffusion process is akin to a random walk, where particle randomly escape or remain in their respective bucket at regularly spaced time intervals. At relativistic intensities, the velocities are bounded to c constraining the maximal distance covered during any time interval τ to $c\tau$. In particular, a particle cannot cross more than one bucket border during $\tau = T_0/2$, corresponding to a whole stretching and folding duration. It is also forbidden for a particle to cross the same border back and forth during that interval. This would indeed require a sudden change of direction, inconsistent with the ballistic motion observed during the stretching phase.

In order to illustrate the random walk, some typical particle trajectories are plotted along time in Fig. 8.16–a in an interference field formed by two p-polarized waves at $a_0 = 3$. As usual, the magnetic nodes are represented as black dashed lines. The different electrons are observed to jump from bucket to bucket in a random fashion. Note however that the different jumps between buckets always occur at a multiple of $T_0/2$ (light grey vertical lines).

We focus in particular on the bottom dark blue trajectory, for which we highlight both the surrounding bucket boundaries (the thick dark blue dash line) and the jumps (white dots). At each half laser period, the particle gets close to a boundary, sometimes it gets through and sometimes it does not. But nothing seems to predict a jump *a priori*: for example, for $5\,T_0 \leq t \leq 7\,T_0$, the trajectories on both subintervals of lengths T_0 are practically the same, however only a single jump occurs. The approach toward a boundary acts as a Bernoulli trial, where a fair coin is tossed at every multiple of $T_0/2$, *head* would be a jump and *tail* would be a stay. Both of these

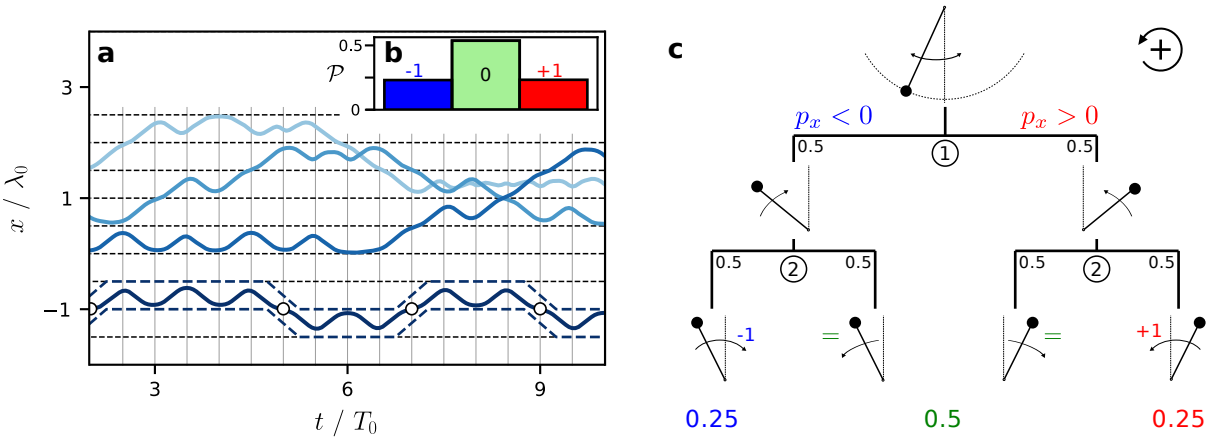

Figure 8.16: **Particle trajectories as a random walk** - In panel (a), four particle trajectories are plotted with different shades of blue. The magnetic nodes are drawn as black dash lines. For the bottom dark blue trajectory, we highlight its current buckets (dark blue dash line) as well as the positions and times at which jumps from one bucket to another occur (white dots). At the end of every $T_0/2$ period, a particle can either cross a boundary and then change bucket ($= \pm 1$) or stay in its bucket ($= 0$). We report on panel (b) the proportions of the three different outcomes summed over a whole simulation for all the 10^5 electrons and $a_0 = 3$. Finally, panel (c) displays a probability tree discussed in detail in the text.

events ends up to be equiprobable.

Probability to change buckets. Back to the pendulum analogy, we sketch a probability tree presented in Fig. 8.16–c. For a simple analysis, let us consider that all particles are ultra relativistic (i.e., $|v_x| = c$ at any time) and do not change direction in a whole $T_0/2$ period. These conditions are very often fulfilled in practice as soon as the laser intensity becomes high enough (see Fig. 8.16–a). Then, a coin toss strictly occurs one time for any particle every $T_0/2$ period. As a pendulum, it means that the equivalent bob always approaches the top position during that time. The probability tree in Fig. 8.16–c presents two stages:

- for the first stage (1) we divide the particles into two populations based on the sign of p_x. Starting from an electron distribution at rest, each sign is as likely as the other and the probabilities to approach an X point from the left or from the right are both equal to 0.5.
- The second stage (2) is the coin toss at the boundary. A particle has 50% chance to cross the border and then lose a turn if its momentum is negative or gain a turn if it is positive. Otherwise, it just stays in its bucket but its direction is reversed (see the sign of the arrow for the second bottom pendulum for example).

Overall, any particle is remaining in its bucket 50% of the time ($\mathcal{P}_0 = 0.5$) and crossing 25% of the time in each direction ($\mathcal{P}_{\pm 1} = 0.25$).

For the same simulation as in Fig. 8.16–a, we estimate the corresponding probabilities and report them as a bar chart in Fig. 8.16–b. The simulated probabilities are matching relatively well with the model and we find $\mathcal{P}_0 \simeq 0.54$ and $\mathcal{P}_1 \simeq \mathcal{P}_{-1} \simeq 0.23$. The slight discrepancy may come from deeply trapped particles, for which $|v_x| \ll c$. These kind of particles rarely experiment a coin toss and stay near an electric field node during many periods (e.g., the light blue trajectory in Fig. 8.16–a after $7.5T_0$). Since they are not taken into account in our model for which $|v_x| = c$, their presence artificially inflates the value of $\mathcal{P}_0$. However, as a_0 is increased, it is expected to

find less and less trapped particles and to get closer to the predicted probabilities. For example, for a simulation with $a_0 = 10$, we find that the different probabilities become $\mathcal{P}_0 \simeq 0.506$ and $\mathcal{P}_1 \simeq \mathcal{P}_{-1} \simeq 0.247$.

Probabilistic distribution of particles. Now that the probabilities of any outcome are well established for a single event lasting $T_0/2$, it is possible to derive the probability mass function after a sequence of n such independent events. Knowing this function would give a fairly good estimation of the electron position distribution after $n\,T_0/2$.

Many important results can be derived from a simple binary random walk (for example in [Papoulis, 1921]), where the random variable follows a binomial distribution and takes values -1 and $+1$ with a probability $\mathcal{P}_{\pm 1} = 0.5$. At first glance, this seems a bit different from our case, where three outcomes are possible: -1, 0 and $+1$.

But, let us consider a random variable X_n following a binomial distribution with a probability $\mathcal{P} = 0.5$ for both failure/success but this time X_n is moved by $-1/2$ or $+1/2$ at each time step. The probability mass function of X_n to toss k times the value $+1/2$ among n trials is given by:

$$\mathcal{P}(X_n = k) = \frac{1}{2^n}\binom{n}{k} = \frac{1}{2^n}\,\frac{n!}{k!(n-k)!}, \tag{8.51}$$

where $\binom{n}{k}$ designates the binomial coefficient n *choose* k.

After 2 tries ($n = 2$), the two consecutive coin tosses may present the same outcome, which gives $X_2 = 1$ for two successes or $X_2 = -1$ for two failures. The probabilities of these events are both equal to $\mathcal{P}_{\pm 1} = 0.25$. By contrast, if the two consecutive coin tosses present different outcomes, $X_2 = 0$, with a probability $\mathcal{P}_0 = 0.5$. The probabilities and outcomes corresponding to X_2 exactly match our random walk law previously presented in Fig. 8.16. Then, assigning Y_n the random variable corresponding to our random walk, Y_n is simply related to X_n as $Y_n = X_{2n}$.

Now, let us reckon the probability to toss k times among n trials the value $+1$ for the variable Y_n. It is equivalent to toss $2k$ times among $2n$ the value $+1/2$ for the variable X_{2n}. It can be expressed in term of binomial coefficients:

$$\mathcal{P}(Y_n = k) = \mathcal{P}(X_{2n} = 2k) = \frac{1}{2^{2n}}\binom{2n}{2k} = \frac{1}{4^n}\binom{2n}{2k}. \tag{8.52}$$

The probabilistic particle position x_n after n iterations can be obtained by considering g the net gain obtained after tossing $2k$ times the value $+1/2$ for X_{2n} (and then tossing $2n-2k$ times the value $-1/2$):

$$\begin{aligned} g &= \left(+\frac{1}{2}\right)\cdot 2k + \left(-\frac{1}{2}\right)\cdot(2n-2k) = 2k - n \\ \Leftrightarrow\quad k &= (n+g)/2. \end{aligned} \tag{8.53}$$

Then the probability that the particle ends in the bucket g reads:

$$\mathcal{P}(x_n = g) = \mathcal{P}(Y_n = (n+g)/2) = \frac{1}{4^n}\binom{2n}{n+g} = \frac{1}{4^n}\,\frac{(2n)!}{(n+g)!(n-g)!}. \tag{8.54}$$

This formula gives us the occupancy rate of the different buckets and is valid as soon as most of the particles present relativistic velocities. However, under this form, there is no physical

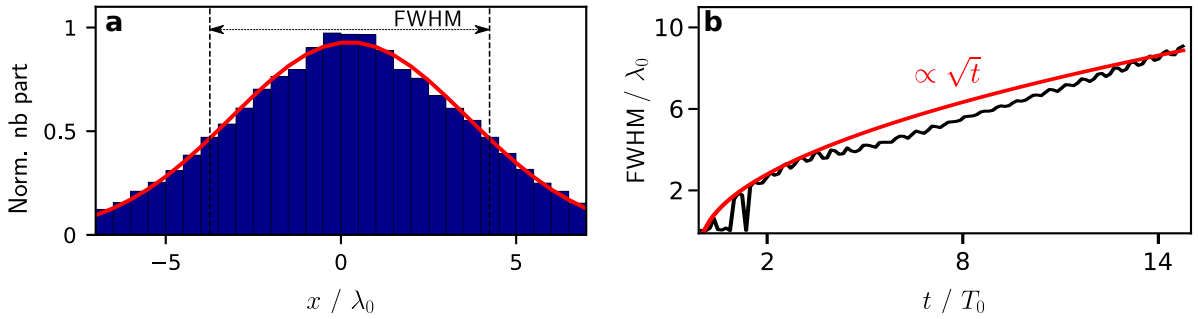

Figure 8.17: **Distribution of particle positions for $n = 18$** - In panel (a), the electron positions are plotted as a 1D-histogram at $t = 9T_0$ for the same simulation as in Fig. 8.16. Each bar corresponds to a magnetic bucket. On top of the histogram is plotted a red line corresponding to the theoretical Gaussian distribution written in Eq. (8.56). In panel (b), we plot the evolution of the full width at half maximum (FWHM) of the distribution of panel (a) along time as well as a function varying as $\sqrt{t}$.

intuition on what the electron position distribution would look like. The limit behaviour at large n gives a much better understanding. To do so, we use the Stirling's approximation to approach factorials:

$$n! \sim \sqrt{2\pi n}\left(\frac{n}{e}\right)^n, \tag{8.55}$$

Replacing each factorial of Eq. (8.54) by its equivalent form, the particle distribution after n iterations reads (the details of the derivation can be found in appendix A):

$$\boxed{\mathcal{P}(x_n = g) = \frac{1}{\sqrt{n\pi}} \exp\left(-\frac{g^2}{n}\right).} \tag{8.56}$$

The particle distribution thus approaches a Gaussian distribution for large n. The mathematical expectation of the law is of course zero, since we start from a population centered around $x = 0$ and its standard deviation is $\sqrt{n/2}$. A standard deviation evolving as $\sqrt{n}$ (or overall $\sqrt{t}$) is characteristic of a *normal diffusion*.

In Fig. 8.17–a, the particle positions for the same simulation as in Fig. 8.16 at $t = 9\,T_0$ (or $n = 18$) are plotted as a dark blue histogram as well as the theoretical Gaussian distribution pictured as a red line. As one can see, the model agrees well with the simulated results. It is also possible to fit the full width at half maximum (FWHM) of the distribution of electrons at each time step. For a Gaussian distribution, the FWHM is linear with the standard deviation and as shown in Fig. 8.17–b, its evolution in time also follows a law varying as $\sqrt{t}$. The evolution of the particle positions in space is then completely described by the simple model of random walk introduced in this section.

Evolution of the energy distribution. The distribution of energy will not be derived here but is inspired from the kinetic theory of gases. In the most general case, the statistical distribution of velocities in an idealized gas follows a Maxwell-Boltzmann distribution [Maxwell, 1860; Boltzmann, 1872]. It is closely related to the particle random motion and stochastic processes such as elastic collisions. An idealized gas is also known to diffuse according to Fick's law [Fick, 1855]:

$$\frac{\partial n_g}{\partial t} = D\boldsymbol{\nabla}^2 n_g, \tag{8.57}$$

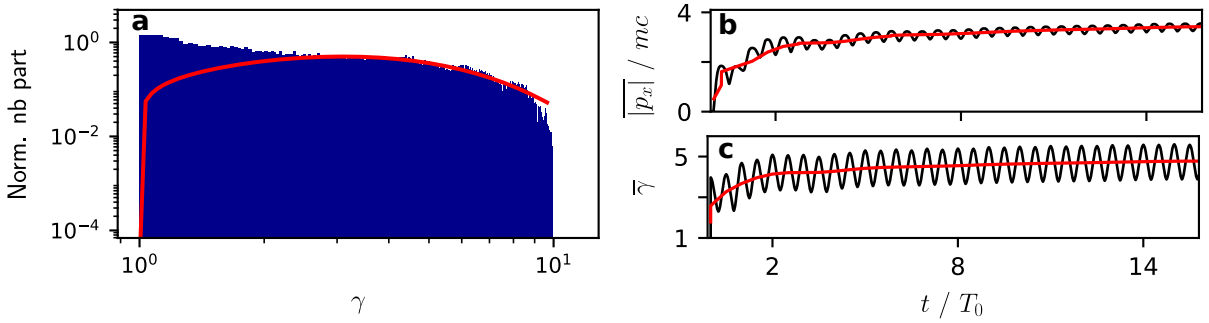

Figure 8.18: **Distribution of particle energy for $n = 18$** - The distribution of energy for two p/p lasers with $a_0 = 3$ is displayed as a blue histogram on panel (a) in log-log scale. Then, we fit the hot electron tail with a Maxwell-Jüttner distribution (see Eq. (8.59)) and plot it as a red curve. Panels (b) shows the average momentum along x and panel (c) the average γ as a function of time, as black lines. The red curves are obtained after averaging the previous quantities over $T_0/2$.

where n_g is the gas density and D the diffusion coefficient. In infinite space, and if all particles start initially from $x = 0$, the 1D-solution of Eq. (8.57) is:

$$n_g(x,\, t) = \frac{n_{g,0}}{\sqrt{4\pi D t}} \exp\left(-\frac{x^2}{4Dt}\right), \tag{8.58}$$

where $n_{g,0}$ is the initial gas density. The solution is identical to a Gaussian distribution with mathematical expectation zero and variance $2Dt$. Its general form looks like Eq. (8.56): electrons in two p-polarized waves diffuse in similar fashion to gas particles in space.

Since the two position distributions are such akin, we expect the energy distribution of electrons in an interference field to follow a Maxwell-Boltzmann distribution as well. In practice, because electrons are relativistic, the expected distribution must be a Maxwell-Jüttner distribution [Jüttner, 1911], limit of the Maxwell-Boltzmann distribution at relativistic velocities. Indeed, for a Maxwell-Boltzmann distribution, the velocities are arbitrary large and may become greater than c. In 1911, Ferencz Jüttner included relativistic effects into the Boltzmann derivation and proposed a corrected distribution as a function of γ:

$$f(\gamma) = \frac{\gamma^2 \beta}{\theta K_2(1/\theta)} \exp\left(-\frac{\gamma}{\theta}\right), \tag{8.59}$$

where $\theta = k_B T / mc^2$ the normalized temperature, $k_B \simeq 1.38 \times 10^{-23}$ J.K^{-1} the Boltzmann constant, $\beta = \sqrt{1 - 1/\gamma^2}$ and K_2 the modified Bessel function of the second kind.

The γ distribution at $t = 9\, T_0$ for the same simulation as in Fig. 8.16 is plotted in Fig. 8.18–a in log-log scale as well as a red fit line following the Eq. (8.59). It does match well with the distribution of hot electrons. Numerically, we find $\theta \simeq 1.398$ or $T \simeq 715$ keV. It legitimates the use of *heating* in stochastic heating because it does create a thermalized distribution.

Another interesting point is that the system indeed reaches a thermodynamic equilibrium after few laser periods. Actually, the average values of both p_x (defined as $\overline{|p_x|}$) and γ (as $\overline{\gamma}$) seem to saturate after $t \geq 3\, T_0$ (see Figs. 8.18–b, c). The heating is thus not significantly enhanced by longer pulses. In experiments on laser interactions on solid targets with a long gradient, the laser presents a finite waist and electrons are expelled from the interference zone quite rapidly.

Despite the short time of interaction, it may be sufficient to acquire the maximal possible energy.

This section closes our long study about electron motion in two counter-propagating waves. Now, let us be closer to the experimental conditions by adding an angle of incidence and show how it affects the electron dynamics.

8.5 Influence of the Laser Angle of Incidence

8.5.1 Electron distributions in Bourdier's frame

All the work presented so far was done assuming that the two plane waves were counter-propagating, which is different from a typical experimental setup of laser-plasma interaction. In this section, we introduce an angle α between the two waves and study how it changes electron dynamics. We also define $\varphi = \alpha/2$, as displayed in Fig. 8.19. For two counter-propagating waves, we would have $\alpha = \pi$ and $\varphi = \pi/2$.

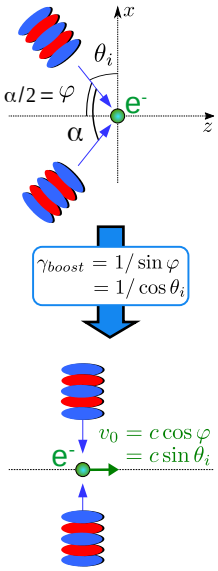

Figure 8.19: **Emulation of a 2D plane wave problem at oblique incidence to a 1D plane wave problem at normal incidence in a boosted frame.**

Introducing an angle between the two waves does not change the method of solving the equations of motion. It is always possible to emulate a 2D plane wave problem at oblique incidence with a 1D plane wave problem at normal incidence using Lorentz transformation in the Bourdier frame (see Sec. 3.3.2, page 50).

In such a frame, we have already seen that most quantities are rescaled by a factor $\gamma_{boost} = 1/\sin\varphi$. In addition, the particles acquires a drift velocity $v_d = c\cos\varphi$ in the direction of the boost, $\boldsymbol{z}$. Besides that, the conservation of the transverse canonical momentum (Eq. (8.7), page 120) is still preserved. The only difference with the previous sections is that the distribution of electrons presents a non-zero initial momentum $p_{z,|t=0}$, corresponding to the drift momentum:

$$\begin{aligned} p_{z,|t=0} &= m\gamma_{boost} v_d, \\ &= mc\,\tan\theta_i = mc\,\cot\varphi, \end{aligned} \tag{8.60}$$

where $\cot\varphi$ is the cotangent of φ. The conservation of the transverse canonical momentum in the boosted frame reads:

$$\begin{cases} p_y = eA_y, \\ p_z = eA_z + p_{z|t=0} = eA_z + mc\,\cot\varphi. \end{cases} \tag{8.61}$$

With a similar derivation to the one of Sec. 8.1 (page 120), but now with the new expression of p_z, it comes:

$$\boxed{\frac{\mathrm{d}^2x}{\mathrm{d}t^2} + \frac{e^2}{2m^2\gamma^2}\left(\frac{\partial}{\partial x} + \frac{\dot{x}}{c^2}\frac{\partial}{\partial t}\right)\left(A_y^2 + A_z^2\right) + \frac{ec}{m\gamma^2}\cot\varphi\left(\frac{\partial}{\partial x} + \frac{\dot{x}}{c^2}\frac{\partial}{\partial t}\right)A_z = 0} \tag{8.62}$$

or

$$\frac{\mathrm{d}^2x}{\mathrm{d}t^2} + \frac{ec}{m\gamma^2}\left(\frac{eA_z}{mc} + \cot\varphi\right)\left(\frac{\partial}{\partial x} + \frac{\dot{x}}{c^2}\frac{\partial}{\partial t}\right)A_z + \frac{e^2}{2m^2\gamma^2}\left(\frac{\partial}{\partial x} + \frac{\dot{x}}{c^2}\frac{\partial}{\partial t}\right)A_y^2 = 0, \tag{8.63}$$

where we highlight the new terms introduced by the oblique incidence in blue.

When there is an angle between the two wave propagation directions, a third term is added depending on both $\cot\varphi$ and the derivatives of A_z. A_y and A_z are both oscillating at frequency $\omega_0 \sin\varphi$ (angular frequency in the boosted frame), while their squares are oscillating at the frequency $2\omega_0 \sin\varphi$. The mix of two different laser frequencies usually tends to reduce the chaos threshold as we will show later.

Now, let us derive the electron dynamics for different interference field configurations. Similarly to Sec. 8.2, all theoretical developments are based on the classical form of equations of motion, more convenient to work with.

Electron motion in two p/p waves. In the interference field formed by two p/p waves, only A_z exists. Replacing A_z by its value given in Eq. (8.24) (page 125) leads to the equation of motion:

$$\frac{\mathrm{d}^2x}{\mathrm{d}t^2} \underbrace{-a_0^2c^2k_0' \sin\left(2k_0'x\right)\left(1-\cos\left(2\omega_0't\right)\right)}_{F_p} \underbrace{-2a_0c^2k_0' \cot\varphi \sin\left(k_0'x\right)\sin\left(\omega_0't\right)}_{F_d} = 0 \tag{8.64}$$

or

$$\frac{\mathrm{d}^2x}{\mathrm{d}t^2} - 2a_0c^2k_0' \sin\left(k_0'x\right)\sin\left(\omega_0't\right)\Big(2a_0\sin\left(\omega_0't\right)\cos\left(k_0'x\right) + \cot\varphi\Big) = 0 \tag{8.65}$$

where $k_0' = k_0 \sin\varphi$ and $\omega_0' = \omega_0 \sin\varphi$, the quantities in the boosted frame. The total force, F_{tot}, is a combination of two forces: F_p, the ponderomotive force (same force as in two counter-propagating waves) and F_d a new force, which we call *inertial force* and which depends on φ. In the laboratory frame, the interference field is stationary along $\boldsymbol{x}$ but drifts along $\boldsymbol{z}$. The force F_d represents, in the laboratory frame, the displacement of the electron population towards positive $\boldsymbol{z}$, dragged by the interference field and accelerated by E_z. It was shown in [Serebryakov et al., 2017] that indeed, in the grazing incidence regime, electrons could be accelerated on top of solid target surfaces by surfing within the interference field created by the combination of incident and reflective pulse.

If we define as before $\theta \to \pi + 2k_0'x$, the temporal evolution of the system after a time shift $(t \to t + \pi/2\omega_0')$ is given by:

$$\frac{\mathrm{d}^2\theta}{\mathrm{d}t^2} + \omega^2 \sin\theta\left(1+\cos(2\omega_0't)\right) + 2\omega^2 a_0^{-1} \cot\varphi \cos\left(\theta/2\right)\cos\left(\omega_0't\right) = 0, \tag{8.66}$$

with $\omega^2 = 2\,a_0^2\omega_0'^2$. It does not look like a standard pendulum equation but it can still be viewed as the equation of a Kapitza'spendulum with two drivers of different frequencies.

When increasing $\cot\varphi$, F_d become the leading force over F_p and new dynamics appear, oscillating at a characteristic frequency ω_0'. According to Eq. (8.65), the turning point occurs for $\cot\varphi \sim a_0$, which might impose grazing incidences ($\varphi \to 0°$ and $\cot\varphi \to +\infty$) when a_0 becomes too high: for example for $a_0 = 0.1$, $\varphi \simeq 84.3°$ and for $a_0 = 3$, $\varphi \simeq 18.4°$. Because $F_d \propto a_0$ and $F_p \propto a_0^2$, the magnitude of F_d quickly becomes negligible at high intensities if $\cot\varphi$ is not increased accordingly. Oppositely, in term of relativistic inertia, when $\cot\varphi \gg a_0$, the electrons

drift at ultra-relativistic velocities and their inertial mass is larger. Then, the laser intensity needs to be strong enough to impair the drift motion.

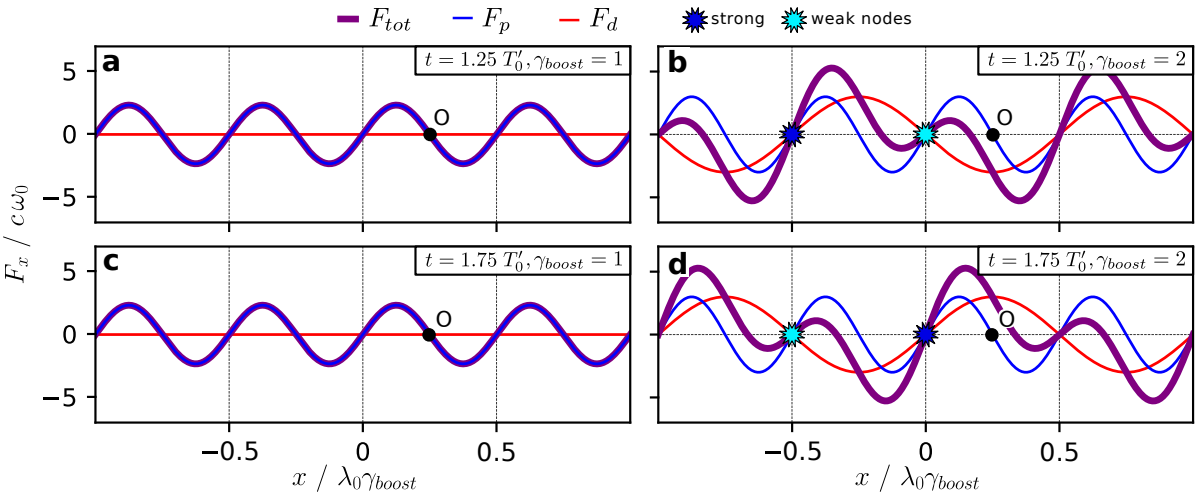

Figure 8.20: **Spatial profile of the different forces at various times and angles of incidence** - For each panel, we plot three curves corresponding to different ponderomotive forces as a function of the position in the boosted frame: F_p in blue, F_d in red and F_{tot} in purple. The different times or γ_{boost} are reported in labels. The O point designates one position of an electric field node, while the vertical dashed lines indicate the positions of magnetic field nodes. These can either be strong or weak at oblique incidence.

In Fig. 8.20, we plot F_p, F_d and F_{tot}, for $\varphi = 90°$ (counter-propagative case) and 30° and for two different times separated by half a laser period. Here and in all the following, the electron position x, is normalized to the laser wavelength in the boosted frame, $\lambda'_0 = \lambda_0\gamma_{boost}$ and each time t to the laser period in the boosted frame $T'_0 = T_0\gamma_{boost}$. The locations of the electromagnetic nodes are unchanged, when considering the quantities in the boosted frame: electric field nodes for each $k'_0 x = \pi/2 + n\pi$ ($\forall n \in \mathbb{Z}$) and magnetic field nodes for each $k'_0 x = n\pi$. From Fig. 8.20 comes few comments:

- in comparison to F_p, the sign of F_d does depend on both the sign of its spatial and temporal terms ($\sin(\omega'_0 t)$ can be negative). It means that oppositely to Sec. 8.3, the total force on particles, F_{tot} ($= F_p + F_d$), is no more necessarily positive on the left part of an electric field node (O point) and negative on the right part.
- F_p is $T'_0/2$-periodic in time and does not depend on φ so the blue curves are identical for all panels.
- For the counter propagating case, in Figs. 8.20–a, c, F_d is identically zero and of course, $F_{tot} = F_p$.
- When $\cot\varphi \neq 0$ and $\gamma_{boost} > 1$ (see Figs. 8.20–b, d), the red curves exhibit a periodic behaviour with a space period twice larger than the blue ones. In addition, because the time period is also twice larger, F_d is different at $t = 1.25$ and $1.75\,T'_0$.
- The spatial variation of the total force around two consecutive magnetic nodes is now different. In the following, we will refer to a *strong node* (dark blue stars), when $|\partial F_{tot}/\partial x| \gg 0$ (e.g., around $x = -0.5\lambda'_0$ in Fig. 8.20–b) and a *weak node* (light blue stars), when

$|\partial F_{tot}/\partial x| \simeq 0$ (e.g., around $x = 0$ in Fig. 8.20–b). Each node is alternatively strong and weak along time (Figs. 8.20–b vs d). Around a strong node, particles will rapidly diverge, while around a weak node, they will follow a ballistic motion.

- The total amplitude of F_{tot} is also stronger in oblique incidence suggesting that electrons would be more accelerated in this case.

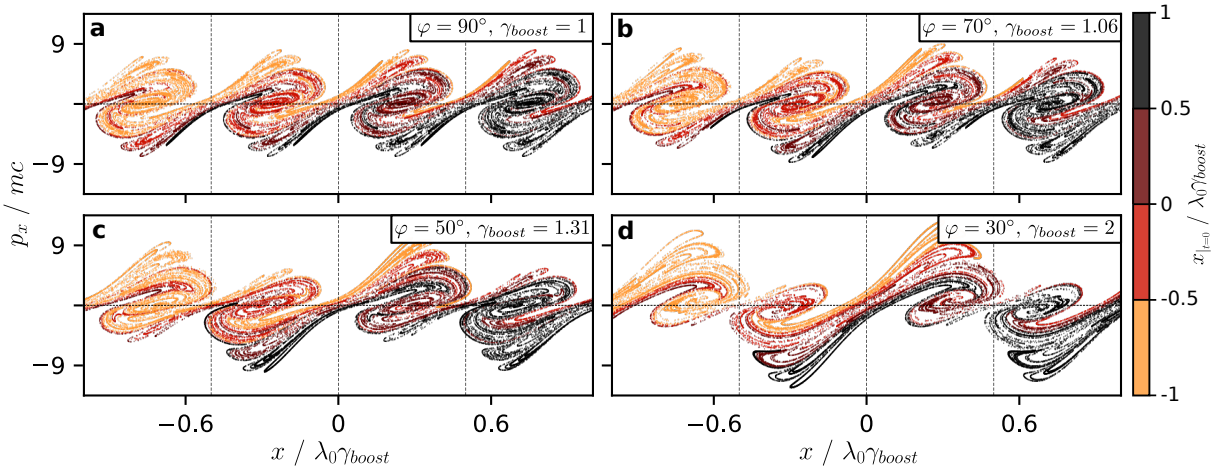

Figure 8.21: **Electron dynamics in the p/p case for different angles of incidence** - Each panel represents the electron distribution in phase space at $t = 2.8T'_0$ and $a_0 = 3$ for different angles of incidence indicated in labels. As always, the different colors correspond to the initial positions within buckets.

The distributions in phase space of electrons exposed to these forces are pictured in Fig. 8.21 for φ varying from 90° to 30° and $a_0 = 3$. There is a continuous transition from a stretching and folding pattern, where the profiles in all buckets look similar (Fig. 8.21–a), to a larger scale behaviour where the distribution is different around two successive magnetic nodes (Fig. 8.21–d).

The particular profile of Fig. 8.21–d resembles to what we found in PIC simulations in the previous chapter (see Fig. 7.4–d, page 104 or Figs. 7.8–b, c, page 108 for example). The energy of electrons in the fields is also growing with $\cot\varphi$ as suggested by the variation of F_{tot}.

The distribution of Fig. 8.21–d seems more complex but still presents key signatures of the previous stretching and folding. The distribution seems to fold around fixed points (e.g., around $x = -0.5\lambda'_0$ in Fig. 8.21–d), which indicates a phase of folding but it is also stretched (e.g., around $x = 0$), which might be caused by a stretching phase.

We propose to analyze the temporal evolution of the electron distribution step by step, in the similar way as in Fig. 8.7 (page 132). The results are reported in Fig. 8.22. Once again, the corresponding profile of the total force is plotted on top of each panel but this time, we choose different shades of blues to highlight weak (light blue) and strong nodes (dark blue). We have already seen that introducing an angle adds new effects, which take place on larger time and space scales. It is then necessary to consider at least two full periods in space and time.

Starting at $t = 2.8T'_0$ (Fig. 8.22–a), the total force stays close to zero, which as we know, lets the particle follow a ballistic motion (straight blue arrows in Fig. 8.22–b). The whole distribution is thus elongated along the x-axis. We recognize a stretching phase, very similar to the case

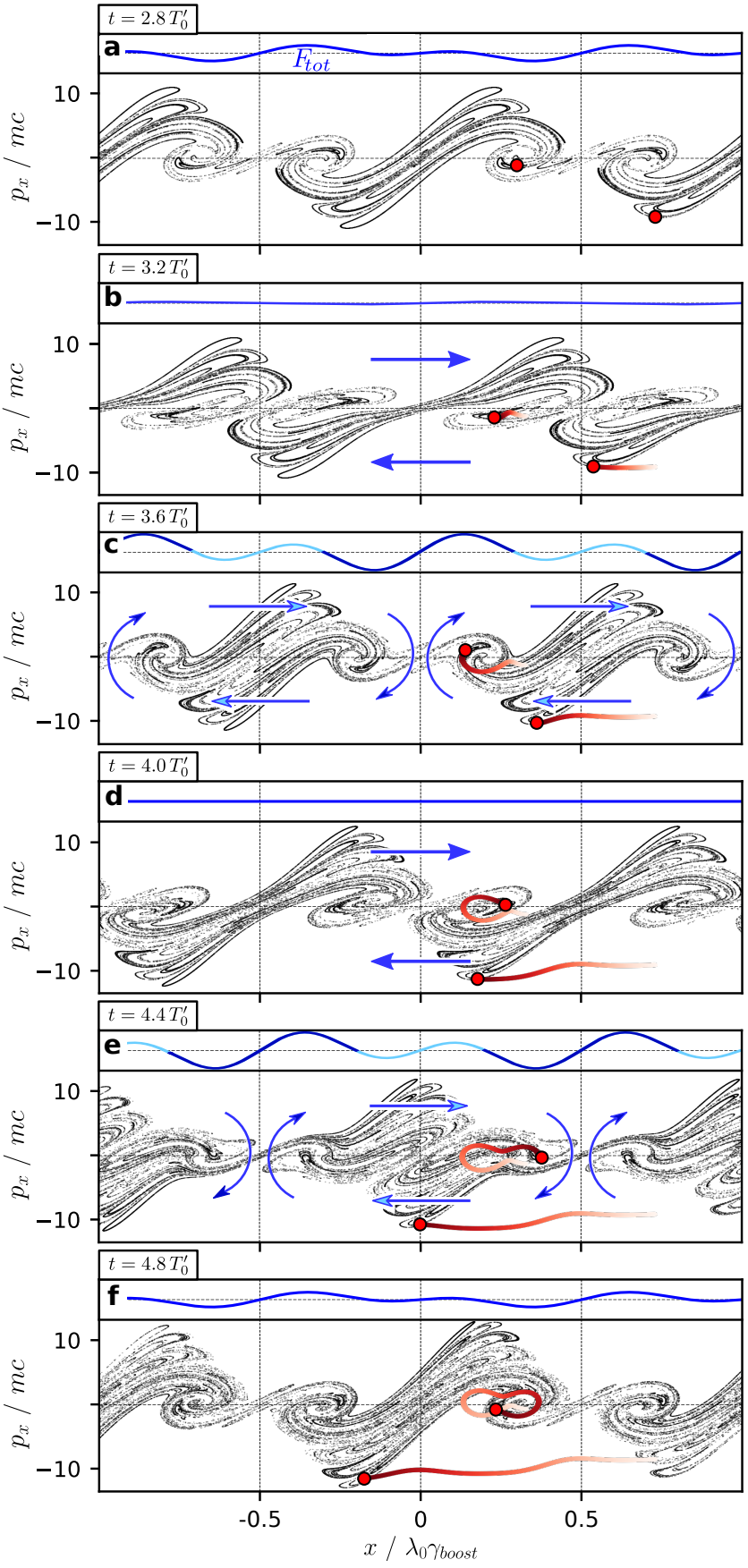

Figure 8.22: **Temporal evolution of the distribution of electrons in the p/p case in oblique incidence** - Same figures as Figs. 8.6 and 8.7 (pages 131 and 132) but with an angle of incidence $\varphi = 30°$. Each panel corresponds to different snapshots of the electron distribution in phase space for $a_0 = 3$ at different times. On top of each panel, we plot the corresponding spatial profile of F_{tot} in different shades of blue to highlight strong (dark) and weak (light) nodes.

$\varphi = 90°$. It persists during half a laser period (between Figs. 8.22–a and c). Another stretching phase is clearly visible in Fig. 8.22–d.

A more interesting mechanism occurs for both Figs. 8.22–c and e. This time, the total force is non zero and different processes happen around magnetic nodes depending on their type (weak or strong):

- **Around strong nodes** (e.g., $x = 0$ in Fig. 8.22–c), the total force is intense and the particles are rotating. Considering a single bucket, it would be almost as if the distribution were folding only in the half space between the strong node and the electric node (see the dark blue curved arrow on the left part of the third bucket, $0 < x/\lambda_0' < 0.5$, in Fig. 8.22–c).

- **Around weak nodes** (e.g., $x = 0.5\lambda_0'$ in Fig. 8.22–c), the total force amplitude remains low and particles do not feel much of any force. Then it is not so different from a stretching phase and the particles located in the other half space of a bucket are almost ballistic (see the light blue straight arrows on the right part of the third bucket in Fig. 8.22–c).

Now, let us focus on particle trajectories. In Fig. 8.22, two particles are drawn in red, one trapped and one circulating. In the previous sections, a trapped particle described a quasi-elliptic trajectory centered around an electric node. However, based on the spatial profile of the whole ponderomotive force in Fig. 8.21–b, d, the position where the force vanishes, does not perfectly match an electric field node anymore. In fact, this position is always closer to the weak node and no more fixed in time. The trapped particles are now oscillating around two limit attractive points instead of one, depending on which side of the bucket the weak node is. The resulting trajectory is shaped as a butterfly (see Fig. 8.22–f).

Oppositely, some particles are circulating. If they are located at a right position, they may even follow a quasi-ballistic motion during multiple laser periods. In counter-propagating incidence, the whole electron distribution rotated when the ponderomotive force started to be intense. When $\varphi \neq 90°$, the force might be neglected near a weak node, even during the folding phase. It is then possible for a particle not to feel any force during most of the interaction and thus keep a ballistic motion. Such a particle is pictured in red at the bottom of the different panels of Fig. 8.22). From Figs. 8.22–a to f, this electron is traveling through zones where the force remains low, because it is either a stretching phase or around a weak node (see the blue straight arrows). As a consequence, its trajectory stays almost horizontal.

From an experimental point of view, increasing the angle of incidence can be worthwhile to increase the plasma heating, while keeping the same laser intensities. However, this only works if the laser polarization is in the plane of incidence. In two s-polarized waves, there is no influence from the angle of incidence.

Electron distribution in two s/s waves. When the laser polarization is switched from p to s, just A_y remains, while A_z disappears and with it the dependency on $\cot\varphi$. Then, the equation of motion, Eq. (8.62) (page 147), is strictly equivalent to the counter-propagating case (Eq. (8.10), page 121) no matter the angle between the two waves. In s-polarization, the electric field is always orthogonal to the plane of incidence and the electric interference field created by the two waves is invariant by φ. Since only the Lorentz electric force is working, the energy gained by electrons along their motion cannot depend on φ.

When the laser polarizations are orthogonal to the plane of incidence, there is no benefit to increase the angle between the two waves for the longitudinal component. In the chapters 5 and 7, the PIC simulations and experiments were performed in oblique incidence and we noticed slight differences in the density profile and energy between p and s-polarizations. In p/p configuration, the counter-propagating case seems always disadvantageous and changing φ tends to increase the particle energy (see Fig. 8.21). Oppositely, in s/s configuration, every oblique incidence is equivalent to the case $\varphi = 90°$ for the longitudinal dynamics. The non-dependence in φ in this case can explain the observed differences of electron energy in experiments.

Electron distribution in two circularly polarized waves. Finally, we treat the RHC/LHC configuration. As a reminder, this case was stable in the Liouville sense, when $\varphi = 90°$. However, we show now that in oblique incidence, the system is no more predictable. Here, the vector potential was defined in Eq. (8.17) (page 124). After some math, the classical equation of motion reads:

$$\frac{\mathrm{d}^2 x}{\mathrm{d}t^2} \underbrace{-a_0^2 c^2 k_0' \sin\left(2k_0' x\right)}_{F_p} + \underbrace{2a_0 c^2 k_0' \cot\varphi \sin\left(k_0' x\right) \sin\left(\omega_0' t\right)}_{F_d} = 0. \tag{8.67}$$

As before, we write the last terms as two forces and recognize a first force F_p corresponding to a simple pendulum and a second force F_d depending on $\cot\varphi$. F_d is identical in the p/p case, because this force only depends on A_z, defined by the same formula (see Eq. (8.17), page 124, and Eq. (8.24), page 125). The equation of motion is now rather complex and exhibits different oscillators.

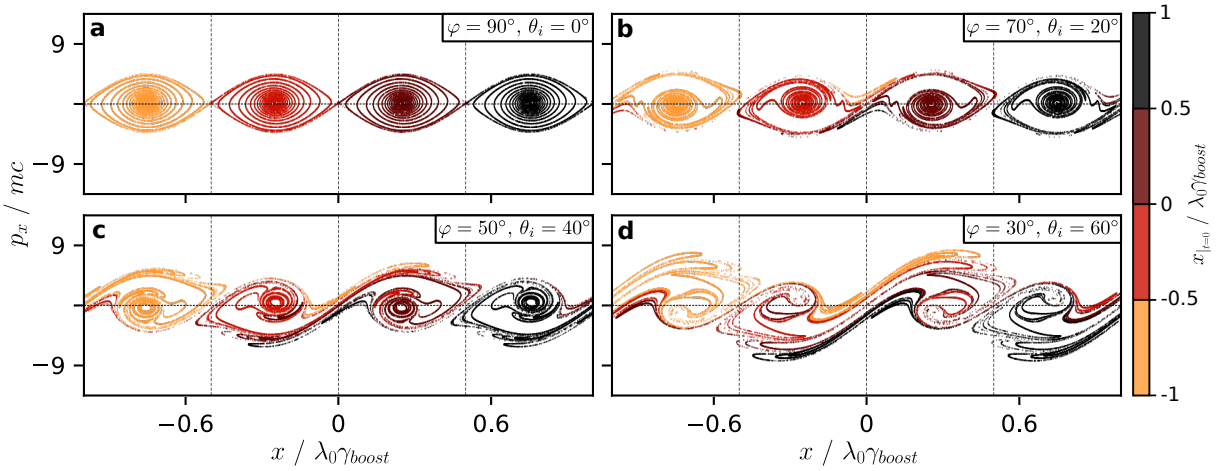

Figure 8.23: **Electron dynamics in the RHC/LHC case for different angle of incidence** - Same figure as Fig. 8.21 but for a different laser polarization.

In Fig. 8.23, we plot the distributions of electrons in phase space for different angles. Although the electron dynamics are stable in Fig. 8.23–a, when $\varphi \neq 90°$, particle manage to escape from their initial buckets and the different colors are mixing. It is an indication that chaotic behaviours appear.

It is interesting to note that the limit profile when $\varphi \to 0°$, tends to the p/p case (see Fig. 8.23–d vs Fig. 8.21–d). At grazing incidences, the impact of the field components along y in the electron motion is lowered and $F_d \gg F_p$. Then, both equations of motion tend to the same equation.

Through equations of motion, we were able to understand the distribution of electrons in multiple cases in the boosted frame for different γ_{boost}. When the angle of incidence is changed from 90°, a slower component appears, which modifies the stretching and folding. It introduces chaos in initially predictable configurations and more generally increases particle energy.

8.5.2 Energy evolution

When two p-polarized waves interfere with different angles of incidence, the electron energy seems to increase. This gain can be quantified trough equations of motion, at least at low intensity. To do so, we follow the same mathematical reasoning performed in Sec. 8.3.2 and derive the equation of the separatrix, when the energy is expected to be at its maximum, i.e., just before a stretching phase. When adding an angle, the folding phase was decomposed into two regimes, around strong and weak nodes. We decide to consider a strong node for $x = 0$, which gives $t = 3\,T_0'/4$. Eq. (8.64) near that time simplifies as:

$$\frac{\mathrm{d}^2x}{\mathrm{d}t^2} = 2a_0^2c^2k_0' \sin\left(2k_0'x\right) + 2a_0c^2k_0' \cot\varphi \sin\left(k_0'x\right). \tag{8.68}$$

Multiplying both members by $\dot{x}$ and integrating the result, we find the quadrature as:

$$\frac{1}{2}\left(\frac{\mathrm{d}x}{\mathrm{d}t}\right)^2 = -a_0^2c^2 \cos\left(2k_0'x\right) - 2a_0c^2 \cot\varphi \cos\left(k_0'x\right) + C^{st}. \tag{8.69}$$

Eq. (8.69) defines closed orbits similarly to the case without angle (see Sec. 8.3.2, page 133) but this time, they are no more elliptical. We decide to label each orbit by the point $(x_0,\, 0)$, where x_0 is the position along the orbit, when $v_x = 0$.

$$\begin{aligned} & C^{st} = a_0^2c^2 \cos\left(2k_0'x_0\right) + 2a_0c^2 \cot\varphi \cos\left(k_0'x_0\right), \\ \Leftrightarrow \quad & p_x = mc\sqrt{2a_0}\sqrt{a_0\Big(\cos\left(2k_0'x_0\right) - \cos\left(2k_0'x\right)\Big) + 2\cot\varphi\Big(\cos\left(k_0'x_0\right) - \cos\left(k_0'x\right)\Big)}, \end{aligned} \tag{8.70}$$

where we used p_x instead of v_x. It is of course an approximation because we start from the classical form of the equations of motion. It will give good results at low a_0 but the model might give inaccurate results, when the intensity becomes too high. Also, the canonical momentum conservation gives a value for p_z near $t = 3\,T_0'/4$:

$$\begin{aligned} p_z &= eA_z + mc\cot\varphi \\ &= mc\Big(\cot\varphi - 2a_0\cos\left(k_0'x\right)\Big), \end{aligned} \tag{8.71}$$

and finally γ:

$$\begin{aligned}\gamma &= \sqrt{1+\left(p_x^2+\cancel{p_y^2}+p_z^2\right)/m^2c^2} \\ &= \sqrt{1+2a_0\Big(a_0\Big(\cos\left(2k_0'x_0\right)-\cos\left(2k_0'x\right)\Big)+2\cot\varphi\Big(\cos\left(k_0'x_0\right)-\cos\left(k_0'x\right)\Big)\Big) \\ &\qquad +\Big(\cot\varphi-2a_0\cos\left(k_0'x\right)\Big)^2} \\ &= \sqrt{1+\cot^2\varphi+2a_0\Big(a_0\Big(\cos\left(2k_0'x_0\right)-\cos\left(2k_0'x\right)+2\cos^2\left(k_0'x\right)\Big) \\ &\qquad +2\cot\varphi\Big(\cos\left(k_0'x_0\right)-2\cos\left(k_0'x\right)\Big)\Big)}\end{aligned}$$

$$\gamma = \sqrt{\gamma_{boost}^2+2a_0\Big(2a_0\cos^2\left(2k_0'x_0\right)+2\cot\varphi\Big(\cos\left(k_0'x_0\right)-2\cos\left(k_0'x\right)\Big)\Big)}. \tag{8.72}$$

where we used:

- $1+\cot^2\varphi = 1/\sin^2\varphi = \gamma_{boost}^2$,
- $$\begin{aligned}\cos\left(2k_0'x_0\right)-\cos\left(2k_0'x\right)+2\cos^2\left(k_0'x\right) &= 2\cos\left(k_0'x_0\right)-1-2\cos^2\left(k_0'x\right)+1+2\cos^2\left(k_0'x\right) \\ &= 2\cos\left(k_0'x_0\right).\end{aligned} \tag{8.73}$$

The equation on γ is valid on any orbit, but the separatrix is the one which allows the largest domain of validity and for which the cosines of $k_0'x_0$ are equal to 1. The limit γ is given by:

$$\boxed{\gamma = \sqrt{\gamma_{boost}^2+4a_0^2+2a_0\cot\varphi\Big(1-3\cos\left(k_0'x\right)\Big)}} \tag{8.74}$$

In Fig. 8.24, we plot for two angles of incidence $\varphi = 70°$ and $30°$ the different electron distributions as a function of p_x and γ as well as their respective separatrix (defined for p_x as Eq. (8.70) and for γ as Eq. (8.74)). We chose $a_0 = 3$ and despite our approximations, the theoretical separatrices still fit the evolution of particle energy well, even in the relativistic regime.

In Eq. (8.74), the energy is expressed in the boosted frame. For direct comparison with experimental observables, its value in the laboratory frame is mandatory. It can be obtained after reverse Lorentz transformation:

$$\begin{aligned}\gamma_{lab} &= \gamma_{boost}\gamma+\beta_{boost}\gamma_{boost}\frac{p_z}{mc} \\ &= \gamma_{boost}\sqrt{\gamma_{boost}^2+4a_0^2+2a_0\cot\varphi\Big(1-3\cos\left(k_0'x\right)\Big)}+\cot\varphi\Big(\cot\varphi-2a_0\cos\left(k_0'x\right)\Big)\end{aligned} \tag{8.75}$$

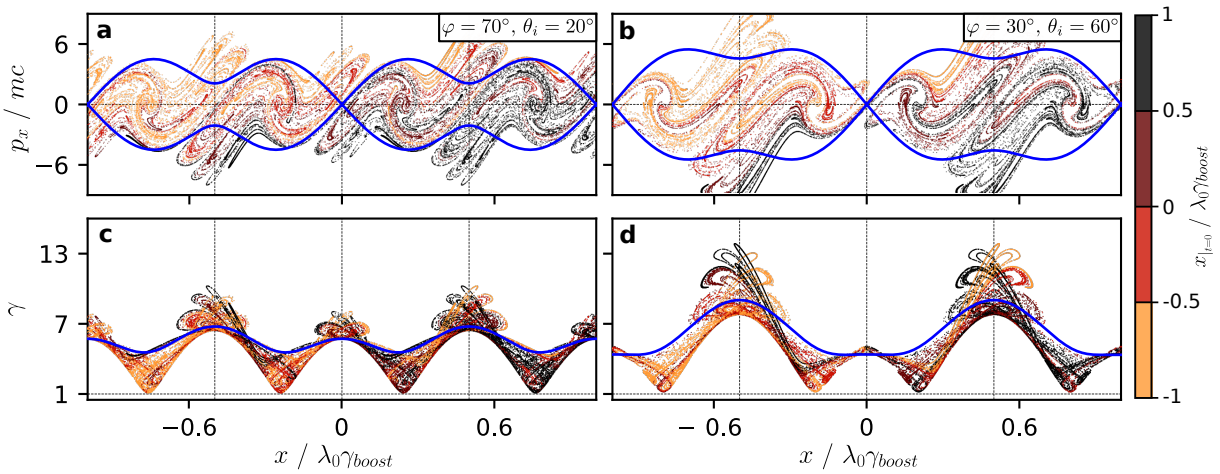

Figure 8.24: **Phase space distributions and energy separatrices for different angles of incidence** - Each panel represents the electron distribution at $t = 2.75\, T_0\gamma_{boost}$ and $a_0 = 3$ for different angles of incidence: (a, c): $\theta_i = 20°$, (b, d): $\theta_i = 40°$ in different spaces: (a, b): (x, p_x) and (c, d): (x, γ). The theoretical separatrices are plotted on top in blue and correspond to Eq. (8.70) for p_x and to Eq. (8.74) for γ.

The mean energy of electrons can be obtained by averaging γ_{lab} along x. The integral of Eq. (8.75) is not simple and can be expressed with elliptical function of the second kind. An approximate value can be obtained by zeroing the cosines:

$$\gamma_{lab} \simeq \cot^2\varphi + \frac{1}{\sin\varphi}\sqrt{\frac{1}{\sin^2\varphi} + 4a_0^2 + 2a_0\cot\varphi} \tag{8.76}$$

This formula allows for direct comparisons with experimental observables of stochastic heating with solid targets.

As a reminder, the stochastic heating was found to be the prevailing mechanism in laser-solid target interaction, when the characteristic density gradient length L_{grad} in front of the surface was sufficiently long ($L_{grad} \sim \lambda_0$). In [Chopineau et al., 2019] are discussed experimental evolutions of the energy of ejected electrons as a function of L_{grad} and the laser angle of incidence on target — $\theta_i = \pi/2 - \varphi$. The main results of this scan are reported in Fig. 8.25–a, where the bottom region corresponding to the short gradient regime is hatched. The plotted quantity is $\mathcal{E}$, the average energy of all electrons recorded on the detector.

Firstly, $\mathcal{E}$ is increasing with θ_i, which is coherent with the theoretical study presented earlier in the manuscript. For $L_{grad} = 0.3\,\lambda_0$, the profile of $\mathcal{E}$ as a function of θ_i is plotted in Fig. 8.25–b as well as the analytical energy $(\gamma_{lab} - 1)mc^2$ defined in Eq. (8.76). There is no perfect match between the two curves but our model still gives fair quantitative results and reproduces the energy growth.

Secondly, $\mathcal{E}$ is hardly affected by L_{grad} as far as the density gradient is long enough so that stochastic heating occurs in the under dense part of the plasma gradient . This reinforces the choice of simulating free electrons and neglecting all effects that are expected to play a major role in denser parts of the gradient. It also means that one does not need an extreme contrast control of the main impulsion. A too strong pedestal would lead precisely to density gradient

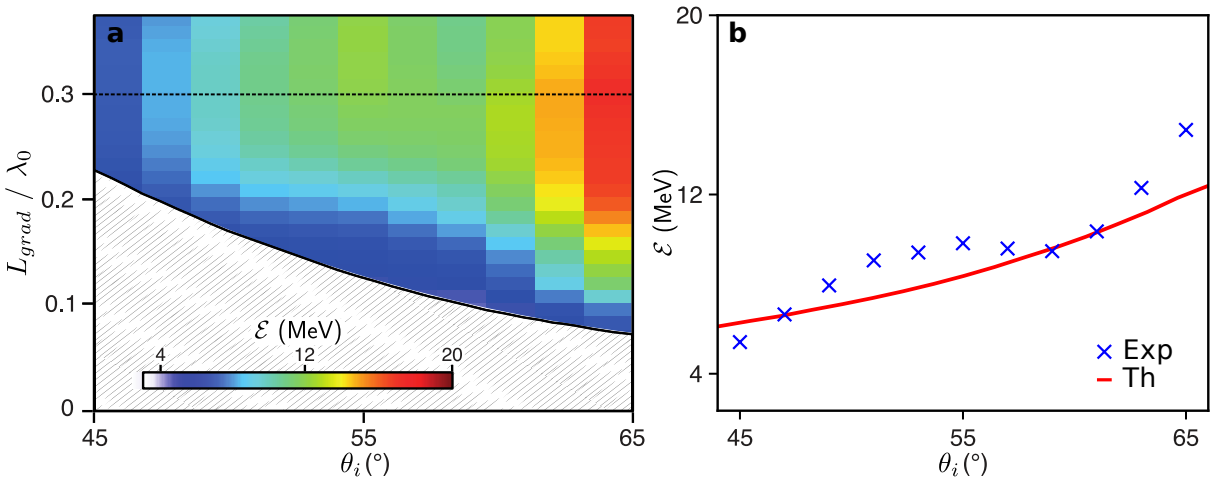

Figure 8.25: **Measured averaged energy of ejected electrons as a function of θ_i and L_{grad}** - On panel (a), we report experimental results presented in [Chopineau et al., 2019], for which we only retain the part dealing with the long gradient regime, where the stochastic heating is predominant. On panel (b), we plot a line out corresponding to $L_{grad} = 0.3\,\lambda_0$. The experimental data are displayed as blue crosses, while the theoretical energy — $\mathcal{E} = (\gamma_{lab} - 1)mc^2$ — is pictured in red.

scale lengths of the order of λ at the arrival of the main pulse and stochastic heating is likely to be dominant. Then, for a given angle of incidence, a measure of the ejected electron energy could give an indication of the value of a_0 at the time of the interaction:

$$a_0 \simeq \frac{1}{4}\left(-\cot\varphi + \sqrt{\cot^2\varphi - \frac{4}{\sin^2\varphi} + 4\sin^2\varphi\left(\gamma_{lab} - \cot^2\varphi\right)} \right) \tag{8.77}$$

or

$$a_0 \simeq \frac{1}{4}\left(-\tan\theta_i + \sqrt{\tan^2\theta_i - \frac{4}{\cos^2\theta_i} + 4\cos^2\theta_i\left(\gamma_{lab} - \tan^2\theta_i\right)} \right) \tag{8.78}$$

It would be interesting to perform an experimental scan to test the validity domain of our model, for a large range of laser intensity, θ_i and polarizations. If the outcomes agree with our analytical results, it might be possible to design a diagnostic, which gives the laser intensity at focus, shot to shot. It does not necessarily require a good control of the contrast in front of the laser pulse, which could facilitate its use in most laser facilities dealing with solid targets.

Conclusion

In this chapter, the mechanism behind stochastic heating was extensively investigated. Unlike most of previous studies, we tried to explain the different behaviours, with simple physical concepts, which can be easily understandable by non-specialist of chaos theory or Hamiltonian formalism.

To this end, we showed that electron dynamics in different laser polarizations, can be modeled as different pendulum equations, which might be predictable or chaotic. In particular, the equations of motion in two p-polarized waves can be written as a forced pendulum, known as Kapitza's pendulum, which exhibits chaotic properties if laser intensities become too high.

Decomposing the time evolution of the pendulum driving force using a constant piecewise function, we distinguish two phases, one when the force on the particles is identically zero, resulting in a ballistic motion — the stretching phase— and one when the force is intense and the particles are rotating around electric nodes — the folding phase. Based on that stretching and folding effect and by simple geometric and probabilistic models, we developed a model for the chaos threshold as a function of laser intensity as well as a particle diffusion model.

Introducing an angle between the two waves complicates the mechanism but the energy gained by the electrons is observed to increase. It is possible to write the full equations of motion in the Bourdier frame, letting appear a new force oscillating at a different frequency. The stretching and folding phases are modified in this case and we observe a succession of strong and weak foldings, which change the profiles of the electron distributions.

Finally, we are able to derive the different equations for the separatrices and propose a mean value for the ejected electron energy as a function of both angle of incidence and laser intensity. This energy should be compared to experimental data. In a case of a well agreement, it might be possible to design an experimental diagnostic, which gives an idea of the real laser intensity reached at focus, shot to shot.

Conclusion and Future Prospects

This PhD work sheds light on the major coupling mechanisms between ultra-intense lasers and dense plasmas. This study heavily relies on numerical simulations that reproduce and support experiments conducted at CEA Saclay.

All along this manuscript, direct interpretations of experimental observations have been made possible by performing accurate Particle-In-Cell (PIC) simulations with the WARP+PXR code. As opposed to standard PIC codes, this code advances Maxwell's equations in Fourier space (= pseudo-spectral solver), which greatly reduces numerical dispersion of electromagnetic waves in vacuum as well as numerical noise. This numerical dispersion induces spurious effects in the simulation that, when applied to laser-plasma mirror interactions, severely deflect the high-order harmonic beam emitted by the plasma mirror. This effect was extensively studied and a simple toy model based on the Snell-Descartes law was developed. It allows us to finely predict the angular deviation of harmonics depending on the spatio-temporal resolution and the Maxwell solver used in the simulations. In particular, it was found that the use of pseudo-spectral solvers as the ones implemented in the WARP+PXR code completely mitigates the spurious deviation and thus renders physically realistic and reliable simulations of the interaction between a laser and a dense plasma.

Couplings mechanisms between a laser and an overdense plasma

Based on pseudo-spectral PIC simulations performed with WARP+PXR, we investigated the influence of the density gradient scale length L_g in front of the target surface on the experimentally observed emission of light and particles, when a high-power laser pulse ($a_0 > 1$) reflects off a dense plasma. When the plasma surface is steep ($L_g \sim \lambda_0/15$), the plasma behaves as a plasma mirror, capable of generating a comb of high order harmonics as well as a high charge relativistic electron beam ($\sim$ 1 nC at 10 MeV). The electron and harmonic signals are synchronized in time and angularly separated by few tens of milliradians. By contrast, for larger gradient scale lengths ($L_g \sim \lambda$), the electron and harmonic signals radically change. The harmonic signal completely collapses, while the electron distribution broadens angularly. The electron energy is also higher and hardly varies with the angle of incidence of the laser on the plasma.

Our numerical and theoretical investigation indicates that two different coupling mechanisms between light and matter are responsible for such recorded electron and harmonic signals. We provide unambiguous evidence for a transition between the temporally periodic Brunel absorption to the — chaotic — stochastic heating at relativistic laser intensities. Our work complements previous investigations concentrated at lower intensity that expected a transition from Brunel absorption to yet another mechanism, known as resonance absorption.

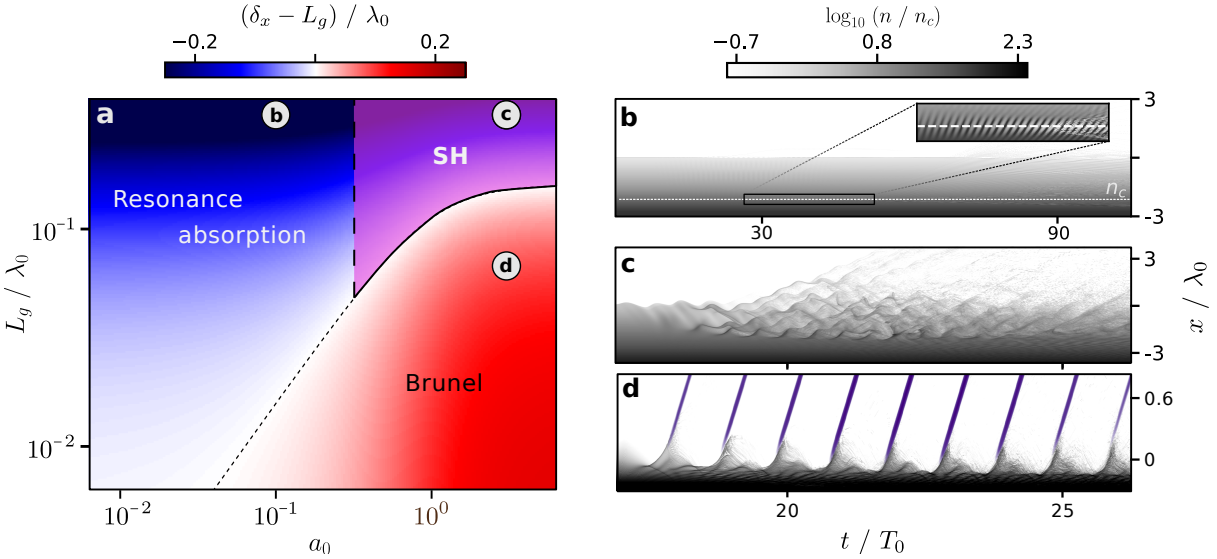

Figure Concl.1: **Transition diagram between different coupling mechanisms at play in the interaction between a laser and an overdense plasma** - Panel (a) displays three different regions corresponding to the dominant coupling mechanisms as a function of a_0 and L_g. In the other panels are recalled the different behaviours of the target surface in each different case. Grey dots in panel (a) indicate the condition on a_0 and L_g leading to the right panels.

We summarize in Fig. Concl.1 our understanding of the laser dense plasma interaction so far at the end of this thesis:

- starting at low intensity and large gradients (Fig. Concl.1–b), the dominant mechanism is **resonance absorption**, which has been widely studied for many years. During the interaction, some laser energy may tunnel from the reflective point up to the critical density n_c in the form of an evanescent wave, where it drives a resonant plasma wave. This plasma wave will eventually break after some time, propelling electrons out of the plasma.

- When the laser intensity is increased for a fixed L_g (Fig. Concl.1–c), a new mechanism appears on top of resonance absorption: **stochastic heating**. Characterizing this mechanism was precisely one of the main goal of my thesis. In the underdense part of the plasma, electrons are exposed to the standing wave formed in front of the overcritical part of the plasma by superposition of incidence and reflected beams. While evolving in the two waves, electrons behave chaotically and absorb an important fraction of the laser energy. The transition from resonance absorption to stochastic heating is smooth: the two mechanisms actually coexist for a wide range of intensity starting from the onset of chaos ($a_0 \sim 0.15$) to the disappearance of plasma wave growth near n_c by relativistic transparency ($a_0 \sim 2.87$). Indeed, at higher intensities, the laser reflects on a density higher than n_c, which prevents the resonance to happen.

- When L_g is lowered, the underdense part of the plasma subject to the standing wave shrinks. Stochastic heating is then expected to faint in favor of the well-known **Brunel mechanism** as soon as the quivering motion of electrons in the laser field exceeds the gradient scale length (see Fig. Concl.1–c). In this case, the surface electrons are first pulled out of the plasma into vacuum by the laser component normal to the plasma surface.

When this component changes sign the electrons are pushed back to the target. Additionally, numerical simulations show that a fraction of electrons still manages to escape the plasma surface towards vacuum in the form of attosecond bunches. At high intensities, these Brunel electrons reach relativistic velocities when they escape the plasma and induce a relativistic Doppler effect on the reflected laser field. It results in the generation of high-order harmonic comb through a process called the Relativistic Oscillating Mirror mechanism.

This work should prove extremely useful for the interpretation of a broad range of experiments and simulations performed with high-power ultrashort lasers on dense targets (related to particle acceleration or high harmonic generation) principally for two reasons.

First, stochastic heating is likely to be dominant in experiments which do not require (or simply do not feature) a high temporal contrast. The picosecond pedestal in front of the main pulse would lead precisely to density gradient scale lengths of the order of λ before the arrival of the main pulse. With the advent of petawatt class lasers worldwide, generating pulses that preserve the target structure will be even more challenging. The intensities reached on target would exceed 10^{22-23} W.cm^{-2} and a contrast as high as 10^9 will no more prevent target ionization and plasma expansion. In that matter, additional optical components will have to be introduced to strongly lower the intensity of the not-so weak pedestal (e.g., double plasma mirror or more).

Second, we provide several simple observables that can help finding which coupling mechanisms dominate in the regimes of interaction. In addition to electron and harmonic emissions, the redistribution of the initial laser energy after the laser-plasma interaction provides clear signatures of each mechanism. In Fig. Concl.2, the different distributions obtained for both short and long gradient regimes, and for both p and s laser polarizations, are displayed as pie charts . For short gradients and p-polarization (pictured as the left chart Fig. Concl.2–a), around 25% of the laser is converted into harmonics of the laser frequency (mostly low-orders), and about 30% is deposited as particle kinetic energy (including the relativistic electrons observed

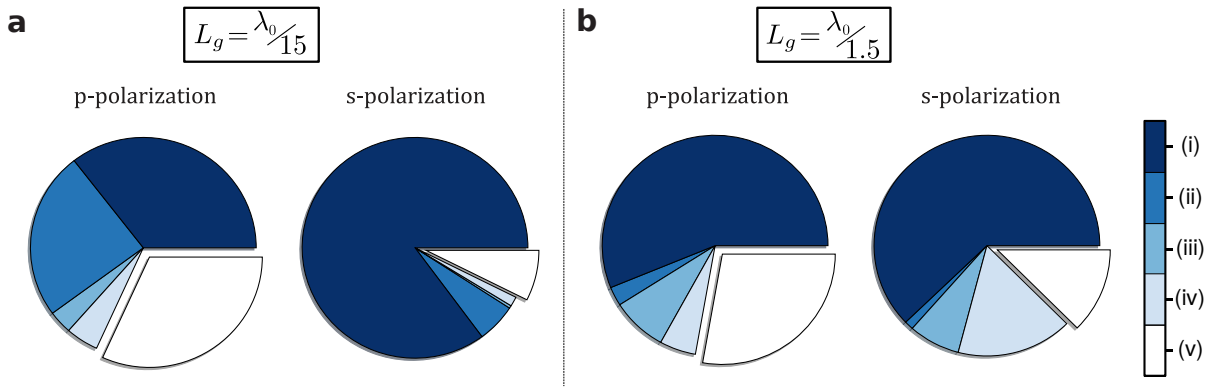

Figure Concl.2: **Distribution of the initial laser pulse energy after the interaction, in different laser-plasma configurations** - These pie charts summarize how the laser energy is distributed after the laser plasma interaction, in the short (panel (a)) and long (panel (b)) gradient regimes, for p and s-polarizations. Five categories have been numerically separated as followed: (i) electromagnetic (EM) energy in the fundamental laser frequency in the specular direction, (ii) in the harmonics of the laser frequency in the specular direction, (iii) in quasi-static fields (i.e. with a frequency lower than the laser frequency), (iv) in non-static fields in the non-specular direction, and (v) kinetic energy of plasma particles.

in the experiments). When the polarization is switched to s (right chart Fig. Concl.2–a), these two contributions get considerably reduced, down to around 5% each, leading to a much higher reflectivity of the fundamental laser frequency. By contrast, for long gradients (Fig. Concl.2–b), very little energy is converted into harmonics, regardless of polarization. As already emphasized, quasi-static fields around the plasma surface are observed in the long gradient regime that drain a significant fraction of the laser energy compared to the short gradient regime. In p-polarization, the fraction of energy going into particle kinetic energy is only slightly weaker than in the short gradient case, and gets reduced by about 50% in s-polarization. A proper understanding of the different coupling mechanisms can help finding optimal conditions in experiments and allow for a better control of the interaction.

A novel approach to describe stochastic heating in two colliding waves

Another important part of this PhD thesis was dedicated to the derivation of a model for stochastic heating understandable by non-specialists of chaos theory or Hamiltonian formalism. Our approach precisely bridges the gap between a partially-predictive but non-intuitive heavy Mathematical formalism and intuitive but not predictive physical reasoning. We demonstrated that it is possible to reduce the equations of motion of particles in two waves to well-known physical systems such as simple gravity pendulum or Kapitza's pendulum. That correspondence gives deep physical intuitions on how electrons behave in different laser configurations (intensity, polarization or angle of incidence).

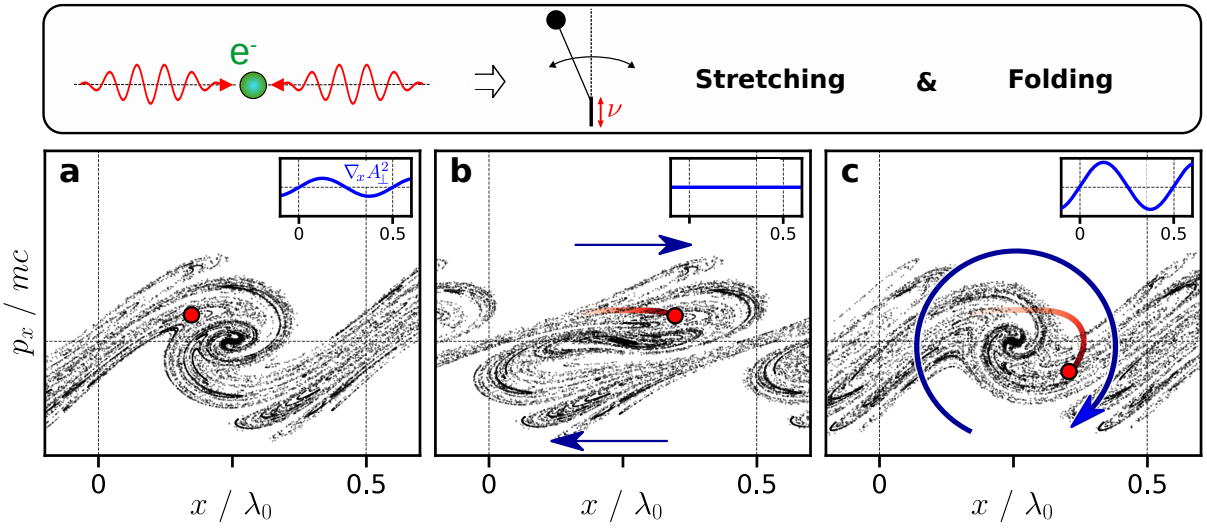

Figure Concl.3: **Stretching and folding of electron distribution in two waves** - This figure recalls the principal features of electron motion in two waves: it is formally equivalent to the bob motion of a Kapitza's pendulum, for which the phase space is stretched and folded over time.

In two linearly polarized waves, we observe a strong **stretching and folding** effect on the phase space distribution around electric nodes of the standing wave imposed by the temporal evolution of the ponderomotive force (see Fig. Concl.3). This effect is held responsible for chaos onset and to a loss of predictability each time a particle approaches a magnetic field node. For a chaotic system, it is a vain effort to perfectly approach the converged trajectories in numerical simulations, because both the numerical scheme and the finite precision of the floating point format introduce small errors that diverge exponentially over time. Instead, the whole electron

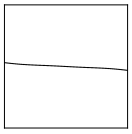

distribution can be modeled as a probabilistic random variable. Based on a random walk model, it was shown in particular that the probabilistic law for electron diffusion approaches a Gaussian distribution, when the intensity is sufficiently high.

Finally, the model was extended to oblique incidence and gives insights on the typical electron energy gained in the two waves. This energy explicitly depends on the angle between the two waves and their intensity and corresponds to the mean energy of emitted electrons recorded in the experiments. From there, further experiments can substantiate these preliminary results and demonstrate the feasibility of a new measurement technique that assesses the intensity at focus. This technique is independent from the gradient scale length as long as stochastic heating remains the dominant mechanism. Furthermore, the measurement only necessitates a single laser shot and does not require complex data processing. Users from most high-power laser facilities could thus benefit from this technique.

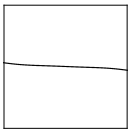

Appendices

A Probabilistic Distribution for Large n

Here we detail the derivation that gives the limit behaviour at large n of the probability law found in the manuscript (Eq. 8.54, page 144):

$$\mathcal{P}(x_n = g) = \frac{1}{4^n} \frac{(2n)!}{(n+g)!(n-g)!}. \tag{A.1}$$

We approach each factorial term of Eq. (8.54) by the Stirling's approximation:

$$n! \sim \sqrt{2\pi n}\Big(\frac{n}{e}\Big)^n, \tag{A.2}$$

It reads:

$$\mathcal{P}(x_n = g) = \frac{1}{4^n\sqrt{2\pi}} \frac{\sqrt{2n}}{\sqrt{(n-g)(n+g)}} \frac{e^{n-g}.e^{n-g}}{e^{2n}} \frac{(2n)^{2n}}{(n+g)^{n+g}(n-g)^{n-g}}. \tag{A.3}$$

We treat each term separately:

- $$\frac{\sqrt{2n}}{\sqrt{(n-g)(n+g)}} = \sqrt{\frac{2}{n}}\Big(1 - \frac{g^2}{n^2}\Big)^{-1/2} \tag{A.4}$$
$$= \sqrt{\frac{2}{n}}\Big(1 + \frac{g^2}{2n^2}\Big) \tag{A.5}$$
$$= \sqrt{\frac{2}{n}} \quad \text{at order 1} \tag{A.6}$$

- $$\frac{e^{n-g}.e^{n-g}}{e^{2n}} = 1 \tag{A.7}$$

(A.8)

- $$\begin{aligned}\frac{(2n)^{2n}}{(n+g)^{n+g}(n-g)^{n-g}} &= \frac{4^n n^{2n}}{n^{n+g}(1+g/n)^{n+g}\, n^{n-g}(1-g/n)^{n-g}} \\ &= \frac{4^n}{\exp\left((n+g)\log(1+g/n)\right).\exp\left((n-g)\log(1-g/n)\right)} \\ &= 4^n\left(\exp\left(\Big(n+g\Big).\Big(\frac{g}{n}-\frac{g^2}{2n^2}\Big)\right).\exp\left(\Big(n-g\Big).\Big(-\frac{g}{n}-\frac{g^2}{2n^2}\Big)\right)\right)^{-1} \text{ at order 1} \\ &= 4^n\left(\exp\left(g-\frac{g^2}{2n}+\frac{g^2}{n}\right).\exp\left(-g-\frac{g^2}{2n}+\frac{g^2}{n}\right)\right)^{-1} \qquad \text{(A.9)} \\ &= 4^n\exp\left(-\frac{g^2}{n}\right)\end{aligned}$$

Finally:

$$\boxed{\mathcal{P}(x_n=g)=\frac{1}{\sqrt{n\pi}}\exp\left(-\frac{g^2}{n}\right)} \qquad \text{(A.10)}$$

The particle distribution thus approaches a Gaussian distribution for large n.

B List of Publications and Attended Conferences

Publications

Pseudospectral Maxwell solvers for an accurate modeling of Doppler harmonic generation on plasma mirrors with particle-in-cell codes
G. Blaclard, H. Vincenti, R. Lehe, J.L. Vay
Physical Review E (2017), doi: 10.1103/PhysRevE.96.033305

Identification of Coupling Mechanisms between Ultraintense Laser Light and Dense Plasmas
L. Chopineau, A. Leblanc, G. Blaclard, A. Denoeud, M. Thévenet, J-L. Vay, G. Bonnaud, Ph. Martin, H. Vincenti, F. Quéré
Physical Review X (2019), doi: 10.1103/PhysRevX.9.011050

Sub-cycle control of relativistic plasma mirrors
L. Chopineau, G. Blaclard, A. Denoeud, H. Vincenti, F. Quéré, S. Haessler
To be submitted to Physical Review Letters

Stochastic heating of charged particles in colliding electromagnetic waves: a physical approach
G. Blaclard, H. Vincenti, G. Bonnaud, F. Quéré
To be submitted to Physical Review X

Conferences

Argonne Training Program on Extreme-Scale Computing 2017
Two weeks program on HPC computing

BLAST Workshop 2018
Oral presentation

46th European Physical Society Conference on Plasma Physics (2019)
Oral presentation
Best Research Video and Communication Skills award winner (`https://www.epsplasma2019.eu/wp-content/uploads/2019/07/V2_Blaclard.mp4?_=2`)

C Résumé en Français

Ce travail de thèse met en lumière les principaux mécanismes de couplage entre lasers ultra-intenses et plasmas denses. Cette étude s'appuie largement sur des simulations numériques, qui reproduisent et supportent les expériences effectuées au CEA Saclay.

Tout au long de ce manuscrit, l'interprétation directe des observations expérimentales a été rendue possible grâce à des simulations de type Particle-In-Cell (PIC) réalisées avec le code WARP+PXR. Contrairement à la plupart des autres codes PIC, les équations de Maxwell sont résolues dans l'espace de Fourier (on parle alors de code pseudo-spectral), ce qui réduit grandement les effets de la dispersion numérique des ondes électromagnétiques dans le vide ou du chauffage numérique. En particulier, la dispersion numérique introduit des effets non physiques dans la simulation qui vont, par exemple dans le cadre de l'interaction entre un laser et de la matière dense, dévier sévèrement les harmoniques élevées émises par le miroir plasma. Cette déflexion a été étudiée de façon extensive dans le manuscrit par l'intermédiaire d'un modèle simple se reposant sur les lois de la réfraction de Snell-Descartes. Il permet de prédire précisément l'angle de déviation des harmoniques en fonction de leur ordre, la résolution spatio-temporelle de la simulation ou encore du solveur de Maxwell considéré. Ainsi, il a été démontré que l'utilisation d'un solveur pseudo-spectral, comme celui implémenté dans WARP+PXR, réduit totalement la plupart des effets non physiques, rendant ainsi possible des simulations réalistes non accessibles auparavant. Les résultats de ces simulations vont alors pouvoir être comparés directement aux grandeurs des expériences.

Mécanismes de couplage entre laser et matière dense

Grâce à l'utilisation du solveur pseudo-spectral de WARP+PXR, nous avons pu étudier l'influence du gradient de densité, caractérisé par une longueur L_g et situé à l'avant de la face éclairée par le laser, sur les émissions de lumière et de particules observées expérimentalement lors de l'interaction entre un laser de haute puissance ($a_0 > 1$) et un plasma surcritique. Quand la surface du plasma est raide ($L_g \sim \lambda_0/15$), la cible se comporte comme un miroir plasma capable de produire des trains d'harmoniques d'ordres élevés associés à des faisceaux d'électrons ultra relativistes de haute charge ($\sim$ 1 nC à 10 MeV). Ces signaux électroniques et harmoniques sont synchronisés temporellement et séparés angulairement de quelques dizaines de milliradians. En revanche, pour des gradients plus longs ($L_g \sim \lambda$), l'aspect de ces deux différents signaux varie radicalement. En effet, il a été observé que dans ce cas-là, l'intensité du signal harmonique s'effondre complètement, tandis que le signal électronique s'élargit angulairement. De plus, l'énergie des électrons est plus élevée et varie avec l'angle d'incidence du laser sur le plasma.

Notre étude numérique et théorique indique que ce changement de caractère de l'émission peut être attribué à une transition entre deux différents mécanismes de couplage entre lumière et matière. En particulier, nous proposons des preuves irréfutables d'un passage entre un mécanisme de Brunel périodique à un chauffage stochastique, apériodique et chaotique. Ce travail réalisé dans un régime où l'intensité du laser est élevée vient compléter les résultats bien connus à bas flux, où une autre transition est observée entre l'absorption de Brunel vers un troisième mécanisme, l'absorption résonnante.

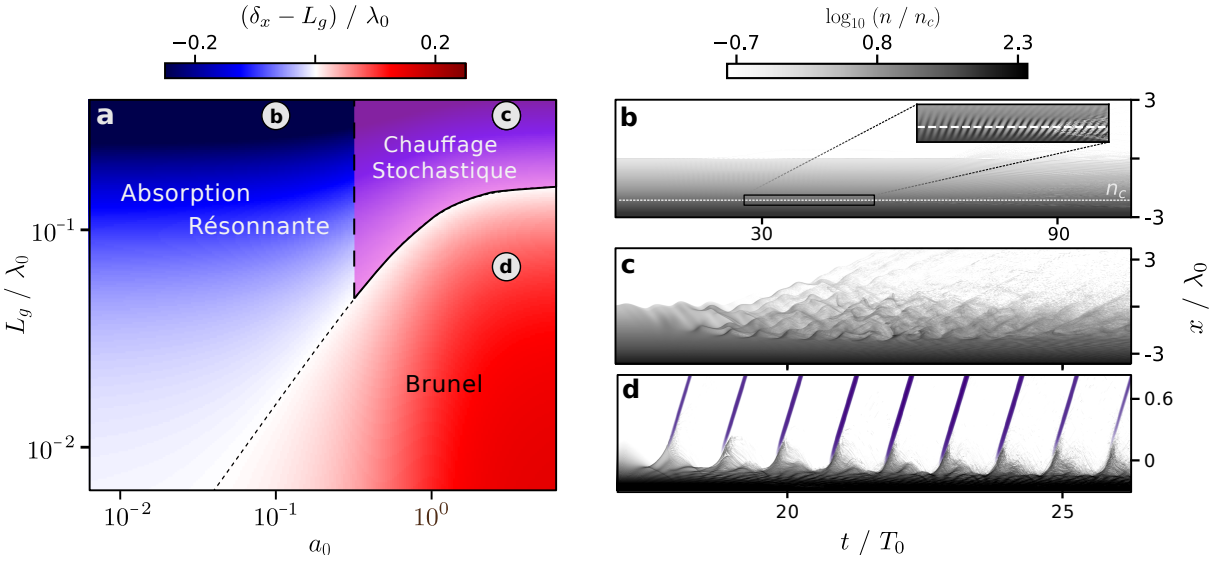

Figure C.1: **Diagramme de transition entre les différents mécanismes de couplage en jeu lors de l'interaction entre un laser et un plasma surcritique** - Sur la figure (a), trois différentes régions sont tracées dans un diagramme (a_0, L_g). Chaque région indique lequel des trois mécanismes de couplage considérés est prépondérant. Dans chacune des zones indiquées par des points gris, on trace à droite l'évolution spatio-temporelle d'une couche de plasma.

Nous résumons notre compréhension globale des différents mécanismes dans la figure Fig. C.1:

- commençant à basse intensité et gradients longs (Fig. C.1–b), le mécanisme dominant est l'**absorption résonnante**, très largement étudiée depuis de nombreuses années. Lors de l'interaction, une partie de l'énergie du laser va pouvoir se propager par effet tunnel du point de réflexion jusqu'à la densité critique n_c du plasma sous la forme d'une onde évanescente. De là, elle va pouvoir exciter une onde plasma résonnante. Après une quantité suffisante d'énergie apportée à cette onde plasma, celle-ci va déferler, propulsant de nombreux électrons hors du plasma.

- Quand l'intensité du laser augmente à L_g fixé (Fig. C.1–c), un nouveau mécanisme apparaît en plus de l'absorption résonnante : le **chauffage stochastique**. Caractériser ce mécanisme moins connu que les deux autres a été précisément le cœur de ma thèse. Celui-ci est mis en jeu lorsque des électrons évoluent dans deux ondes, leur mouvement devient alors chaotique et ils peuvent absorber une large fraction de l'énergie laser. Pour un gradient long, la deuxième onde n'est autre que l'onde réfléchie par le miroir qui va venir interférer avec l'onde incidente dans une zone de plasma située entre le vide et le point de réflexion. La transition depuis l'absorption résonnante est douce, les deux mécanismes vont coexister pendant une large gamme d'intensité allant de l'apparition du

chaos ($a_0 \sim 0.15$) à la disparition de la densité critique n_c par transparence relativiste ($a_0 \sim 2.87$), empêchant ainsi une résonance de s'y développer.

- À haute intensité, quand la longueur de gradient diminue, la zone de plasma sujette aux deux ondes se rétrécit. Ainsi, le chauffage stochastique doit disparaître au profit du bien connu **mécanisme de Brunel** dès que la distance parcourue par les électrons dans l'onde laser dépasse la longueur de gradient (Fig. C.1–d). Dans ce cas, les électrons sont d'abord extraits du plasma vers le vide sous l'action de la composante normale du champ électrique. Si le champ est fort, les électrons sont accélérés fortement jusqu'à des vitesses relativistes et vont introduire un effet Doppler relativiste sur le champ laser réfléchi. Ceci va aboutir à la génération d'un train d'harmonique d'ordre élevé conformément au modèle du Miroir Plasma Relativiste (ou ROM en anglais). Ensuite, quand le signe du champ électrique s'inverse, les électrons sont repoussés vers le centre de la cible à des vitesses balistiques. Quand l'intensité du laser est élevée, certains de ces électrons de Brunel arrivent à s'échapper du champ de rappel du fond ionisant et sont introduits dans le laser réfléchi.

Ce travail permet donc une meilleure compréhension des différents phénomènes en jeu lors de l'interaction entre un laser intense et un plasma dense. En particulier, le chauffage stochastique est très probablement le mécanisme principal de gain d'énergie dans les expériences qui ne nécessitent pas un bon contraste temporel (ou qui ne le maitrisent pas correctement). En effet, le piédestal devant l'impulsion principale peut introduire des gradients de densité caractérisés par des longueurs L_g de l'ordre de λ_0 avant l'arrivée du laser intense, soit précisément le régime en haut à droite de la figure Fig. C.1, qui correspond au chauffage stochastique.

Une nouvelle approche pour décrire le chauffage dans deux ondes

Une importante partie de cette thèse est consacrée à la dérivation d'un modèle du chauffage stochastique qui soit compréhensible même par des non spécialistes du chaos ou du formalisme Hamiltonien. Notre approche se situe à l'interface entre un modèle hautement mathématique et peu intuitif et un modèle plus empirique mais moins prédictif. Nous démontrons ainsi qu'il est possible d'écrire les équations du mouvement de particules dans deux ondes sous la forme de systèmes physiques bien connus tels que le pendule simple ou le pendule dit de Kapitsa. Cette correspondance apportent de solides intuitions physiques sur comment les électrons se comportent dans telle ou telle configuration laser (intensité, polarisation ou encore angle d'incidence).

En particulier, dans deux ondes polarisées linéairement est observé un intense phénomène d'**élongation et de repliement** (**stretching and folding** en anglais) des distributions de particules dans l'espace des phases autour des nœuds de champ électrique dû à l'évolution temporelle de la force pondéromotrice. Cet effet est tenu responsable de l'apparition du chaos et de la perte en prédictibilité à chaque fois que les particules se rapprochent d'un nœud magnétique cette fois. Pour un système chaotique, il est alors totalement vain d'essayer d'approcher parfaitement les trajectoires de ces particules avec une simulation numérique parce qu'à la fois le schéma numérique mais aussi la troncature d'un nombre à virgule flottante introduisent à chaque pas de temps de petites erreurs qui vont grandir exponentiellement. À l'inverse, on va plutôt privilégier un modèle probabilistique, basé sur une marche aléatoire pour approcher la loi de diffusion des particules au cours du temps. Il a été observé que cette loi tend vers une loi normale quand l'intensité du laser est suffisamment élevée.

Enfin, ce modèle a pu être également étendu à des incidences obliques pour se rapprocher au plus près des expériences sur cibles denses à long gradient. Dans ce cas, l'énergie des particules

dépend explicitement de l'angle d'incidence entre les deux ondes et de leur intensité et coïncide avec l'énergie moyenne des électrons éjectés observée dans les expériences. À partir de là, de plus amples séries de mesures expérimentales doivent être menées pour venir valider ces résultats préliminaires et démontrer la faisabilité d'une nouvelle technique de mesure de l'intensité du laser au foyer. Cette technique serait globalement indépendante de la longueur de gradient tant que l'on s'assure que le chauffage stochastique reste bien le mécanisme dominant. De plus, cette technique ne nécessiterait potentiellement que d'un seul tir laser pour donner des résultats quantitatifs sans recourir à des procédés d'analyse de données complexes. Ainsi, les utilisateurs de la plupart des installations laser actuellement disponibles pourraient bénéficier de ce diagnostic.

Bibliography

Albritton, J. and P. Koch (1975). "Cold Plasma Wavebreaking: Production of Energetic Electrons". *The Physics of Fluids*, 18(9), pp. 1136–1139. DOI: 10.1063/1.861300 (cited on page 14).

Allen, L., M. W. Beijersbergen, R. J. C. Spreeuw, and J. P. Woerdman (1992). "Orbital Angular Momentum of Light and the Transformation of Laguerre-Gaussian Laser Modes". *Physical Review A*, 45(11), pp. 8185–8189. DOI: 10.1103/PhysRevA.45.8185 (cited on page 66).

Arber, T. D., K. Bennett, C. S. Brady, A. Lawrence-Douglas, M. G. Ramsay, N. J. Sircombe, P. Gillies, R. G. Evans, H. Schmitz, A. R. Bell, and C. P. Ridgers (2015). "Contemporary Particle-in-Cell Approach to Laser-Plasma Modelling". *Plasma Physics and Controlled Fusion*, 57(11), p. 113001. DOI: 10.1088/0741-3335/57/11/113001 (cited on pages 3, 45).

Baeva, T., S. Gordienko, and A. Pukhov (2006). "Theory of High-Order Harmonic Generation in Relativistic Laser Interaction with Overdense Plasma". *Physical Review E*, 74, p. 046404 (cited on pages 3, 25, 94).

Barr, H. C., P. Mason, and D. M. Parr (2000). "Electron Parametric Instabilities of Relativistically Intense Laser Light in under and Overdense Plasma". *Physics of Plasmas*, 7(6), pp. 2604–2615. DOI: 10.1063/1.874102 (cited on page 116).

Bendixson, I. (1901). "Sur les courbes définies par des équations différentielles". *Acta Mathematica*, 24, pp. 1–88. DOI: 10.1007/BF02403068 (cited on page 38).

Bergmann, A. and P. Mulser (1993). "Breaking of Resonantly Excited Electron Plasma Waves". *Physical Review E*, 47(5), pp. 3585–3589. DOI: 10.1103/PhysRevE.47.3585 (cited on page 14).

Birdsall, C. K. and A. B. Langdon (1985). *Plasma Physics Via Computer*. New York, NY, USA: McGraw-Hill, Inc. (cited on pages 3, 45).

Blaclard, G., H. Vincenti, R. Lehe, and J. L. Vay (2017). "Pseudospectral Maxwell Solvers for an Accurate Modeling of Doppler Harmonic Generation on Plasma Mirrors with Particle-in-Cell Codes". *Physical Review E*, 96(3). DOI: 10.1103/PhysRevE.96.033305 (cited on pages 59, 61, 63, 80).

Blinne, A., D. Schinkel, S. Kuschel, N. Elkina, S. G. Rykovanov, and M. Zepf (2018). "A Systematic Approach to Numerical Dispersion in Maxwell Solvers". *Computer Physics Communications*, 224, pp. 273–281. DOI: 10.1016/j.cpc.2017.10.010 (cited on page 57).

Bocoum, M., F. Böhle, A. Vernier, A. Jullien, J. Faure, and R. Lopez-Martens (2015). "Spatial-Domain Interferometer for Measuring Plasma Mirror Expansion". *Opt. Lett.* 40(13), pp. 3009–3012. DOI: 10.1364/OL.40.003009 (cited on page 75).

Boltzmann, L. (1872). *Weitere Studien Über Das Wärmegleichgewicht Unter Gasmolekülen*. Wiesbaden. DOI: 10.1007/978-3-322-84986-1_3 (cited on page 145).

Boris, J. P. (1972). "Proceedings : Fourth Conference on Numerical Simulation of Plasmas, November 2, 3, 1970", pp. 3–67 (cited on page 47).

Borot, A. (2012). "Génération d'impulsions attosecondes sur miroir plasma à très haute cadence". PhD thesis. Ecole Polytechnique X (cited on page 3).

Bouchard, G. (2020). "Étude Théorique et Numérique de La Génération d'harmoniques XUV à l'aide de Laser Ultra-Intenses Sur Feuilles Minces." (cited on page 3).

Bourdier, A. (1983). "Oblique Incidence of a Strong Electromagnetic Wave on a Cold Inhomogeneous Electron Plasma. Relativistic Effects". *The Physics of Fluids*, 26(7), pp. 1804–1807. DOI: 10.1063/1.864355 (cited on page 51).

Bourdier, A., D. Patin, and E. Lefebvre (2005). "Stochastic Heating in Ultra High Intensity Laser-Plasma Interaction". *Physica D: Nonlinear Phenomena*, 206(1), pp. 1–31. DOI: 10.1016/j.physd.2005.04.017 (cited on pages 100, 119).

Boyd, T. J. M. and R. Ondarza-Rovira (2008). "Anomalies in Universal Intensity Scaling in Ultrarelativistic Laser-Plasma Interactions". *Physical Review Letters*, 101(12), p. 125004. DOI: 10.1103/PhysRevLett.101.125004 (cited on page 94).

Brunel, F. (1987). "Not-so-Resonant, Resonant Absorption". *Physical Review Letters*, 59(1), pp. 52–55. DOI: 10.1103/PhysRevLett.59.52 (cited on page 15).

Bulanov, S. V. (2005). "Ion Acceleration in a Dipole Vortex in a Laser Plasma Corona". *Plasma Physics Reports*, 31(5), p. 369. DOI: 10.1134/1.1925787 (cited on pages 110, 111).

Bulanov, S. V., N. M. Naumova, and F. Pegoraro (1994). "Interaction of an Ultrashort, Relativistically Strong Laser Pulse with an Overdense Plasma". *Physics of Plasmas*, 1(3), pp. 745–757. DOI: 10.1063/1.870766 (cited on page 22).

Burov, A. A. and V. I. Nikonov (2019). "On the Nonlinear Meissner Equation". *International Journal of Non-Linear Mechanics*, 110, pp. 26–32 (cited on page 133).

Childs, H., E. Brugger, B. Whitlock, J. Meredith, S. Ahern, D. Pugmire, K. Biagas, M. Miller, C. Harrison, G. H. Weber, H. Krishnan, T. Fogal, A. Sanderson, C. Garth, E. W. Bethel, D. Camp, O. Rübel, M. Durant, J. M. Favre, and P. Navrátil (2012). "VisIt: An End-User Tool For Visualizing and Analyzing Very Large Data". In: *High Performance Visualization–Enabling Extreme-Scale Scientific Insight*, pp. 357–372 (cited on page 66).

Chopineau, L., A. Leblanc, G. Blaclard, A. Denoeud, M. Thévenet, J.-L. Vay, G. Bonnaud, P. Martin, H. Vincenti, and F. Quéré (2019). "Identification of Coupling Mechanisms between Ultraintense Laser Light and Dense Plasmas". *Physical Review X*, 9(1). DOI: 10.1103/PhysRevX.9.011050 (cited on pages 50, 73, 76, 85, 156, 157).

Chopineau, L. (2019). "Physique Attoseconde Relativiste Sur Miroirs Plasmas". thesis. Paris Saclay (cited on page 3).

Cline, D., L. Shao, X. Ding, Y. Ho, Q. Kong, and P. Wang (2013). "First Observation of Acceleration of Electrons by a Laser in a Vacuum". *Journal of Modern Physics*, 4(1), pp. 1–6. DOI: 10.4236/jmp.2013.41001 (cited on page 25).

Cole, J. B. (1997). "A High-Accuracy Realization of the Yee Algorithm Using Non-Standard Finite Differences". *IEEE Transactions on Microwave Theory and Techniques*, 45(6), pp. 991–996. DOI: 10.1109/22.588615 (cited on page 57).

— (2002). "High-Accuracy Yee Algorithm Based on Nonstandard Finite Differences: New Developments and Verifications". *IEEE Transactions on Antennas and Propagation*, 50(9), pp. 1185–1191. DOI: 10.1109/TAP.2002.801268 (cited on page 57).

Corde, S., K. Ta Phuoc, G. Lambert, R. Fitour, V. Malka, A. Rousse, A. Beck, and E. Lefebvre (2013). "Femtosecond x Rays from Laser-Plasma Accelerators". *Reviews of Modern Physics*, 85(1), pp. 1–48. DOI: 10.1103/RevModPhys.85.1 (cited on page 2).

Courant, R., K. Friedrichs, and H. Lewy (1928). "Über die partiellen Differenzengleichungen der mathematischen Physik". *Mathematische Annalen*, 100(1), pp. 32–74. DOI: 10.1007/BF01448839 (cited on page 56).

Cowan, B. M., D. L. Bruhwiler, E. Cormier-Michel, E. Esarey, C. G. R. Geddes, P. Messmer, and K. M. Paul (2011). "Characteristics of an Envelope Model for Laser–Plasma Accelerator Simulation". *Journal of Computational Physics*, 230(1), pp. 61–86. DOI: 10.1016/j.jcp.2010.09.009 (cited on page 57).

Dawson, J. M. (1983). "Particle Simulation of Plasmas". *Reviews of Modern Physics*, 55(2), pp. 403–447. DOI: 10.1103/RevModPhys.55.403 (cited on pages 3, 45).

Debayle, A., J. Sanz, and L. Gremillet (2015). "Self-Consistent Theory of High-Order Harmonic Generation by Relativistic Plasma Mirror". *Physical Review E*, 92(5), p. 053108 (cited on page 25).

Decker, C. D., W. B. Mori, K. Tzeng, and T. Katsouleas (1996). "The Evolution of Ultra-intense, Short-pulse Lasers in Underdense Plasmas". *Physics of Plasmas*, 3(5), pp. 2047–2056. DOI: 10.1063/1.872001 (cited on page 116).

Denisov, N. (1957). "On a Singularity of the Field of an Electromagnetic Wave Propagated in an Inhomogeneous Plasma". *SOVIET PHYSICS JETP-USSR*, 4(4), pp. 544–553 (cited on page 15).

Drake, J. F. and Y. C. Lee (1976). "Relativistic Effects in Resonance Absorption". *The Physics of Fluids*, 19(11), pp. 1772–1778. DOI: 10.1063/1.861373 (cited on page 15).

Dromey, B., M. Zepf, A. Gopal, K. Lancaster, M. S. Wei, K. Krushelnick, M. Tatarakis, N. Vakakis, S. Moustaizis, R. Kodama, M. Tampo, C. Stoeckl, R. Clarke, H. Habara, D. Neely, S. Karsch, and P. Norreys (2006). "High Harmonic Generation in the Relativistic Limit". *Nature Physics*, 2, pp. 456–459. DOI: 10.1038/nphys338 (cited on pages 3, 21).

Einstein, A. (1905). "Zur Elektrodynamik Bewegter Körper". *Annalen der Physik*, 322(10), pp. 891–921. DOI: 10.1002/andp.19053221004 (cited on page 22).

Eliseev, V., D. Pesme, W. Rozmus, V. T. Tikhonchuk, and C. E. Capjack (1998). "Filamentation of a Laser Beam Interacting with an Underdense Plasma and Its Coupling to Stimulated Brillouin Scattering". *Physica Scripta*, 1998(T75), p. 112. DOI: 10.1238/Physica.Topical.075a00112 (cited on page 116).

Esarey, E., R. F. Hubbard, W. P. Leemans, A. Ting, and P. Sprangle (1997). "Electron Injection into Plasma Wakefields by Colliding Laser Pulses". *Physical Review Letters*, 79(14), pp. 2682–2685. DOI: 10.1103/PhysRevLett.79.2682 (cited on page 19).

Esarey, E., C. B. Schroeder, and W. P. Leemans (2009). "Physics of Laser-Driven Plasma-Based Electron Accelerators". *Reviews of Modern Physics*, 81(3), pp. 1229–1285. DOI: 10.1103/RevModPhys.81.1229 (cited on pages 2, 19).

Esirkepov, T. Z. (2001). "Exact Charge Conservation Scheme for Particle-in-Cell Simulation with an Arbitrary Form-Factor". *Computer Physics Communications*, 135(2), pp. 144–153. DOI: 10.1016/S0010-4655(00)00228-9 (cited on page 46).

Estabrook, K., E. J. Valeo, and W. L. Kruer (1975). "Two-dimensional Relativistic Simulations of Resonance Absorption". *The Physics of Fluids*, 18(9), pp. 1151–1159. DOI: 10.1063/1.861276 (cited on page 14).

Estabrook, K. and W. L. Kruer (1978). "Properties of Resonantly Heated Electron Distributions". *Physical Review Letters*, 40(1), pp. 42–45. DOI: 10.1103/PhysRevLett.40.42 (cited on page 14).

Evans, M. W. and F. H. Harlow (1957). *The Particle-In-Cell Method for Hydrodynamic Calculations*. LA-2139. Los Alamos Scientific Lab., N. Mex. (cited on pages 2, 45).

Fabbro, R. and P. Mora (1982). "Hot Electrons Behavior in Laser-Plane Target Experiments". *Physics Letters A*, 90(1-2), pp. 48–50 (cited on page 110).

Faure, J., Y. Glinec, A. Pukhov, S. Kiselev, S. Gordienko, E. Lefebvre, J.-P. Rousseau, F. Burgy, and V. Malka (2004). "A Laser–Plasma Accelerator Producing Monoenergetic Electron Beams". *Nature*, 431(7008), pp. 541–544. DOI: 10.1038/nature02963 (cited on page 2).

Faure, J., C. Rechatin, A. Norlin, A. Lifschitz, Y. Glinec, and V. Malka (2006). "Controlled Injection and Acceleration of Electrons in Plasma Wakefields by Colliding Laser Pulses". *Nature*, 444(7120), pp. 737–739. DOI: 10.1038/nature05393 (cited on pages 19, 101).

Fick, A. (1855). "Ueber Diffusion". *Annalen der Physik*, 170(1), pp. 59–86. DOI: 10.1002/andp.18551700105 (cited on page 145).

Fornberg, B. (1990). "High-Order Finite Differences and the Pseudospectral Method on Staggered Grids". *SIAM Journal on Numerical Analysis*, 27(4), pp. 904–918. DOI: 10.1137/0727052 (cited on page 58).

Forslund, D. W., J. M. Kindel, K. Lee, E. L. Lindman, and R. L. Morse (1975). "Theory and Simulation of Resonant Absorption in a Hot Plasma". *Physical Review A*, 11(2), pp. 679–683. DOI: 10.1103/PhysRevA.11.679 (cited on page 14).

Freidberg, J. P., R. W. Mitchell, R. L. Morse, and L. I. Rudsinski (1972). "Resonant Absorption of Laser Light by Plasma Targets". *Phys. Rev. Lett.* 28(13), pp. 795–799. DOI: 10.1103/PhysRevLett.28.795 (cited on page 14).

Fubiani, G., E. Esarey, C. B. Schroeder, and W. P. Leemans (2004). "Beat Wave Injection of Electrons into Plasma Waves Using Two Interfering Laser Pulses". *Physical Review E*, 70(1), p. 016402. DOI: 10.1103/PhysRevE.70.016402 (cited on page 19).

Geddes, C. G. R., C. Toth, J. van Tilborg, E. Esarey, C. B. Schroeder, D. Bruhwiler, C. Nieter, J. Cary, and W. P. Leemans (2004). "High-Quality Electron Beams from a Laser Wakefield Accelerator Using Plasma-Channel Guiding". *Nature*, 431(7008), pp. 538–541. DOI: 10.1038/nature02900 (cited on page 2).

Geindre, J. P., R. S. Marjoribanks, and P. Audebert (2010). "Electron Vacuum Acceleration in a Regime beyond Brunel Absorption". *Physical Review Letters*, 104(13), p. 135001. DOI: 10.1103/PhysRevLett.104.135001 (cited on page 26).

Gibbon, P. (2005). *Short Pulse Laser Interactions with Matter*. published by Imperial College Press and distributed by World Scientific Publishing co. DOI: 10.1142/p116 (cited on pages 10, 11, 14, 15).

Ginsburg, V. L. (1964). *The Propagation of Electromagnetic Waves in Plasmas*. OCLC: 223896953. Oxford: Pergamon Press (cited on page 14).

Gonoskov, A. A., A. V. Korzhimanov, A. V. Kim, M. Marklund, and A. M. Sergeev (2011). "Ultrarelativistic Nanoplasmonics as a Route towards Extreme-Intensity Attosecond Pulses". *Physical Review E*, 84(4). DOI: 10.1103/PhysRevE.84.046403 (cited on page 25).

Gonsalves, A. J., K. Nakamura, J. Daniels, C. Benedetti, C. Pieronek, T. C. H. de Raadt, S. Steinke, J. H. Bin, S. S. Bulanov, J. van Tilborg, C. G. R. Geddes, C. B. Schroeder, C. Tóth, E. Esarey, K. Swanson, L. Fan-Chiang, G. Bagdasarov, N. Bobrova, V. Gasilov, G. Korn, P. Sasorov, and W. P. Leemans (2019). "Petawatt Laser Guiding and Electron Beam Acceleration to 8 GeV in a Laser-Heated Capillary Discharge Waveguide". *Physical Review Letters*, 122(8), p. 084801. DOI: 10.1103/PhysRevLett.122.084801 (cited on page 2).

Grassberger, . and I. Procacia (1983). "Measuring the Strangeness of Strange Attractors". *Measuring the strangeness of strange attractors*, 9(1-2), pp. 189–208 (cited on page 32).

Grassi, A., L. Fedeli, A. Sgattoni, and A. Macchi (2016). "Vlasov Simulation of Laser-Driven Shock Acceleration and Ion Turbulence". *Plasma Physics and Controlled Fusion*, 58(3), p. 034021. DOI: 10.1088/0741-3335/58/3/034021 (cited on page 44).

Guénot, D., D. Gustas, A. Vernier, B. Beaurepaire, F. Böhle, M. Bocoum, M. Lozano, A. Jullien, R. Lopez-Martens, A. Lifschitz, and J. Faure (2017). "Relativistic Electron Beams Driven by kHz Single-Cycle Light Pulses". *Nature Photonics*, 11(5), pp. 293–296. DOI: 10.1038/nphoton.2017.46 (cited on page 2).

Guérin, S., P. Mora, J. C. Adam, A. Héron, and G. Laval (1996). "Propagation of Ultraintense Laser Pulses through Overdense Plasma Layers". *Physics of Plasmas*, 3(7), pp. 2693–2701. DOI: 10.1063/1.871526 (cited on page 12).

Haber, I., R. Lee, H. Klein, and J. Boris (1973). *Advances in electromagnetic simulation techniques in: Proc. Sixth Conf. on Num. Sim. Plasmas, Berkeley*, 8(1), pp. 46–48. (Cited on page 59).

Habib, S., V. Morozov, H. Finkel, A. Pope, K. Heitmann, K. Kumaran, T. Peterka, J. Insley, D. Daniel, P. Fasel, N. Frontiere, and Z. Lukic (2012). "The Universe at Extreme Scale: Multi-Petaflop Sky Simulation on the BG/Q". In: *SC '12: Proceedings of the International Conference on High Performance Computing, Networking, Storage and Analysis*. SC '12: Proceedings of the International Conference on High Performance Computing, Networking, Storage and Analysis, pp. 1–11. DOI: 10.1109/SC.2012.106 (cited on page 58).

Hartemann, F. V., S. N. Fochs, G. P. Le Sage, N. C. Luhmann, J. G. Woodworth, M. D. Perry, Y. J. Chen, and A. K. Kerman (1995). "Nonlinear Ponderomotive Scattering of Relativistic Electrons by an Intense Laser Field at Focus". *Physical Review E*, 51(5), pp. 4833–4843. DOI: 10.1103/PhysRevE.51.4833 (cited on page 121).

Hausdorff, F. (1919). "Dimension Und Äußeres Maß". *Mathematische Annalen*, 79, pp. 157–179 (cited on page 32).

Higuera, A. V. and J. R. Cary (2017). "Structure-Preserving Second-Order Integration of Relativistic Charged Particle Trajectories in Electromagnetic Fields". *Physics of Plasmas*, 24(5), p. 052104. DOI: 10.1063/1.4979989 (cited on page 48).

Hockney, R. W. and J. W. Eastwood (1988). *Computer Simulation Using Particles* (cited on page 45).

Jalas, S., I. Dornmair, R. Lehe, H. Vincenti, J.-L. Vay, M. Kirchen, and A. R. Maier (2017). "Accurate Modeling of Plasma Acceleration with Arbitrary Order Pseudo-Spectral Particle-in-Cell Methods". *Physics of Plasmas*, 24(3), p. 033115. DOI: 10.1063/1.4978569 (cited on page 59).

Jüttner, F. (1911). "Das Maxwellsche Gesetz Der Geschwindigkeitsverteilung in Der Relativtheorie". *Annalen der Physik*, 339(5), pp. 856–882. DOI: 10.1002/andp.19113390503 (cited on page 146).

Kahaly, S., S. Monchocé, H. Vincenti, T. Dzelzainis, B. Dromey, M. Zepf, P. Martin, and F. Quéré (2013). "Direct Observation of Density-Gradient Effects in Harmonic Generation from Plasma Mirrors". *Physical Review Letters*, 110(17), p. 175001. DOI: 10.1103/PhysRevLett.110.175001 (cited on pages 75, 76).

Kallala, H., J.-L. Vay, and H. Vincenti (2018). "A Generalized Massively Parallel Ultra-High Order FFT-Based Maxwell Solver" (cited on page 58).

Kapitza, P. (1951a). "Dynamic Stability of a Pendulum When Its Point of Suspension Vibrates". *Soviet Phys. JETP*, 21, pp. 588–597 (cited on page 126).

— (1951b). "Pendulum with a Vibrating Suspension". *Usp. Fiz. Nauk*, 44, pp. 7–15 (cited on page 126).

Karkkainen, M., E. Gjonaj, T. Lau, and T. Weiland (2006). "Low-Dispersionwake Field Calculation Tools". *Proceedings of the International Computational Accelerator Physics Conference, Chamonix, France*, pp. 35–40 (cited on page 57).

Kautz, R. (2010). *Chaos: The Science of Predictable Random Motion*. OUP Oxford. 385 pp. (cited on pages 29, 34, 38).

Kemp, A. J., Y. Sentoku, and M. Tabak (2009). "Hot-Electron Energy Coupling in Ultraintense Laser-Matter Interaction". *Phys. Rev. E*, 79(6), p. 066406. DOI: 10.1103/PhysRevE.79.066406 (cited on page 100).

Kirchen, M., R. Lehe, B. B. Godfrey, I. Dornmair, S. Jalas, K. Peters, J.-L. Vay, and A. R. Maier (2016). "Stable Discrete Representation of Relativistically Drifting Plasmas". *Physics of Plasmas*, 23(10), p. 100704. DOI: 10.1063/1.4964770 (cited on pages 49, 59).

Kruer, W. L. (1988). *The Physics of Laser Plasma Interactions*. Westview Press (cited on pages 11, 14).

Kruer, W. L. and K. Estabrook (1985). "J×B Heating by Very Intense Laser Light". *The Physics of Fluids*, 28(1), pp. 430–432. DOI: 10.1063/1.865171 (cited on pages 18, 83).

Krygier, A. G., D. W. Schumacher, and R. R. Freeman (2014). "On the Origin of Super-Hot Electrons from Intense Laser Interactions with Solid Targets Having Moderate Scale Length Preformed Plasmas". *Physics of Plasmas*, 21(2), p. 023112. DOI: 10.1063/1.4866587 (cited on page 100).

Kumar, A., C. Shukla, A. Das, and P. Kaw (2018). "Energy Principle for Excitations in Plasmas with Counterstreaming Electron Flows". *AIP Advances*, 8(5), p. 055213 (cited on page 110).

Lamb, W. E. (1964). "Theory of an Optical Maser". *Physical Review*, 134 (6A), A1429–A1450. DOI: 10.1103/PhysRev.134.A1429 (cited on page 1).

Leblanc, A. (2016). "Miroirs et Réseaux Plasmas En Champs Lasers Ultra-Intenses : Génération d'harmoniques d'ordre Élevé et de Faisceaux d'électrons Relativistes" (cited on page 3).

Lee, P. and J.-L. Vay (2019). "Convergence in Nonlinear Laser Wakefield Accelerators Modeling in a Lorentz-Boosted Frame". *Computer Physics Communications*, 238, pp. 102–110. DOI: 10.1016/j.cpc.2018.12.013 (cited on page 59).

Lefebvre, E. and G. Bonnaud (1995). "Transparency/Opacity of a Solid Target Illuminated by an Ultrahigh-Intensity Laser Pulse". *Physical Review Letters*, 74(11), pp. 2002–2005. DOI: 10.1103/PhysRevLett.74.2002 (cited on page 12).

Lehe, R., M. Kirchen, B. B. Godfrey, A. R. Maier, and J.-L. Vay (2016). "Elimination of Numerical Cherenkov Instability in Flowing-Plasma Particle-in-Cell Simulations by Using Galilean Coordinates". *Physical Review E*, 94(5), p. 053305. DOI: 10.1103/PhysRevE.94.053305 (cited on pages 49, 59).

Lévy, A., T. Ceccotti, P. D. Oliveira, F. Réau, M. Perdrix, F. Quéré, P. Monot, M. Bougeard, H. Lagadec, P. Martin, P. Audebert, and J. Geindre (2007). "Double Plasma Mirror for Ultrahigh Temporal Contrast Ultraintense". *Optics Letter*, 32(3), p. 310 (cited on pages 3, 74).

Li, Y., X. Yuan, M. Xu, Z. Zheng, Z. Sheng, M. Chen, Y. Ma, W. Liang, Q. Yu, Y. Zhang, et al. (2006). "Observation of a Fast Electron Beam Emitted along the Surface of a Target Irradiated by Intense Femtosecond Laser Pulses". *Physical review letters*, 96(16), p. 165003 (cited on page 110).

Lichters, R., J. Meyer-ter-Vehn, and A. Pukhov (1996). "Short-pulse Laser Harmonics from Oscillating Plasma Surfaces Driven at Relativistic Intensity". *Physics of Plasmas*, 3(9), pp. 3425–3437. DOI: 10.1063/1.871619 (cited on pages 3, 21–23).

Liu, Q. H. (1997). "The PSTD Algorithm: A Time-Domain Method Requiring Only Two Cells per Wavelength". *Microwave and Optical Technology Letters*, 15(3), pp. 158–165. DOI: 10.1002/(SICI)1098-2760(19970620)15:3<158::AID-MOP11>3.0.CO;2-3 (cited on page 59).

Lorenz, E. (1972). "Predictability: Does the Flap of a Butterfly's Wing in Brazil Set off a Tornado in Texas?" *Proceedings of the 139th meeting of the American Association for the Advancement of Science* (cited on page 30).

Lorenz, E. N. (1963). "Deterministic Nonperiodic Flow". *Journal of the Atmospheric Sciences*, 20(2), pp. 130–141. DOI: 10.1175/1520-0469(1963)020<0130:DNF>2.0.CO;2 (cited on pages 29–31).

Ma, G., W. Dallari, A. Borot, F. Krausz, W. Yu, G. D. Tsakiris, and L. Veisz (2015). "Intense Isolated Attosecond Pulse Generation from Relativistic Laser Plasmas Using Few-Cycle Laser Pulses". *Physics of Plasmas*, 22(3), p. 033105. DOI: 10.1063/1.4914087 (cited on page 21).

Maiman, T. H. (1960). "Stimulated Optical Radiation in Ruby". *Nature*, 187(4736), pp. 493–494. DOI: 10.1038/187493a0 (cited on page 1).

Malka, G., E. Lefebvre, and J. Miquel (1997). "Experimental Observation of Electrons Accelerated in Vacuum to Relativistic Energies by a High-Intensity Laser". *Physical review letters*, 78(17), p. 3314 (cited on pages 25, 84).

Mangles, S. P. D., C. D. Murphy, Z. Najmudin, A. G. R. Thomas, J. L. Collier, A. E. Dangor, E. J. Divall, P. S. Foster, J. G. Gallacher, C. J. Hooker, D. A. Jaroszynski, A. J. Langley, W. B. Mori, P. A. Norreys, F. S. Tsung, R. Viskup, B. R. Walton, and K. Krushelnick (2004). "Monoenergetic Beams of Relativistic Electrons from Intense Laser–Plasma Interactions". *Nature*, 431(7008), pp. 535–538. DOI: 10.1038/nature02939 (cited on page 2).

Markeev, A. P. (2011). "On Nonlinear Meissner's Equation". *Nonlinear Dynamics*, 7(3), pp. 531–547 (cited on page 133).

Markeev, A. (2015). "Stability of an Equilibrium Position of a Pendulum with Step Parameters". *International Journal of Non-Linear Mechanics*, 73, pp. 12–17 (cited on page 133).

Maxwell, J. C. (1860). "Illustrations of the Dynamical Theory of Gases". *The London, Edinburgh, and Dublin Philosophical Magazine and Journal of Science*, 19(124), pp. 19–32. DOI: 10.1080/14786446008642818 (cited on page 145).

Meissner, E. (1918). "Über Schüttel Erscheinungen in Systemen Mit Periodisch Veränderlicher Elastizität". *Schweizerische Bauzeitung*, 72(11), pp. 95–98 (cited on page 133).

Melzani, M., C. Winisdoerffer, R. Walder, D. Folini, J. M. Favre, S. Krastanov, and P. Messmer (2013). "Apar-T: Code, Validation, and Physical Interpretation of Particle-in-Cell Results". *Astronomy & Astrophysics*, 558, A133. DOI: 10.1051/0004-6361/201321557 (cited on page 44).

Mendonça, J. T. and F. Doveil (1982). "Stochasticity in Plasmas with Electromagnetic Waves". *Journal of Plasma Physics*, 28(03), p. 485. DOI: 10.1017/S002237780000043X (cited on pages 18, 19, 100, 101).

Mendonca, J. (1983). "Threshold for Electron Heating by Two Electromagnetic Waves". *Physical Review A*, 28(6), p. 3592 (cited on pages 18, 100, 102, 119).

Monchocé, S. (2014). "Contrôle et Métrologie de La Génération d'harmoniques Sur Miroir Plasma". thesis. Paris 11 (cited on page 3).

Morse, R. L. and C. W. Nielson (1969). "One-, Two-, and Three-Dimensional Numerical Simulation of Two-Beam Plasmas". *Physical Review Letters*, 23(19), pp. 1087–1090. DOI: 10.1103/PhysRevLett.23.1087 (cited on pages 2, 45).

Nakatsutsumi, M., Y. Sentoku, A. Korzhimanov, S. Chen, S. Buffechoux, A. Kon, B. Atherton, P. Audebert, M. Geissel, L. Hurd, et al. (2018). "Self-Generated Surface Magnetic Fields Inhibit Laser-Driven Sheath Acceleration of High-Energy Protons". *Nature communications*, 9(1), p. 280 (cited on page 110).

Nantel, M., J. Itatani, A. C. Tien, J. Faure, D. Kaplan, M. Bauvier, T. Buma, P. V. Rompay, J. Nee, P. P. Pronko, D. Umstadter, and G. A. Mourou (1998). "Temporal Contrast in Ti:Sapphire Lasers, Characterization and Control". *IEEE Journal of Selected Topics in Quantum Electronics*, 4(2), pp. 449–458. DOI: 10.1109/2944.686755 (cited on page 3).

Papoulis, A. (1921). *Probability Random Variables and Stochastic Processes* (cited on page 144).

Paradkar, B. S., S. I. Krasheninnikov, and F. N. Beg (2012). "Mechanism of Heating of Pre-Formed Plasma Electrons in Relativistic Laser-Matter Interaction". *Physics of Plasmas*, 19(6), p. 060703. DOI: 10.1063/1.4731731 (cited on page 100).

Patin, D., E. Lefebvre, A. Bourdier, and E. D'humieres (2006). "Stochastic Heating in Ultra High Intensity Laser-Plasma Interaction: Theory and PIC Code Simulations". *Laser and Particle Beams*, 24(2), pp. 223–230 (cited on page 100).

Pérez, F., A. J. Kemp, L. Divol, C. D. Chen, and P. K. Patel (2013). "Deflection of MeV Electrons by Self-Generated Magnetic Fields in Intense Laser-Solid Interactions". *Phys. Rev. Lett.* 111(24), p. 245001. DOI: 10.1103/PhysRevLett.111.245001 (cited on page 110).

Poincaré, H. (.-1. A. du texte (1892–1899). *Les Méthodes Nouvelles de La Mécanique Céleste. Invariants Intégraux ; Solutions Périodiques Du Deuxième Genre ; Solutions Doublement Asymptotiques / Par H. Poincaré,...* (Cited on page 29).

— (1908). *Science et Méthode (Edition Définitive) / Henri Poincaré* (cited on page 29).

Quéré, F., C. Thaury, P. Monot, S. Dobosz, P. Martin, J.-P. Geindre, and P. Audebert (2006). "Coherent Wake Emission of High-Order Harmonics from Overdense Plasmas". *Physical Review Letters*, 96(12), p. 125004. DOI: 10.1103/PhysRevLett.96.125004 (cited on pages 3, 17).

Quesnel, B., P. Mora, J. C. Adam, S. Guérin, A. Héron, and G. Laval (1997). "Electron Parametric Instabilities of Ultraintense Short Laser Pulses Propagating in Plasmas". *Physical Review Letters*, 78(11), pp. 2132–2135. DOI: 10.1103/PhysRevLett.78.2132 (cited on page 116).

Quesnel, B. and P. Mora (1998). "Theory and Simulation of the Interaction of Ultraintense Laser Pulses with Electrons in Vacuum". *Phys. Rev. E*, 58(3), pp. 3719–3732. DOI: 10.1103/PhysRevE.58.3719 (cited on pages 26, 68, 70, 84).

Rassou, S., A. Bourdier, and M. Drouin (2014). "Role of Stochastic Heating in Wakefield Acceleration When Optical Injection Is Used". *Physics of Plasmas*, 21(8), p. 083101. DOI: 10.1063/1.4890977 (cited on pages 19, 101).

Rax, J. M. (1992). "Compton Harmonic Resonances, Stochastic Instabilities, Quasilinear Diffusion, and Collisionless Damping with Ultra-high-intensity Laser Waves". *Physics of Fluids B: Plasma Physics*, 4(12), pp. 3962–3972. DOI: 10.1063/1.860299 (cited on pages 18, 100, 119).

Rechatin, C. (2009). "Accélération d'électrons Dans l'interaction Laser-Plasma : Développement et Caractérisation d'un Injecteur Optique". thesis. Palaiseau, Ecole polytechnique (cited on pages 19, 119).

Remington, B. A., R. P. Drake, H. Takabe, and D. Arnett (2000). "A Review of Astrophysics Experiments on Intense Lasers". *Physics of Plasmas*, 7(5), pp. 1641–1652. DOI: 10.1063/1.874046 (cited on page 1).

Richards, F. H. (1905). "Process of Making Candy". U.S. pat. 790920A. Francis H Richards (cited on page 130).

Ruhl, H., Y. Sentoku, K. Mima, K. Tanaka, and R. Kodama (1999). "Collimated Electron Jets by Intense Laser-Beam–Plasma Surface Interaction under Oblique Incidence". *Physical review letters*, 82(4), p. 743 (cited on page 110).

Sakharov, A. S. and V. I. Kirsanov (1994). "Theory of Raman Scattering for a Short Ultrastrong Laser Pulse in a Rarefied Plasma". *Physical Review E*, 49(4), pp. 3274–3282. DOI: 10.1103/PhysRevE.49.3274 (cited on page 116).

Schawlow, A. L. and C. H. Townes (1958). "Infrared and Optical Masers". *Physical Review*, 112(6), pp. 1940–1949. DOI: 10.1103/PhysRev.112.1940 (cited on page 1).

Sentoku, Y., V. Bychenkov, K. Flippo, A. Maksimchuk, K. Mima, G. Mourou, Z. Sheng, and D. Umstadter (2002). "High-Energy Ion Generation in Interaction. of Short Laser Pulse with High-Density Plasma". *Applied Physics B*, 74(3), pp. 207–215. DOI: 10.1007/s003400200796 (cited on pages 19, 101).

Serebryakov, D. A., E. N. Nerush, and I. Y. Kostyukov (2017). "Near-Surface Electron Acceleration during Intense Laser–Solid Interaction in the Grazing Incidence Regime". *Physics of Plasmas*, 24(12), p. 123115. DOI: 10.1063/1.5002671 (cited on page 148).

Sheng, Z.-M., K. Mima, Y. Sentoku, M. S. Jovanović, T. Taguchi, J. Zhang, and J. Meyer-ter-Vehn (2002). "Stochastic Heating and Acceleration of Electrons in Colliding Laser Fields in Plasma". *Physical Review Letters*, 88(5). DOI: 10.1103/PhysRevLett.88.055004 (cited on pages 19, 100, 102).

Sheng, Z.-M., K. Mima, J. Zhang, and J. Meyer-ter-Vehn (2004). "Efficient Acceleration of Electrons with Counterpropagating Intense Laser Pulses in Vacuum and Underdense Plasma". *Physical Review E*, 69(1), p. 016407. DOI: 10.1103/PhysRevE.69.016407 (cited on page 19).

Strickland, D. and G. Mourou (1985). "Compression of Amplified Chirped Optical Pulses". *Optics Communications*, 56(3), pp. 219–221 (cited on pages 1, 74).

Strogatz, S. H. (2018). *Nonlinear Dynamics and Chaos: With Applications to Physics, Biology, Chemistry, and Engineering*. CRC Press (cited on pages 29, 105).

Sudan, R. N. (1993). "Mechanism for the Generation of 10 9 G Magnetic Fields in the Interaction of Ultraintense Short Laser Pulse with an Overdense Plasma Target". *Physical Review Letters*, 70(20), pp. 3075–3078. DOI: 10.1103/PhysRevLett.70.3075 (cited on page 110).

Tajima, T. and J. M. Dawson (1979). "Laser Electron Accelerator". *Physical Review Letters*, 43(4), pp. 267–270. DOI: 10.1103/PhysRevLett.43.267 (cited on page 2).

Tatarakis, M., A. Gopal, I. Watts, F. N. Beg, A. E. Dangor, K. Krushelnick, U. Wagner, P. A. Norreys, E. L. Clark, M. Zepf, and R. G. Evans (2002). "Measurements of Ultrastrong Magnetic Fields during Relativistic Laser–Plasma Interactions". *Physics of Plasmas*, 9(5), pp. 2244–2250. DOI: 10.1063/1.1469027 (cited on pages 110, 112).

Thaury, C. and F. Quéré (2010). "High-Order Harmonic and Attosecond Pulse Generation on Plasma Mirrors: Basic Mechanisms". *Journal of Physics B: Atomic, Molecular and Optical Physics*, 43(21), p. 213001. DOI: 10.1088/0953-4075/43/21/213001 (cited on pages 3, 17).

Thaury, C., F. Quéré, J. Geindre, A. Lévy, T. Ceccotti, P. Monot, M. Bougeard, F. Réau, P. D'Oliveira, P. Audebert, R. Marjoribanks, and P. Martin (2007). "Plasma Mirrors for Ultrahigh Intensity Optics". *Nature Physics*, 3, pp. 424–429. DOI: 10.1038/nphys595 (cited on page 78).

Thaury, C. (2008). "Génération d'harmoniques d'ordres Élevés Sur Miroir Plasma". thesis. Paris 11 (cited on page 3).

Thaury, C., P. Mora, A. Héron, J.-C. Adam, and T. Antonsen (2010). "Influence of the Weibel Instability on the Expansion of a Plasma Slab into a Vacuum". *Physical Review E*, 82(2), p. 026408 (cited on page 110).

Thévenet, M., A. Leblanc, S. Kahaly, H. Vincenti, A. Vernier, F. Quéré, and J. Faure (2016). "Vacuum Laser Acceleration of Relativistic Electrons Using Plasma Mirror Injectors". *Nature Physics*, 12(4), pp. 355–360. DOI: 10.1038/nphys3597 (cited on pages 3, 25–27, 84, 85, 89, 95, 98).

Thévenet, M., H. Vincenti, and J. Faure (2016). "On the Physics of Electron Ejection from Laser-Irradiated Overdense Plasmas". *Physics of Plasmas*, 23(6), p. 063119. DOI: 10.1063/1.4954822 (cited on pages 18, 85, 90).

Thévenet, M. (2016). "Modeling the Interaction between a Few-Cycle Relativistic Laser Pulse and a Plasma Mirror : From Electron Acceleration to Harmonic Generation". thesis. Paris Saclay (cited on pages 90, 93, 95, 96).

Thiffeault, J.-L. (2018). "The Mathematics of Taffy Pullers". *The Mathematical Intelligencer*, 40(1), pp. 26–35. DOI: 10.1007/s00283-018-9788-4 (cited on page 130).

Tian, Y., J. Liu, W. Wang, C. Wang, A. Deng, C. Xia, W. Li, L. Cao, H. Lu, H. Zhang, Y. Xu, Y. Leng, R. Li, and Z. Xu (2012). "Electron Emission at Locked Phases from the Laser-Driven Surface Plasma Wave". *Physical Review Letters*, 109(11), p. 115002. DOI: 10.1103/PhysRevLett.109.115002 (cited on page 26).

Tsakiris, G. D., K. Eidmann, J. Meyer-ter-Vehn, and F. Krausz (2006). "Route to Intense Single Attosecond Pulses". *New Journal of Physics*, 8, pp. 19–19. DOI: 10.1088/1367-2630/8/1/019 (cited on page 21).

Umstadter, D., J. K. Kim, and E. Dodd (1996). "Laser Injection of Ultrashort Electron Pulses into Wakefield Plasma Waves". *Physical Review Letters*, 76(12), pp. 2073–2076. DOI: 10.1103/PhysRevLett.76.2073 (cited on page 19).

Van der Pol, B. (1926). "LXXXVIII. On "Relaxation-Oscillations"". *The London, Edinburgh, and Dublin Philosophical Magazine and Journal of Science*, 2(11), pp. 978–992. DOI: 10.1080/14786442608564127 (cited on page 32).

Vay, J.-L. (2007). "Noninvariance of Space- and Time-Scale Ranges under a Lorentz Transformation and the Implications for the Study of Relativistic Interactions". *Physical Review Letters*, 98(13), p. 130405. DOI: 10.1103/PhysRevLett.98.130405 (cited on page 49).

— (2008). "Simulation of Beams or Plasmas Crossing at Relativistic Velocity". *Physics of Plasmas*, 15(5), p. 056701. DOI: 10.1063/1.2837054 (cited on page 48).

Vay, J.-L., C. G. R. Geddes, E. Cormier-Michel, and D. P. Grote (2011). "Numerical Methods for Instability Mitigation in the Modeling of Laser Wakefield Accelerators in a Lorentz-Boosted Frame". *Journal of Computational Physics*, 230(15), pp. 5908–5929. DOI: 10.1016/j.jcp.2011.04.003 (cited on page 57).

Vay, J.-L., I. Haber, and B. B. Godfrey (2013). "A Domain Decomposition Method for Pseudo-Spectral Electromagnetic Simulations of Plasmas". *Journal of Computational Physics*, 243, pp. 260–268. DOI: 10.1016/j.jcp.2013.03.010 (cited on pages 58, 59).

Vincenti, H. (2011). "Génération d'impulsions Attosecondes Sur Miroir Plasma Relativiste" (cited on pages 3, 45, 53).

Vincenti, H. and F. Quéré (2012). "Attosecond Lighthouses: How To Use Spatiotemporally Coupled Light Fields To Generate Isolated Attosecond Pulses". *Phys. Rev. Lett.* 108(11), p. 113904. DOI: 10.1103/PhysRevLett.108.113904 (cited on page 21).

Vincenti, H. and J.-L. Vay (2016). "Detailed Analysis of the Effects of Stencil Spatial Variations with Arbitrary High-Order Finite-Difference Maxwell Solver". *Computer Physics Communications*, 200, pp. 147–167. DOI: 10.1016/j.cpc.2015.11.009 (cited on page 58).

Vincenti, H. (2018). "Achieving Extreme Light Intensities Using Relativistic Plasma Mirrors" (cited on pages 50, 94).

— (2019). "Achieving Extreme Light Intensities Using Optically Curved Relativistic Plasma Mirrors". *Physical Review Letters*, 123(10), p. 105001. DOI: 10.1103/PhysRevLett.123.105001 (cited on page 21).

Vincenti, H. and J.-L. Vay (2018). "Ultrahigh-Order Maxwell Solver with Extreme Scalability for Electromagnetic PIC Simulations of Plasmas". *Computer Physics Communications*, 228, pp. 22–29. DOI: https://doi.org/10.1016/j.cpc.2018.03.018 (cited on pages 58, 59, 80).

Vlasov, A. A. (1968). "The Vibrational Properties of an Electron Gas". *Physics-Uspekhi*, 10(6), pp. 721–733 (cited on page 44).

Von der Linde, D. and K. Rzàzewski (1996). "High-Order Optical Harmonic Generation from Solid Surfaces". *Applied Physics B*, 63(5), pp. 499–506. DOI: 10.1007/BF01828947 (cited on page 21).

VonNeumann, J. and R. D. Richtmyer (1950). "A Method for the Numerical Calculation of Hydrodynamic Shocks". *Journal of Applied Physics*, 21(3), pp. 232–237. DOI: 10.1063/1.1699639 (cited on page 55).

Wilks, S. C. (1993). "Simulations of Ultraintense Laser–Plasma Interactions*". *Physics of Fluids B: Plasma Physics*, 5(7), pp. 2603–2608. DOI: 10.1063/1.860697 (cited on page 22).

Yee (1966). "Numerical Solution of Initial Boundary Value Problems Involving Maxwell's Equations in Isotropic Media". *IEEE Transactions on Antennas and Propagation*, 14(3), pp. 302–307. DOI: 10.1109/TAP.1966.1138693 (cited on pages 46, 54).

Yeh, C. (1965). "Reflection and Transmission of Electromagnetic Waves by a Moving Dielectric Medium". *Journal of Applied Physics*, 36(11), pp. 3513–3517. DOI: 10.1063/1.1703029 (cited on page 22).

Young, P., H. A. Baldis, P. Cheung, W. Rozmus, W. Kruer, S. Wilks, S. Crowley, W. Mori, and C. Hansen (2001). *Critical Density Interaction Studies*. UCRL-ID-142776. Lawrence Livermore National Lab. (LLNL), Livermore, CA (United States). DOI: 10.2172/15013547 (cited on page 116).

Zewail, A. H. (1994). *Femtochemistry: Ultrafast Dynamics of the Chemical Bond: Volume I*. Vol. 3. World Scientific Series in 20th Century Chemistry. World Scientific Publishing Company. DOI: 10.1142/2331-vol1 (cited on page 1).

Zewail, A. H. (1988). "Laser Femtochemistry". *Science*, 242(4886), pp. 1645–1653. DOI: 10.1126/science.242.4886.1645 (cited on page 1).

Zhang, P., N. Saleh, S. Chen, Z. M. Sheng, and D. Umstadter (2003). "Laser-Energy Transfer and Enhancement of Plasma Waves and Electron Beams by Interfering High-Intensity Laser Pulses". *Physical Review Letters*, 91(22), p. 225001. DOI: 10.1103/PhysRevLett.91.225001 (cited on pages 19, 101).

List of Figures

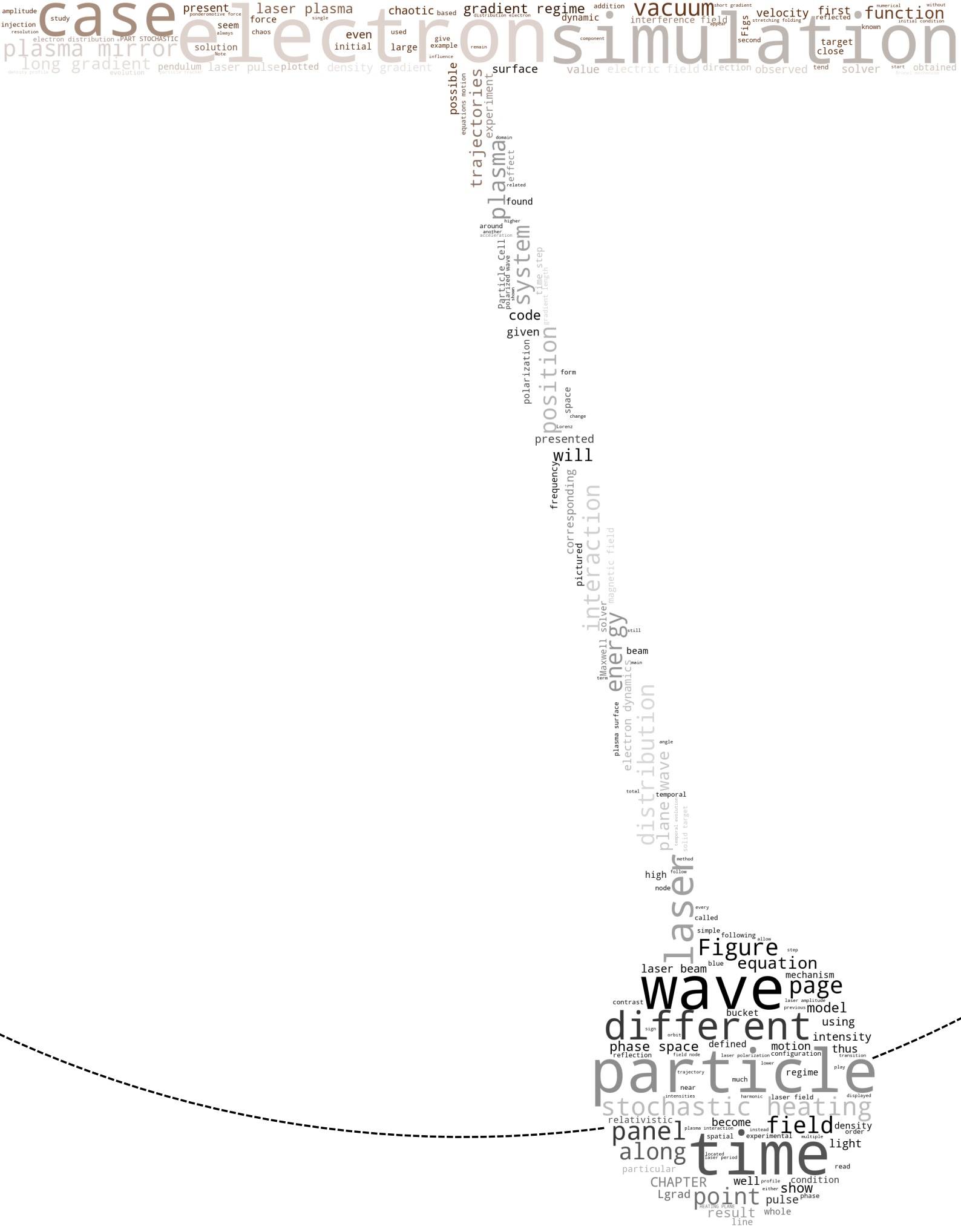

Pendulum drawn with the most used words in this thesis

université PARIS-SACLAY
ÉCOLE DOCTORALE
Ondes et matière (EDOM)

Titre : Laser Ultra Intense sur Plasmas Denses : Dynamiques Périodiques vers Chaotiques

Mots clés : miroirs plasmas relativistes, simulations PIC, chaos, solveurs de Maxwell pseudo-spectraux

Résumé :
L'émergence des lasers ultra-brefs et ultra-intenses a permis le développement d'une nouvelle branche de la physique encore largement inexplorée : la physique UHI (pour Ultra-High Intensity). Lors de la réflexion d'un tel laser sur une cible solide, l'intensité au foyer peut atteindre des valeurs aussi importantes que 10^{18-20} W.cm^{-2}, suffisamment pour ioniser complétement la matière. Le plasma ainsi formé se détend sur une longueur caractéristique L, nommée longueur de gradient. Quand $L \ll \lambda$ (longueur d'onde du laser), le plasma dense se comporte comme un miroir de qualité optique capable de réfléchir spéculairement la lumière incidente : c'est un miroir plasma. Ce système physique remarquable peut être utilisé dans de multiples applications principalement comme source compacte de faisceaux de particules à hautes charges et hautes énergies ou de lumière intense, principalement ultraviolet ou X, grâce à un phénomène de génération d'harmoniques d'ordres élevés. Le bon contrôle de ces sources nécessite de clairement identifier les différents mécanismes de couplage entre lumière et matière en jeu lors de l'interaction.
Dans ce manuscrit, cela est rendu possible grâce à de précises simulations de type Particle-In-Cell (PIC) réalisées avec le code WARP+PXR. Ce nouveau code emploie un solveur pseudo-spectral pour résoudre les équations de Maxwell. Celui-ci améliore grandement la précision des simulations et notamment des émissions harmoniques et électroniques, que les solveurs plus standards ne parviennent à décrire, même à hautes résolutions. Grâce à des simulations WARP+PXR, nous avons étudié l'influence de L sur les observables expérimentales que sont les émissions de lumière et de particules, quand un laser de puissance ($I = 10^{19}$ W.cm^{-2}) se réfléchit sur un plasma dense. Notre étude révèle une claire transition entre un mécanisme périodique en temps et un processus chaotique quand l'interface devient plus lisse.
Nous nous sommes principalement concentrés sur le deuxième mécanisme, appelé chauffage stochastique pour lequel des études en profondeur vont être menées en fonction de différents paramètres d'interaction. Dans ce régime, les électrons de la partie sous-dense du plasma subissent une dynamique chaotique dans l'onde stationnaire formée par la superposition des ondes incidente et réfléchie, ce qui leur permet d'absorber une importante part de l'énergie laser. La nature fondamentale de la dynamique en jeu est révélée grâce aux équations du mouvement au sein des deux ondes que l'on peut réduire en équations de pendules forcés (comme celui de Kapitza), systèmes bien connus comme chaotiques. Cette correspondance apporte une intuition physique profonde sur le comportement des électrons pour différentes configurations laser. Ceci nous permet in fine de prédire les principaux aspects du chauffage stochastique.

Title : Ultra-High Intense Laser on Dense Plasmas : from Periodic to Chaotic Dynamics

Keywords : relativistic plasma-mirrors, PIC simulations, chaos, pseudo-spectral Maxwell solvers

Abstract :
The advent of high power femtosecond lasers has paved the way to a promising and still largely unexplored branch of physics called Ultra-High Intensity physics (UHI). Once such a laser is focused on a solid target, the laser intensity can reach values as large as 10^{18-20} W.cm^{-2}, for which matter is fully ionized. The plasma thus formed expands towards vacuum on a spatial scale characterized by a quantity L called the density gradient scale length. When $L \ll \lambda$ the laser wavelength, the dense plasma therefore acts as an optical mirror that specularly reflects the incident light :, it is a plasma mirror. This remarkable physical system can be used in many scientific applications as compact source of high-energy and high-charge particle beams (electrons, ions) or bright source of radiations ranging from extreme ultraviolet-rays to X-rays through high harmonic generation processes. In order to finely control these sources, it is required to properly identify the different coupling mechanisms between light and matter at play during the interaction.
In this manuscript, this has been made possible by performing accurate Particle-In-Cell (PIC) simulations with the WARP+PXR code. This recently developed code advances Maxwell's equations in Fourier space, which proves to correctly model harmonic/electron emissions that standard codes fail to accurate describe even at high resolution. Based on WARP+PXR PIC simulations, we investigate the influence of L on the experimentally observed emission of light and particles, when a high-power laser pulse ($I = 10^{19}$ W.cm^{-2}) reflects off a dense plasma. Our study reveals an unambiguous transition from a temporally periodic mechanism to a chaotic process as the interface becomes smoother.
In particular, the latter mechanism, named stochastic heating, is fully characterized as well as its domain of validity in terms of laser-plasma parameters. In this regime, electrons in the underdense part of the gradient are exposed to the standing wave formed in front of the overcritical part of the plasma by superposition of incidence and reflected beams. While evolving in the two waves, electrons behave chaotically and absorb an important fraction of the laser energy. The nature of the interaction is revealed by reducing the equations of motion of particles in two waves to physical systems, such Kapitza's pendulum, well-known to exhibit chaos. That relation gives deep physical intuitions on how electrons behave in different laser configurations, which allows us to predict major features of stochastic heating.

Université Paris-Saclay
Espace Technologique / Immeuble Discovery
Route de l'Orme aux Merisiers RD 128 / 91190 Saint-Aubin, France